Library Copy

THE DESIGN AND TESTING

OF

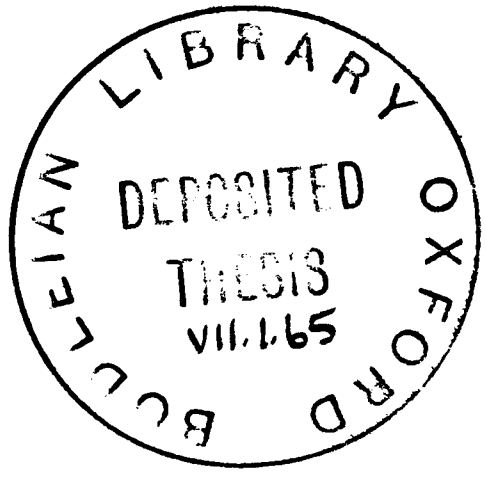
DIELECTRIC-LOADED

LINEAR ELECTRON ACCELERATOR STRUCTURES

by

M.F.B. Moffat

Keble College, Oxford,
August, 1964



D.Phil. thesis for deposit in the Bodleian Library

Candidates borrowing the library copy of their thesis for use at the oral examination must ensure that the thesis is returned to the Secretary of Faculties immediately after the oral examination and in any case at least seven days before the day on which they propose to take their degree.

Abstract

The usefulness of a linear electron accelerator in providing short bunches of relativistic electrons for injection into interwave sources such as magnetic undulators and Cerenkov couplers is pointed out. Shorter bunch lengths can result in coherent radiation at shorter wavelengths. An experimental example of this effect is given, and the design of a linac to produce short electron bunches is then described. The historical background to the choice of a dielectric disc-loaded slow-wave structure is explained together with the reasons for adopting a 2 MeV beam energy and a 1.8 cm operating wavelength. Periodically loaded waveguides and their mode of operation as linac slow-wave structures are described, and the reasons for favouring travelling-wave operation with a phase change per periodic length of $\pi/3$ radians are given.

Phase space concepts applied to the design of the electron buncher and main accelerator section are shown to give an accurate description of the fields and wave velocities required for good bunching and small beam energy spread. The theoretical design to give an effective bunch length of 0.3 mm is described.

Measurements and proving tests at high and low R.F. power, and the investigation of physical and chemical properties relating to linac fabrication and operation indicate that certain titania and magnesium titanate ceramics are suitable as loading material, provided that some precautions are taken against surface breakdown. This appears to be

initiated by sparking between the dielectric-loading disc rims and the metallic wall of the linac structure. The sparking can be greatly reduced by grinding the rims to a fine finish and metallizing them with copper. Surface breakdown can be inhibited by coating the discs with a thin protective layer of lead borate glaze or P.T.F.E. Electron multipactor resonances between discs are largely avoided by excluding oil from the evacuated system. The dielectric surface conductivity is very low and so a well focused electron beam is essential if surface charging is to be avoided.

Theoretical and experimental results for the test structures are not in close agreement, especially for shunt impedance. Ohmic losses are about four times higher than the theory suggests. This is thought to be due partly to inexact boundary-matching of fields in the theory, and partly to surface effects giving rise to a relatively high resistivity in the waveguide wall. Practical test cavities give consistent and repeatable results, and the necessary high degree of physical accuracy has been attained in their construction.

A practical design and fabrication method is given for the main accelerator section, and the proposed physical realisation of the buncher-accelerator system is described.

CONTENTS

		Page
1.	Introduction	1
	1.1 Purpose of the Project: Interwave Generation and Application	1
	1.2 Historical Background to the Dielectric Loaded Linac	2
	1.3 Accelerator Parameters and Terminology	6
	1.4 Plan of the Dissertation	9
2.	Preliminary Considerations in the Accelerator Design	12
	2.1 Outline of Linear Accelerator Operation	12
	2.1.1 Basic Acceleration Mechanism	12
	2.1.2 The Accelerating Field	13
	2.2 Previous Experience with Undulators and 10 cm Linacs	14
	2.3 Choice of Operating Characteristics	16
	2.3.1 Output Energy and Beam Power	16
	2.3.2 Wavelength	16
	2.3.3 Effective Bunch Length	17
	2.3.4 Other Characteristics	17
	2.4 Metal Loading versus Dielectric Loading	17
	2.4.1 Efficiency and Shunt Impedance	17
	2.4.2 Properties of Available Dielectric Materials	21
	2.4.3 Choice of Dielectric Material	22
3.	The Mode of Operation	24
	3.1 The Periodically-Loaded Waveguide	24
	3.2 Travelling Wave versus Standing Wave Operation	27
	3.2.1 Shunt Impedance	28
	3.2.2 The Advantages of R.F. Feedback	29
	3.2.3 The Optimum, Attenuation-Limited and Practical Lengths	31
	3.2.4 The Build-Up Time of the Fields	36
	3.2.5 Energy Velocity and Group Velocity	37
	3.2.6 Resonant Mode Separation and Frequency Stability Considerations	38
	3.3 Summary and Conclusions	42

Page

4. The Theoretical Postulates For Good Bunching 45

4.1 The Equations of Particle Motion 45
4.2 General Design Considerations 51
4.3 Pre-bunching 55
4.3.1 Matching of Axial Ratios 55
4.3.2 A Pre-bunching Cavity 56
4.4 The Linac Design for Good Bunching 59
4.4.1 The Bunching Section 59
4.4.2 The Main Accelerating Section 63
4.5 Trajectory Computations 65
4.6 The Effects of Errors in Fields and Velocities 67
4.6.1 Errors in Phase Velocity 68
4.6.2 Errors in Accelerating Field 69
4.6.3 Errors in Beam Injection Velocity 69

5. The Assessment of the Properties of Titania Ceramics 70

5.1 The Measurement of K and tan δ at 1.8 cm Wavelength . . . 70
5.2 Practical Physical and Chemical Considerations 71
5.2.1 Temperature Coefficients of Permittivity and Linear Expansion 72
5.2.2 The Metallising of Disc Rims 73
5.2.3 The Glazing of the Discs. 75
5.2.4 P.T.F.E. Coating 80
5.2.5 Chemical Attack and Electroforming 81
5.2.6 D.C. Surface Conductivity 83
5.2.7 Dimensional Tolerances and Machining 84
5.3 High Power Tests 88
5.3.1 Previous Experiments at S-Band 89
5.3.1.1 The A.E.R.E. Titania-Loaded Linac . . . 89
5.3.1.2 The Experiments at Queen Mary College and Vancouver 91
5.3.2 The Test-Cavity Design 93
5.3.2.1 Cavity Dimensions 94
5.3.2.2 Physical Features 96

Page

5.3.3 Preliminary Low Power Tests 99
5.3.3.1 Coupling and Tuning. 99
5.3.3.2 Measurements of Q_o 101
5.3.3.3 Measurement of r_{sh}/Q_o 103
5.3.4 The High Power Tests 106
5.3.4.1 Glazed Titania Disc 106
5.3.4.2 Unglazed Titania Disc 109
5.3.4.3 Glazed and Metallised Titania Disc . . 110
5.4 General Assessment 112

6. The Theory of the Accelerator Structure 114

6.1 The Dielectric-Loaded Slow Wave Structure 114
6.2 The Anisotropic Theory 115
6.3 The Discrete Disc Theory 119

7. The Practical Design of the Accelerator Structure 122
7.1 The General Design 122
7.2 Bunching Section Design 124
7.2.1 Use of the Anisotropic Approximation 124
7.2.2 Comparison of Theory with Experiment 125
7.2.3 The Relaxation Method 130
7.3 The Main Accelerating Section 131
7.3.1 The Primary Objectives 131
7.3.2 Fabrication Methods 132
7.3.3 Theoretical Perturbation Results: Physical Tolerances 135
7.3.4 Design Procedure for Main Section 138
7.3.5 Summary of Low Power Test Cavity Results . . . 149
7.4 High Power Tests: Second Series 151
7.4.1 Glazed Disc Structure 151
7.4.2 P.T.F.E. Coated Disc Structure 155
7.4.3 Interpretation of the Results 157
7.4.4 Conclusions 161

Page

8. The Proposed Physical Realisation of the Buncher-Accelerator System 162

8.1 The Microwave Circuit 162

8.1.1 General Features 162

8.1.2 Special Waveguide Components 163

8.1.2.1 R.F. Source Protection 163

8.1.2.2 R.F. Feedback Bridge 164

8.1.2.3 R.F. Couplers 166

8.1.3 The Modulators 170

8.2 The Linac Structure 171

8.2.1 General Scheme 171

8.2.2 Evacuation 172

8.2.3 Heat Dissipation 173

8.3 Beam Focusing 175

Conclusions 178

Appendices:-

I The Equations of Motion for Exponential Change in Axial Ratio

II The Accelerating Field and the Phase Velocity

III The Effect of the Beam on the Accelerating Field

IV A Method of Solution of Transcendental Equations

V Dielectric Properties of Titania Ceramics at Microwave Frequencies

References

Principal Symbols Used

List of Figures

Fig.		Immediately Following Page
1.	Phase Relations between Particles and Wave	12
2.	Cylindrical Disc-Loaded Waveguide	13
3.	Variation of Shunt Impedance with Dielectric tan δ	22
4.	Reference Planes in π-Mode Structure	24
5.	Dispersion Curves	25
6.	Variation of Shunt Impedance with β L	29
7.	Basic Microwave Feedback Circuit	30
8.	Variation of Figure of Merit with Structure Length	34
9.	Confluent and Non-Confluent Pass Bands	38
10.	Basic Bunching and Accelerating System	45
11.	Particle Stability in the Phase Plane	49
12.	Variation of Bunching Ratio with Initial Phase Velocity	54
13.	Example of Phase-Plane Trajectories of Particles	54
14.	Linac Acceptance with Pre-bunching Cavity	57
15.	Variation of Peak Axial Electric Field and Phase Velocity along Buncher	62
16.	Particle Trajectories without Beam Loading	66
17.	Particle Trajectories with 75 mA Beam Loading	66
18.	Pilot Plant for Vacuum Coating	74
19.	Angular Variation of Annular Width of Sample Disc	85
20.	Surface Breakdown on Unglazed Titania Disc	92
21.	High Power Test Cavity, Schematic	93
22.	Solid Disc Cavity	94
23.	Low Power Test Circuit	99
24.	Illustrating Degrees of Coupling	100
25.	Illustrating the Measurement of Q	101
26.	r_{sh}/Q Measurement Apparatus	104
27.	Copper Bead for Field Perturbations	104
28.	High Power Test Circuit	107
29.	Effect of Rim Sparking on R.F. Pulse Reflected from Cavity	107
30.	Glazed Titania Disc after High Power Test	107

Fig.		Immediately Following Page
31.	Rim Breakdown on Glazed and Unglazed Titania Discs	113
32.	Laminated Dielectric Medium	113
33.	Dispersion Curves: Titania Loading : v_s = 0.5c (Design)	125
34.	Dispersion Curves: Titania Loading : v_s = 0.815c (Design)	125
35.	Structure Jig and Mandrel	134
36.	Perturbation Results : Anisotropic Theory	135
37.	Perturbation Results : Discrete Disc Theory	135
38.	Perturbation Results : Discrete Disc Theory	136
39.	Low Power Cavity Test Rig	142
40.	Variation of v_s with b : Discrete Disc Theory	143
41.	25 Titania Disc Test Section	144
42.	Experimental Dispersion Curves; Early Cavities . . .	144
43.	Experimental Dispersion Curves; Unglazed 12 Disc and Glazed 6 Disc Cavities	144
44.	Experimental Dispersion Curve; 25 Disc Cavity	144
45.	Experimental Dispersion Curve; 37 Disc Cavity	144
46.	Variation of Phase Velocity and Energy; Synchronous Conditions	148
47.	Variation of the Ratio of Disc Thickness to Pitch; Synchronous Conditions	149
48.	Axial Field Measured in a 12 Disc Cavity; $\beta L = \pi/3$ . .	150
49.	High Power Test Circuit (Second Version)	153
50.	Glazed Titania Discs after High Power Test (Second Series)	155
51.	P.T.F.E. Coated Titania Discs after High Power Test (Second Series)	155
52.	Linac Microwave Circuit	163
53.	Field Build-Up Factor using Feedback	164
54.	R.F. Couplers	166
55.	The Linac Structure	172
56.	Variation of Focusing Magnetic Field	176

List of Tables

		On or Immediately Following Page
1.	Properties of some Linear Electron Accelerators . . .	18
2.	Chemical Attack on some Possible Linac Structure Materials	82
3.	Bonding between Metallised Disc Structure and an Electroformed Copper Waveguide Tube	82
4.	Mechanical Tolerances on Manufactured Titania Discs. .	85
5.	Methods for Measuring Ceramic Discs	88
6.	Bunching Section Design : Anisotropic Approximation. .	124
7.	Bunching Section Design : Anisotropic Approximation; Copper Loss Doubled	124
8.	Summary of Low Power Test Cavity Results	146

ACKNOWLEDGEMENTS

The author wishes to thank Dr. Hans Motz, the supervisor of this project, for his advice and support throughout the course of this work.

Thanks for advice and assistance are also due to Dr. Donald Walsh and the author's colleagues at the University Engineering Laboratory, Oxford. Special mention should be made of those most closely concerned with the J-Band Linac Project, namely, Mr. A.G.A.M. Armstrong, Dr. J.M. Free, Mr. E.V. Gilbert, Dr. A.J. Lichtenberg and Mr. E. Sang. Excellent technical assistance was given by Mr. D.G. Powles and Mr. P. Stannard. The precision engineering of the disc structures was ably carried out by Mr. B. Kronsteiner and Mr. E. Henneage under the supervision of Mr. H. Gearing.

The assistance of Mrs. J. Waring and the author's wife in the final preparation of the thesis is greatly appreciated.

The author is indebted to the Department of Scientific and Industrial Research for personal financial support during the course of the work. Grateful acknowledgement for general financial support is made to the Paul Fund of the Royal Society and the United States Air Force.

CHAPTER 1

Introduction

1.1 Purpose of the Project: Interwave Generation and Applications

Although devices have been made which will generate coherent radiation with power densities of many hundreds of watts per square centimeter at wavelengths less than 0.1 mm, and with peak powers of several tens of kilowatts at a few millimetres wavelength, no coherent sources are yet available which will generate above about 10 mW in the waveband 0.1 mm to 1 mm. To the author's knowledge, the most successful device to date has been the 'O' Carcinotron of Convert et al.,[1] which has produced 5 mW at about 0.6 mm.

The need for coherent sources of adequate power operating in this "interwave" region, a name coined by Motz, is felt chiefly in the fields of solid-state spectroscopy, plasma physics and communications. Workers dealing with paramagnetic and cyclotron resonances in solids, and molecular chemists engaged in infra-red spectroscopy would welcome an interwave source. In the work on high temperature plasmas, electron densities corresponding to interwave plasma frequencies have to be investigated. In the communications field, the ever increasing need for larger available bandwidths could be well met by an interwave system. Concise surveys of the motivation and the achievements of workers concerned with filling in this "gap in the spectrum" have recently been given by Coleman.[2,76]

The work to be described here is concerned with the theoretical and experimental exploration following the proposals of Motz[3] that relativistic electron beams can be made to radiate coherent power at interwave frequencies in devices such as the magnetic undulator (see Chapter II) and Cerenkov coupler.[87] The prime requisite in this scheme is a tightly bunched, relativistic electron beam with a high current. We are, therefore, primarily concerned with the design and construction of a most convenient source of such a beam, namely, a linear electron buncher-accelerator, or "linac".*

1.2 Historical Background to the Dielectric Loaded Linac

Amongst the earliest references to linear systems in which charged particles are progressively and synchronously accelerated by high axial electric fields produced by R.F. sources is that of Wideroe.[4] In his scheme potassium ions passed through a series of coaxial metal tubes in synchronism with R.F. voltages applied to the tubes. The electric field between tubes was always in a direction to accelerate the ions as they passed from the interior of one tube to the interior of the next. The idea was developed and used by Sloan and Lawrence[5,6] in producing X-rays with 1 Me V mercury ions using valve oscillators of wavelength 30 m and 50 m as their R.F. sources. They predicted that the production of 10 Me V particle beams was "an entirely practicable matter".
In 1939 Woodyard took up the idea and published a comparison with the betatron in 1946.[12] Also in 1946, Alvarez and his colleagues at Berkeley suggested a similar approach to the design of a proton linac[7] utilising 200 Mc/s radar components developed during the war. Other

* Other bunched beam sources include the Rebatron[88] and the Microton.[89]

workers were investigating the possibilities of using the high power of magnetrons and klystrons in microwave linacs for electrons. New ways of keeping the particles in an accelerating field were suggested. Most schemes involved slowing down a transverse magnetic (TM) wave to the particle speed by loading a waveguide through which both beam and wave were passing with periodic obstacles, metallic or dielectric. Phasing was arranged such that energy was transferred from the wave to the beam. Representative of this effort were the works of Slater, et al.,[8,9] Ginzton, et al.,[10] and Fry, et al.[11] In early 1948 there were at least eight teams engaged on this aspect of electron acceleration, seven in the U.S.A., and the British group at TRE, Malvern. This does not take into account the interest being taken in the problem by industrial laboratories such as General Electric, Metropolitan-Vickers and Standard Telephones and Cables.

Most of these projects were successful, and linac particle energies steadily approached 1 Ge V as the years passed by. The 2 mile, 35 Ge V electron linac being built at Stanford exemplifies the fact that the requisite components can now be reliably produced in great quantity.

Chiefly because of simpler fabrication problems, most of the effort was devoted to the metal-disc-loaded, cylindrical waveguide linacs, but several authors[13,14] suggested slow-wave structures comprising metal-sheathed dielectric rods with a small axial bore for the electron beam to pass through. These "solid" dielectric structures were

investigated closely[15-19] but it was found that the ohmic losses were possibly higher than those in the corrugated metal waveguides. At least one "solid" structure was built and tested using a quartz tube[20], but was found to be unsatisfactory at high power because of dielectric breakdown and surface charging in the bore.

Apart from high losses in "solid" dielectric structures, it was shown that the energy density was very much higher in the dielectric itself than in the central region where the high fields were really required.[21] The "anisotropic dielectric" loading of the waveguide suggested by Shersby-Harvie,[15,22,23] in which the dielectric constant of the material was several times larger in the transverse plane than in the axial direction, proved to be a key to the problem. This scheme was shown to combine the required variation in wave slowing factor with an axial field higher than that attainable in a dielectric tubular structure. The proposed practical structure to simulate the anisotropic dielectric consisted of a metal tube in which were spaced washer-shaped ceramic discs, the relative dimensions being similar to those encountered in metal-loaded linacs.

The construction of a travelling-wave machine designed on this basis was begun at A.E.R.E., Malvern. Its designed and actual performance are the subject of several papers. A final review of the work, including the relevant references[24] appeared in 1956.

The difficulties in accounting for the discrepancies between the predicted and actual properties of this 1.5 Me V, 15 m A machine prompted the continuation of similar research at Queen Mary College, London.

Particular attention was given to the following problems:

(a) The breakdown of the titania ceramics used as loading material when subjected to high electric fields.[25]

(b) The criteria for choice between a resonant and a travelling-wave linac.[26]

(c) The multipactor effect on dielectric loaded structures,[27] first reported by the A.E.R.E. group.[28]

A high velocity resonant section loaded with glazed titania discs was operated at 10 cm wavelength using a low current β-ray source of electrons. The chief feature of this accelerator was that its operation at the π-mode was made more stable by making the pass-bands confluent, thereby increasing the mode separation.[29]

As will be seen in later chapters, the efficiency of a dielectric loaded linac becomes considerably greater than that of its metal loaded counterpart as the operating wavelength is shortened. Also, it is found that the attainable phase bunching of the accelerated particles does not alter much as the operating wavelength is decreased. Interwave generators fed by relativistic electron beams require the spatial bunching of the particles to be less than one half wavelength of the radiation if the output is to be reasonably phase coherent. It was therefore considered worthwhile assessing the possibility of constructing a linac specifically designed to feed undulators and Cerenkov generators.[30,31] Originally, it was planned to carry out the linac design study at Queen Mary College and the undulator work at Oxford.

However, Dr. Walker's team broke up and it was decided that all the work on the project should be done in Oxford. Several members of the Q.M.C. group joined Dr. Walker at the University of British Columbia and continued to do valuable work on dielectric breakdown, dielectric loaded tubes, and microwave windows, but one of the group came to work on the Oxford project.

The above outline of the dielectric-loaded linac development up to the beginning of the Oxford project makes little mention of the metal-loaded structures and high-power resonant cavities which have been used as interwave generator injectors hitherto. An example of the former type will be discussed in Chapter II.

1.3 Accelerator Parameters and Terminology

To describe the operation of a linac we use sets of parameters relating to the wave dispersive properties of the particle-wave interaction structure, and to the energy dissipative behaviour of the system. We shall now define the more important quantities.

1.3.1 The phase velocity of the synchronous wave

$$v_s = \frac{\omega}{\beta} \tag{1.1}$$

where ω is the angular frequency and β is the phase constant of propagation.

1.3.2 The group velocity of the synchronous wave

$$v_g = \frac{d\omega}{d\beta} \tag{1.2}$$

We shall postpone a discussion of the relationship between group and energy velocity until section 3.2.5.

1.3.3 The shunt impedance

$$r_{sh} = \frac{E^2_{ms}}{P_d} \qquad (1.3)$$

Where E_{ms} is the maximum axial electric field of the synchronous wave and P_d is the power dissipated per unit length of the structure.

1.3.4 The series impedance of a travelling-wave accelerator

$$r_{se} = \frac{E^2_{ms}}{P} \qquad (1.4)$$

where P is the power flux along the structure.

1.3.5 The loss length l_o is here defined as the length over which the power flux falls from P_1 , its initial value to P_1 /e with no beam loading.*

$$\text{Since } r_{sh} = \frac{E^2_{ms}}{P_d}$$

$$= \frac{E^2_{ms}}{-\frac{\partial P}{\partial z}}$$

$$\text{we have } \frac{r_{sh}}{r_{se}} = \frac{P}{-\frac{\partial P}{\partial z}}$$

$$\text{or } \int \frac{dP}{P} = - \int \frac{r_{se}}{r_{sh}} \cdot dz$$

* e is the base of natural logarithms

Integrating, we get

$$P = P_1 e^{-\alpha z} \tag{1.6}$$

where $$\alpha = \frac{r_{se}}{r_{sh}}$$

Whence $$\ell_o = \frac{1}{\alpha} = \frac{r_{sh}}{r_{se}} \tag{1.7}$$

1.3.6 The maximum kinetic energy gained by a particle

$$eV = \int_o^{\ell} eE_s \, dz \tag{1.8}$$

where ℓ is the length of the accelerator,

E_s is the accelerating field experienced by the particle

V is the output beam voltage

and e is the electronic charge.

1.3.7 The efficiency with beam loading

$$\eta = \frac{V I}{P_s} \tag{1.9}$$

where I is the beam pulse current

and P_s is the pulse power delivered by the source.

1.3.8 The figure of merit, which is rather more useful than η when comparing performances of different linear accelerators

$$\eta' = \frac{V^2}{P_s \ell} \tag{1.10}$$

1.3.9 The "Q per unit length"

$$Q_l = \frac{\omega U}{P_d} \qquad (1.11)$$

where U is the stored energy per unit length of structure. The usefulness of Q_l should become apparent when the analysis of structure losses is made.

1.4 Plan of the Dissertation

Earlier in this chapter we have described the reasons for trying to design and produce a 1.8 cm linac for electrons, and we have outlined the history of linac development. Section 1.3 is intended to define the basic quantities which are generally used in describing linacs. Several more specialised quantities will be introduced as the dissertation progresses.

In the next chapter we shall describe experiments at 10 cm wavelength which have added impetus to the desire to construct a shorter wavelength electron linac for undulators. Also in chapter II and in chapter III the collation of information about the most suitable type of linac is presented together with the reasoning which led to the selection of the basic features of the proposed machine.

We then look more closely at the R.F. electromagnetic fields required for good bunching and tolerable energy spread, and calculate the effects of field and velocity errors on particle trajectories.

The dielectric properties of the chosen loading material (titanium dioxide, see section 2.4.3) are surveyed in chapter V.

The experiments on this material have been carried out in parallel with all the design work on the linac because the dielectric tests should be carried out as far as possible in typical linac structures and conditions.

Chapter VI deals with the theoretical basis of determining the linac dimensions and performance figures which will make it possible to subject an electron beam to the fields prescribed in Chapter IV.

The chapters summarised so far lead to the stage where we have the theoretical basis for the periodic structure, and where we know that acceptable behaviour of protected titania loading discs under high-power accelerator conditions is likely to be attainable. Chapter VII is intended to show how the accurate dimensions of the required periodic structure are determined by a step-by-step combination of theory and experiment. Emphasis is placed upon the design of the "uniform" high velocity section. The difficulties of bunching section design are explained together with the suggested remedy currently being attempted by other workers in this laboratory. Multi-disc structures similar to those to be used in the linac itself have been tested at high power. A description of these tests concludes Chapter VII. Chapter VIII describes the proposed physical form of the system, and discusses the required properties of the components.

Finally, there are several Appendices which give useful peripheral information and elucidate some of the more complicated points raised in the text.

CHAPTER II

Preliminary Considerations in the Accelerator Design

2.1 Outline of Linear Accelerator Operation

2.1.1 Basic Acceleration Mechanism

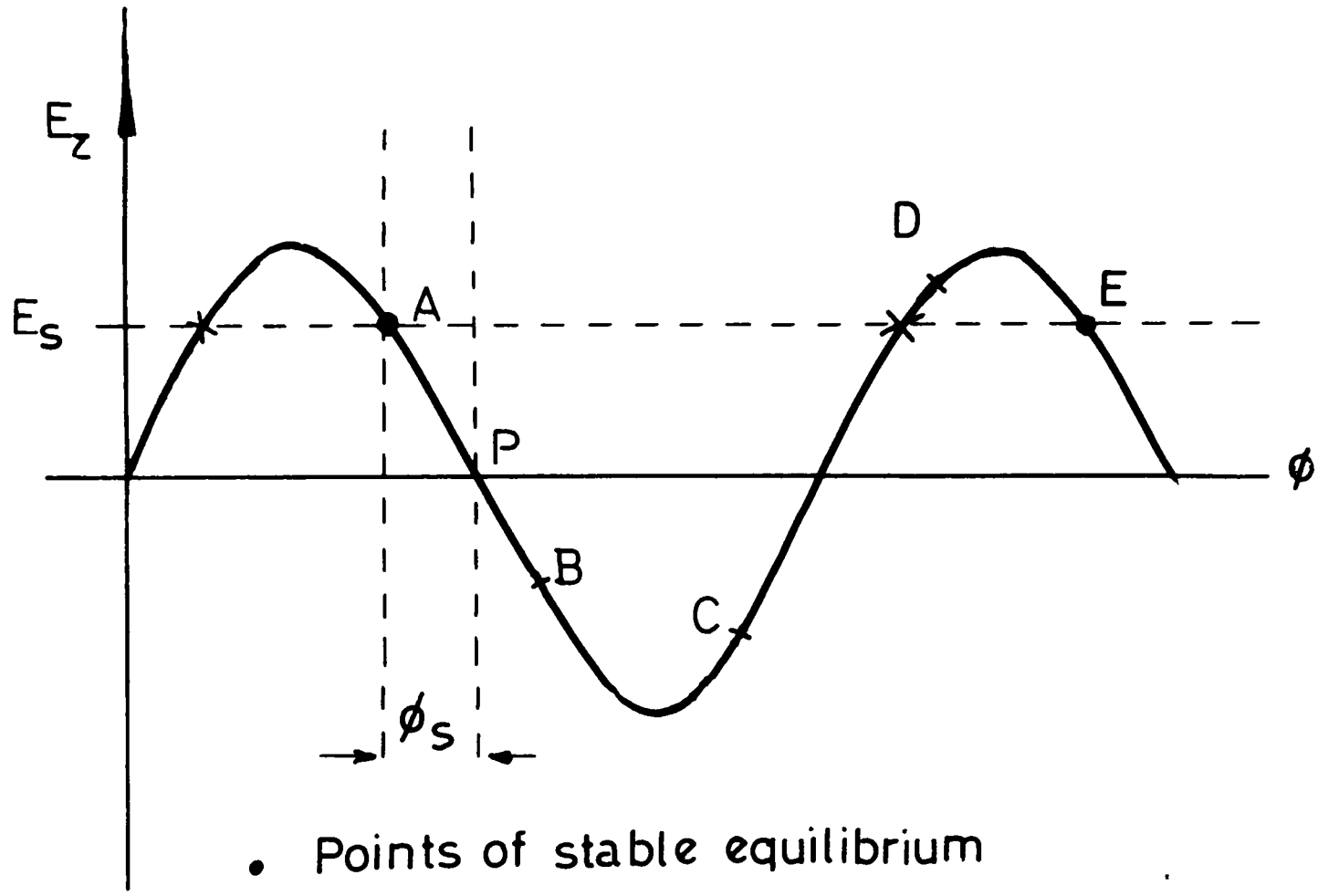
We shall firstly illustrate the significance of ϕ_s, the phase angle of the particles moving in synchronism with the accelerating wave, and show how acceleration and bunching can come about. Fig. 1 shows the instantaneous phase relation between four negatively charged particles and the longitudinal component of electric field in an electromagnetic wave travelling in the same direction as the particles and initially with the same speed. We have tacitly assumed some method of slowing the wave velocity to less than c, the velocity of light.

Particle A lies in an acceleration region, and as time progresses it will move forward in phase towards the field node at P unless the wave velocity is increased at the same rate as that of the particle, i.e. in synchronism with the particle. If we arrange that particle A is accelerated in a fixed phase

$$\phi = \pi - \phi_s \qquad (2.1)$$

then the wave velocity and particle velocity must necessarily be equal at all times. We symbolise this synchronous velocity as v_s.

Assuming that particle A is accelerated synchronously we can qualitatively examine the phase shifts of particles B, C and D. Particles B and C will be slowed down and will slip back in phase. Depending upon the magnitude of E_z the electric field, v_s, and ϕ_s they



• Points of stable equilibrium

x Points of unstable equilibrium

FIG. 1. PHASE RELATIONS BETWEEN PARTICLES AND WAVE

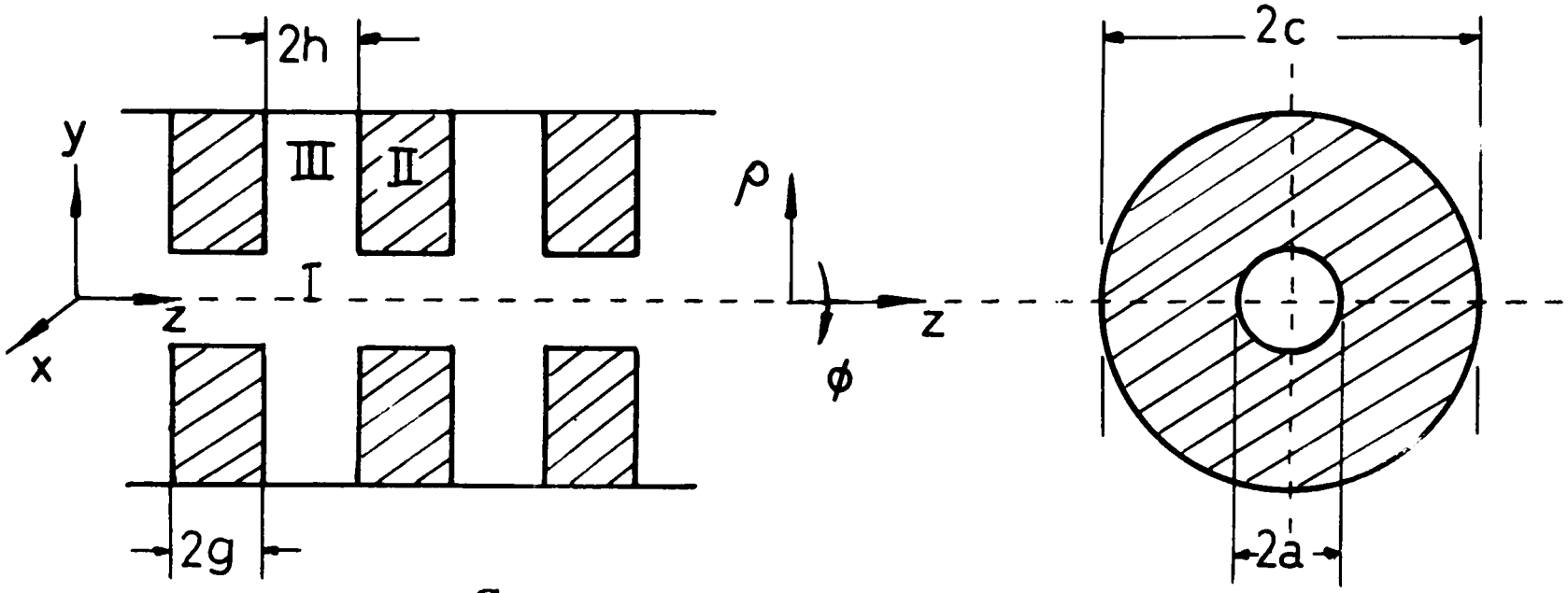
may be 'caught' and perform phase oscillations about A. Otherwise they will continue to fall back in phase and will not be accelerated. Particle D will initially move forward in phase and eventually perform phase oscillations about the point E. All captured particles will perform phase oscillations about A (and E, etc.), and longitudinal phase bunching about A (and E, etc.) can be achieved by varying E_z and v_s so that the oscillations are damped.

The above is intended to be an introductory physical picture only. A more exact treatment of particle trajectories is given in Chapter IV.

2.1.2. The Accelerating Field

In section 1.2 we described the historical development of the linac without detailing the operation of each type of machine. In this sub-section we shall show how modern linac structures provide the accelerating field, and in subsequent sections a detailed discussion of these structures will be presented.

Throughout the development of the linac the idea of cascading acceleration regions (due to Ising[42]) has persisted. Modern linacs comprise circular waveguides loaded periodically with metal or dielectric discs which have a central hole through which the beam passes (see Fig. 2). In unloaded circular waveguides E and H modes propagate at phase velocities which decrease towards c as the frequency is raised. In linac waveguides the wave velocity may be made considerably less than c so that an E mode with an axial component of electric field can travel



$$b=\frac{g}{g+h} \qquad L=2(g+h)$$

FIG. 2. CYLINDRICAL DISC-LOADED WAVEGUIDE

at the speed of the beam and transfer energy to it. The E_{01} mode is normally used because it has an electric field maximum along the axis.

We can see how slowing down of waves in metal-loaded linacs comes about if we think of the structure as a series of cascaded resonant cavities (cf. Wideroe[4]) coupled by axial holes. Because each cavity stores more energy per unit volume than the disc-free waveguide for a given power flux, they can be thought of as inductively coupled resonant L-C-R lumped circuits. The consequent phase delay in a signal passing through these circuits is manifest by the reduction in the phase velocity of a wave propagated down the structure.

In a dielectric loaded structure the wave is slowed because the phase velocity of electromagnetic waves is less than c in a medium where K, the relative permittivity is greater than unity.

2.2 Previous Experience with Undulators and 10 cm Linacs

Apart from the many theoretical treatments of radiation from fast electron beams, the results of experiments with bunched beams in various types of radiator have indicated that the effective axial bunch length limits the degree of phase coherence which can be achieved in the radiated output.[32-39] To illustrate this point we shall briefly describe the undulator work in which the author assisted Dr. D. Walsh, and which is fully reported elsewhere.[40,41]

Two extreme conditions of the electron beam injected into the undulators can be considered. The infinitely bunched beam in which n electrons form a point charge of magnitude ne will radiate phase-coherent power proportional to n^2 when undulated. The n-electron bunch which is long compared with the radiated wavelength and in which the electrons are randomly disposed will radiate power proportional to n, and this radiation will not be phase-coherent.

The output bunched condition of the 2MeV electron beam from the 10 cm wavelength metal-loaded linac used in the Oxford undulator experiments lay between these two extremes. Experiments with undulators designed to radiate at 8 mm and 4 mm showed that if the output power was assumed to be proportional to n^{α} then

at 8 mm $\quad \alpha \approx 1.7$

and at 4 mm $\quad \alpha \approx 1$

With one of the undulators set up for 8 mm, α was found to be 1.7, and the detected undulator radiation was of 550 mW when the beam current was 20 mA. If the bunch length had been short enough for α to have approached 2.0 then the radiated power would have been about 400 W. Calculation of the effective axial bunch length would be an arduous process but we can at least reasonably deduce that it was less than 8 mm and was possibly about 4 mm. These two values correspond to electrons being packed into phase regions of width 29° and 14° respectively with the linac operating wavelength at 10 cm.

Clearly, to generate higher powers in the undulator we need to pack the electrons axially into as small a fraction of the linac wavelength as possible, and we must make the linac wavelength itself as small as possible. This axial bunching must not entail inordinate radial debunching or energy spread. Both of these latter effects could cause increased loss of beam along the undulator, and an increase in energy spread would widen the undulator spectrum.

2.3 Choice of Operating Characteristics

2.3.1 Output Energy and Beam Power

Undulator mode theory shows that a beam energy of about 2 MeV can be used in radiators of practicable dimensions to generate waves in the region 0.1 mm to 1.0 mm. Experience indicates that 2 MeV electrons can be produced by a device about 1 metre long, and the corresponding undulator need only be one or two metres in length. Therefore 2 MeV was chosen as a guiding value.

Taking undulator radiated powers of about a watt as a target a beam current of some tens of milliamps (peak) was considered to be both desirable and feasible.

2.3.2 Wavelength

Knowledge of the fields obtainable in 10 cm linacs for various input powers served as a guide to the range of power likely to be needed for the 2 MeV output energy at shorter wavelengths. It was found that 1.8 cm was the shortest practicable wavelength using

existing power sources.*

2.3.3 Effective Bunch Length

From the considerations discussed in section 2.2 we see that if coherent undulator radiation at a wavelength λ is to be generated, then the bunch length should not be more than about $\lambda/2$. For $\lambda = 0.5$ mm the corresponding maximum bunch length is 5^{o} (0.25 mm) of the operating wavelength (1.8 cm). The actual trajectory computations which were carried out resulted in a design with a 6^{o} (0.3 mm) bunch length (see section 4.5).

2.3.4 Other Characteristics

The choice of operating mode, loading material and the efficiency considerations are discussed later in separate sections. This section (2.3) is intended to highlight those linac characteristics which will markedly affect the performance of submillimetre radiators fed by fast electron beams.

2.4 Metal Loading versus Dielectric Loading[80]

2.4.1 Efficiency and Shunt Impedance

As pointed out by Shersby-Harvie[15], comparisons of the "efficiencies" of various types of linac waveguide structure are better

---

* At the time the choice was made (five years ago), the most appropriate available source was a Ferranti bombardment heated magnetron which delivered up to 350 kW peak at 1.8 cm with a duty ratio of about 1 : 2000. This source remains a most suitable choice and is of proven reliability; certain valves have been successfully run at over 500 kW.

made by consideration of their shunt impedance

$$\frac{E^2_{ms}}{P_d}$$

rather than their efficiency defined in section 1.3 as

$$\frac{V^2}{P_s \ell}$$

The latter function depends directly upon the type of structure and many subsidiary factors and is useful in assessing how well the available power has been used to establish the axial RF field, whereas the shunt impedance is precisely defined and does not introduce much complication.

To illustrate the order of magnitude of these quantities which has been achieved in practice, we have set out in Table 1 the results obtained for several linacs which operate at 10 cm wavelength. They are all of the disc-loaded type. The theoretical basis for the copper-loaded machines has been described by Slater,[9] Chu and Hansen,[48] and many others. The theories of Shersby-Harvie[50] and Walkinshaw[49] were used as the basis for the titania-loaded machines.

The method of constructing the loaded waveguide influences the shunt impedance that can be attained. It is therefore noteworthy that the high value of r_{sh} for linac 3 might well be associated with its structure of copper discs spaced in a copper tube which was shrunk on to them. The wall currents of the E_{01} mode flow parallel to the tube axis so that losses due to discontinuities in the wall would be eliminated within each section of linac 3. One integral disc-and-spacer per periodic length was used in linacs 1, 2 and 4.

	Electron Accelerator	Type	Waveguide Loading Material	r_{sh} MΩ/m	η' MΩ/m	Waveguide Construction	References
1.	4 MeV, AERE Malvern (1948)	Travelling Wave	Copper	16.7	4	Soldered Disc-and-Spacers	43, 44
2.	8 MeV, Metropolitan-Vickers (1953)	Travelling Wave	Copper	25	7	Soldered Disc-and-Spacers	47
3.	400 MeV, Stanford Mk III (1955)	Travelling Wave	Copper	50	38	Shrunk-on Tube	45
4.	1 GeV, Orsay (1963)	Travelling Wave	Copper	38	34	Clamped Disc-and-Spacers; Indium Gaskets	78
5.	1.4 MeV, AERE Malvern (1953)	Travelling Wave	Titania	30	2.5	Clamped Split Tube	24, 46
6.	Queen Mary College, London (1958)	Standing Wave	Titania	62.8†	-	Clamped Disc Rings and Spacers	26, 27

† N.B. $r_{sh}(T.W.) = 2\, r_{sh}(S.W.)$. See Section 3.2.1

TABLE 1

In linacs 1 and 2 the units were soldered together, and in linac 4 they were clamped together with indium gaskets between. The designers of linac 4 claimed that this latter technique gave a more accurate structure, albeit with a lower shunt impedance. In linac 5 the titania discs were clamped in a longitudinally split tube. In linac 6 the disc rims were silvered, and copper rings were shrunk on to the discs before they were stacked in a ring-and-spacer fashion clamped axially.

Linac 5 was the first machine to have been built on the anisotropic dielectric basis, and its actual r_{sh} fell well below the theoretical value. However, its r_{sh} was nearly twice that of linac 1 which was built earlier by the same AERE team. The work on linac 5 lent guidance to the team who built linac 6. The latter machine had a shunt impedance twice that of the former, and was within 15% of its theoretical value. Even the carefully built linac 3 and the more recent linac 4 did not have theoretical or actual shunt impedances as high as linac 6. These results add experimental confirmation to the theoretical assertion by Shersby-Harvie[15,22] that dielectric-loaded structures can give higher shunt impedances than their metal-loaded counterparts.

In the linac slow-wave structure comprising dielectric 'washers' spaced periodically in a circular copper tube the power losses may be divided between the metal walls (P_{dm}) and the dielectric material (P_{dd}) so that

$$P_d = P_{dm} + P_{dd} \qquad (2.2)$$

and we can define two associated shunt impedances so that

$$r_{shm} = \frac{E^2_{ms}}{P_{dm}} \qquad r_{shd} = \frac{E^2_{ms}}{P_{dd}} \tag{2.3}$$

and $$\frac{1}{r_{sh}} = \frac{1}{r_{shm}} + \frac{1}{r_{shd}} \tag{2.4}$$

It can then be shown[24] that

$$r_{shm} \propto \frac{1}{\lambda^{\frac{1}{2}}}$$

and $$r_{shd} \propto \frac{1}{\lambda}$$

Also, for a metal-loaded structure

$$r_{sh} \propto \frac{1}{\lambda^{\frac{1}{2}}}$$

and therefore if the dielectric and metal losses are roughly the same, i.e. $P_{dm} \approx P_{dd}$, then r_{sh} will rise more quickly for the dielectric structure than for its metal counterpart as the operating wavelength is reduced. This suggests that we should use dielectric loading for operation at a wavelength of 1.8 cm.

To conclude this section we shall draw attention to a comparison of dielectric and metal loading made by Shersby-Harvie[15]. P_{dd} is assumed to be zero so that the above wavelength argument is invalidated, $r_{sh} = r_{shm}$, and $r_{sh} \propto \frac{1}{\lambda^{\frac{1}{2}}}$.

He calculates that for the ideal dielectric-loaded structure with copper walls, and for $v_s = c$,

$$r_{sh}, \text{ maximum} \approx \frac{1.94.10^8}{\lambda^{\frac{3}{2}}} \quad \text{ohm/metre}$$

This compares with

$$r_{sh}, \text{ maximum} \approx \frac{0.627.10^8}{\lambda^{\frac{3}{2}}} \quad \text{ohm/metre}$$

obtained from the treatment by Walkinshaw[51] of the ideal copper-loaded structure for $v_s = c$.

Assuming that a low loss loading material of acceptable relative permittivity is available, the foregoing discussion favours dielectric loading for 1.8 cm operation.

2.4.2 Properties of Available Dielectric Materials

The theoretical work referred to above has indicated that the desirable range of relative permittivity K is 10 to 100, and that a loss tangent $\tan \delta$ of up to about 10^{-3} is acceptable. In addition, the loading material must be chemically stable and free from breakdown in the presence of high electromagnetic fields and energetic particles. The material must also be machinable to an accuracy governed by the value of K and the precision required of the slow-wave structure characteristics.

After the work on the AERE and Queen Mary College structures it was known that a range of sintered ceramic materials could be made to conform with these general requirements, at least at 10 cm wavelength. The magnesium oxide - titanium dioxide ceramics* appeared to possess the

*Manufactured by Dr. Erich Schaefer's Laboratory, Cambridge.

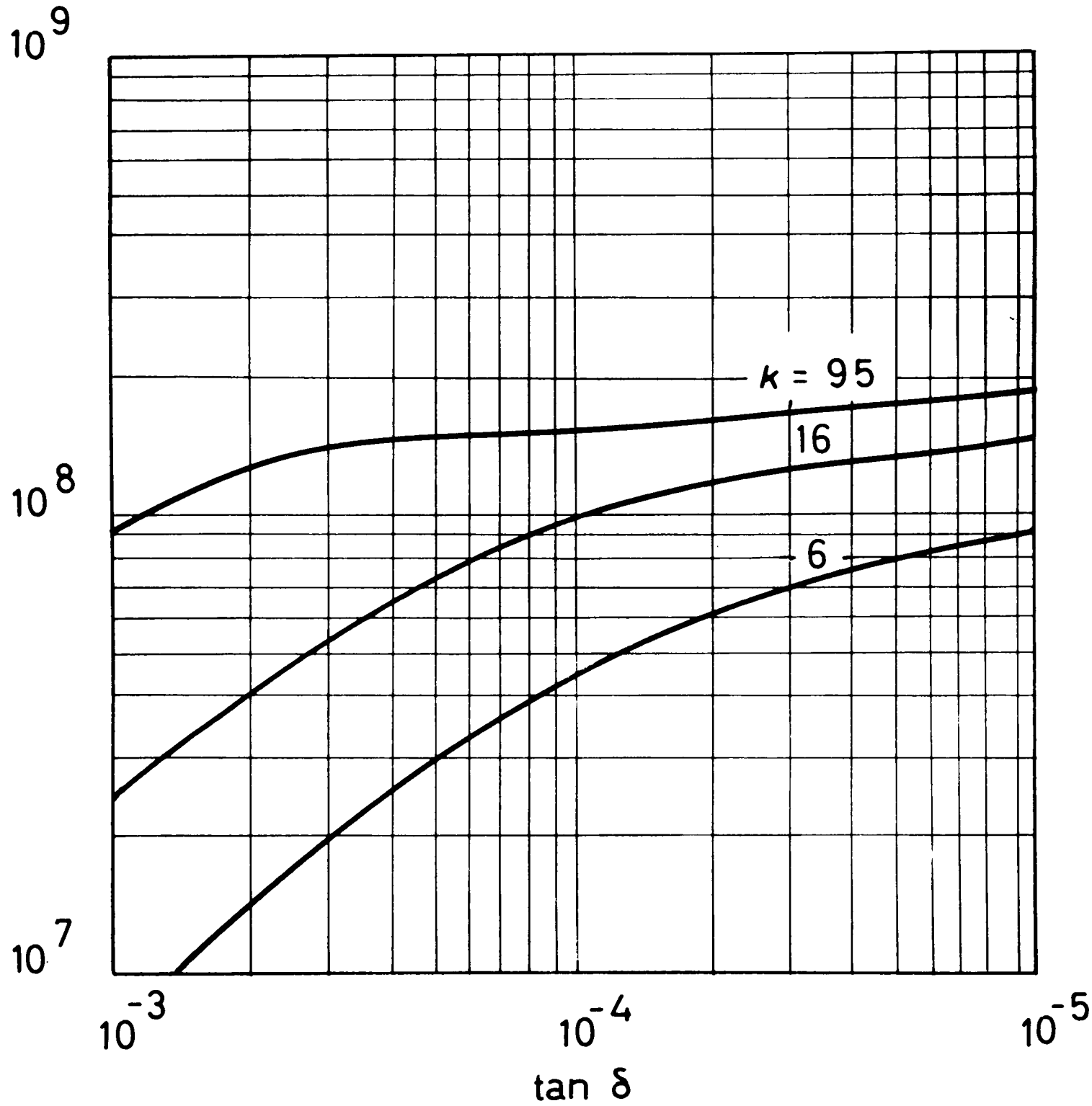
desired properties at low power.

Successful high power operation of structures at 10 cm using glazed titania ceramic discs was reported by Walker and Lewis,[25] and the unglazed AERE titania structure was operable at axial field strengths of about 3 MV/m provided the vacuum was not contaminated by oil vapour. Linear scaling of dimensions from 10 cm to 1.8 cm wavelength did not immediately suggest that any insuperable fabrication difficulties would be encountered with these materials. Also, it was not apparent that impossibly close tolerances might be required, but it was realised that a detailed investigation would be necessary to decide whether a 6^{o} bunch length was feasible.

It was concluded that the apparent advantages of dielectric loading at 10 cm, coupled with the probable availability of a suitable loading material merited a preliminary study of the operation of a dielectric-loaded linac-buncher at 1.8 cm.

2.4.3 Choice of Dielectric Material

The magnesium oxide - titanium dioxide ceramics possess a suitable range of K and tan δ at 10 cm[52] and 8 mm wavelengths[53]. The published measurements show that K lies between 10 and 100, and tan δ varies from one to five times 10^{-4}. This point is here illustrated by reproducing in Fig. 3 curves of r_{sh} versus tan δ for various values of K. The curves are based on those derived by Shersby-Harvie, et al., from the anisotropic-dielectric theory.[24] No other materials were known to possess more suitable basic properties at microwave frequencies.



λ = 0·1 m b = 0·3

v_s = c a = 0·01 m

VARIATION OF SHUNT IMPEDANCE WITH DIELECTRIC TAN δ

FIG. 3.

A magnesium titanate mix yielding a K of about 14.3 was found to have the smallest tan δ (not more than 10^{-4}) at $\lambda = 10$ cm, and values for an almost pure titania sample were found to be about 93 and 4.10^{-4} respectively.[52] Fig. 3 suggests that these two samples would result in almost the same shunt impedance. It was therefore decided to select these two ceramics for possible linac usage, and to postpone choosing between them until their basic dielectric properties at 1.8 cm had been evaluated.

CHAPTER III

The Mode of Operation

We need to decide how much phase change per period there should be along the disc-loaded structure in order to achieve the highest shunt impedance and efficiency. We must also decide whether it is better to establish the RF field which couples energy to the beam by a wholly forward-travelling-wave system or by a resonant system. These two factors are interrelated and depend upon the velocity-dispersive properties of the periodically-loaded waveguide.

3.1 The Periodically-Loaded Waveguide

In a uniform waveguide, propagation is possible at all frequencies above the cut-off value at which the wavelength is so long in relation to the dimensions of the waveguide that only evanescent waves can exist. If periodic loading obstacles such as metal or dielectric "washers" are introduced there will be reflected waves from them which will generally cancel out the forward waves when there are $2/n$ obstacles per guide wavelength, n being integral (or zero). This condition is termed the $n\pi$-mode of operation. At these wavelengths the group velocity (which for the moment we shall assume equals the energy velocity) falls to zero and the waveguide is, in effect, resonant. That there are at least two frequencies with a stop-band between at the $n\pi$-mode may be seen by taking the case where $n = 1$ and referring to Fig. 4. In the case of transverse magnetic $n\pi$-mode operation, we may place perfectly conducting end-walls at nodal planes (over which $E_\rho = 0$)

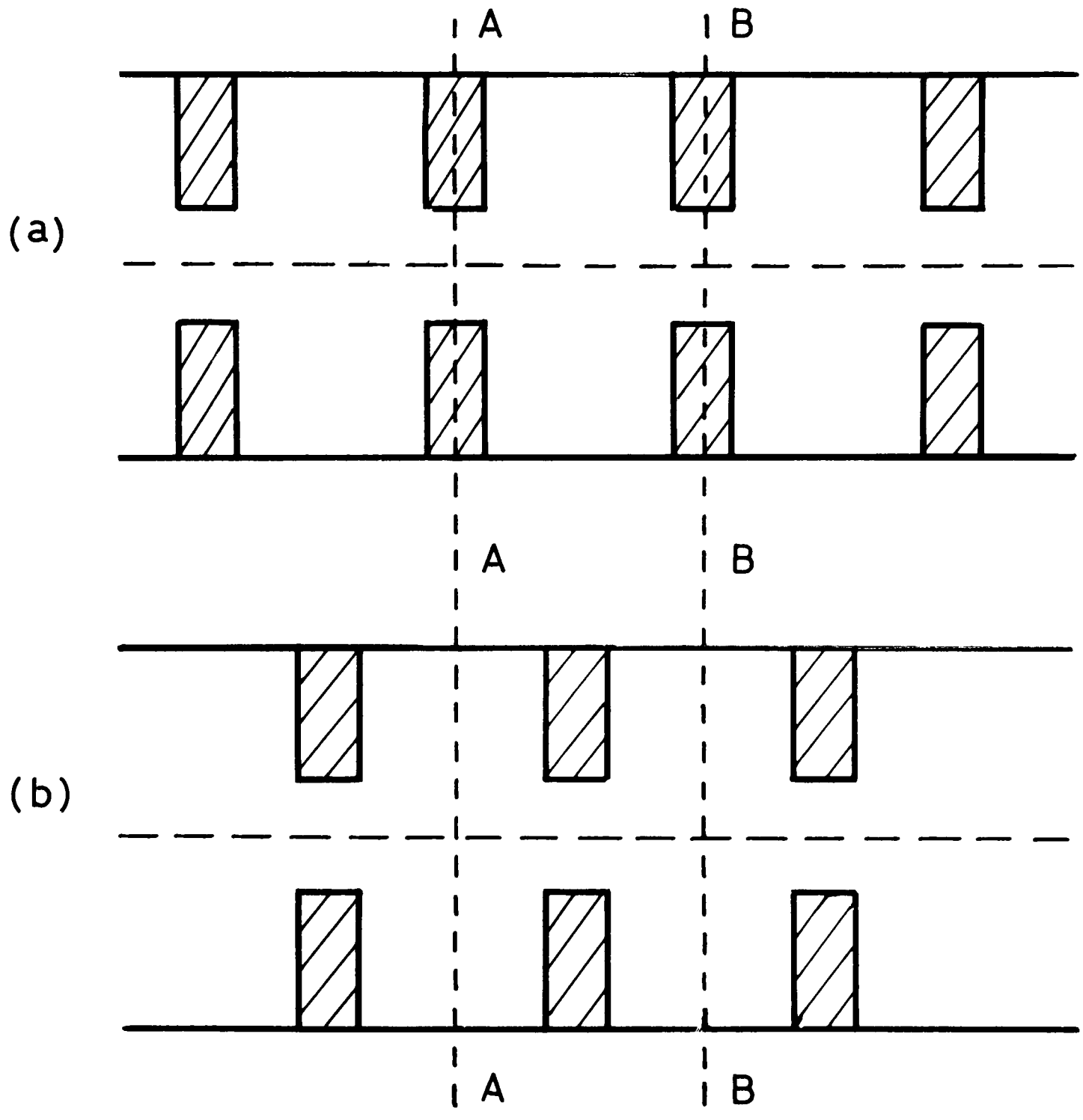


FIG. 4. REFERENCE PLANES IN π-MODE STRUCTURE

$\frac{\lambda g}{2}$ apart without disturbing the field pattern. Symmetry leads us to consider the two possibilities indicated, Fig. 4(a) and (b). In case (a) the half-discs within the resonant cavity (AA, BB) lie within a different field configuration from those in case (b). In general, cavity (a) will not resonate at the same π-mode frequency as cavity (b). This fact is illustrated by the dispersion curve for the periodically loaded structure, a plot of ω against βL the phase change per period, where β is the phase constant and L is the periodic length (Fig. 5).

The wave function giving the form of the fields along the structure must express the periodic nature of the structure.[54] In a long periodic structure one transverse reference plane is indistinguishable from a second reference plane one periodic length away, so that the wave functions at these planes can only differ from each other by a constant factor. Let us write this constant as $e^{-\gamma L}$, where L is the periodic length and γ is a constant, in general, complex. We can see that a function which reflects the structure periodicity in the manner just described is simply $e^{-\gamma z}$. This function is made more general by multiplying it by an arbitrary periodic function of z with period L. Such a periodic function can be expressed as a Fourier series of exponentials $e^{\frac{-2\pi n j z}{L}}$ where n is an integer. Thus the wave function can be expressed as a sum of exponentials $e^{-(\gamma + \frac{2\pi n j}{L})z}$, with coefficients depending upon the type of periodic structure.

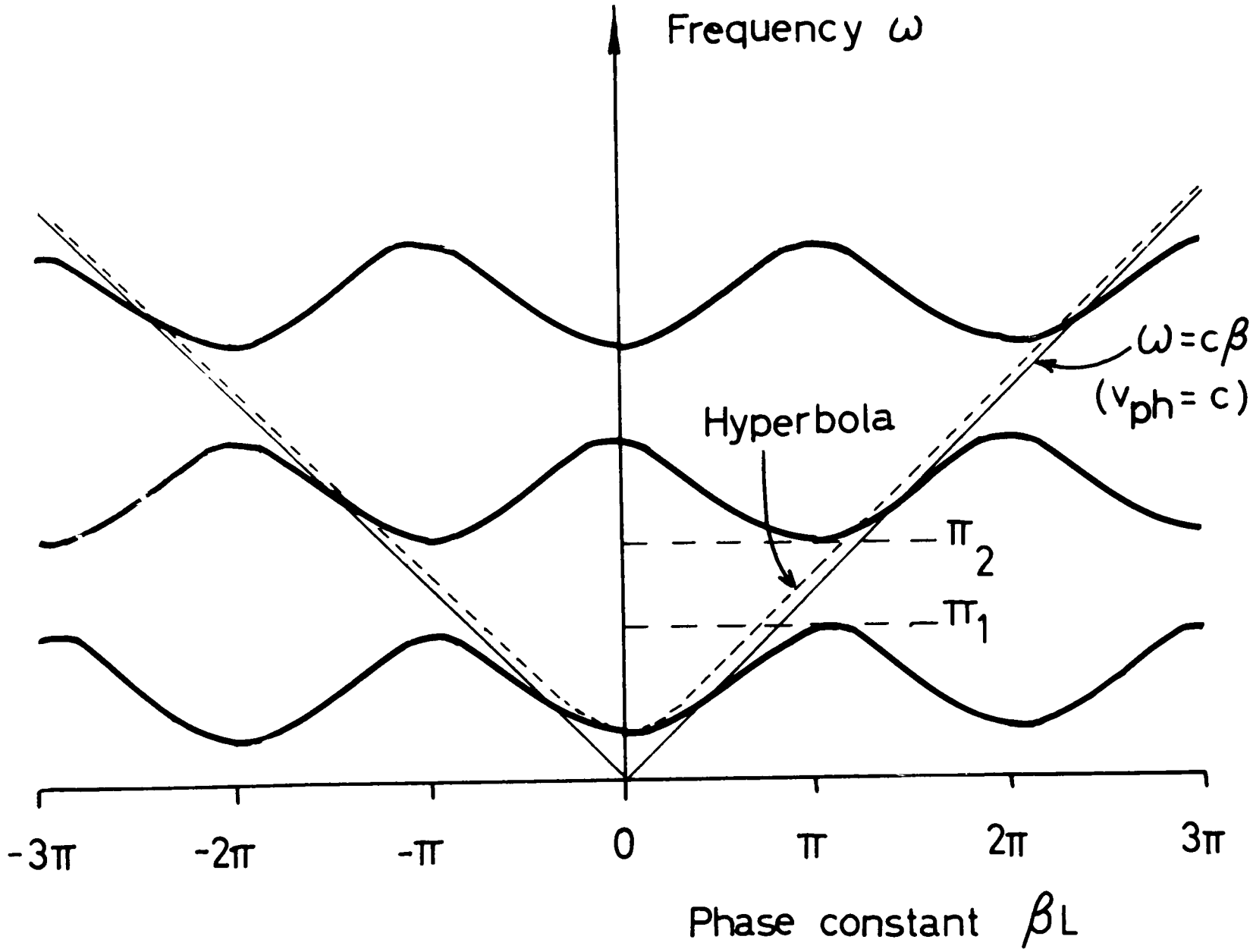


FIG. 5. DISPERSION CURVES

If the structure is lossless it can be shown that γ must be either real or imaginary. If γ is real then the fields are attenuated (the energy is reflected), but if it is imaginary then propagation occurs without loss and we may write

$$\gamma = j\beta_o \quad \text{where } \beta_o \text{ is real}$$

Then $$e^{-(\gamma + \frac{2\pi nj}{L})z} = e^{-j\beta_n z}$$

where $$\beta_n = \beta_o + \frac{2\pi n}{L}$$

We can now make two observations about the relation between ω and β without embarking on the task of obtaining the functional relation in detail. At the given frequency we have seen that βL can take on values of $\beta_o L + 2\pi n$ where n is integral. Therefore ω must be periodic in βL. The direction of axial propagation is immaterial so that βL can also take on values of $-\beta_o L + 2\pi n$ at the given frequency. Therefore ω must be an even function of βL.

For the unloaded waveguide we know that for a given mode

$$\left(\frac{\omega}{c}\right)^2 = \beta^2 + \left(\frac{2\pi}{\lambda_c}\right)^2$$

where λ_c is the cut off wavelength for the mode. This shows that the unloaded-guide plot of ω against β is a hyperbola which is asymptotic to the lines $\omega = \pm c\beta$. When we introduce light periodic loading, i.e. discs of low shunt admittance, all the factors which we have discussed above become apparent on the ω–β plot. The important characteristics of the curve are as follows:-

1. The series of alternate pass and stop frequency bands. For $\beta L = \pi$ we designate the operating conditions at the top and

bottom of the lowest stop band above cut-off as the π_2 and π_1 modes respectively.

2. For certain values of βL the dispersion curves fall below the asymptote $\omega = c\beta$, thereby indicating that propagation is possible at a phase velocity less than the velocity of light. Upon this possibility hangs the whole idea of energy transfer from an RF wave to a particle travelling synchronously with the wave.

The details of the relevant dispersion relation and the analysis of the electromagnetic fields will be dealt with in Chapter VI.

3.2. Travelling Wave versus Standing Wave Operation

A standing wave pattern may be treated as a series of running waves, each forward component being complemented by a backward component. Hence it might appear that for a given power input it would be better to use a wholly forward-travelling-wave structure to couple energy to the particles rather than waste half the power in the complementary backward wave of a resonant structure. But this consideration, although very important, is not the whole story as regards the most efficient and practical operating mode. We shall now list the chief points to be taken into account when choosing between standing wave and travelling wave operation, and then discuss them in turn:-

(a) The standing wave and travelling wave shunt impedances of a given structure for a given value of phase constant.

(b) The advantages of positive RF feedback in a travelling wave linac.

(c) The optimum length of a structure, and the probable length of the 2 MeV structure.

(d) The build-up time of the electromagnetic field.

(e) Energy velocity and group velocity.

(f) Mode separation in a resonant structure and the source frequency-stability requirements.

3.2.1 Shunt Impedance

If we consider only the fundamental E-wave, i.e. a wave pattern whose βL lies between 0 and π, and whose frequency lies between the cut-off value and the π_1-mode frequency, then we can see that the definition of r_{sh}(1.3) leads to the following conclusion. Assuming that the forward and backward components of the standing wave set up in a resonant structure are orthogonal[54], we can state that the power dissipated per unit length in a travelling-wave (T.W.) structure is equal to twice the power dissipated per unit length in a standing-wave (S.W.) structure, given physically identical structures and equal maximum electric fields. Only the forward (synchronous) component of the S.W. field can transfer energy to the beam. Its amplitude is one half of the maximum S.W. field, and so by definition (1.3)

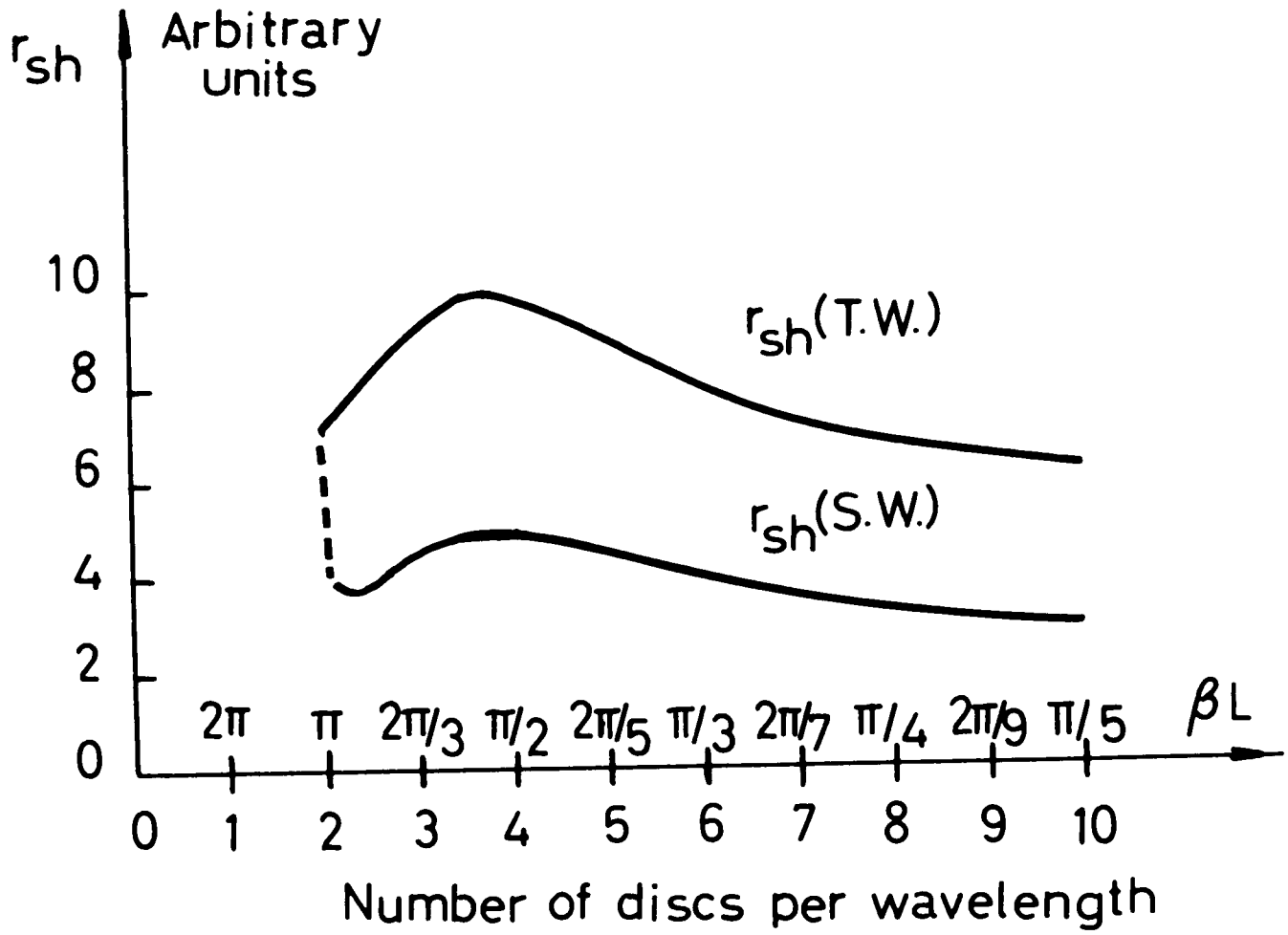
$$r_{sh}(\text{T.W.}) = 2\, r_{sh}(\text{S.W.}) \qquad (3.1)$$

The space-harmonic waves of frequency equal to the fundamental forward wave, with values of βL outside the range 0 to π, will affect the value of the maximum electric field in the periodic structure. However, if we arrange that the beam velocity v_b is equal to the phase velocity of the fundamental forward wave, then none of the other space-harmonics can transfer energy to the beam because their phase velocities

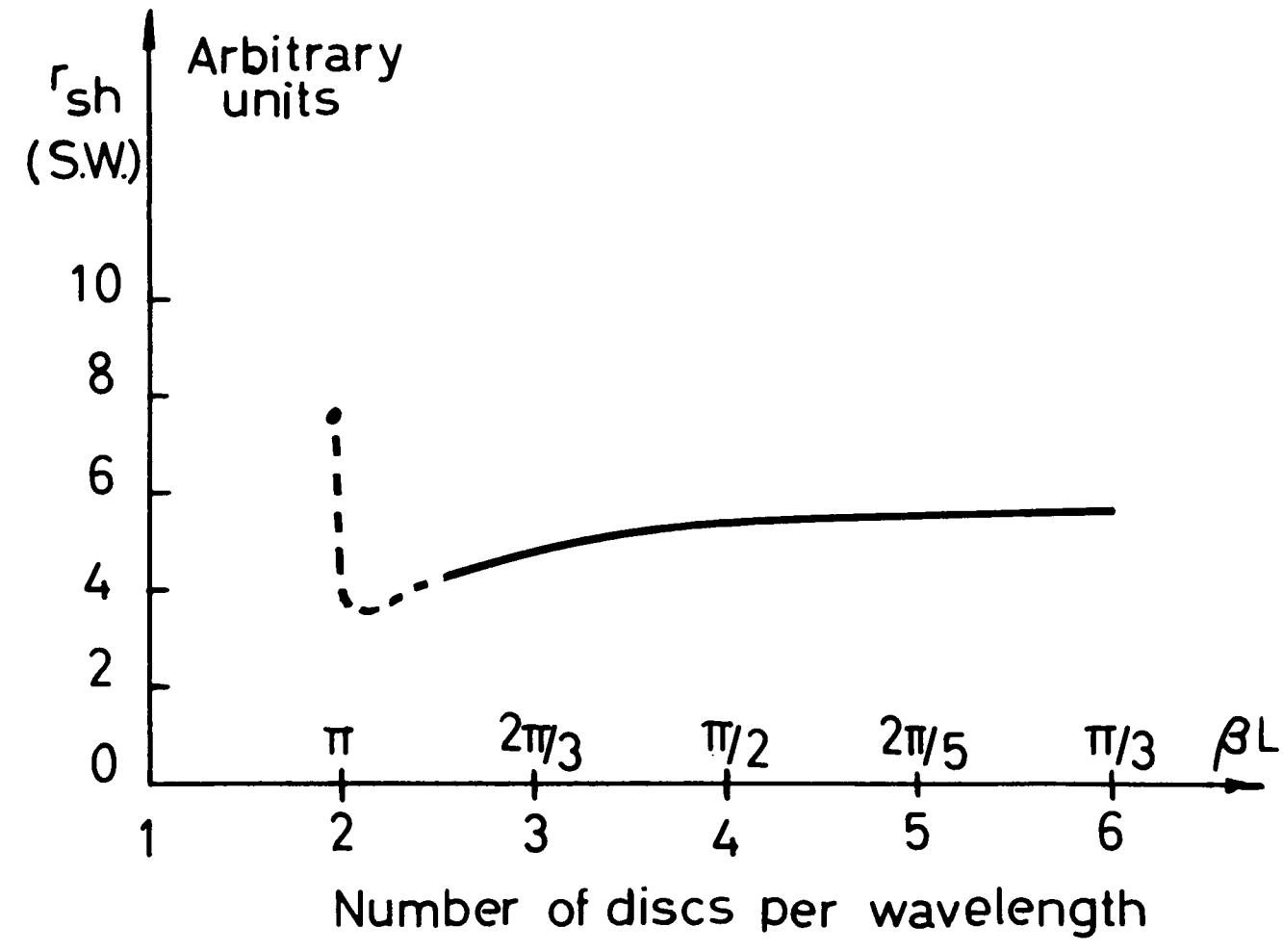
differ from v_b. But at the π-mode the fundamental wave and the first backward wave with positive phase velocity have identical velocities. The structure is then resonant and, in effect, $r_{sh}(T.W.) = r_{sh}(S.W.)$. If the end walls are treated as in Fig. 4(b), the π_1 mode is excited and the two coalesced waves add in phase. This means that $r_{sh}(S.W.)$, π_1-mode, is approximately twice the $r_{sh}(S.W.)$ obtained when βL is just less than π. The variation of r_{sh} with βL at 10 cm wavelength for a metal-loaded structure computed by Fry and Walkinshaw[55] is outlined in Fig. 6(a), and for a titania-loaded structure, computed by Walker and West[29], in Fig. 6(b). It should be noted that in both examples the highest value of r_{sh} is obtained when βL is less than π.

3.2.2 The Advantages of R.F. Feedback

In a linac with an attenuation of only one or two decibels along its periodic structure, travelling-wave operation could necessitate a considerable RF power being ejected and dissipated in a matched load. The extent to which this apparent waste is reflected by diminished values of $r_{sh}(T.W.)$ and $V^2/P_s l$ depends upon the length of the structure in relation to its energy losses. This aspect is discussed below under 3.2.3. However, we shall now point out the chief advantages of operating in a travelling-wave mode with positive feedback irrespective of the structure length. The only proviso is that the electron energy required is above that normally attainable in single resonant cavities loaded with only a few discs or no discs at all, i.e. above about 1 MeV.



Ref. 55 (a) METAL LOADED STRUCTURE. λ=10cm.



Ref. 29 (b) DIELECTRIC LOADED STRUCTURE, λ=10cm.

FIG. 6.

Although a resonant structure with a high Q could act as a frequency stabiliser for a magnetron source[56], up to 50% of the available R.F. power would need to be dissipated in the impedance transformer coupling the magnetron to the structure. This stabilising effect is helpful when π-mode operation is used, as we shall see under 3.2.5 below. However, with the prescribed beam energy for the J-Band linac, we cannot afford to lose such a large fraction of the magnetron power available. (A simple scaling of the series impedance achieved by the AERE team[24] at 10 cm indicates that at least 100 kW at 1.8 cm would be required for a 2 MeV beam energy). Very low loss impedance transformers can be made to couple almost all the output power from a magnetron source to a non-resonant periodic structure. It is therefore apparent that our power requirements call for a travelling-wave system.

A second advantage of the T.W. scheme is that greater control over the fields in the structure can be achieved by the adjustment of a phase shifting element incorporated in the feedback waveguide. Fig. 7 illustrates a basic scheme using a four-port ring junction, or 'rat-race', as the feedback bridge. The ring is normally made so that the mean line lengths are $\lambda_g/4$ between arms 1 and 2, 2 and 3, 3 and 4 respectively and $3\lambda_g/4$ between 4 and 1. This means that if arms 2 and 4 are terminated in matched loads then when power is fed in through arm 1 no signal will be detected in arm 3. The input power divides equally between arms 2 and 4. Similarly if power is fed in

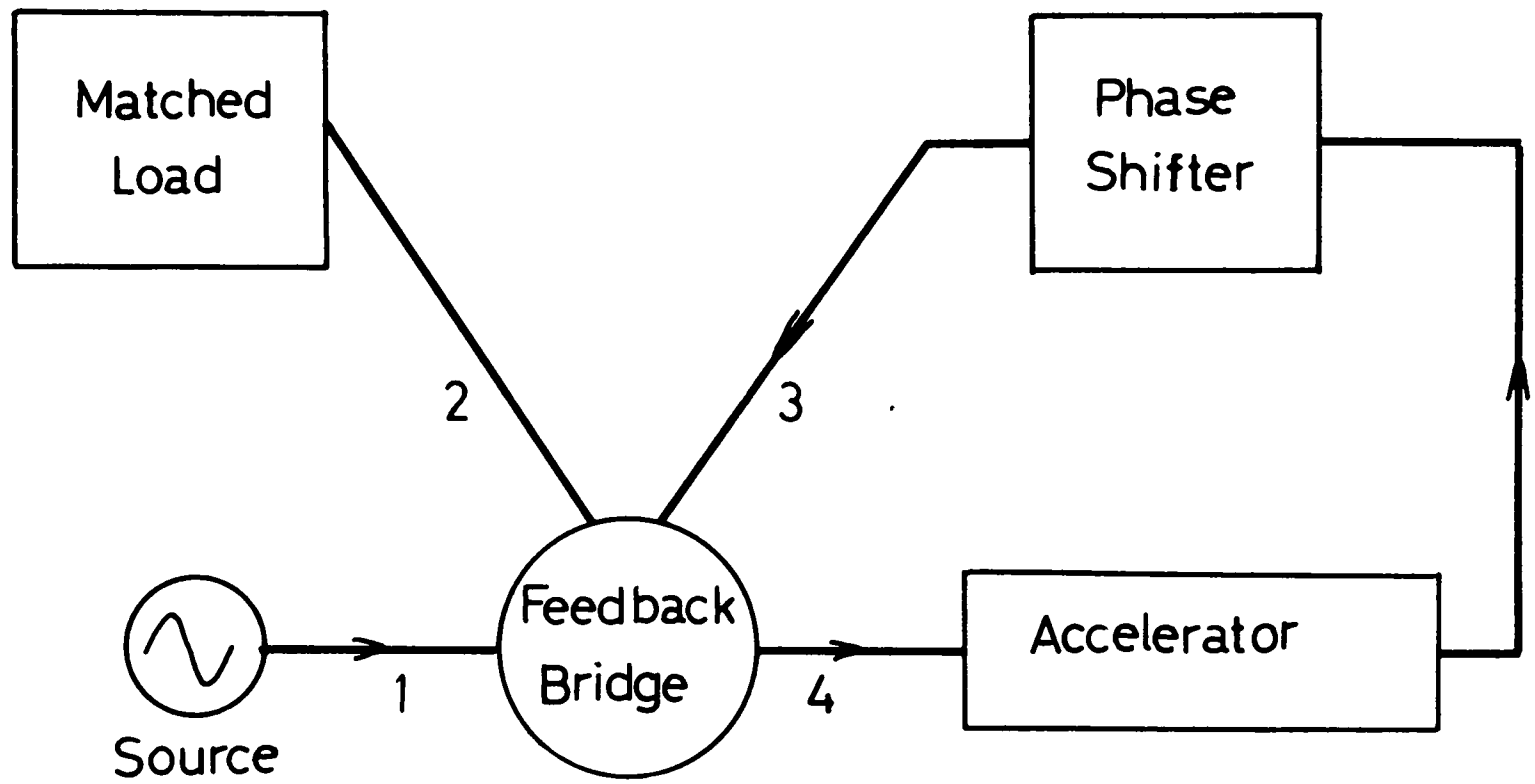


FIG. 7. BASIC MICROWAVE FEEDBACK CIRCUIT

through arm 3 it will divide equally between arms 2 and 4. In the illustrated scheme the phase of the fedback power can be adjusted so that the power dissipated in the load in arm 2 is minimised and the power delivered to the linac is maximised. If the linac attenuation is 3 dB and the feedback system is lossless, then the power flux into the linac at arm 4 is twice the power flux into the rat-race, and no power is dissipated in the load at arm 2.

The practical considerations of feedback bridges which can optimise the power flux build-up for various values of linac attenuation will be discussed in Chapter VIII. But we can see that we have here a useful means of controlling the accelerating field, especially under operational conditions, and a way of alleviating practical difficulties incurred because of insufficient R.F. power.

3.2.3 The Optimum, Attenuation-Limited, and Practical Lengths

From the definitions set out in Section 1.3 we have

$$E_{ms} = \left[r_{se} P_1 \, e^{-\alpha z} \right]^{\frac{1}{2}} \tag{3.2}$$

and, if we assume that $\phi_s =$,

$$V = \int_0^{\ell} \left[r_{se} P_1 \, e^{-\alpha z} \right]^{\frac{1}{2}} dz \tag{3.3}$$

Now $$\eta' = \frac{V^2}{P_s \ell} \tag{1.10}$$

and the structure input power is ideally equal to the power delivered by the source, so that

$$\eta' = \frac{4 r_{se}}{\alpha^2 \ell} \left(1 - e^{\frac{-\alpha \ell}{2}}\right)^2 \tag{3.4}$$

By equating $\frac{\partial \eta'}{\partial \ell}$ to zero we find that the value of $\alpha\ell$ corresponding to the maximum value of η' is given by

$$\alpha \ell_{opt} = 2.512 \tag{3.5}$$

where, for a given value of α, ℓ_{opt} is the structure (optimum) length for which η' is maximised.

The corresponding value of

$$\eta'_{max} = 0.8146\ r_{sh} \tag{3.6}$$

and the ratio

$$\frac{\eta'}{\eta'_{max}} = 1.955 \frac{\ell_{opt}}{\ell} \left(1 - e^{\frac{-1.256\ell}{\ell_{opt}}}\right)^2 \tag{3.7}$$

The restatement of terms in equations 3.5 and 3.6 follow from the relationship

$$\frac{r_{se}}{r_{sh}} = \alpha$$

derived in Section 1.3.5.

Equation 3.7 shows how the figure of merit will vary with the length of a structure having a certain attenuation constant. We shall now derive the similar relationship which takes into account a fraction n of the power delivered by the source being fed back with a loss of x nepers occurring in the feedback loop. We define n as the feedback ratio where

$$n = \frac{P_l - P_s}{P_s} \tag{3.8}$$

By equations 3.3 and 1.10 therefore

$$\eta'_{fb} = \frac{4r_{se}(1+n)\left(1-e^{\frac{-\alpha\ell}{2}}\right)^2}{\alpha^2\ell} \qquad (3.9)$$

and $$\frac{\eta'_{fb}}{\eta'_{max}} = 1.955\frac{\ell_{opt}}{\ell}\,\frac{\left(1-e^{\frac{-1.256\ell}{\ell_{opt}}}\right)^2}{\left(1-e^{-2.512\frac{\ell}{\ell_{opt}}}\right)^{-2x}} \qquad (3.10)$$

where η'_{fb} is the figure of merit with feedback.

When a standing wave system is used

$$V = \int_0^{\ell} \frac{E_m}{2}\,dz \qquad (3.11)$$

where E_m is the peak axial electric field, and where $\phi_s = \frac{\pi}{2}$ as before.

$$\text{Then } V = \frac{E_m\ell}{2}$$

$$= \left[\frac{P_1\, r_{sh}}{\ell}\right]^{\frac{1}{2}}\ell \qquad (3.12)$$

Now n = 0 and therefore $P_1 = P_s$, hence

$$\eta'(S.W.) = r_{sh}(S.W.) \qquad (3.13)$$

and since

$$r_{sh}(T.W.) = 2\, r_{sh}(S.W.) \qquad (3.1)$$

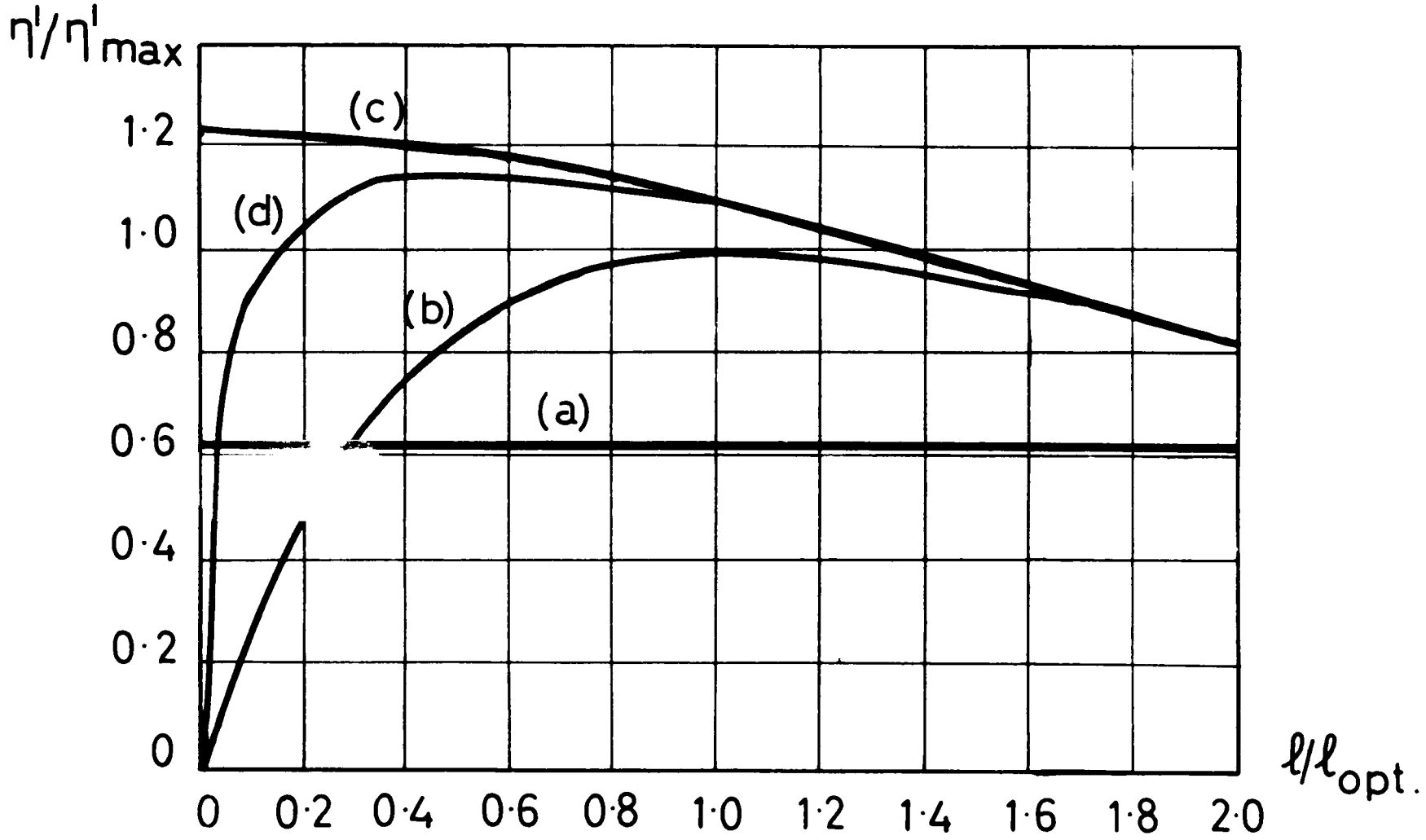
$$\frac{\eta'(S.W.)}{\eta'_{max}} = \frac{0.5\, r_{sh}(T.W.)}{0.8146\, r_{sh}(T.W.)}$$

$$= 0.6138 \qquad (3.13)$$

We now have sufficient information to show graphically how the required length of a structure (for a given attenuation constant) can govern the choice between travelling-wave and resonant operation taking η'/η'_{max} as the efficiency criterion. Using equations 3.7, 3.10 and 3.13 we have plotted in Figure 8 the variation of η'/η'_{max} with l/l_{opt} for four operating conditions. Curve (a) shows the level achieved using a resonant structure when $P_l = P_s$. Curve (b) is for a travelling-wave structure with no external feedback circuit. We have used this scheme as a reference when defining the optimum length of a given structure. However, when feedback is employed and there is negligible feedback loss then the figure of merit does not vary quickly with l/l_{opt} (curve (c)). In a real feedback system there will be a detectable loss of course, and curve (d) illustrates how η' changes when the loss is 0.05 nepers (about 0.5 dB).

If T.W. operation without feedback were to be used these results indicate that we should only expect a figure of merit higher than the S.W. value if l/l_{opt} is greater than about 0.3. If half of the R.F. source power were to be used in a source frequency stabilisation system when resonant operation was employed[56] then this critical value of l/l_{opt} would be reduced to about 0.1.

The curves of Fig. 8 imply that if we exceed a certain length of structure (with a given attenuation constant) then we can expect a diminution of η' because of waveguide attenuation. This 'certain length' is termed the attenuation limited length l_a, and it is equal



(a) Resonant structure

(b) Travelling-wave, no feedback

(c) Travelling-wave, feedback without loss

(d) Travelling-wave, feedback loss 0·05 neper

FIG. 8.

to ℓ_{opt} in the case of T.W. operation with no feedback. Curves (c) and (d) show how ℓ_a/ℓ_{opt} increases from zero as the feedback loss is increased from zero.

Experience gained by previous workers[57] suggests that a feedback loss of 0.05 neper is a practical value so that curve (d) represents a likely experimental condition. We deduce that if ℓ/ℓ_{opt} is greater than about 0.03 then we should expect a higher figure of merit using a travelling-wave system with feedback than using a resonant system. Also, we note that $\ell_a \approx 0.5\ell_{opt}$ when x = 0.05 neper.

We now need to estimate the ratio ℓ/ℓ_{opt} which might be encountered in practice. The 80 cm structure of titania discs loading circular copper waveguide which was used at AERE to produce 1.4 MeV electrons[24] had a power loss of about 1 dB at 10 cm wavelength (S-Band). This gives a value of 0.091 for ℓ/ℓ_{opt} which suggests that T.W. with feedback would have been the best mode of operation on the basis of our present criterion. The machine was actually operated T.W. without feedback partly because the project was an investigation of the anisotropic-dielectric-loading theory and was not primarily concerned with optimising η'. In our J-Band case we need to make the best use of the available power which implies optimising η'.

In the AERE machine, the maximum S-Band accelerating field was about 2.5 MV/m with a power flux of 1 MW and this produced 1.4 MeV electrons when the interaction length (ℓ) equalled 0.8 m. Therefore the required field to produce 2 MeV electrons should be about 4 MV/m

for the same value of ℓ. The loss length ℓ_o $(= \frac{1}{\alpha})$ will scale as the (wavelength)$^{\frac{3}{2}}$, approximately, and therefore so will ℓ_{opt} since $\alpha \ell_{opt} = \frac{\ell_{opt}}{\ell_o} = 2.512$. This means that if $\frac{\ell}{\ell_{opt}} = 0.091$ at S-Band then $\frac{\ell}{\ell_{opt}} \approx 1.20$ at J-Band ($\lambda = 1.8$ cm) for the same value of ℓ. Since the series impedance is dependent upon the geometry of the waveguide cross-section it will scale as the inverse wavelength squared, approximately, so that we should be able to achieve the 4 MV/m with a power flux of about 100 kW at J-Band keeping the structure length at 0.80 m. Hence our estimate for $\frac{\ell}{\ell_{opt}}$ of 1.20 is a likely value, and is sufficiently high for us to state that T.W. operation with or without feedback should yield a higher value of η'/η'_{max} than resonant operation would for the 2 MeV J-Band structure. In any case, the use of feedback should be considered for the reasons given in Section 3.2.2, and as suggested by curve (d) of Fig. 8.

3.2.4 The Build-Up Time of the Fields

In this discussion we have neglected to take into account the time taken for the accelerating field to build up to a steady value after the initiation of the R.F. power flux. The work of Harvie[58] and Mullett[57] on T.W. systems with feedback showed that the time taken for the fields to build up to within 10% of their steady-state value was about twice the filling time, t_f, where $t_f = \ell / v_g$. We have assumed here that the group velocity v_g equals the velocity of energy propagation (see next sub-section). The filling time of the AERE titania-loaded structure was about 0.05 μsec,

i.e. the build-up time was about 0.1 μsec. In the case of a resonant structure Slater's work[54] showed that the build-up of fields is exponential such that they reach 90% of their final value in a time $2.3\ Q_o/\omega$ where Q_o is the unloaded Q factor of the structure. This expression gives a value of about 2 μsec for the Queen Mary College accelerator. The Q of a resonant structure is nearly independent of l, and it scales as $\lambda^{\frac{1}{2}}$ approximately. Therefore at 1.8 cm wavelength we might expect the resonant build-up time to be about 0.2 μsec. Because the length of the J-Band structure and the group velocity therein will be about the same as that of the AERE machine, we can again expect a travelling-wave (with feedback) build-up time of 0.1 μsec. Therefore there is not much difference between the expected relative powers used in field build-up in resonant and travelling-wave operation.

3.2.5 Energy Velocity and Group Velocity

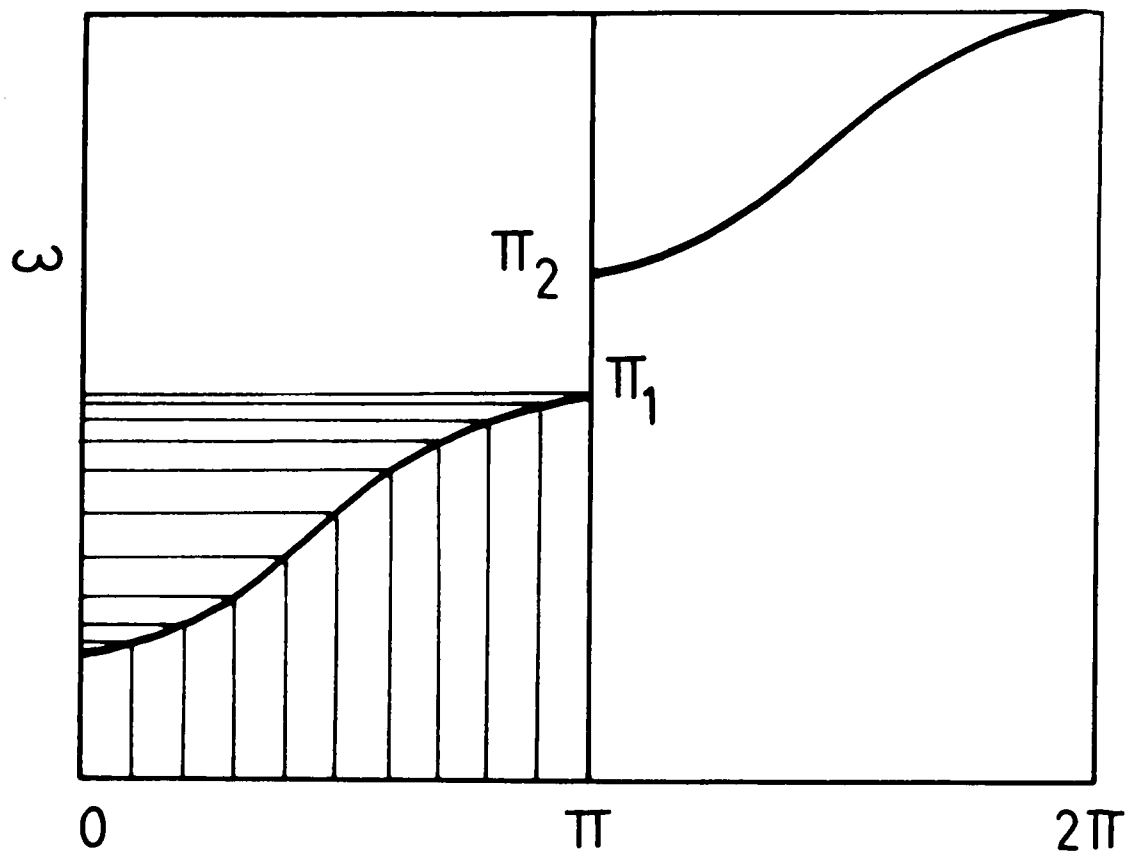
On several occasions we have assumed the equivalence of group velocity and the speed of propagating energy along the structure, the energy velocity. This assumption can be justified for the metal loaded structure[54] and for the dielectric-disc-loaded structure.[59] In the latter case, however, the equivalence apparently fails when $\beta L = \pi$ and the wave impedances are matched at the dielectric-air interfaces. This matched condition was achieved at 10 cm wavelength by Walker and West[29]. Each disc is ostensibly reflectionless, there are apparently no backward waves, and the first two pass bands become

confluent (see Fig. 9). But the analytical expression for v_g, derived by Walker and Engelfield[59], gives a value considerably greater than that of the energy velocity derived assuming that no backward waves exist. This disparity was explained by noting that the ratio of the forward and backward wave amplitudes in the dielectric was indeterminate at the matched π-mode, indicating that any combination of forward and backward waves would satisfy the boundary conditions. Computations of the ratio just above and below the π-mode frequency for a particular structure demonstrated that it was continuous through the π-mode point. Its π-mode value was found by interpolation. Recalculation of the energy velocity then gave close agreement with v_g. It was concluded that at the matched π-mode the field pattern which will exist in practice is that for which the ratio suffers no discontinuity with a small change of frequency. This is the only case of physical significance and here the group and energy velocity equivalence is upheld.

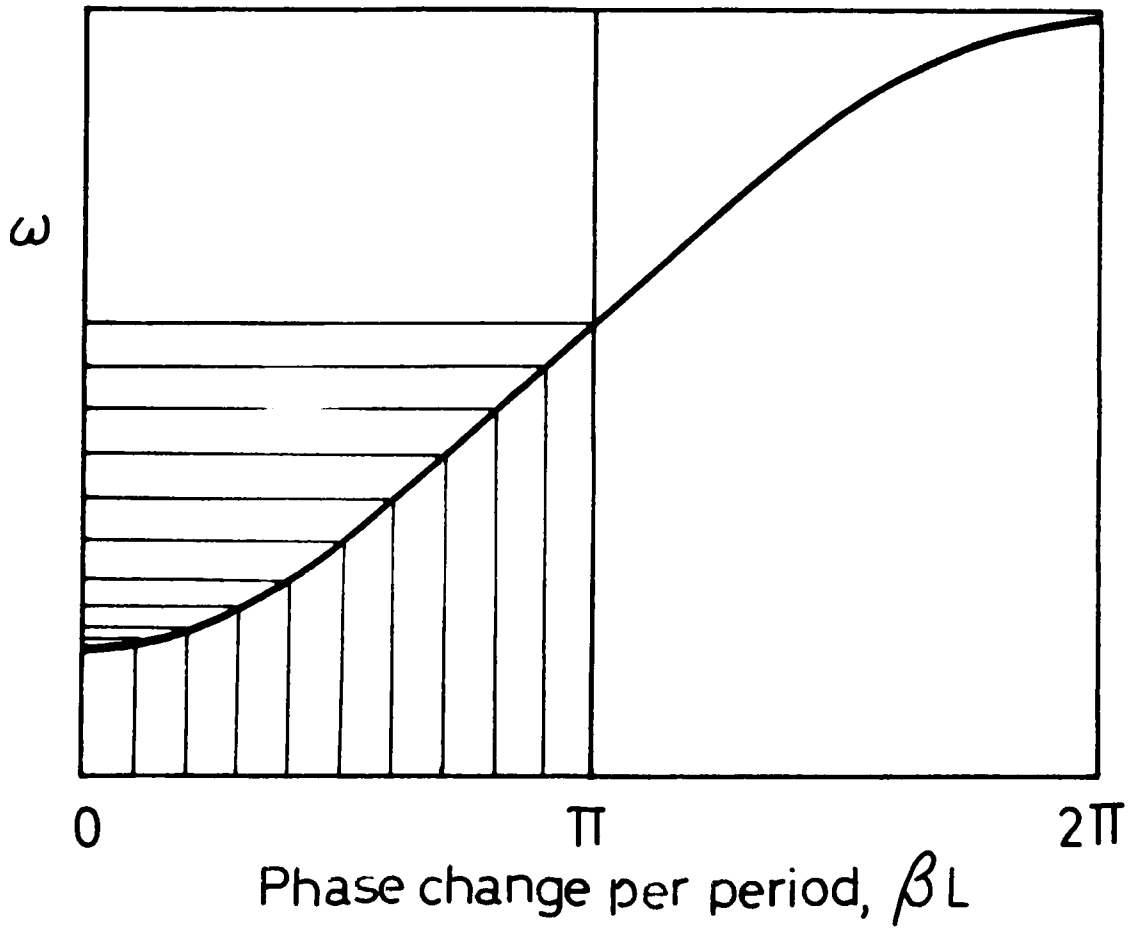
The significance of this conclusion to our present discussion lies in the fact that although the first stop band of a dielectric-disc-loaded structure can be eliminated, the implication that there are no backward waves is not true; a pure forward travelling-wave in the ('matched') confluent π-mode does not exist.

3.2.6 Resonant Mode Separation and Frequency Stability Considerations

In Fig. 9(a) we have drawn part of a typical dispersion curve. If we consider a resonant structure of 10 equally spaced dielectric discs with end walls situated as in Fig. 4(b), there will be



(a) NON-CONFLUENT PASS BANDS



(b) CONFLUENT PASS BANDS

FIG. 9.

11 frequencies at which the total phase change along the structure is zero or an integral multiple of π, i.e. there will be 11 resonances between $\beta L = 0$ and $\beta L = \pi$, at $10\beta L = 0$, $10\beta L = \pi$, $10\beta L = 2\pi$,..... $10\beta L = 10\pi$. The resonances with their equal intervals of βL $(= \frac{\pi}{10})$ are shown on the diagram. The resonant frequencies are clearly closer together near $\beta L = 0$ and $\beta L = \pi$, and the larger the number of discs in the structure the smaller is the resonant mode separation. This leads to the concept of the frequency limited length which we here arbitrarily define as that length of structure for a given period for which the percentage mode separation

$$\frac{\omega_r - \omega_{r-1}}{\omega_r} = \frac{2}{Q_r}$$

where ω_r is the resonant frequency of the r^{th} mode, and Q_r is the unloaded Q factor of the structure at the r^{th} mode. To illustrate this feature we can take the results of Slater[9] obtained on the 28 MeV electron linac (metal-loaded) built at M.I.T. in 1948. Each of this machine's five resonant sections was 24 periods long (4 feet per section). Stable S-Band operation at the π-mode was achieved with 0.1% mode separation, but with longer sections the 0.05% mode separation obtained was found to cause mode interference and instability. Therefore the successful structure was not far from its frequency limited length.

The impedance matching of the dielectric disc to the air spaces discussed in the previous sub-section provides a useful way

of improving the mode separation in a given structure. Walker and West[29] showed that by small adjustments of the diameter of the structure they could increase the mode separation by factors of up to 20. The confluent pass band condition and its effect upon the mode-separation are illustrated in Fig. 9(b). It should be noted that impedance matching at the disc-air interfaces, and therefore confluence, cannot be achieved in a metal loaded waveguide. The mode separation characteristics of the dielectric loaded waveguide can be made by far the better. For example, Walker and West increased the mode separation in a 20 disc, S-Band titania loaded cavity from about 0.05% to 1% by a 3% change in tube diameter. This test cavity was of fixed pitch.

Because the bunch length is of prime importance, we shall probably require a varying pitch in the J-Band structure to expedite close control of fields and velocities. This requirement would probably make it very difficult to maintain π-mode confluence along the structure. The Q of the S-Band cavity was about 20,000. If we scale this to J-Band by a $\lambda^{\frac{1}{2}}$ law and if we assume that π-mode confluence is not attainable, then we see that the 20 disc J-Band structure length is about half its frequency limited length whereas its S-Band counterpart is only a fifth. Thus increased structure losses can seriously affect the minimum tolerable mode separation.

In the case of a travelling-wave structure there is no mode separation problem and so we require a different definition of the frequency limited length. It is the cumulative phase error along the structure for a given value of source frequency stability that

is the limiting factor.

At the time t the phase of a particle at axial position z may be written

$$\phi = \omega t - \beta z$$

$$= \frac{\omega z}{v_b} - \beta z$$

where v_b is the particle velocity, assumed to be constant.

Then $$\frac{d\phi}{d\omega} = \frac{z}{v_b} - \frac{z}{v_g}$$

and so

$$\delta\phi = 2\pi \frac{zc}{\lambda}\left[\frac{1}{v_b} - \frac{1}{v_g}\right] \frac{\delta f}{f}$$

If $v_b = c$, $\lambda = 1.8$ cm, $v_g = 0.05c$ (typical of the AERE dielectric structure) and $\frac{\delta f}{f} = \pm 0.01\%$, then the length of structure corresponding to a phase error of $2\pi/10$ radian is 0.95 metre. Such a phase error represents a practical maximum tolerable value. If it is exceeded few particles are likely to be efficiently accelerated. We define that length of travelling-wave structure for which the cumulative phase error due to source frequency instability is $2\pi/10$ radian as the frequency limited length. We may compare the frequency limited length in the above example with the estimated attenuation limited length of the J-Band structure without feedback, namely 0.67 m, i.e. the AERE titania structure's l_a, 8.8 m, scaled from $\lambda = 10$ cm to $\lambda = 1.8$ cm by a $\lambda^{\frac{3}{2}}$ law. This example demonstrates that the attenuation limited length of this type of structure is likely to be less than its frequency limited length at J-Band. The reverse is

true at S-Band, where the respective values for the AERE machine are 8.8 m and 5.3 m.

3.3 Summary and Conclusions

The shunt impedance of the travelling-wave structure is twice that of the resonant structure except at the π_1 mode where the two are equivalent. T.W. operation with positive R.F. feedback can provide a field build-up in the structure about 50% greater than that attainable without feedback. A phase-shifter in the feedback loop provides a convenient field control which reduces the need to vary the source power and the electron gun voltage during full-power operation. T.W. operation with feedback is more economical with the available power than a resonant system which requires source frequency stability. Because the estimated J-Band structure length slightly exceeds the estimated optimum length, the figure of merit should be almost the same for T.W. operation with and without feedback, but its T.W. value should be about twice its S.W. value. If travelling-wave operation with feedback were used the value of η' would not vary much for structure lengths differing quite widely from the optimum, and the attenuation limited length would be a less important consideration in the choice of structure length (see Fig. 8).

Although both the r_{sh}(S.W.) and the resonant mode separation are optimised in the confluent π-mode, it may be difficult to maintain confluence along the varying-period structure which is likely to be needed because of bunching requirements. This difficulty could lead to mode interference and fluctuations in phase velocity. In any

case the optimum r_{sh}(S.W.) is likely to be 40% less than the optimum r_{sh}(T.W.), as indicated by Fig. 6.

The estimated field build-up times in both T.W. and S.W. J-Band structures are nearly the same and are sufficiently short to be compatible with the R.F. pulse length available from the selected magnetron (Section 2.3.2.). The relative power used during field build-up is not excessive in either scheme, but the resonant structure has a varying impedance during build-up which has to be matched with the source by, for example, magic-tee arrangements[60] or a high power ferrite circulator.

Source frequency instabilities are not likely to be troublesome in either the S.W. or the T.W. scheme at J-Band. Resonant operation can incorporate source frequency stabilisation, and the travelling-wave frequency limited length is estimated to be about 40% greater than the optimum length (the attenuation limited length without feedback).

The conclusion to be drawn is that we should base our designs on a travelling-wave system but postpone the decision on feedback until we have a more accurate knowledge of J-Band dielectric-loaded structures, their length, attenuation and irregularities.

Given a T.W. system we must choose an average value of βL, the phase change per period. Fortunately the value of r_{sh}(and η') varies quite slowly with βL (see Fig. 6). Constructional difficulties can be lessened and mechanical accuracy improved if we keep the number of discs per wavelength reasonably low. Also, for

a fixed disc thickness, the greater the value of βL the smaller is the chance of the damaging multipactor effect occurring. The AERE structure was operated with $\beta L = 0.222\pi$ (9 discs per wavelength) when the disc thickness was 4 mm and the phase velocity was c. Multipactor troubles were encountered[46]. However, if we increase the value of βL too much the simple anisotropic dielectric theory becomes less accurate and we have to invoke the more complicated discrete disc theory (see Chapter VI). Therefore, as a compromise, we have chosen 6 discs per wavelength ($\beta L = 0.333\pi$) as the average phase change per period.

The relatively small number of widely spaced loading discs used in confluent π-mode operation[29] make the S.W. scheme worthwhile bearing in mind should serious multipactor effects or physical inaccuracies cause practical difficulties.

CHAPTER IV

The Theoretical Postulates for Good Bunching *

The basic bunching and accelerating system is illustrated in Fig. 10. The electrons pass with random phases from the gun into a pre-bunching cavity, similar to a klystron cavity, where they are bunched axially in phase to an extent which allows most of them to be captured by the accelerating wave in the slow wave structure, as described in Section 2.1. There they are bunched more tightly and accelerated, care being taken to minimise the inevitable increase in axial momentum variation within each bunch. The phase bunching is carried out before the electrons become too relativistically massive, and the final acceleration is performed in the nearly uniform part of the structure. We shall now examine the particle trajectories through the system.

4.1 The Equations of Particle Motion

Essentially we have a one-dimensional régime and a convenient way of describing the motion is by expressing the particle axial momentum as a function of an axial position co-ordinate and time.

---

* The work on the J-Band linac and its associated interwave generators is naturally a team effort. Dr. A.J. Lichtenberg investigated most of the problems to be discussed in this chapter, and he drafted a report which was edited by the author and distributed as a Technical Report[61]. It is here necessary to re-state much of the information given in the Report together with some corrections so that the thesis may be made more complete and comprehensible.

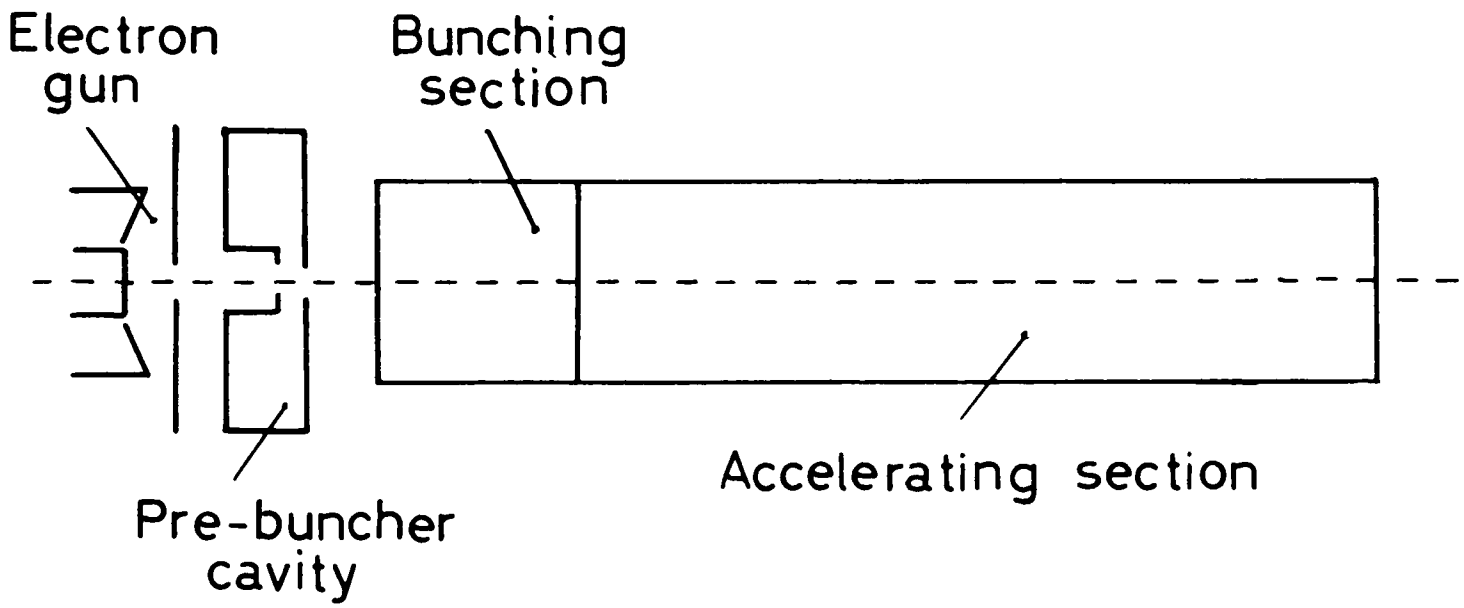


FIG. 10. BASIC BUNCHING AND ACCELERATING SYSTEM.

If we write the relationship as $\mathcal{H}(p, q, t)$ where p is the momentum, q is the co-ordinate and t is the time, and if $\mathcal{H}$ satisfies the pair of relationships

$$\frac{dp}{dt} = -\frac{\partial \mathcal{H}}{\partial q}$$

$$\frac{dq}{dt} = +\frac{\partial \mathcal{H}}{\partial p} \qquad (4.1)$$

then $\mathcal{H}$ is termed the Hamiltonian for the motion, and p and q are the canonical co-ordinates of the motion. Putting the equations in Hamiltonian form has two great advantages. First, if $\mathcal{H}$ does not depend explicitly on time then $\mathcal{H}$ is a constant of the motion. We may then write

$$\mathcal{H}(p, q) = \text{constant}$$

The trajectories can be plotted in a p, q (phase) plane, and for an oscillating particle the maximum extension in momentum and position can be calculated from the initial momentum and position which determine the value of $\mathcal{H}$. A second advantage to a Hamiltonian formulation of our problem is that certain conservation theorems can be applied, even when the Hamiltonian changes with time. If the parameters of the motion change slowly with time then the adiabatic theorem[54] states that the area in the phase plane,

$$\int p \, dq$$

enclosed by the trajectory of an oscillating particle, will be conserved. This theorem, as we shall see, is very useful in determining the general properties of a given linac bunching system.

The force equation for an electron may be written

$$\frac{dp}{dt} = e E_{ms} \sin \phi \tag{4.2}$$

where

$$\phi = \omega t - \omega \int_o^z \frac{dz}{v_s} \tag{4.3}$$

The symbols introduced here are: e the electron charge and ϕ the instantaneous phase angle of the wave at the particle. We shall ignore the radial dependence of the accelerating field (a second order variation) and deal only with the effect of the synchronous wave.

Captured particles will perform oscillations about the phase stable position (ϕ_s) as described in Section 2.1, and the rate of change of ϕ is obtained by differentiating (4.3)

$$\frac{d\phi}{dt} = \frac{\omega(v_s - v_b)}{v_s} \tag{4.4}$$

Equations (4.2) and (4.4) describe the motion completely but can only be solved by numerical methods which we shall discuss later. Here we shall look for a simple description by examining the motion about the phase stable position.

For the phase stable particle the force equation is

$$\frac{dp_s}{dt} = e E_{ms} \sin \phi_s \tag{4.5}$$

where ϕ_s is taken to be constant during the oscillation of a particle about the phase stable position. We now introduce dashed symbols ϕ', p', and v' denoting the particle phase, momentum, and velocity, all with

respect to the phase stable position such that

$$\begin{aligned} \phi &= \phi_s + \phi' \\ p &= p_s + p' \\ v_b &= v_s + v' \end{aligned} \tag{4.6}$$

From (4.6) and (4.2) we obtain the force equation for the perturbed motion

$$\frac{dp'}{dt} = e E_{ms} \sin (\phi_s + \phi') - \sin \phi_s \tag{4.7}$$

and from (4.6) and 4.4) we obtain

$$\frac{d\phi'}{dt} = - \frac{\omega v'}{v_s} \tag{4.8}$$

since $\frac{d\phi_s}{dt}$ is taken to be zero. If we assume that E_{ms} and v_s are constant during a single particle oscillation we can obtain a time independent Hamiltonian for the system. But first we must express the equations of the perturbed motion, (4.7) and (4.8), in terms of canonical variables satisfying Hamilton's equations of motion.

We introduce z' such that

$$z' = z - z_s$$

Then from (4.8) $$\phi' = - \frac{\omega z'}{v_s} \tag{4.9}$$

We can now express v' in terms of p' by considering the expansion of p in powers of v_b derived from the relativistic relationship

$$p = \frac{m_o c}{(1-\gamma^2)^{\frac{1}{2}}} \tag{4.10}$$

where $$\gamma = \frac{v_b}{c}$$

and m_o is the rest mass of the electron. Expanding (4.10) and

neglecting second and higher order terms in v', we get

$$p' = m_\ell v' \tag{4.11}$$

where

$$m_\ell = \frac{m_o}{(1-\gamma^2)^{\frac{3}{2}}} \tag{4.11a}$$

Substituting for ϕ' and v' from (4.9) and (4.11) in (4.7) and (4.8) we have

$$\frac{dp'}{dt} = e E_{ms} \left[\sin\left(\phi_s - \frac{\omega z'}{v_s} \right) - \sin \phi_s \right] \tag{4.12}$$

and

$$\frac{dz'}{dt} = \frac{p'}{m_\ell} \tag{4.13}$$

These equations of motion (4.12) and (4.13) are in Hamiltonian form, i.e.

$$\frac{dp'}{dt} = -\frac{\partial \mathcal{H}'}{\partial z'}$$

$$\frac{dz'}{dt} = \frac{\partial \mathcal{H}'}{\partial p'}$$

whence

$$\mathcal{H}' = \frac{p'^2}{2m_\ell} - e E_{ms} \left[\frac{v_s}{\omega} \cos\left(\phi_s - \frac{\omega z'}{v_s} \right) - z' \sin \phi_s \right] \tag{4.14}$$

This Hamiltonian is a constant of the motion as long as E_{ms} and v_s remain constant. We obtain a family of Hamiltonians, one corresponding to each set of initial conditions, and each one corresponding to a curve in the p', ϕ phase plane. The relationships between E_z the electric field, V' the potential part (second term) of the Hamiltonian, and p' the momentum are plotted in the phase plane in Fig. 11. Providing the total energy of the particle relative to the phase stable

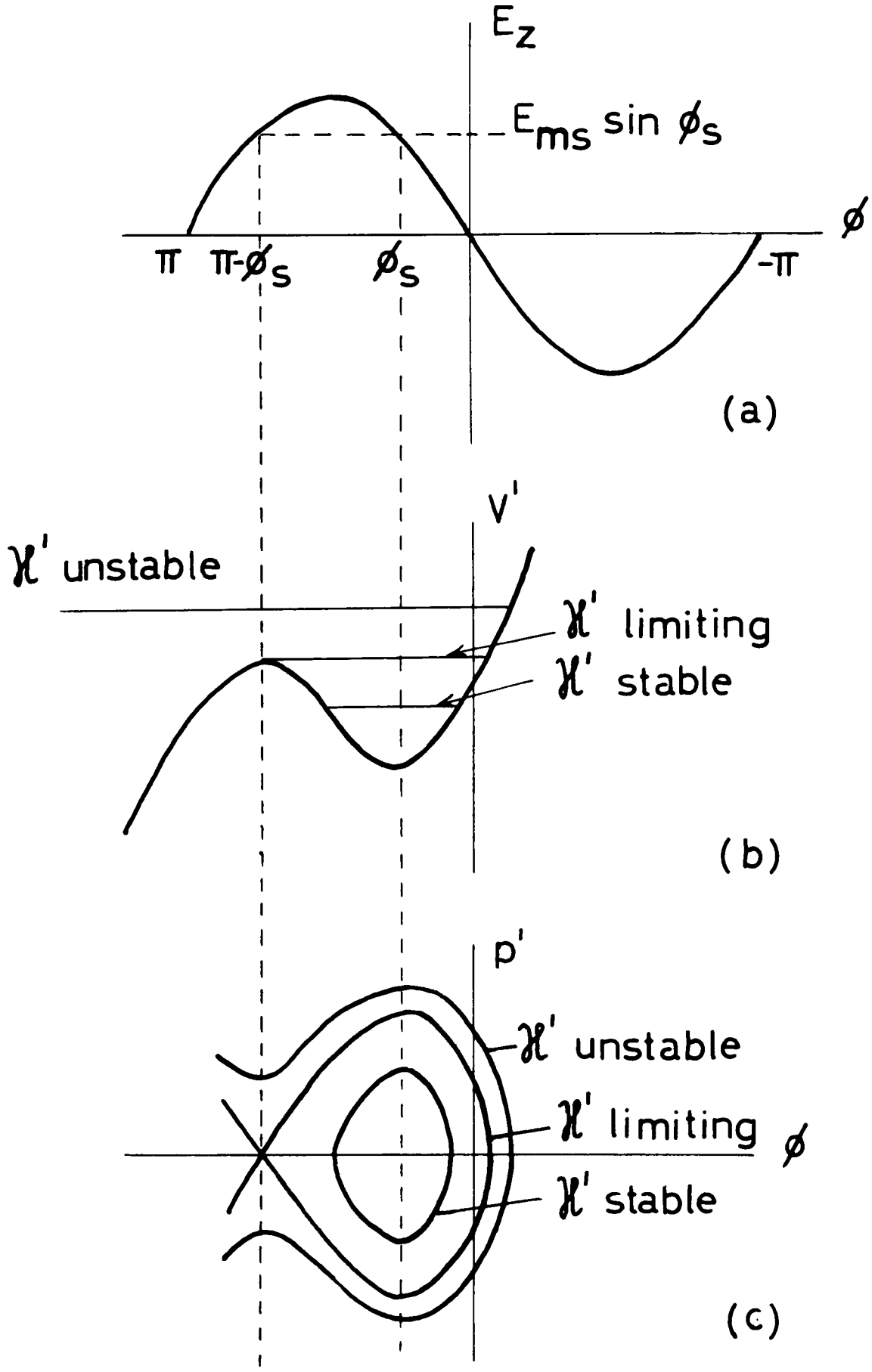

E_z
$E_{ms} \sin \phi_s$
ϕ
π
$\pi-\phi_s$
ϕ_s
$-\pi$
(a)
V'
$\mathcal{H}'$ unstable
$\mathcal{H}'$ limiting
$\mathcal{H}'$ stable
(b)
p'
$\mathcal{H}'$ unstable
$\mathcal{H}'$ limiting
$\mathcal{H}'$ stable
ϕ
(c)

FIG. 11.

position does not exceed the value indicated by '$\mathcal{H}'$ limiting' in Fig. 11(b), the particle will oscillate in the potential well about the phase stable position. If this limiting value is exceeded, the motion will be unstable and the particle will slip back in phase relative to the wave.

If we consider the stable oscillations about $\phi = \phi_s$ which have small amplitudes, i.e. $\phi_s \approx \frac{\omega z'}{v_s}$, we can deduce the frequency of the oscillations from (4.12) and (4.13). Expanding the sine term in (4.12) and retaining only the first order terms in $\frac{\omega z'}{v_s}$, and substituting for p' from (4.13) we have

$$\frac{d^2 z'}{dt^2} + \omega_o{}^2 z' = 0 \qquad (4.15)$$

where $$\omega_o = \left[\frac{e E_{ms}}{m \ell} \cdot \frac{\omega}{v_s} \cos \phi_s\right]^{\frac{1}{2}} \qquad (4.16)$$

Equation (4.15) is the equation to a simple harmonic motion of frequency $\frac{\omega_o}{2\pi}$ and solution

$$z' = z'_{max} \sin \omega_o (t - t_1), \; t_1, \text{ a constant.} \qquad (4.17)$$

Differentiating (4.17) we get v', and then from (4.11)

$$p' = m \ell \omega_o z'_{max} \cos \omega_o (t - t_1) \qquad (4.18)$$

If we assume that E_{ms}, v_s and ϕ_s change slowly with time we can invoke the adiabatic theorem

$$\int p' \, dz' = k', \text{ a constant} \qquad (4.19)$$

Substituting for p' and z' in (4.19) from (4.18) and (4.17), and integrating over an integral number of oscillations we obtain

$$\pi m_{\ell}\omega_o(z'_{max})^2 = k' \tag{4.20}$$

Equations (4.20) and (4.18) give us the maximum extension in momentum and displacement for a given particle motion.

$$z'_{max} = \frac{k''}{(m_{\ell}\omega_o)^{\frac{1}{2}}} \tag{4.21}$$

$$p'_{max} = (m_{\ell}\omega_o)^{\frac{1}{2}} k''$$

where $k'' = \frac{k'}{\pi}$

4.2 General Design Considerations

We can now translate the derived equations into terms of energy and positional spread in the bunched electron beam.

Firstly we note that the total energy U may be written

$$U = \frac{U_o}{(1-\gamma^2)^{\frac{1}{2}}} \tag{4.22}$$

where $U_o = m_o c^2$

Next we consider ΔU, the difference between the total energy of a given particle and that of the phase stable particle. If we neglect terms in v' of second order and above we find that

$$\Delta U = \frac{U_o v' v_s}{c^2\left(1-(\frac{v_s}{c})^2\right)^{\frac{3}{2}}}$$

which becomes

$$\Delta U = \frac{U_o v' v_s}{c^2(1-\gamma^2)^{\frac{3}{2}}}$$

for $v' \ll v_s$.

Therefore, since

$$m_\ell = \frac{m_o}{(1-\gamma^2)^{\frac{3}{2}}}$$

$$\text{and} \quad p' = m_\ell v' \tag{4.11}$$

$$\Delta U = v_{sp} p' \tag{4.23}$$

Using equations (4.21) and making substitutions from equations (4.11a), (4.22) and (4.23) we find that

$$\frac{(z'_m)_f}{(z'_m)_i} = \left[\frac{U_i}{U_f}\right]^{\frac{3}{4}} \left[\frac{v_{sf} E_i \cos \phi_{si}}{v_{si} E_f \cos \phi_{sf}}\right]^{\frac{1}{4}} \tag{4.24}$$

$$\text{and} \quad \frac{(\Delta U_m)_f}{(\Delta U_m)_i} = \left[\frac{U_f v_{sf}}{U_i v_{si}}\right]^{\frac{3}{4}} \left[\frac{E_f \cos \phi_{sf}}{E_i \cos \phi_{si}}\right]^{\frac{1}{4}} \tag{4.25}$$

where the subscripts i and f refer to the conditions at the beginning (initial) and end (final) of the bunch trajectory through the slow-wave structure, and where

$$z'_m \equiv z'_{max}$$

$$\text{and} \quad E \equiv E_{ms}$$

The beam injected to the linac system from the electron gun will have very large phase spread and little energy spread. This means that we are more interested in the final energy spread introduced by bunching the beam to a degree given by $(z'_m)_f/(z'_m)_i$ than in the ratio $(\Delta U_m)_f/(\Delta U_m)_i$ which will be very large. We shall derive the expression for the maximum final difference from the phase stable

particle's energy of an electron injected at phase angle ϕ_i.

Rewriting the Hamiltonian (4.14) we have

$$\mathcal{H}' = \frac{(p'_i)^2}{2m_{\ell i}} - e E_i \left[\frac{v_{si}}{\omega} \cos \phi_i + \frac{v_{si}}{\omega} (\phi_i - \phi_{si}) \sin \phi_{si} \right]$$

$$= \frac{(p'_i)^2}{2m_{\ell i}} - e E_i \frac{v_{si}}{\omega} \left[f(\phi_i) + \cos \phi_{si} \right]$$

where $f(\phi_i) = \cos \phi_i + (\phi_i - \phi_{si}) \sin \phi_{si} - \cos \phi_{si}$

The totel energy of each electron in the injected beam is approximately that of the phase stable particle so that

$$\mathcal{H}' = - e E_i \frac{v_{si}}{\omega} \cos \phi_{si}$$

and therefore $$p'_i = \left[\frac{2m_{\ell i} e E_i v_{si} f(\phi_i)}{\omega} \right]^{\frac{1}{2}} \qquad (4.26)$$

In equation (4.25) $(\Delta U_m)_i$ for a single particle is simply

$$(\Delta U)_i = v_{si} p'_i \qquad (4.27)$$

so that on making substitutions from (4.27), (4.26), (4.22) and (4.11a) we re-write (4.25) in the form

$$(\Delta U_m)_f = \left[\frac{2m_o e}{U_o^3 \omega} \right]^{\frac{1}{2}} (v_{si} v_{sf} U_i U_f)^{\frac{3}{4}} \left[E_f E_i \frac{\cos \phi_{sf}}{\cos \phi_{si}} \right]^{\frac{1}{4}} (f(\phi_i))^{\frac{1}{2}} \qquad (4.28)$$

Equations (4.24) and (4.28) can now act as a general guide to choosing the way in which we should vary the field and the wave velocity to achieve maximum bunching and minimum energy spread. The desired output energy determines U_f and v_{sf}, and largely governs the value of E_f when the structure length has been decided. Therefore

we can see that the initial value of electric field should be as small as possible to give both good bunching and the minimum energy spread. The bunching ratio $(z'_m)_f/(z'_m)_i$ varies as

$$\left\{\left(\frac{v_{si}}{c}\right)^{\frac{2}{3}}\left[1-\left(\frac{v_{si}}{c}\right)^2\right]\right\}^{-1} = \left[\gamma_i^{\frac{2}{3}}(1-\gamma_i^2)\right]^{-1}$$

and this function of γ_i has been plotted in Fig. 12. From this curve we deduce that to improve the bunching the initial velocity should be as high as possible provided that it does not exceed about 0.5c. This initial velocity requirement is not compatible with that for minimum energy spread, but since the bunching ratio is not very sensitive to changes in v_{si} when v_{si} is about 0.5c (see Fig. 12) a compromise value can be chosen which is consistent with the practical limitations of the electron gun. Consideration of $f(\phi_i)$ in equation (4.28) leads to the conclusion that it is highly desirable to have an initially bunched beam for reducing both energy and phase spread. Prebunching is discussed in the next section, but we must remember here that the small velocity spread introduced by pre-bunching means that E_i must be high enough to maintain an acceptable degree of electron capture. Assuming that the high R.F. power is fed in at the beginning of the buncher, there will also be a lower limit to E_i set by the practical structure.

The above factors combined with those discussed in Sections 2.3.2 and 3.2.3 led to the following choice of accelerator parameters:-

$$E_f = 6 \text{ MV/m} \qquad E_i = 0.45 \text{ MV/m}$$

$$v_{si} = 0.4c \qquad \phi_{si} = 45^\circ$$

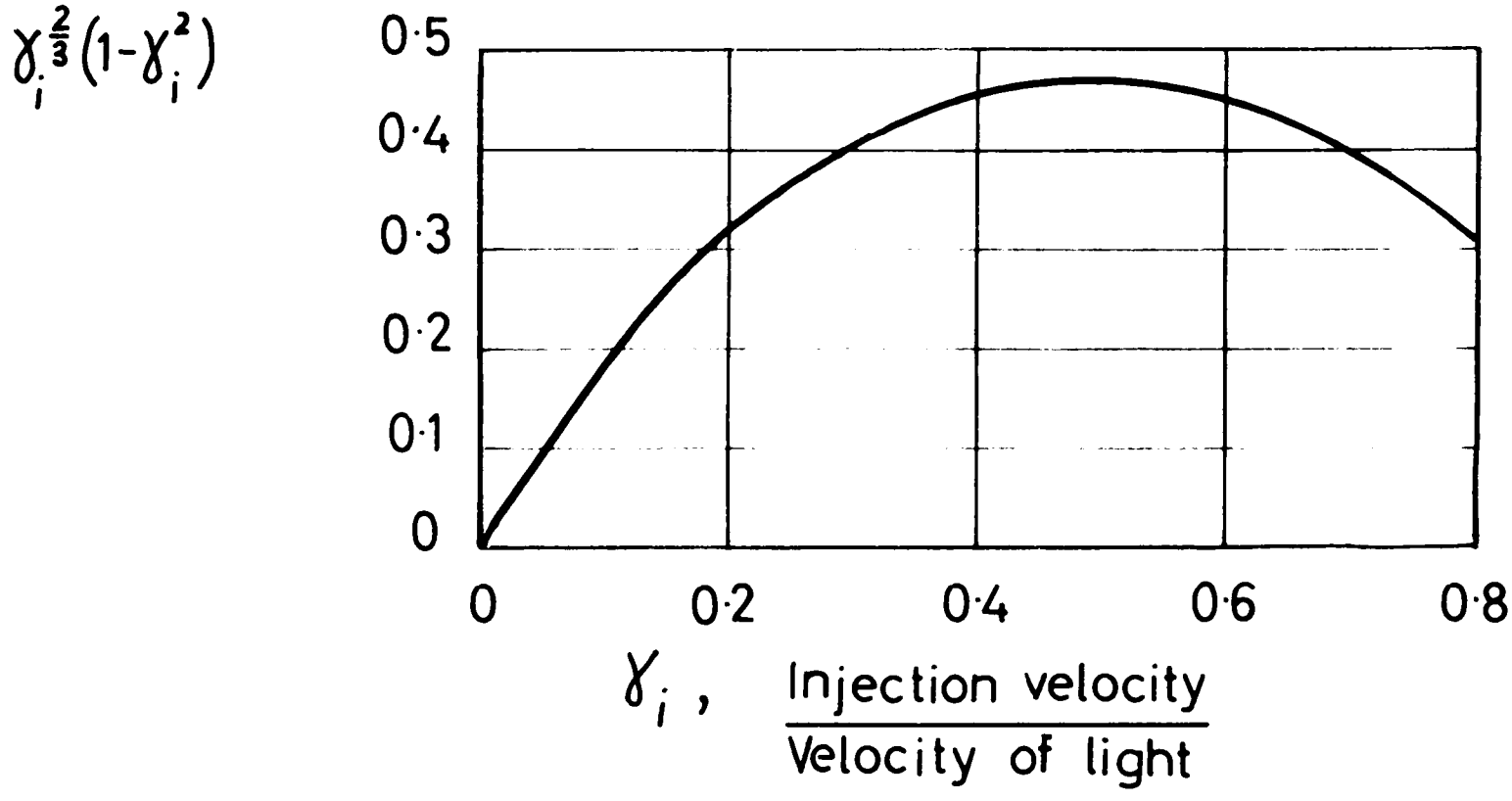

$\gamma_i^{\frac{2}{3}}(1-\gamma_i^2)$
0·5
0·4
0·3
0·2
0·1
0
0
0·2
0·4
0·6
0·8
γ_i , Injection velocity / Velocity of light

FIG. 12.

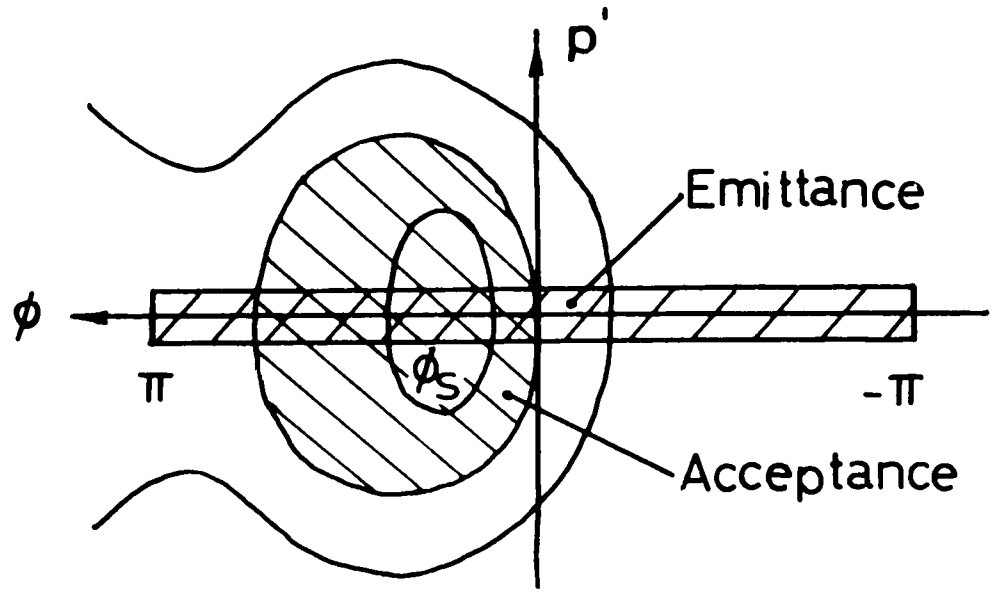

p'
Emittance
ϕ
ϕ_s
π
$-\pi$
Acceptance

FIG. 13.

The phase stable position, $\phi_{si} = 45^{o}$, was chosen to give a reasonable percentage electron capture (about 38% as calculated by equation 4.14) for random input phases, and to ensure a fairly high initial acceleration without risking instability caused by operating near the phase of maximum field. We also choose to design the field-velocity régime by keeping ϕ_s constant along the structure and determining E_{ms} and v_s together (see Section 4.4).

4.3 Pre-bunching

In this section we look more closely at the need for bunching the electrons emitted by the source before injecting them along the bunching section of the slow-wave structure.

4.3.1 Matching of Axial Ratios

Fig. 13 shows the closed curves (near ellipses) which represent the phase plane trajectories of particles which oscillate stably in the linac, together with the open curves of the non-oscillatory trajectories. A particle whose initial Hamiltonian is given by a particular orbit will remain in that orbit during its subsequent motion. If we superpose the initial phase plane area occupied by the electrons from the gun (the emittance) on the linac phase orbit plot, we can see what the subsequent motion will be. We define the acceptance of the linac as those phase plane trajectories which represent stable oscillations (orbits).

Since the emittance covers all phases it is intercepted by all the orbits of constant Hamiltonian in the acceptance. Therefore the

particles will subsequently be swept over the acceptance and will eventually be distributed over most of it because the non-linear restoring forces will cause them to oscillate with different frequencies. Thus the phase area occupied by the particles increases several times. Also, all those particles of the emittance which are not enclosed by the acceptance lie on non-oscillatory trajectories and are not accelerated.

To maximise the number of accepted particles we need to match the emittance to the acceptance. Let us approximate these phase areas by right ellipses. The matching then becomes a question of matching the ratios of momentum spread to phase spread, the axial ratios, without increasing the phase area.[62]

4.3.2 A Pre-bunching Cavity

We shall now outline the operation of a pre-bunching cavity which will match the gun emittance to the linac acceptance, with especial reference to the effect on the accepted charge and on the momentum spread caused by the introduction of the cavity.

From klystron theory[54] we may write an expression for the time t_2 at which a particle reaches a point distant ℓ from the gap across which the R.F. voltage given by $V_m \sin \omega t$ is applied:-

$$t_2 \approx t_1 + \frac{\ell}{v_o}\left[1 - \frac{1}{2}\frac{V_m}{V_o}\sin \omega t_1\right] \qquad (4.29)$$

where t_1 = the time at which the particle crosses the gap

v_o = the initial particle velocity (d.c.)

V_o = the initial particle voltage (d.c.)

Multiplying (4.29) by ω and substituting θ_o for $\frac{\omega \ell}{v_o}$, the d.c. phase change over the distance ℓ we have

$$\omega t_2 - \theta_o = \omega t_1 - \chi \sin \omega t, \qquad (4.30)$$

where $\chi = \frac{\theta_o V_m}{2V_o}$, the bunching parameter

Thus $\omega t_2 - \theta_o$ can represent the input phase ϕ_1 at the linac (provided the cavity and linac R.F. waves are phase synchronised) which is distant ℓ from the cavity gap, and ωt_1 can represent the input particle phase at the gap. A plot of the linac input phase versus cavity input phase for three values of χ is given in Fig. 14(a). Equation (4.14) shows that the linac phase acceptance for the correct beam energy is about $3\pi/4$ for a phase stable position of $\pi/4$. This phase acceptance is shown as $\Delta \phi_i$ on the Figure. If the momentum spread introduced by the cavity is negligible, all of the charge enclosed by the dashed lines is accepted by the linac.

The choice of bunching parameter and the best phase difference between the cavity and linac R.F. fields depends chiefly upon the use to be made of the linac output. In our undulator applications we require good bunching primarily with a somewhat lesser regard to obtaining relatively high beam current.

If we wish to accept the maximum number of particles into stable orbits the phase acceptance ($\Delta \phi_i$) should be symmetric about the cavity bunching curve (Fig. 14(a)) and the value of χ should be such that the stationary points of the bunching curve lie on the phase acceptance limit lines. However, since the charge is densest at these stationary

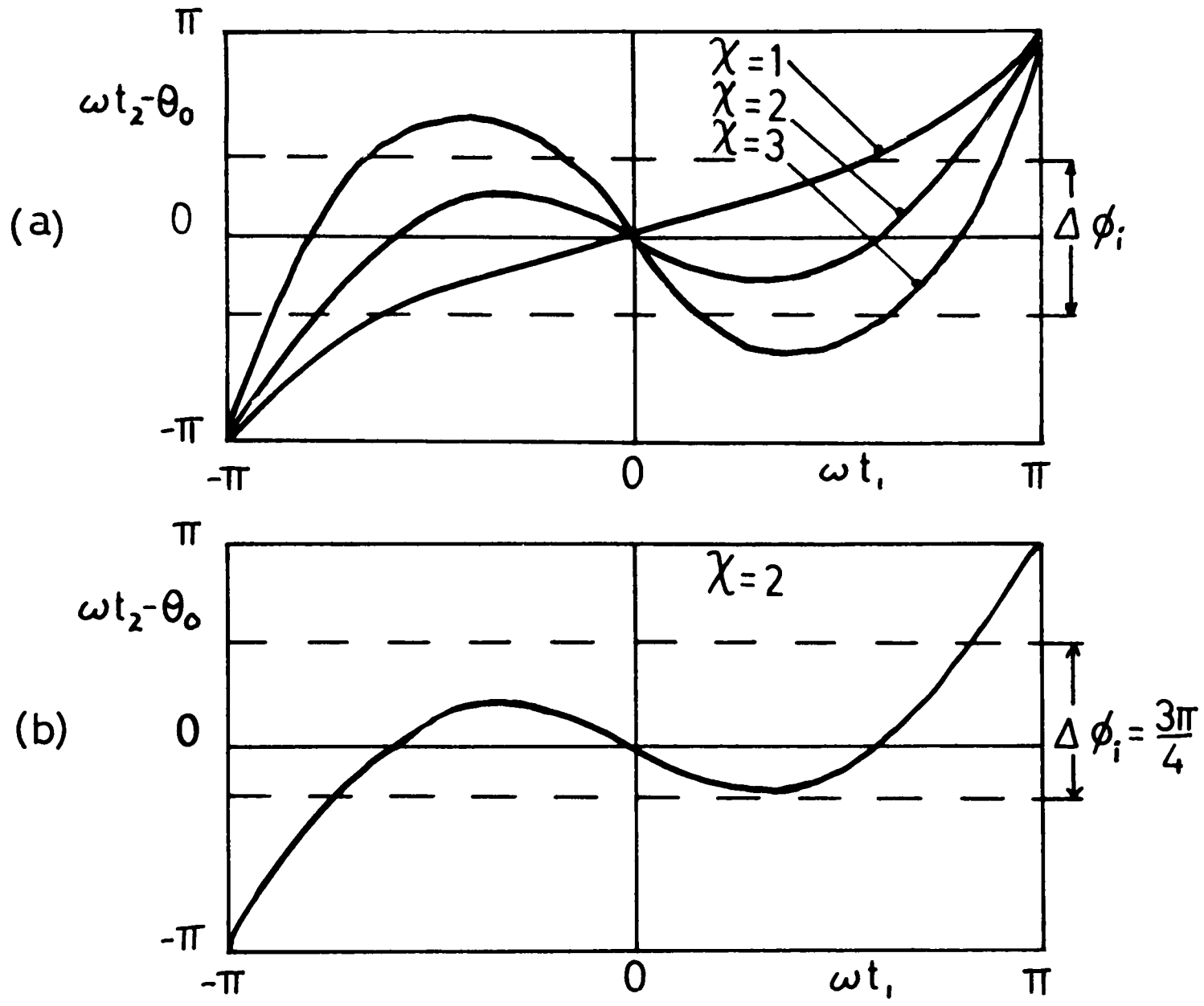


FIG. 14.

points this puts most of the charge on Hamiltonians of large phase and energy spread. In practice we place these stationary points well within the acceptance limits. For undulator applications we should centre the charge distribution on the position of minimum phase and momentum spread at the input to the linac, i.e. at a phase ϕ equal to ϕ_s $(\pi/4)$. Calculations using equations (4.14) and (4.30) show respectively that this implies an asymmetric position for the phase acceptance band about the line $\omega t_2 - \theta_o = 0$, and a corresponding value of $\chi = 2.9$ to give tangency between the upper phase acceptance line and the bunching curve. A conservative value of $\chi = 2$ might be chosen to bring the stationary points within the phase acceptance limits as depicted in Fig. 14(b). Assuming that the charge fed to the cavity is uniformly distributed over all phases, we can estimate the percentage charge accepted by the linac from the projection on to the ωt_1 axis of that part of the bunching curve which lies within the phase acceptance. For $\chi = 2$ the accepted charge is about 80%. However, if we wish to concentrate the dense charge which exists around the stationary points of the bunching curve very near to the centre of the bunch, in an effort to produce the highest frequencies in an undulator for example, then χ should be in the approximate range $1 \leqslant \chi \leqslant 1.5$. Upwards of 65% of the charge would still be accepted.

In the above discussion we have ignored the momentum spread in the beam both entering and leaving the prebunching cavity. The spread from the particle source can always be neglected if we assume that the

gun voltage is constant.[62] For electron linacs the momentum spread introduced by a bunching cavity can also normally be ignored. We can demonstrate this for our particular pre-buncher and linac. With a drift distance of 0.15 m ($\ell = 0.15$), and $\chi = 2$, we find that $V_m = 4.5$ kV (ω and v_o were taken from the chosen linac parameters). From klystron theory we know that for small momentum deviations from the mean value p_o,

$$\Delta p_{max} \approx p_o \frac{V_m}{2V_o} \tag{4.31}$$

where Δp_{max} is the maximum deviation. From the Hamiltonian (4.14) we can solve for p'_{max}, whence

$$\frac{\Delta p_{max}}{p'_{max}} = \frac{1}{23}$$

which indicates that Δp can be neglected, as was done.

4.4 The Linac Design for Good Bunching

4.4.1 The Bunching Section

In section 4.2 we found that there should be about a tenfold increase in electric field along the bunching section. Liouville's theorem tells us that as particles progress along the structure we can at best confine them to the same magnitude of phase area that they occupied upon injection. We have seen that this conservation of phase area can be obtained by slowly (adiabatically) increasing the electric field. In practice we wish the bunching section to be short and field variation is not therefore likely to be adiabatic. However, Lichtenberg

has developed a theory for the linearised problem[62] where two phase plane regions over which the Hamiltonians have axial ratios R_1 and R_3 respectively can be matched by an intermediate region in which particles make one quarter of a phase oscillation with axial ratio R_2 such that

$$R_2 = (R_1 R_3)^{\frac{1}{2}} \tag{4.32}$$

This 'quarter wave-length' matching transformer conserves the occupied phase area. A separate transition region of this type presents considerable engineering design problems. We therefore plan to make the bunching section the best smooth approximation to the quarter wave transformer.

If we take n quarter wave sections in series we find that the variation in axial ratio is given by

$$R_n = R_1 r^n \tag{4.33}$$

where R_n and R_1 are the axial ratios of the n^{th} and the first section respectively, and r is the constant ratio R_n/R_{n-1}. Since the phase change per section is $\frac{\pi}{2}$ radian

$$n = \frac{\sum_{k=1}^{k=n} \beta_{ok} \ell_k}{\pi/2} \tag{4.34}$$

where $\beta_{ok} = \frac{\omega_{ok}}{v_{sk}}$, the effective propagation constant and ℓ_k is the length of the k^{th} section.

We can approximate to the discrete section régime of equations (4.33) and (4.34) with a continuous variation in R where, modifying (4.34)

$$n = \frac{\int_0^{z_n} \beta_o \, dz}{\pi/2} \qquad (4.34)$$

and differentiating (4.33) with respect to the now continuous (distance) variable n

$$\frac{1}{\beta_o} \cdot \frac{dR}{dz} = \epsilon R \qquad (4.35)$$

where ϵ is an arbitrary proportionality constant.

From equations (4.21) we can re-write (4.35) as

$$\frac{d}{dz} (m_\ell \omega_o) = \epsilon \frac{m_\ell \omega_o^2}{v_s} \qquad (4.36)$$

Equation (4.36) must be solved simultaneously with the force equation (4.25) to give the variation in particle momentum and electric field corresponding to the exponential variation in axial ratio prescribed by (4.35). We can transform (4.2) and (4.36) so that they contain only variables p_s, E_{ms}, ϕ_s, and ϵ. After considerable manipulation we obtain the force equation (see Appendix I for derivation of (4.37) and (4.38))

$$\frac{dp_s}{dz} = \frac{e \sin \phi_s}{c} \cdot \frac{E_{ms}}{p_s} (p_s^2 + m_o^2 c^2)^{\frac{1}{2}} \qquad (4.37)$$

and the equation giving the exponential change in axial ratio

$$\frac{dE_{ms}}{dz} = \frac{e \sin \phi_s}{c} \left[(p_s^2 + m_o^2 c^2)^{\frac{1}{2}} p_s^{-2} E_{ms}^2 - 4(p_s^2 + m_o^2 c^2)^{-\frac{1}{2}} F_{ms}^2 \right] + 2\epsilon (e\omega \cos \phi_s)^{\frac{1}{2}} m_o \left(\frac{E_{ms}}{p_s} \right)^{\frac{3}{2}} \quad (4.38)$$

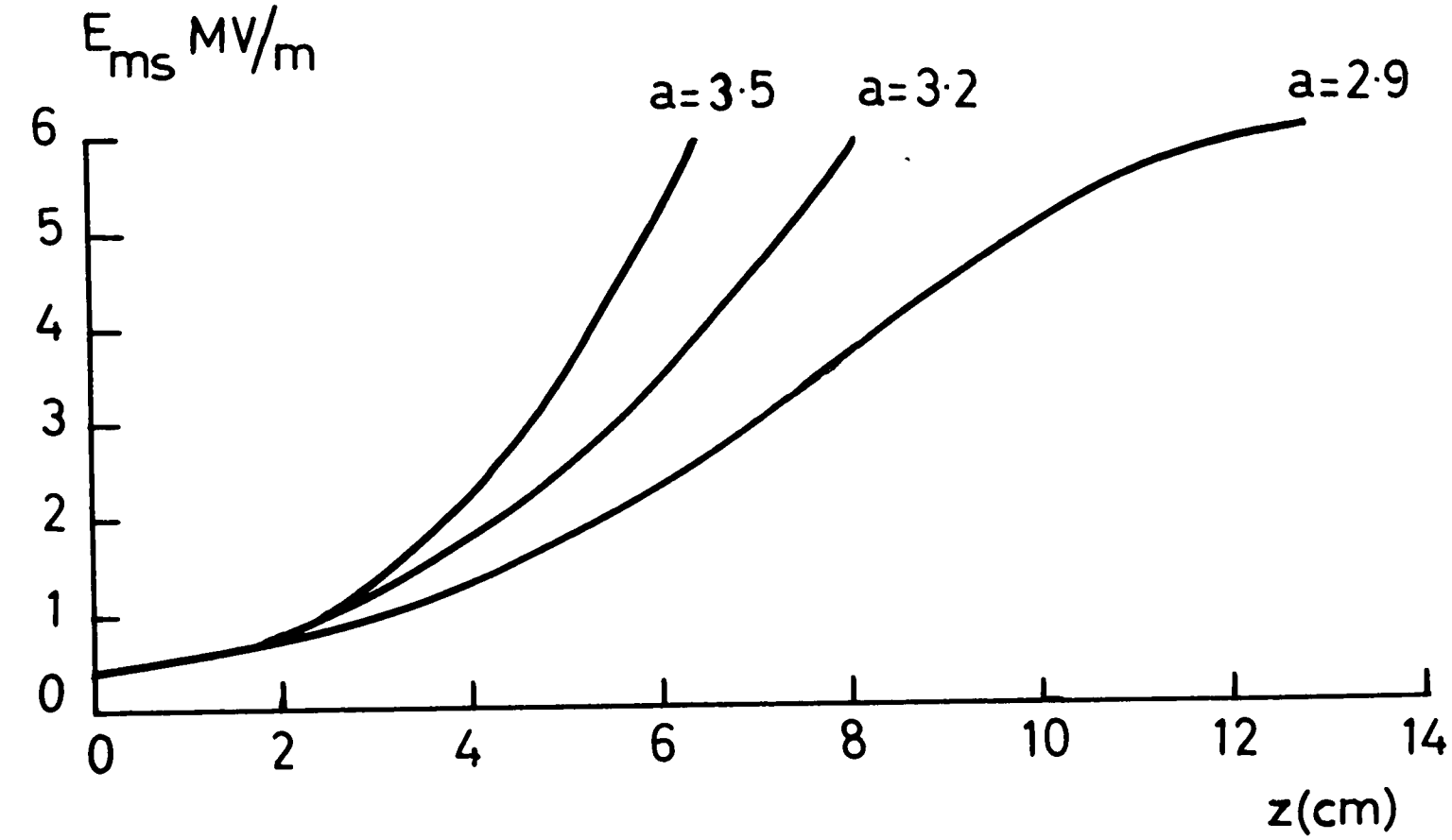
We have decided to keep ϕ_s fixed so that these two first order, non-linear simultaneous equations (4.37) and (4.38) can give a unique solution in terms of the parameter ϵ. The equations are not soluble analytically and so a digital computer was programmed to obtain solutions by numerical methods.[61] We now vary ϵ independently to obtain the desired compromise between phase area conservation and shortness of bunching section. As the desired length of bunching section is about 10 cm, it is fortunate that the value of ϵ corresponding to the desired velocity increase in the section also gives a smooth variation of field from the bunching section to the accelerator proper, i.e. no discontinuity in the first derivative of the field is indicated.

In Fig. 15 the variation of peak field and phase velocity with distance is plotted with a as parameter where

$$a = \frac{\omega}{\omega_{oi} \tan \phi_s} \left[1 - \left(\frac{v_{si}}{c} \right)^2 \right]^{\frac{1}{2}}$$

and ω_{oi} is the initial angular frequency of phase oscillations.

We note that variations in a can affect the overall curves greatly, but do not affect the initial slope appreciably. This initial slope is primarily determined by initial conditions. The altering of a gives us an additional degree of freedom with which either to adjust the length of the bunching section to some reasonable


E_{ms} MV/m
a=3·5
a=3·2
a=2·9
6
5
4
3
2
1
0
0
2
4
6
8
10
12
14
z(cm)

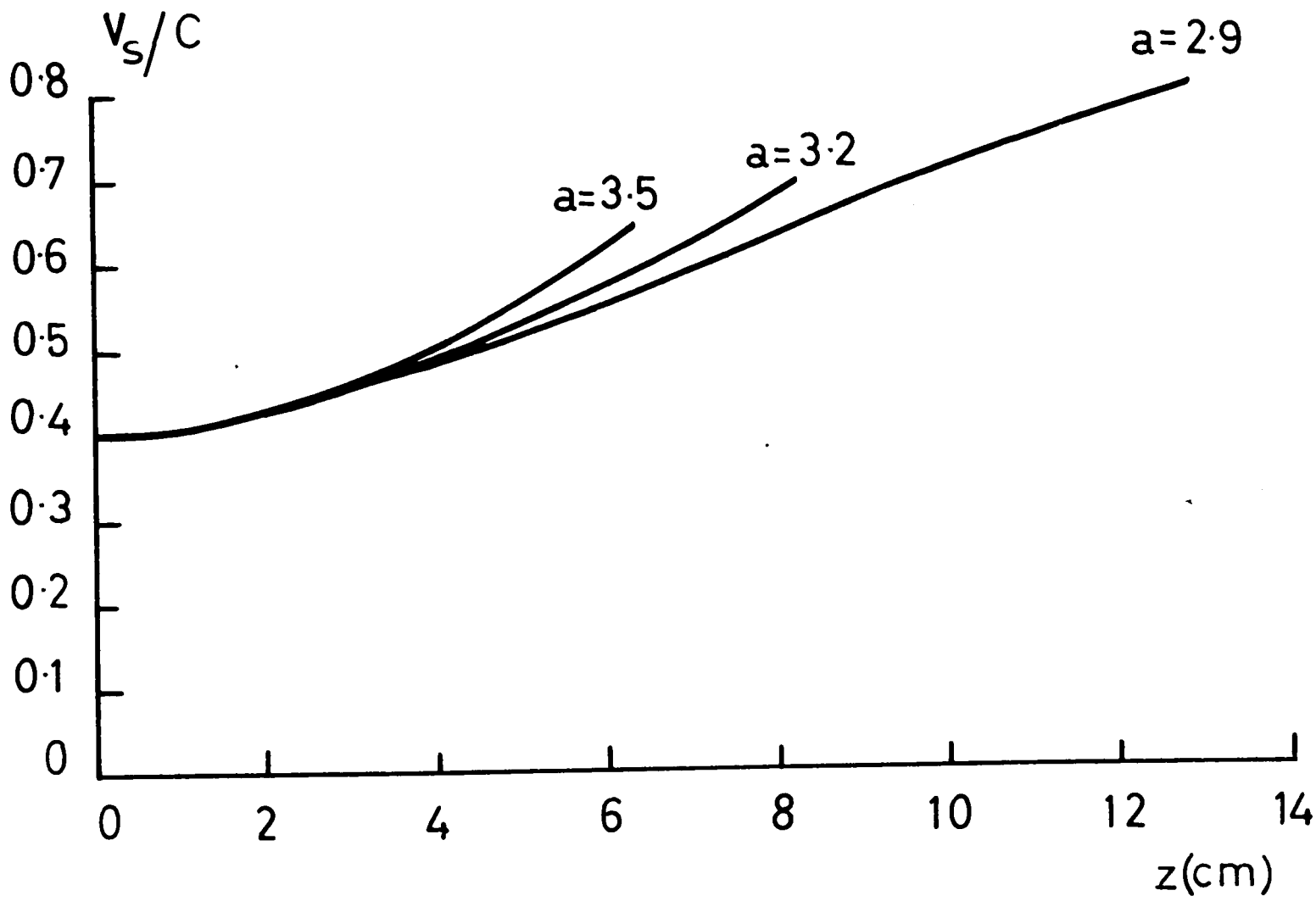

V_s/C
a=2·9
a=3·2
a=3·5
0·8
0·7
0·6
0·5
0·4
0·3
0·2
0·1
0
0
2
4
6
8
10
12
14
z(cm)

FIG. 15.

value, or to give a smooth field transition into the main accelerating section. When the parameter a equals 2.4 these objectives are compatible. The corresponding peak fields, velocities, and axial distances are tabulated in Appendix II.

It should be noted that the form of the field variation in the buncher is not critical. If a system were devised that had a 50% increase in phase area, the resulting increase of about 20% in phase and energy spread would not badly affect the operation of an undulator, for example, fed by the linac. What is more important is the pre-bunching which can concentrate most of the charge in a tight bunch, and the large variation of field in the bunching section which further bunches the beam. However, once a form of field variation is chosen, it is most important that the corresponding phase velocity variation be strictly adhered to so that the bunch remains synchronous with the wave. Large oscillations and loss of beam can result from an incorrect velocity. Errors are discussed in Section 4.6.

4.4.2 The Main Accelerating Section

Since the value of v_s (and v_b) is about 0.75c at the end of the buncher, the velocity in the accelerating section is increased relatively slowly and the waveguide geometry is nearly uniform. Therefore we assume that in this high velocity section the shunt impedance is uniform, the loss length is constant, and the field decays exponentially from the peak value reached at the end of the buncher. We simply vary the phase velocity to keep the electrons

in step with the wave but we make no attempt to vary the field independently. The equations of motion can be written, for no beam loading,

$$\frac{dV}{dz} = E_{ms} \sin \psi \qquad (4.39)$$

and

$$\frac{d\phi}{dz} = \omega\left(\frac{1}{v_b} - \frac{1}{v_s}\right) \qquad (4.40)$$

The effects of introducing beam loading when the particles do not ride at the crest of the travelling R.F. wave have been treated by Johnsen.[63] Following his analysis (which is summarised in Appendix III) we can re-write equation (4.39) to take beam loading and exponential field decay into account as

$$\frac{dV}{dz} = E_{mso} \sin \phi \; e^{-z/2l_o} - r_{sh} I \left(1 - e^{-z/2l_o}\right) \qquad (4.41)$$

where E_{mso} is the peak synchronous field at the end of the buncher, and r_{sh}, l_o, and I are the shunt impedance, loss length and beam pulse current as before.

We shall use estimates for r_{sh} and l_o in these equations in the next section to compute particle trajectories as a test for the buncher design, but we shall postpone presenting the designed variation in phase velocity until we have a better knowledge of the shunt impedance and loss length attainable in the J-Band structure.

The difference between the approaches to bunching section and to accelerating section design exists because we wish to force the electrons to bunch in the first section, but to simply avoid perturbing

the bunch in the second section. We primarily need prescribed fields and phase synchronism in the first section, but only phase synchronism in the second section.

4.5 Trajectory Computations

We shall now describe how the buncher design described above was tested by determining the particle trajectories corresponding to the buncher field and velocity variation given by equations (4.37) and (4.38) with the parameter a at 2.4 (see Fig. 15). The particle trajectories in the buncher were computed by solving the equations of motion (4.39) and (4.40) for energy and phase. In the main accelerator, equations (4.41) and (4.40) were used because the decay of the field due to R.F. losses becomes apparent here as we propose to feed in all the R.F. power at the beginning of the buncher, and because the influence of the beam current upon the R.F. field becomes appreciable. The beam loading term of equation (4.41) has reached about one tenth of the R.F. field term at the end of the buncher where $r_{sh} = 10^8 \Omega/m$, $I = 75$ mA, and $\ell_o = 1$ m. Lichtenberg programmed a digital computer to perform the integrations for a total structure length of 0.75 m, giving an output energy for the phase stable electron of 2.598 MeV without beam loading and 2.364 MeV with 75 mA beam loading, taking $r_{sh} = 10^8 \Omega/m$ and $\ell_o = 1m$.

With beam loading the phase plane region of stability at the output moves towards the phase of higher electric field, and the average particle output velocity in the region is higher than that of the phase

stable particle. The bunch falls behind the wave because the 75 mA of beam loading causes the field to decay more rapidly than it should to keep the phase stable particle in exact synchronism with the wave. However, the electrons fall back as a bunch and their total energy gain is not much less than that obtained without beam loading because they fall back into a higher field region.

The trajectory computations were performed for particles of widely varying input energy and phase around the design values of 0.047 MeV and $\pi/4$ respectively. The trajectories of two particles injected at the designed velocity are shown in Fig. 16 without beam loading and in Fig. 17 with 75 mA beam loading. The emittance ellipse for the accelerator, i.e. the smallest ellipse that encloses the phase plane region in which all the output accelerated particles lie, is shown cross-hatched in the two cases. The small crosses within the emittance show the final positions of some of the other particles whose trajectories were computed. The numbers against the marked points on the trajectories are the axial distance travelled by the particles in centimetres.

The computations gave the following numerical information:-

(a) The linac acceptance indicates that electron capture occurs at phases from $-0.15\ \pi$ to $+0.7\ \pi$, and at kinetic energies from 0.042 MeV to 0.055 MeV. These values should be compared with those derived from the invariant Hamiltonian, namely phases from 0 to $0.75\ \pi$, and kinetic energies from 0.042 MeV to 0.052 MeV. We see that former acceptance area is 30%

Phase stable particle energy at output = 2·598 MeV

Beam Injection Velocity = 0·4c

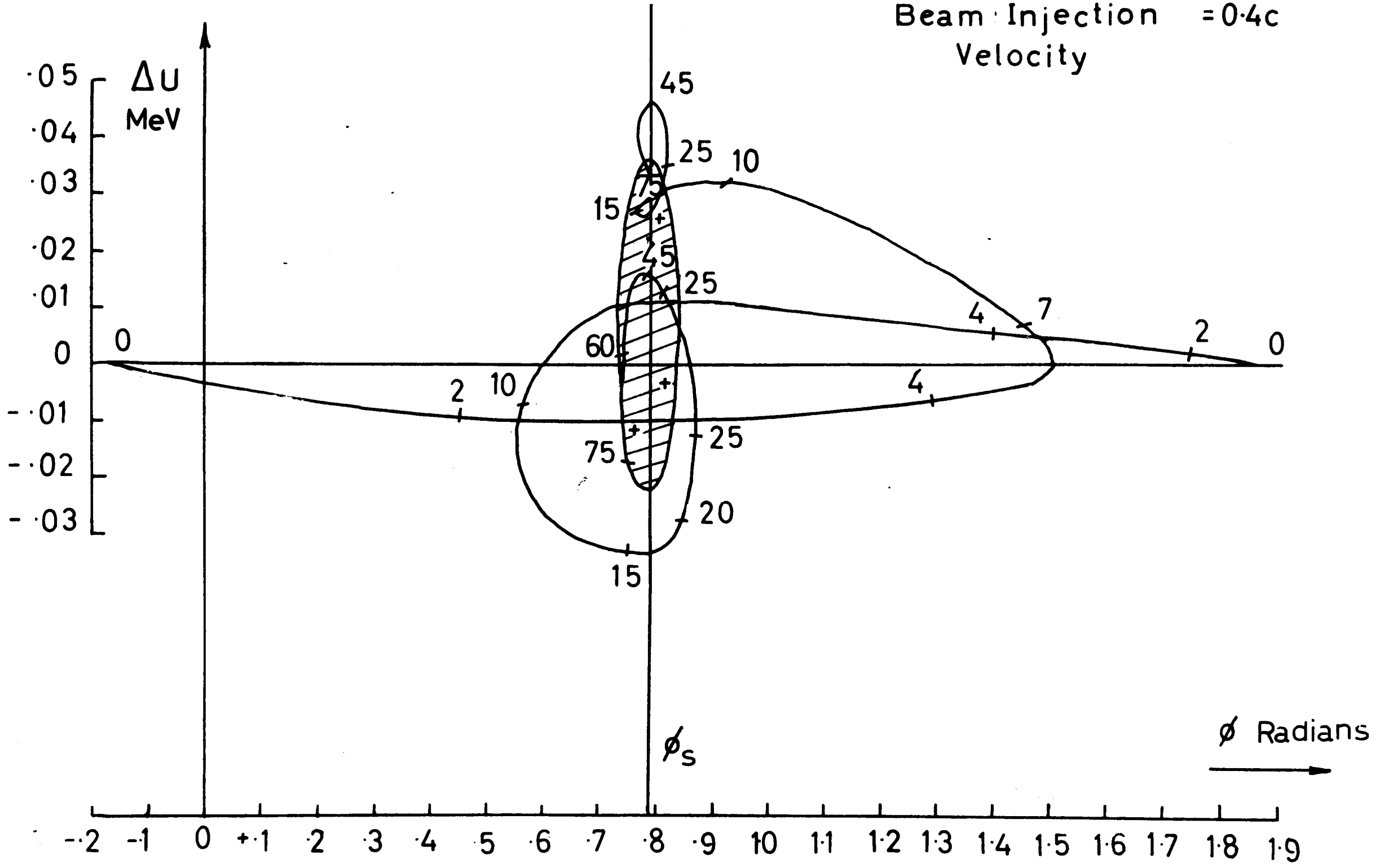


FIG. 16 TRAJECTORIES WITHOUT BEAM LOADING

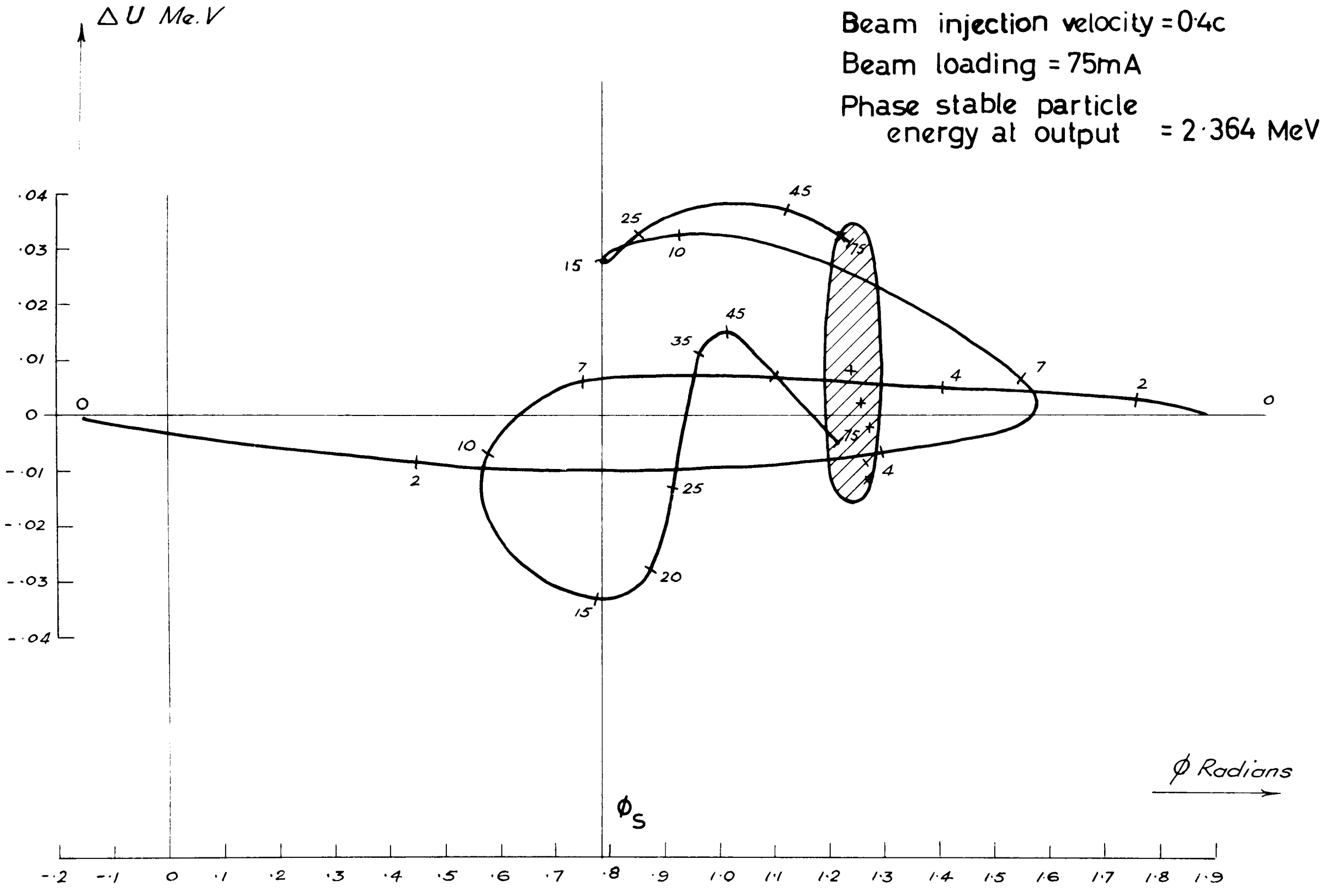


FIG. 17. TRAJECTORIES WITH BEAM LOADING

greater than the latter. Although the acceptance is larger than that expected by the adiabatic theory the phase bunching and energy resolution at the phase and energy limits are quite poor. Therefore we have adopted a working region of acceptance phase from $-0.05\ \pi$ to $0.6\ \pi$. The pre-buncher will be designed to concentrate the charge within this region.

(b) The energy spread at the output is about two per cent of the mean energy, and the phase spread has been reduced to about 0.1 radian or 5.7 degrees. For undulator applications this implies coherent radiation up to the 30th harmonic, i.e. 0.6 mm wavelength when the linac wavelength is 1.8 cm as planned.

(c) The emittance area of the linac is smaller than the acceptance area. Lichtenberg has explained this apparent violation of Liouville's Theorem as a consequence of employing a non-adiabatic variation in the phase plane, and of approximating to the ideal quarter-wave transformer with a continuously varying system.[61,62]

4.6 The Effects of Errors in Fields and Velocities

Errors in the beam injection velocity, accelerating field and wave velocity can cause the following effects:-

(a) The phase stable position can be shifted. If such a shift is time-dependent and is so large that the mean beam energy is seriously reduced, the operation of an undulator or other radiator fed by the linac will be greatly affected. This is because the phase coherence, bandwidth, and power of the

radiation depend partly upon the phase uniformity of the thousands of bunches comprising the beam current pulse, and because the radiated wavelength is increased if the particle energy falls.

(b) The phase and energy spread at the output can be increased. Increased phase spread primarily results in a longer maximum attainable wavelength in a radiator, and increased energy spread will widen the radiated frequency spectrum.

(c) Some particles in the bunch can become unstable and will not be accelerated.

The computer programmes used in Section 4.5 were modified to investigate these effects. We shall now summarise the results given by these computations.[61] The shunt impedance and loss length are taken as $10^8\ \Omega/m$ and 1 m respectively.

4.6.1 Errors in Phase Velocity

With 75 mA beam current an error of up to + 2% does not cause the phase stable position to change by more than -0.04 radian in phase or -1% in mean energy. Random errors in structure dimensions can be treated by introducing a Gaussian distribution of errors* in phase velocity along the linac. A standard deviation σ of 0.01 v_s shifts the bunch to a slightly higher mean energy (+ $\frac{1}{2}$%) but ϕ_s remains almost unchanged and the phase area is not appreciably increased. However, many particles became unstable when σ was set at 0.05 v_s. How this result affects mechanical tolerance is

* At 1 cm intervals

discussed in Chapter VII. The calculations on random errors were performed without beam loading.

4.6.2 Errors in Accelerating Field

An error of $\pm$ 5% in accelerating field causes a corresponding error in mean output energy of about $\pm$ 5% and a phase shift of about $\mp$ 0.07 radian for 75 mA beam loading. Random variations in field integrate along the linac to produce quite small errors in the output phase, energy, and phase area. Without beam loading, a standard deviation of as much as 0.215 E_{ms} in the buncher resulted in only a $\frac{1}{2}$% reduction in energy, a phase advance of 0.05 radian, and a negligible increase in phase area.

4.6.3 Errors in Beam Injection Velocity

In Section 4.5 we saw that the accepted input energy limits were asymmetric about the design value of 0.047 MeV, and that the higher input energies were more favourable. Trajectory computations in the buncher with a -2% (-0.002 MeV) error in beam injection velocity show that some particles are already unstable. These results indicated that a reduction in output phase area should be given by injecting the beam at a velocity slightly greater than that of the wave. Further computations show that an increase of 1.25% in the injection velocity gives a 15% reduction in the phase area at the end of the buncher. This would lead to a slight reduction in the output phase area. It is clearly desirable to err on the higher side of the design injection velocity.

CHAPTER V

The Assessment of the Properties of Titania Ceramics

5.1 The Measurement of K and tan δ at 1.8 cm Wavelength

In sub-section 2.4.2 we noted that the permittivity and loss tangent of certain magnesium oxide-titanium dioxide ceramics conformed with the range of values prescribed by the anisotropic theory for linac structures of high shunt impedance at 10 cm wavelength. Frequency scaling of r_{sh}, and the values of K and tan δ to 8 mm wavelength[53] indicated that these ceramics should be suitable for a J-Band linac structure. Free investigated their suitability at J-Band in experiments at low power.[67] He used an H_{01} mode resonant cavity technique described for the work at 8 mm wavelength.[68,53] The important advantage of this method is that the H_{01} mode metal (silver) wall losses in a cylindrical cavity are small enough for the change in cavity Q when a low-loss specimen (tan $\delta \approx 10^{-4}$) is inserted to be measured with reasonable accuracy.

The J-Band results confirmed that the titania ceramics possessed the expected approximate values of K and tan δ. One group of tested samples was composed of titanium dioxide with a small percentage of kaolin stabiliser, and the other group was composed of about 40% titanium dioxide and 60% magnesium oxide by weight. For linac purposes the product of K and $(\tan \delta)^{-1}$ is a measure of the goodness of a specimen within a group, the higher the product the better. In the titania group the best mix was 96% titania and 4% stabiliser (Manufacturer's reference: K4)

giving a relative permittivity of 96.3 ± 0.3% and a loss tangent of 4.5×10^{-4} ± 20%. The best magnesium titanate sample (60% MgO, 40% TiO_2) had a relative permittivity of 14.3 ± 0.3% with a loss tangent of 1.2×10^{-4} ± 20%. Referring to Fig. 3 in Chapter II we see that the titania mix should give us about a 30% higher shunt impedance in the linac. Although this result favours titania as the linac loading material there are several other properties to be considered where magnesium titanate may score over titania. Fortunately the difference between the two ceramics is not very great as far as the estimated shunt impedance is concerned.

5.2 Practical Physical and Chemical Considerations

The titania ceramics are manufactured in the following way. The constituents are milled to powders, finely sieved, thoroughly mixed (it is here that the manufacturer's skill is critical), and pressed to suitable specimen shapes. The pressings are then sintered at about 1375°C in an oxidising atmosphere. The cooled specimens are finally ground to the required dimensions using carborundum and diamond compounds.

Some occasional defects are immediately apparent in finished specimens. Small surface cavities and inclusions of abrasive and perhaps reduced titania, are to be found. These lead to electromagnetic field irregularities and even local electric breakdown in R.F. structures.

Porosity of the materials is suggested by outward appearances. That the specimens are hygroscopic was clearly shown by Free in the great variation of measured values of K and tan δ for a given specimen

over a period of time, even though the surfaces were kept sensibly clean and grease-free.[67] Steady values of K and tan δ were only obtained if the specimens were dried and kept in a desiccator, or under vacuum. Certain practical considerations require that a number of physical and chemical tests be carried out on the best titania and magnesium titanate specimens. The initial series of tests will now be discussed. Later developments are included in Chapter VII.

5.2.1 Temperature Coefficients of Permittivity and Linear Expansion

The energy dissipation along the slow wave structure will be of the order of 100 W/m. Although most of this will be lost in the cylindrical waveguide walls (diameter ≈ 1 cm) it is important that we should know the extent to which a rise in temperature will affect the disc permittivity. For mechanical reasons we must also know the coefficient of linear expansion. If either of these coefficients is large then the material concerned may be of no practical use for the linac.

The manufacturer quoted the following values:-

	Temperature Coefficient of Permittivity	Temperature Coefficient of Linear Expansion
Titania	$-9.5.10^{-4}$	9.10^{-6}
Magnesium Titanate	$+0.3.10^{-4}$	9.10^{-6}

Because only approximate values for these quantities are needed no independent attempt was made to verify the figures. Clearly magnesium titanate has the more stable permittivity, but the temperature

coefficient for each material is reasonably low. For a 10°C rise in temperature the permittivity of the titania ceramic falls by 1%. In later chapters we shall see whether such a temperature rise is likely and whether the 1% drop in K can be tolerated in the linac structure.

5.2.2 The Metallising of Disc Rims

To minimise the structure losses and to reduce the chance of air breakdown across any small gap existing between a disc rim and the waveguide wall, it is proposed to coat the dielectric rims with a thin metallic layer which will make good electrical contact with the wall. Rim metallising is also a pre-requisite in the electroforming method of construction, discussed below.

Initially the problem was tackled by seeking a simple way of metallising disc rims with a fraction of a skin depth of any reasonable conductor. Experiments were made with Johnson Matthey preparations, solutions and suspensions of platinum and platinum-gold alloy compounds together with adhesion promoting agents in organic liquids. The solutions were brushed on to the ceramics and allowed to dry before firing in an oxidising atmosphere, during which the organic materials were volatilised and the compounds were reduced to metal. "Liquid Bright Platinum" (a Platinum-Gold alloy film) and "Liquid Matt Platinum" were used because of their immediate availability. The latter solution bonded well to both of the ceramics and gave a film of almost pure platinum about 0.35 micron thick (maker's estimate). At 16 Gc/s

the skin depth in platinum is about 1.7 micron so that the "Matt Platinum" film should improve the contact between the wall and the disc, the reduction in ohmic loss being little affected by the platinum resistivity.

For reasons which will be given later, it was decided to fabricate the waveguide tube from copper. To avoid having junctions of dissimilar metals which would be inherently resistive due to diffusion and alloying, consideration was given to metallising with copper. It was also decided that vacuum coating should be tried as it would avoid some of the problems found in the "Liquid Metal" method, such as confining the film to the disc rims and obtaining a uniform thickness. A pilot plant was set up in which a short stack of carefully ground and cleaned* titania discs was slowly rotated at a steady rate under vacuum near to a source of evaporating copper. A sketch of the experimental arrangement is given in Fig. 18. The rate of evaporation was kept approximately constant by varying the current through the tungsten filament so that the pressure was steady at about 10^{-4} torr. The condensed film on the discs appeared to be uniform, and the condensed film on the bell jar walls appeared to build up at a steady rate. The time needed to produce a film thickness of two skin depths, about one micron, was found by experiment. The film thickness was estimated by weighing the discs before and after coating, and the consistency of the copper was checked by simple

* 'Non-touch' technique was used in all ceramic cleaning processes. Any superficial dirt was removed in detergent and warm water. Discs were degreased in iso-propyl-alcohol and rinsed in distilled water before being dried by long-term airtight storage over silica gel, or by overnight drying in a vacuum oven at about 100°C and 10^{-3} torr.

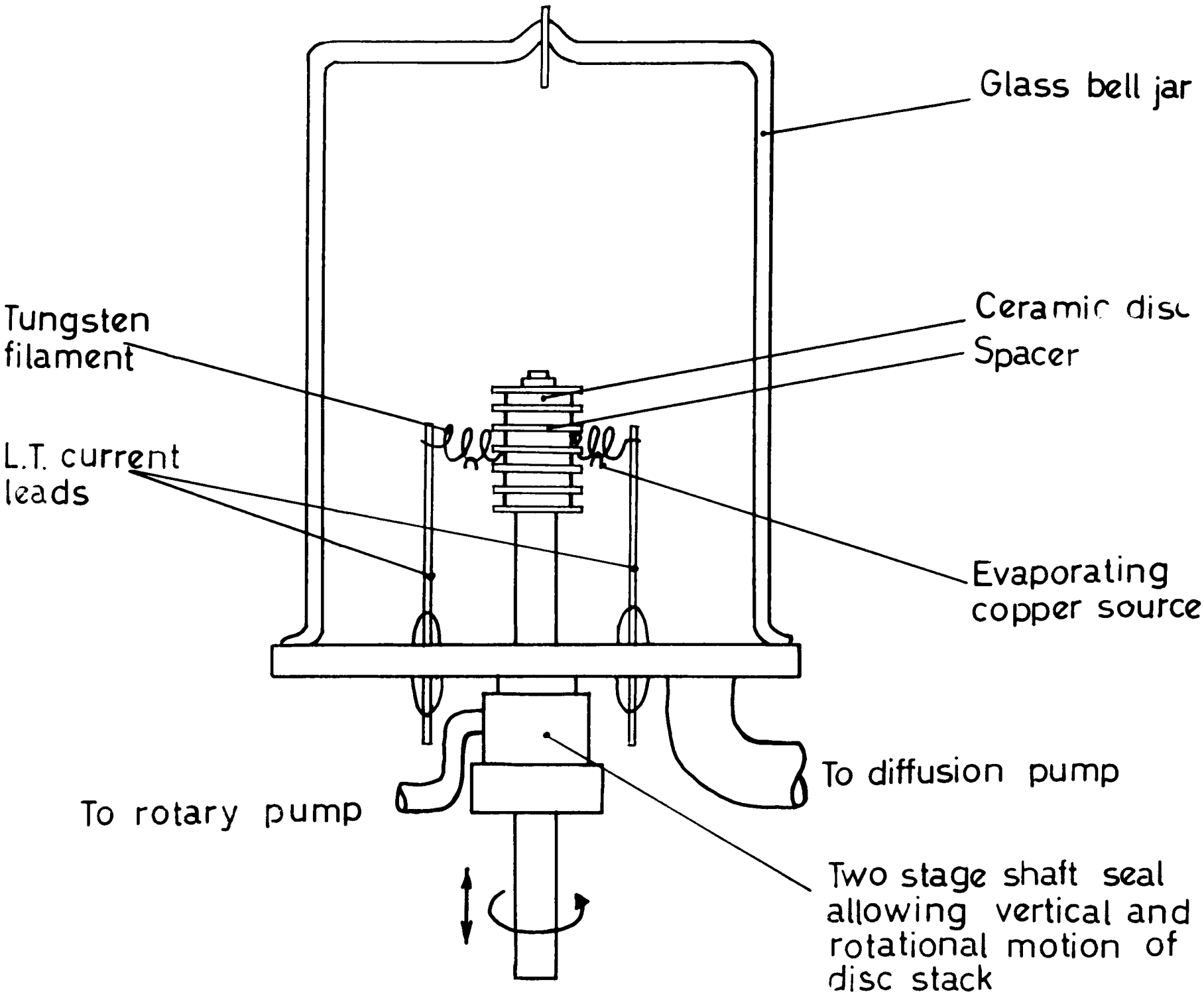


FIG.18. PILOT PLANT FOR VACUUM COATING

d.c. resistance measurements. A negligible amount of copper condensed on the disc faces because the discs had been ground and polished to a thickness uniform to within $\pm$ 0.005 mm, and therefore the faces were effectively masked by the matching polished metal spacers.

It was found that a reasonably durable film was produced provided that the titania was dried in a vacuum oven at about 80°C for 48 hours after the final cleaning before coating, and provided that the metallised titania disc was kept in a desiccator after the coating.

The brazing of the copper waveguide to the discs was considered, but the work of Walker[60] suggested that an intermediate layer of silver is necessary to do this with titania discs. The process requires temperatures of 1000°C so that barrier diffusion would be considerable, and diffusion of molten silver into the ceramic would make the disc diameter indefinite. Also care would have to be taken to avoid localised reduction of the titania to a lower semiconducting oxide. In a vacuum this reduction occurs at about 400°C. It was thought that vacuum-coating was probably the best method of metallising titania discs with copper.

Experimental results with vacuum-coated discs are discussed in Section 5.3 and in Chapter VII.

5.2.3 The Glazing of the Discs

It was known that at 10 cm wavelength the resistance of titania linac discs to surface breakdown was improved by glazing the exposed

surfaces with a lead borate enamel of the kind used for coating wire-wound resistors.[25] Hayes[71] has made a detailed investigation into the problem at D.C. as well as at S-Band. He found that at S-Band the goodness of the metal-ceramic contact at the rim of a disc in an E_{01} mode cavity was of prime importance in preventing breakdown. The difficulty encountered in trying to improve this contact tended to obscure the result of glazing the titania discs, but it was clear that the glazed discs could withstand at least a 50% higher tangential electric field than their unglazed counterparts. However, the main advantage in glazing the discs is that, even if surface sparking occurs, serious damage to the ceramic is prevented since the glaze inhibits the formation of semi-conducting tracks of reduced titania or magnesium titanate.

One important drawback to applying the lead borate glaze used previously, Blythe Colour Works JD 234, is that its relative permittivity is about 16 and its loss tangent about 0.05 at J-Band[67], while the coating is typically 0.025 mm thick. J-Band linac titania discs ($K = 96$) will be about 1 mm thick so that the phase shift through the glaze would be about 2% of the total phase shift through the disc. The effect of the glaze on the propagation constant in the linac would therefore be considerable, but if this effect could be determined and controlled sufficiently precisely, the structure design could take it into account. However, the relatively high loss in the glaze means that even the 0.025 mm coating thickness is sufficient to cause an

appreciable drop in the shunt impedance of the structure. In view of these drawbacks, and others concerned with construction, it was decided to seek an alternative glaze which possessed a low permittivity and loss tangent, and which could be applied more thinly and smoothly.

Blythe Colour Works agreed to consider the requirements and to suggest a more suitable glaze than JD 234. The requirements given to them were as follows:-

1. The composition should be more akin to a glass than JD 234 so that a relative permittivity less than 16 might be attained.
2. The coating should be typically not more than 0.01 mm thick so that the effect on the propagation constant might be reduced.
3. The coating should be as uniform and smooth as possible so that post-glazing grinding could be minimised.
4. The coating should have a slightly higher electrical conductivity than the unglazed discs so that surface charging might be lessened.
5. The coating should resist chemical attack by caustic soda so that electroforming of the structure might be simplified. (See Section 5.2.5). This requirement was given a low priority because of the probable difficulty in preparing a vitreous enamel with this property.
6. The usual requirement that the expansion coefficient of the glaze should be slightly higher than that of the ceramic so that the latter is in slight compression at room temperature to give added mechanical strength.

7. The glazing technique should result as far as possible in a complete coating of each disc. The area of disc support contact during glazing should therefore be minimised. This requirement was included because a thin layer of glaze (with a K of about 10) around the disc rim would tend to fill in the small pits in the ceramic and thus lessen the likelihood of electrical breakdown at the ceramic-air boundary caused by these pits and the sharp discontinuity in relative permittivity. The influence of the high electric fields in surface pits on the initiation of breakdown has been examined by Hayes.[71]

The results of the work done by Dr. K. Davies at Blythe Colour Works Laboratory can be summarised as follows. Requirement (5) was soon dropped because the most likely glaze to meet it permeated the whole of the test disc instead of forming a surface glaze. Several intermediate glazes were produced before reasonable success was achieved.

1. Experiments with a short structure made up with discs coated with the new glaze indicated that the relative permittivity of the glaze was less than 10 (see Chapter VII). Attempts to form a solid disc of the new glaze material so that an H_{01} cavity method might be used to determine its K (as was done with the original glaze) were unsuccessful because of bubble formation and cracking upon cooling from the fusing temperature.
2. The typical coating thickness was 0.01 mm and varied by up to $\pm$ 0.005 mm from disc to disc. Grinding will probably be necessary

to bring the thickness of these glazed discs within tolerance.

3. The coating thickness varied on each disc by about ± 0.005 mm in a typical 1 mm traverse of the disc, although the surface looked 'glazed' and not 'matt'.

4. No special attempt was made to increase the conductivity of the glaze at this stage, because the influence of the new glaze on structure impedance had first to be analysed.

6. This requirement was met without great difficulty.

7. The discs were mounted horizontally in platinum wire jigs for spraying before firing. The jigs were arranged so that contacts with a disc were made at only three small areas of the rim, and since the wire was 0.3 mm diameter most of the ceramic surface was exposed to the spray of glaze. Platinum was used because the glaze did not stick to it after firing. The ceramic discs were only 0.8 mm thick and the glaze particles were suspended in water (to form a suspension of specific gravity 1.6), and therefore surface tension effects during spraying caused the rim coating to be thinner than the coating on the disc face. However, it was hoped that the rim coating would be sufficient to lessen the chance of serious sparking at the rim.

The new glaze represented an improvement upon the original green resistor enamel in several respects, but it was disappointing in that post-glazing grinding was still needed. The performances of the new glaze at low and high power are discussed in Chapter VII and in Section 5.3.

5.2.4. P.T.F.E. Coating

It is not difficult to coat most ceramics with a thin layer of polytetrafluoroethylene (P.T.F.E.). As an alternative to glazing it was decided that P.T.F.E. coating of the linac discs should be examined to see if adequate protection of the ceramic could be achieved by using this low loss, low permittivity material. The effect on the propagation constant and the shunt impedance of a structure should be much less than that due to glaze, as the P.T.F.E. permittivity (2.08) is only an eighth of that of the glaze and tan δ is only 0.0002 at J-Band. The two main drawbacks to using P.T.F.E. are that it would not be as stable as the glaze under the thermal and molecular effects of electron bombardment, and its bulk d.c. resistivity is about 10^{17} ohm. metre[72] compared with about 10^{13} ohm. metre for the glaze.[71] Therefore the accumulation of intercepted charge in the linac would probably be more serious with P.T.F.E. than with the glaze. The bulk d.c. resistivity of fused quartz is about 10^{14} ohm. metre[72], and it was with this material that Flesher and Cohn had surface charging problems in their 'solid' linac structure.[19]

A set of discs was coated with a thin layer of P.T.F.E. by Doulton Research Limited, and the discs were mounted in a short periodic structure. The typical coating thickness was 0.025 mm but

it was possible to skim down the coating with the disc mounted in a ring chuck on a watchmaker's lathe. Further information about structure fabrication, machining, and J-Band tests with P.T.F.E. coated discs is given later under the appropriate section headings.

5.2.5 Chemical Attack and Electroforming

At an early stage in the linac project it was appreciated that every effort had to be made to minimise the ohmic losses in the design of the structure because of the limited power available at 1.8 cm and because of the inherently high material resitivities at this wavelength. Accordingly, considerable thought was given to the possibility of eliminating all R.F. joints in the metal waveguide wall of the structure. One possible method was to form a stack of rim-metallised discs and spacers on a mandrel and electroform the copper waveguide tube around the stack. The mandrel would then be removed, the spacers dissolved and washed out chemically, and the ends of the waveguide machined to fit into R.F. couplers. Such an electroforming technique was successfully used at Stanford to fabricate copper-loaded S-Band structures, and has more recently been used by the Vickers company for X-Band metal-loaded structures.

Apart from the metallising of the discs the chief problem associated with electroforming the dielectric structure wall lies in

the selection of the spacer material. For a test length of electroformed structure using a single glazed (JD 234) titania disc aluminium spacers were used. The spacers were machined to a high degree of accuracy and were quickly washed out after the electroforming with caustic soda. Unfortunately the caustic soda also removed all the glaze from the disc. A slight attack on the glaze had been anticipated of course but its complete removal was disappointing. At this stage only metallic spacers were considered because of the high machining accuracy desired, so certain chemical tests were carried out on the ceramics and the glaze to see what reaction occurred when they were exposed to likely solvents for other types of metallic spacers. The results are summarised in Table 2. It was clear that the glaze in use at that time was chemically unstable and was not likely to be usable in an electroformed structure using metallic spacers.

Difficulty was also experienced in bonding the electroforming copper to the metallised disc rims and to the aluminium spacers. An acid copper bath was used for these experiments, and the metallising preparations used were Liquid Matt and Bright Platinum. The results obtained are summarised in Table 3.

Several improvements were suggested for a second test electroformed structure but it was thought better to postpone this work until the vacuum coating of the disc rims with copper had been achieved and a more suitable glaze found.

Material	Attacked at Room Temperature by				
	H_2SO_4		HCl		NaOH
	Dilute	Conc.	Dilute	Conc.	(80% H_2O by weight)
Magnesium Titanate	No	No	No	No	No
Titanium Dioxide	No	No	No	No	No
JD 234 Glaze	No	Yes	(a)	Yes	(b)
Aluminium	No	Yes	Slowly	Yes	Yes
Duralumin	No	Yes	Slowly	Yes	Yes

Notes: (a) The attack is slight except in the presence of aluminium or Duralumin, in which case the glaze turns black and crumbles.

(b) Similar effect to (a) except that the glaze is not so drastically broken down.

TABLE 2

(From Ref. 31)

Material	Bonding to Acid Copper
Matt Platinum	Good
Bright Platinum	Bad
Duralumin*	Good
Aluminium*	Bad

* Treated by the Sodium Zincate process to inhibit the formation of an aluminium oxide film.

TABLE 3

(From. Ref. 31)

5.2.6 D.C. Surface Conductivity

Because of requirement (4) in Section 5.2.3., i.e. that the surface coating of the discs should allow intercepted charge to drain away to the waveguide walls, an early effort was made to estimate the surface conductivity of glazed and unglazed discs. An electrometer valve and d.c. amplifier circuitwere used to measure the current flowing across the surface and through the bulk of a piece of the ceramic under a known voltage. The experiments were conducted with dried samples in a rough vacuum (about 10^{-1} torr) and contact was made with the ceramic by means of flake silver bonded to the surface. The results indicated that the resistance between a point on the edge of the hole in a disc and the rim is greater than 10^{12} ohms for both glazed and unglazed ceramics.* This is somewhat disturbing because the capacity between the periphery of the hole and the rim is of the order of 1 pF. Hence, the time constant which will give us some idea of the charge decay rate from the central hole is at least 1 sec. This decay time should be compared with the interval between beam current pulses, i.e. about 20 msec. These experiments were done with the old JD234 glaze which, as we shall see, already has too high a conductivity to be useful at J-Band. Consequently the intercepted charge must be virtually zero if charge build-up is to be avoided, unless the secondary emission coefficient of the disc surface is near unity at the relevant primary voltages or the conductivity is temporarily

* Current measurements were made when the absorption currents[71,83] had fallen so far that the indicated current was almost steady (about 15 minutes after applying the voltage). The upper limit of measurable resistance was 10^{12} ohm, set by the conductivity of thick rubber lead-throughs.

increased due to electronic bombardment.[71] The two latter effects are discussed in Section 5.3.

5.2.7 Dimensional Tolerances and Machining

The manufacturer of the titania and magnesium titanate linac discs was originally able to quote an acceptable price per disc for the following dimensional tolerances:-

Thickness, 2g	± 0.02 mm
O.D., 2c	± 0.03 mm
I.D., 2a	± 0.03 mm

It was originally hoped that no further grinding of the discs would be needed, except perhaps after the coating process. Therefore a detailed knowledge of the dimensions of the discs as delivered was sought so that suitable action could be taken when the practical design tolerances became known.

The first set of discs to be examined was a batch of 12 titania discs supplied to the following dimensions.

Thickness	1.00 mm	± 0.02 mm
O.D.	12.44 mm	± 0.03 mm
I.D.	4.18 mm	± 0.03 mm

The thickness was measured with a special micrometer which had flat circular anvils only 0.25 mm in diameter so that variation over the disc could be detected. The O.D. and I.D. were measured with a travelling microscope. Where applicable, the measurements were checked using dial gauges and small bore gauges. The extent of the deviations from nominal and average values is shown in Table 4.

Dimension	Nominal mm	Tolerance %	Average mm	Standard Deviation %	Percentage of discs out of tolerance
Thickness	1.00	2.0	1.001	0.62	0
O.D.	12.44	0.24	12.45	0.11	9
I.D.	4.18	0.72	4.215	0.28	67

TABLE 4

The average thickness near the centre was 0.998 mm and near the periphery it was 1.004. The manufacturer stated that the average I.D. and O.D. would in future be much nearer the nominal values. No hole ovality was noticed on this batch, but the drilling was not accurate enough.

Measurements on a second set of 12 titania discs with the nominal I.D. increased to 5.30 mm showed that the holes were up to 0.2 mm off centre, and that the I.D. and the O.D. tapered by up to 1% and 2% respectively. The nominal annular width of these discs was 3.57 mm with a tolerance of $\pm$ 0.06 mm but several discs had an angular variation in annular width as bad as that shown in Fig. 19.

It was apparent that difficulty was being experienced in maintaining the stipulated tolerances. A project to set up in this laboratory complete machining facilities for handling glazed and unglazed discs was begun because the tolerances could not be relaxed (they later had to be tightened in fact) and the net cost of purchasing narrow tolerance discs was prohibitive. Complementary to the machining problem was the difficulty in measuring the dimensions

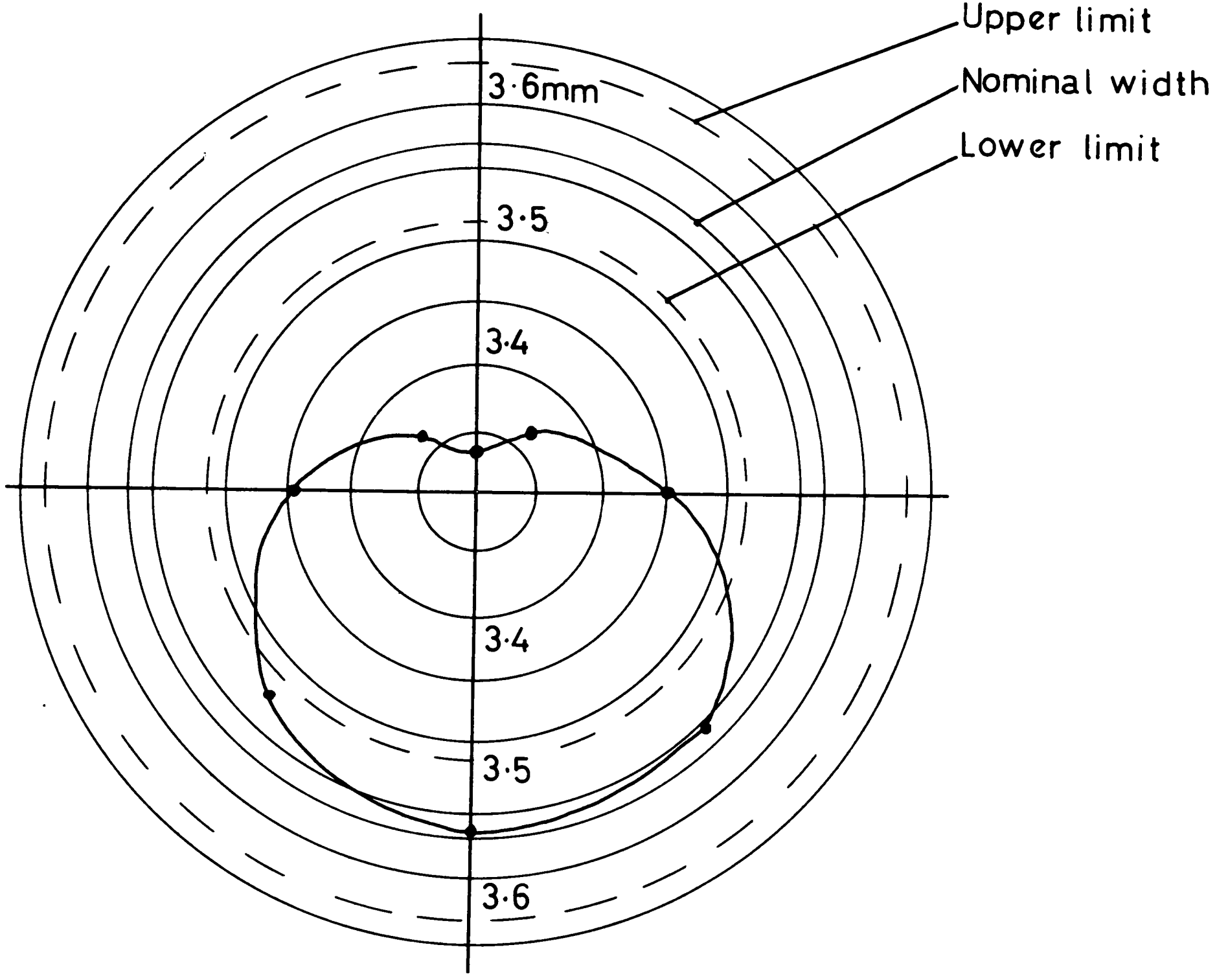


FIG. 19. ANGULAR VARIATION OF ANNULAR WIDTH OF SAMPLE DISC.

accurately and conveniently.

After considerable experiment with silicon carbide and carborundum it was found that diamond pastes gave the best results in grinding and polishing these hard ceramics. The disc faces were dealt with in several ways. For fast stock removal they were mounted with shellac in Duralumin holders on an automatic polishing machine and ground on a cast-iron lap with Hyprez 25 micron water soluble diamond compound. Light grinding and final polishing were done by hand on a cast-iron lap or optically flat glass blocks using 14, 6 and 1 micron diamond compounds. The holes in the discs were ground using diamond pastes on slightly tapered copper rods with the discs mounted in a ring chuck on a watchmaker's lathe. Outside diameters were decreased and trued up by mounting several discs on a mandrel in a collet chuck and then grinding the rims with a diamond-paste on a soft-wood lap mounted on a special lathe accessory. These techniques were found to be suitable for both unglazed and glazed discs. The actual machining tolerances achieved using these methods will be stated where relevant in subsequent sections. Typical disc O.D's were machined to within $\pm$ 0.002 mm.

Several methods were regarded as possibilities for dimensional measurement but only a few of them were practicable for repeated use on discs during machining. For instance, 'non-touch' techniques which would preserve the brittle ceramics from chipping tended to be too lengthy or awkward for routine use in the machine shop. Into

this category came the travelling microscope and the capacitance-sensitive proximity meter.

During an investigation into the honing of thick-wall, machined copper tubing for the linac waveguide the suitability of air gauges, which are normally used in conjunction with honing machines, was assessed. Also, a pilot test was carried out to see if the disc holes could be easily honed without damage to the ceramic. The results of this work showed that

1. The Mercer air gauge, which is a manometer indicating the flow of air out of nozzles in a calibrated cylindrical plug inserted in the bore to be measured, constitutes a fast and practical way of measuring disc I.D's.

2. Holes in titania discs can be honed out using diamond-impregnated honing stones. The technique can be most easily performed on several discs stacked together. This could speed up adjustments to the I.D. of discs for the uniform section of the linac where only the periodic length is likely to be varied.

Precision micrometers and cylindrical plug gauges were used for running measurements of O.D., thickness and I.D. during machining, but great care had to be taken in their use. Several discs sustained slight chipping, which is most serious at the disc rim, and they had to be discarded. Although routine use of the travelling microscope was impracticable, it was used occasionally for control and final checking of the dimensions, but the O.D. and thickness were usually checked with

a bench-mounted high magnification dial gauge accurate to ± 0.0005 mm. The I.D. was usually checked with a Diatest dial indicator bore gauge (accurate to ± 0.0005 mm). This instrument makes contact with the bore at two diametrically opposite points so that ovality of hole can easily be detected, as with the air gauge.

The measurement methods are summed up in Table 5.

Dimension	During Machining	Final Checking
Thickness	Micrometer; H.M.D.G.*(rarely)	H.M.D.G.; Travelling Microscope.
Inside Diameter	Plug gauge; Air gauge	Diatest H.M.D.G.; Air Gauge; Travelling Microscope.
Outside Diameter	Micrometer; H.M.D.G.(rarely)	H.M.D.G.; Travelling Microscope.

*H.M.D.G. = High Magnification Dial Gauge

TABLE 5

5.3 High Power Tests

Previous work at A.E.R.E., Queen Mary College, and the University of British Columbia had shown that titania ceramics were practical possibilities for the periodic loading of slow-wave structures, so that confirmation of an acceptable high-power performance of titania at 1.8 cm wavelength was needed because all the dimensions would be reduced by about a factor of five.

5.3.1 Previous Experiments at S-Band

5.3.1.1 The A.E.R.E. Titania-loaded Linac

Certain difficulties with the unglazed titania discs used in the 10 cm wavelength A.E.R.E. linac are relevant to the J-Band project. The A.E.R.E. machine operated with axial field strengths of about 2.5 MV/m and a peak beam current of 14 mA. No major surface breakdown tracks across the titania discs were reported, but when vacuum oil diffusion pumps were used, brown annular areas and occasionally patches of reduced titania were found on the disc faces.[24,46] They were explained by postulating 'multipactoring'* electrons which oscillated in the corrugations between discs and absorbed a large amount of R.F. power, the effect being promoted by titania surfaces contaminated by oil from the diffusion pumps.[28]

This conclusion was arrived at after a large amount of experimental work had been done to eliminate other possible causes

---

* The 'multipactor' effect[28] is the name given to a troublesome particle resonance experienced in some high power microwave devices. As a simple example, consider a pair of parallel plates of a material in vacuo which has a secondary emission coefficient greater than unity over a range of primary electron energies. If an R.F. electromagnetic field exists around the plates, an electron at one plate could be accelerated towards the other plate and arrive there just as the electric field reversed its sense. Secondary electrons produced at this plate could then be accelerated back towards the first plate and produce more secondaries just as the field again reversed. In this way a build-up of oscillating electrons can quickly occur. Field energy is dissipated in the plates.

of the effect. The sequence may be summarised as follows:-

1. The pulse repetition rate was varied in order to change the mean power, but the excess of attenuation at high power levels was unchanged. Any cause associated with R.F. heating effects was thereby eliminated.

2. Variation of the axial focusing magnetic field did not affect the excess attenuation, provided that a good, steady vacuum had been reached. This eliminated the anomalous attenuation phenomena found in metal-loaded linacs where power is absorbed by spiralling gas ions and electrons (when the vacuum is poor)[73], and where a focusing-field-dependent multipactor resonance absorption can occur.[74]

3. Variation of the system pressure from 10^{-5} torr up to 10^{-2} torr did not alter the excess attenuation. However, when the system was let down to atmospheric pressure and the R.F. power was kept low enough to avoid air breakdown, the excess attenuation (about 8 dB) disappeared. The absorption was apparently due to charged particles, presumed to be electrons because of the independence of the effect upon pressure.

4. The excess attenuation was present when an oil diffusion pump was used to evacuate the system. Certain evidence from work done on various other high-voltage R.F. devices suggested that less trouble from multipactor resonances was experienced when mercury pumps were used. As a first step towards excluding oil vapour from the system, a liquid nitrogen trap was fitted to the

oil pump but the excess attenuation was unaffected. This suggested that if oil played a vital role in the phenomenon then it was in the guise of a thin film on the titania surfaces rather than as a vapour. New discs were then inserted into the structure, the whole system was degreased, and a mercury diffusion pump plus liquid nitrogen trap was used to evacuate the system. The excess attenuation disappeared. The oil pump was then substituted for the mercury pump and the attenuation slowly built up to its previous value. This confirmed that pump oil in the linac was vital to the effect, and that the liquid nitrogen trap was not efficient enough.

5. The annular discoloured area ceased at a radius which gave a theoretical threshold electric field for a multipactor effect between discs corresponding to a primary electron energy of 100 - 150 eV. Secondary emission data offered strong evidence for supposing that the discolouration had therefore been caused by the multipactor phenomenon.

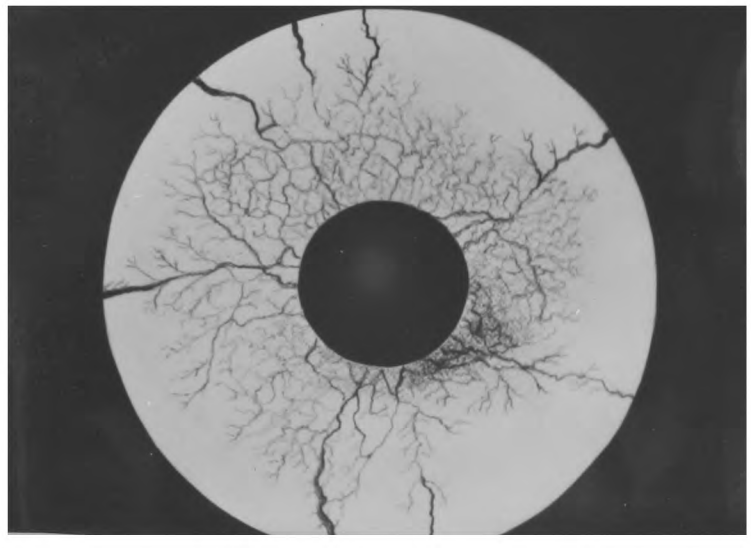
The final conclusion drawn from these experiments was that the use of an oil diffusion pump, even with a liquid nitrogen trap, caused a thin film of oil to form on the disc surfaces, and that this oil film promoted a multipactor resonance between the discs which absorbed R.F. power and which caused reduced patches on the titania discs.

5.3.1.2 The Experiments at Queen Mary College and Vancouver

Following on the work at A.E.R.E. an S-Band dielectric-loaded linac project was begun at Queen Mary College, London. Experiments

with axial electric fields somewhat higher than 2.5 MV/m in cavities loaded with unglazed titania discs produced severe surface breakdown tracks which appeared to emanate from the disc rims.[25] The tracks consisted of a reduced form of titania which behaved as a semi-conductor. A typical disc which suffered surface breakdown in these experiments is depicted in Fig. 20. It was found that a coating of a lead borate glaze on the discs improved the breakdown strength so that breakdown-free operation became possible with axial fields of up to 30 MV/m at S-Band.[75] Both the unglazed and glazed discs had silvered rims. No multipactor effect was reported. The test cavities were operated at the π mode and so the corrugations were probably too long for such an effect to build up. Primary electrons impinging on a disc, having been accelerated from the next disc, would probably have reached an energy for which the secondary emission coefficient was less than unity (the second cross-over potential for most materials does not exceed one or two kilovolts).

Later work reported by Hayes[71] showed that unglazed discs could withstand up to about 10 MV/m peak axial field in an S-Band E_{01}-mode cavity. This improvement was probably due to better silvering and a better contact at the disc rim. Glazed discs could only withstand about 20 MV/m so that the factor by which the glaze increased the tolerable field strength was only two compared with ten in the earlier experiments. These results reflect the practical difficulty of reproducing dielectric-loaded cavities, especially with



Surface Breakdown

on

Unglazed Titania Disc

Fig. 20

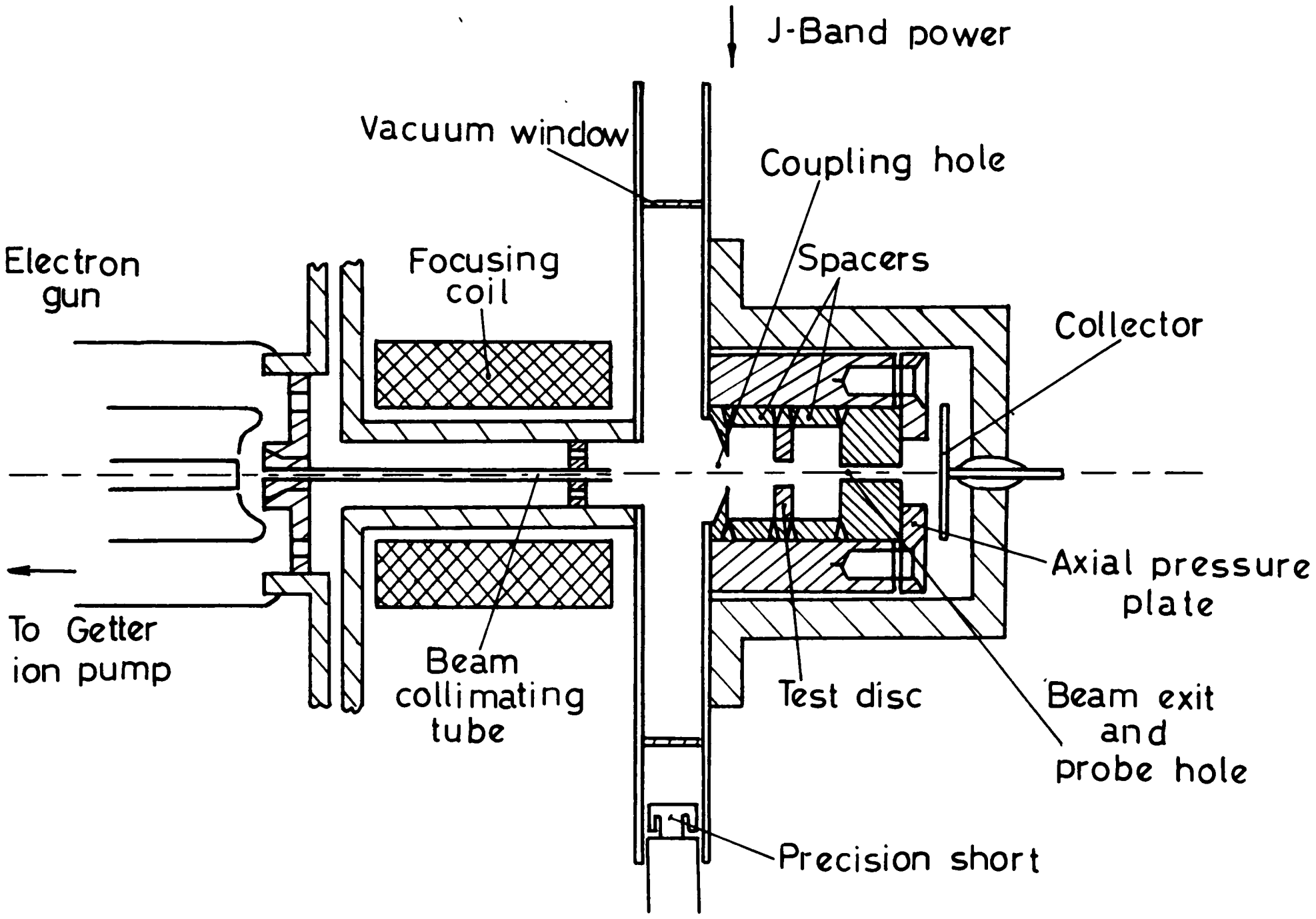
respect to rim contacts.

Some of the later experiments were carried out with a single titania disc mounted in an E_{011}-mode cavity. Annular brown stains on the disc faces, similar to those reported by the A.E.R.E. team, were found to be definitely associated with vacuum grease used at a joint in the cavity wall, and probably associated with a multipactor resonance. In one case, a blackened patch of reduced titania on the face of a disc was in line with a matching black patch on the copper end wall suggesting that either a flashover or a multipactor resonance had occurred.

5.3.2 The Test-Cavity Design

In view of the knowledge gained from S-Band experiments on single titania discs in high-power E_{01}-mode resonant cavities it was decided that the first J-Band experiments should proceed along similar lines.

The general scheme was to couple a cavity loaded with a single titania disc to rectangular J-Band waveguide (WG 18) via a central hole in one end wall of the cavity so that an E_{01}-mode resonance would be excited. Probes could be introduced through a small central hole in the other end wall of the cavity during low power experiments, and this hole was the exit from the cavity for an axial electron beam injected during high power experiments. The general arrangement for high power experiments is shown in simplified form in Fig. 21.



HIGH POWER TEST CAVITY. FIG. 21.

5.3.2.1 Cavity Dimensions

The dimensions of the disc were obtained by scaling linearly with wavelength the dimensions of a typical S-Band linac titania disc. This procedure gave the following dimensions at J-Band, the scaling factor being 0.180 :-

Disc diameter, $2c$ = 14.40 mm

Hole diameter, $2a$ = 3.61 mm

Disc thickness, $2g$ = 0.56 mm

It should be noted that this disc diameter is a typical J-Band cylindrical waveguide diameter, and transmission on either side of the disc will be in a propagating mode (above cut-off). This is not necessarily the case in the linac structure where the transmission between discs can be in an evanescent mode of the unloaded waveguide.

An estimate was made of the cavity length required to give the E_{011}-mode resonance at the magnetron frequency by considering an unglazed solid disc ($2a = 0$) mounted centrally in a simple cylindrical cavity, as shown in Fig. 22. The general expressions for the standing wave pattern in the cavity may be derived by vectorially adding two TM_{01} circular waveguide fields travelling in opposite directions along the z axis. Ignoring losses, we obtain

$$E_z = E_0 J_0(\chi\rho) \cos\beta z \cdot e^{j\omega t} \qquad (5.1a)$$

$$E_\rho = E_0 \frac{\beta}{\chi} J_1(\chi\rho) \sin\beta z \cdot e^{j\omega t} \qquad (5.1b)$$

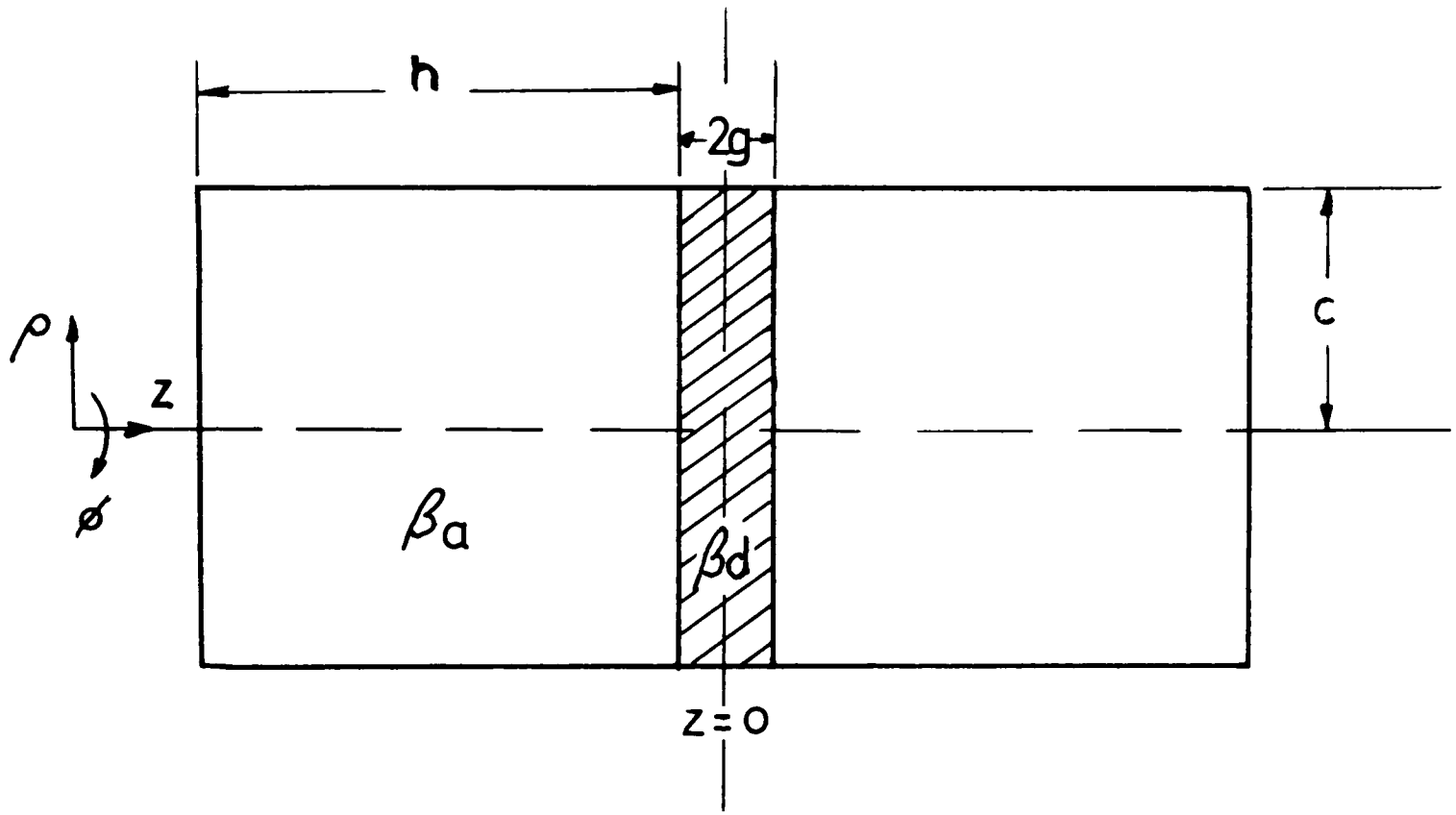


FIG. 22.

$$H_\phi = j\, E_o \frac{\omega\epsilon}{\chi} J_1(\chi\rho) \cos\beta z \cdot e^{j\omega t} \qquad (5.1c)$$

where $\beta^2 = k^2 - \chi^2$

E_o = a constant depending on the power flux

and χ = the radial propagation constant

Separate sets of equations for the fields in the vacuum (air) and dielectric regions of the cavity are now written.

In the right-hand vacuum region of Fig. 22, omitting the time factor,

$$E_z = E_a J_o(\chi\rho) \cos\beta_a(z - (g+h)) \qquad (5.2a)$$

$$E_\rho = - E_a \frac{\beta_a}{\chi} J_1(\chi\rho) \sin\beta_a(z - (g+h)) \qquad (5.2b)$$

$$H_\phi = j\, E_a \frac{\omega\epsilon_o}{\chi} J_1(\chi\rho) \cos\beta_a(z - (g+h)) \qquad (5.2c)$$

and in the dielectric region

$$E_z = E_d\, J_o(\chi\rho) \sin\beta_d z \qquad (5.3a)$$

$$E_\rho = E_d \frac{\beta_d}{\chi} J_1(\chi\rho) \cos\beta_d z \qquad (5.3b)$$

$$H_\phi = j\, E_d \frac{\omega K\epsilon_o}{\chi} J_1(\chi\rho) \sin\beta_d z \qquad (5.3c)$$

The radial propagation constant is the same in both regions because E_z falls to zero at $\rho = c$ in both regions.

Since E_ρ and H_ϕ must be continuous at the boundary between the (perfect) dielectric and the vacuum we find that

$$\tan\beta_a h \cdot \tan\beta_d g = \frac{\beta_d}{K\beta_a} \qquad (5.4)$$

Remembering that for the E_{01} circular waveguide mode

$$\chi = \frac{2.405}{c} \qquad (c = \text{waveguide radius})$$

we can calculate the value of h from equation (5.4) for the given disc at a given magnetron frequency. For the frequency 16.50 Gc/s and a K of 96.3, we find that

$$\beta_a = 0.0655 \text{ radians/mm}, \quad \beta_d = 3.33 \text{ radians/mm},$$

$h = 8.23$ mm, and the cavity length $2(g+h) = 17.02$ mm

This cavity length calculation was intended to serve only as a guide to the practical length, which was found to be 17.76 mm. The discrepancy was almost certainly due to the existence of the hole in the disc and the relatively large coupling hole in one end wall.

5.3.2.2 Physical Features

A 'ring-and-spacer' type of construction for the cavity proper was chosen because it facilitated the changing of test discs and cavity dimensions. A chemically clean oxygen-free high conductivity (O.F.H.C.) copper ring 0.025 mm less in internal diameter than the test disc at room temperature was heated in air until it passed over the (cold) disc. On cooling to room temperature the ring became a secure mount for the test disc, with good electrical and thermal contact between the highly finished surfaces of the copper and titania. The remainder of the cavity length was taken up by O.F.H.C. copper spacers with I.D's equal to the disc diameter. The input coupling hole was incorporated in the 2.5 mm thick O.F.H.C. copper end wall by tapering it sharply from about 15 mm diameter on the source side, well above

cut-off for the E_{01} circular waveguide mode, down to about 5 mm diameter at entry into the cavity. The actual diameter of the coupling hole at entry into the cavity was determined by experiment (see Section 5.3.3). The probe entry or beam exit was via a 3 mm diameter hole bored through the other end wall. The end walls, spacers, and disc ring were all bevelled so that R.F. contacts in the cavity were made on highly finished 0.5 mm wide annular regions at the inner edge of the spacers and disc ring. The R.F. contacts were maintained by applying axial pressure as shown in Fig. 21. In the E_{01} mode, wall currents are normal to the ϕ plane so that the cavity wall losses are high when ring-and-spacer construction is used. However, this disadvantage was outweighed by the flexibility of the ring-and-spacer construction, and by the abundance of R.F. power (about 300 kW) available for these single disc experiments.

A precision short-circuit controlled by a micrometer thread provided the means for fine tuning during experiments. It was of the non-wall-contacting, slotted piston type, and it was operated at atmospheric pressure because no sparking was likely to occur at the anticipated waveguide power levels of about 10 kW.

Axial electron beams of a few milliamps (pulsed) at up to 25 keV were available from an electron gun situated on the opposite side of the J-Band waveguide to the cavity. The gun was designed for a powerful S-Band klystron and was rather large and cumbersome for J-Band work, but a collimating tube attached to the anode ensured

that almost all the electrons flowing through the cavity were in an axial beam of about 1.5 mm diameter. The beam pulse current through the cavity was monitored by collecting it outside the cavity (see Fig. 21), earthing it through a screened 1 kΩ resistor, and observing the voltage drop across the resistor on an oscilloscope. The gun cathode current was also monitored so that any fluctuations in the collected current due to R.F. effects or breakdown in the cavity could be distinguished from fluctuations in the gun emission. A simple solenoid was available to provide an axial magnetic field in the cavity or in the beam collimator for focusing or for investigating apparent multipactor resonances.

The system was evacuated through a half-inch diameter pumping stem connected to the base of the electron gun. Some 'dead' space around the cavity itself was unavoidable because of the relatively simple design of the demountable components. However, demounting the cavity was normally necessary only during preliminary low power tests under atmospheric conditions so that the long pump-down time was not usually an inconvenience. To avoid oil contamination of the cavity surfaces a mercury diffusion pump backed by a rotary pump was used initially, but this sytem was later changed to a getter ion pump backed via a liquid nitrogen trap by a rotary pump. Finally an oil-free system was constructed using a getter ion pump (8 litre/sec Vac Ion, or 5 litre/sec Mullard) backed by a molecular sieve sorption pump (aluminium calcium silicate, 5 Angstrom pore, liquid nitrogen cooled) capable of pumping down a volume of a few litres to about 10^{-3} torr

in 30 seconds. Unfortunately it was not possible to modify the system to take grease-free Viton or copper gaskets in time for this initial series of high-power tests, but the neoprene gaskets ('O' rings) which were used were greased very sparingly with the requisite silicone high-vacuum grease. The pressure was monitored by a triode ionisation gauge situated close to the electron gun, and by the getter ion pump current. The pressure indicated by the triode was multiplied by ten as an estimate of the pressure in the cavity allowing for the intervening pipes and pumping holes. Magnetron resonant output windows (Ferranti; Corning 7070 glass) were used as waveguide vacuum seals.

5.3.3. Preliminary Low Power Tests

Before the high power tests could proceed it was necessary to arrange that the cavity resonated at the magnetron source frequency and was matched to the input waveguide. The shunt impedance had also to be found.

5.3.3.1 Coupling and Tuning

The test cavity length was initially determined from the theory discussed in Section 5.3.2.1 to give an E_{011} resonance at the frequency of the selected magnetron. Using a relatively small coupling hole the cavity was incorporated in the test circuit shown in Fig. 23. Klystron A* was tuned so that the E_{011} cavity resonance was at the

---

* Reflex klystrons K346 (45 mW), X 12 (100 mW) or R9626 (100 mW). For tests with small cavity coupling the R9626 was used as it could deliver up to 250 mW.

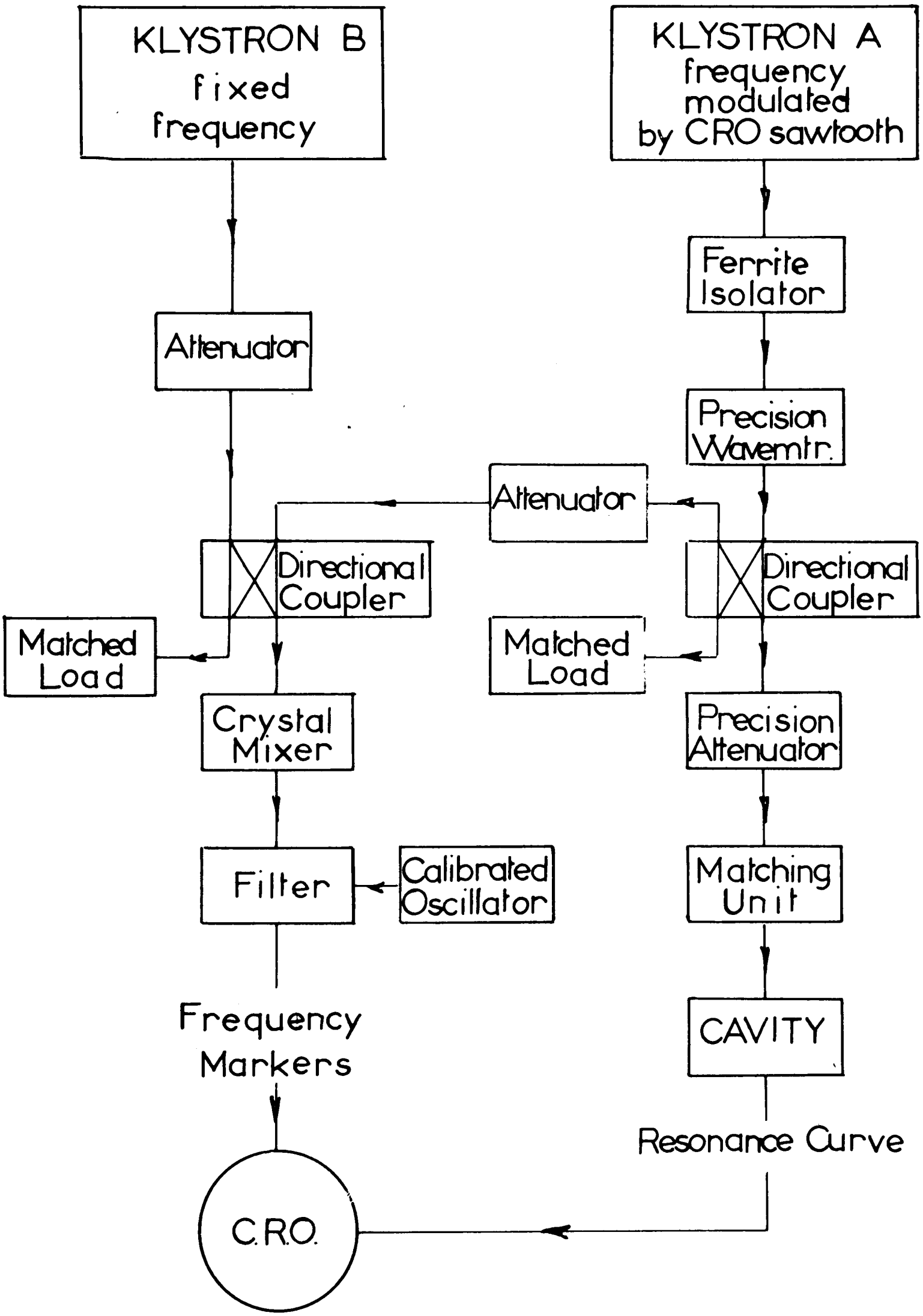
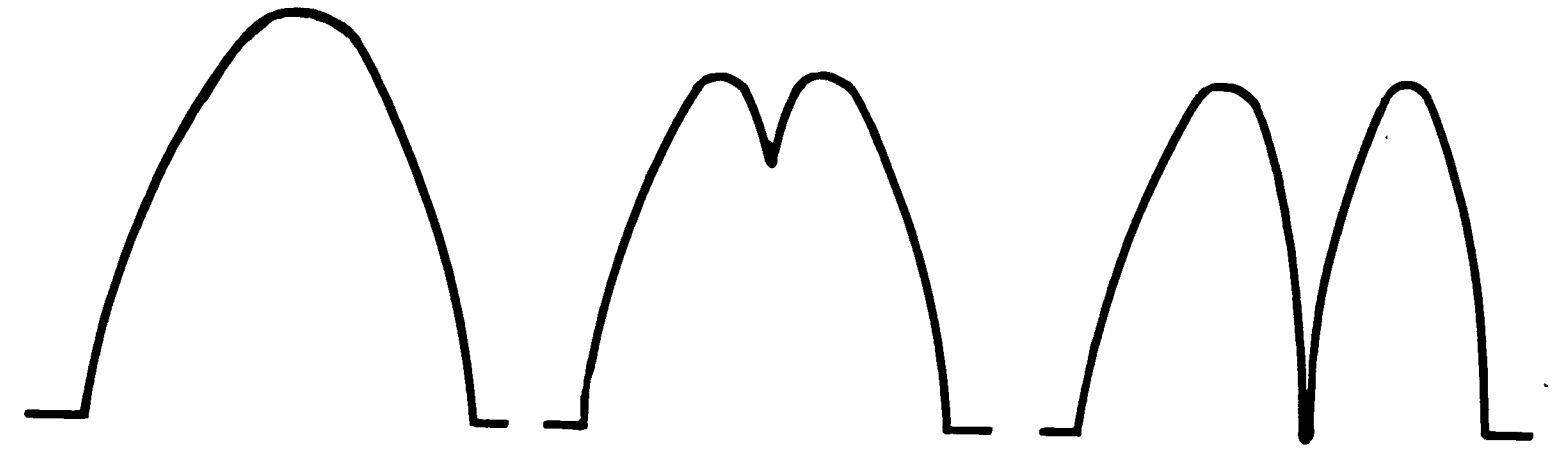

KLYSTRON B
fixed
frequency
KLYSTRON A
frequency
modulated
by CRO sawtooth
Attenuator
Ferrite
Isolator
Precision
Wavemtr.
Attenuator
Directional
Coupler
Directional
Coupler
Matched
Load
Matched
Load
Crystal
Mixer
Precision
Attenuator
Filter
Calibrated
Oscillator
Matching
Unit
Frequency
Markers
CAVITY
Resonance Curve
C.R.O.

FIG. 23.

centre of its swept frequency band of about 150 Mc/s. The resonance was identified by its frequency, and by perturbing the axial region with a small copper bead (about 0.01 cc in volume) attached to taut fisherman's twine drawn along the axis of the cavity. The bead effectively decreased the cavity volume so that the resonant frequency increased slightly, the maximum frequency perturbation occurring when the bead was in the region of maximum electric field strength. On drawing the bead through the cavity the number of peak frequency perturbations and the corresponding bead positions were noted. Two peaks near the end walls corresponded to the peak axial electric fields of the E_{011} resonance. More details about this perturbation technique are given in Sections 5.3.3.3 and 7.3.5.

The reflected signal from the cavity was detected and monitored on one trace of the dual beam oscilloscope. A 150 V sawtooth derived from the C.R.O. time-base modulated the reflector voltage of Klystron A. By adjustment of voltage amplitudes the oscillogram became the major lobe of the power versus reflector voltage klystron characteristic (Fig. 24a) with the cavity absorption superimposed (Fig. 24b). When the cavity was reflectionless at resonance (Fig. 24c) it was said to be critically coupled to the input waveguide.

The coupling hole diameter was gradually increased until critical coupling was approached. The coupling was then checked with a slotted-guide, standing-wave indicator. A two step procedure, first adjusting the cavity length (usually with 0.5 mm spacers) and then the



a. No coupling b. Small coupling c. Critical coupling

FIG. 24.

coupling hole diameter, was carried on until the resonant frequency equalled the selected magnetron frequency, critical coupling having been maintained throughout. At each stage the precision short-circuit (Fig. 21) was used as a fine control on the coupling and resonant frequency. It was not difficult to bring the cavity to within 5 Mc/s of the desired frequency with a V.S.W.R. of less than 1.05 with this method.

5.3.3.2 Measurement of Q_o

The basic method used for determining the unloaded Q of the cavity Q_o was described by Adlam, James and Mullett[77] although there were several differences in experimental details. Referring again to Fig. 21, an electric field probe introduced through the cavity end wall was coupled to a tunable crystal detector by a rigid coaxial line. The signal from the detector was amplified and fed to the Y_1-plates of of the oscilloscope so that the cavity resonance curve was displayed (Fig. 25a). The second oscilloscope trace could display the reflected signal as before, but it was here used to provide a calibrated cursor for determining the fractional bandwidth (Q^{-1}) of the resonance curve. This was done by attenuating the reflected signal until it gave a virtually horizontal trace. The residual signal was mixed with a stronger signal from Klystron B which was tuned to oscillate at the resonant frequency of the cavity. The mixed signal was detected and a.c. coupled in parallel with a calibrated R.F. oscillator to a low pass filter (cut-off at about 100 kc/s). After amplification

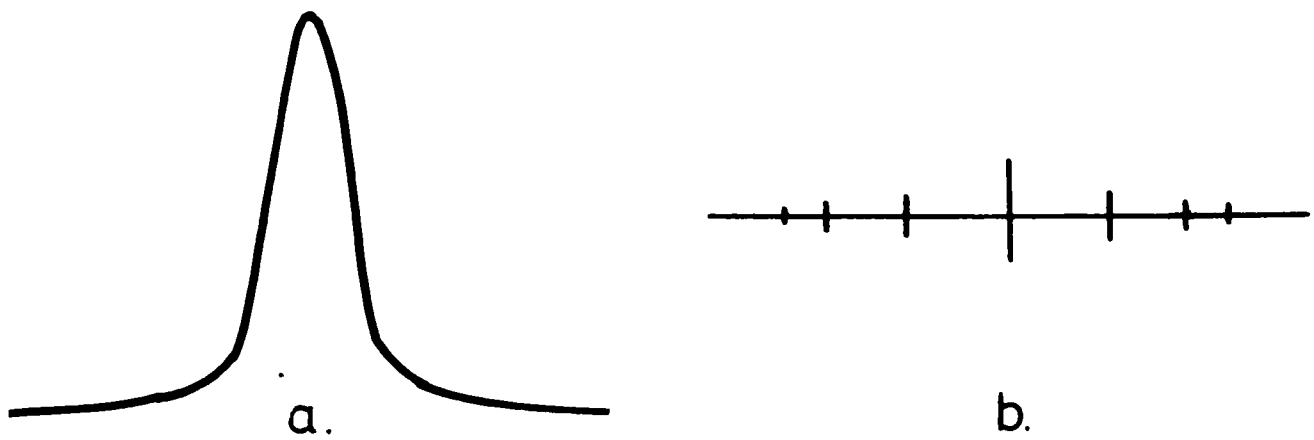


FIG. 25.

the resulting signal was applied to the Y_2 plates of the C.R.O.

The signal mixing arrangement produced marker pips on the Y_2 trace at intervals equivalent to the frequency of the calibrated R.F. oscillator. The centre pip was produced when the two klystron frequencies were equal.

Mixing the calibrated R.F. oscillator and the Klystron B signals gave a resultant signal with components at frequencies f where

$$f = f_B \pm nf_o \qquad n \geqslant 0 \text{ and integral}$$

f_B = frequency of Klystron B

f_o = R.F. oscillator frequency

The component amplitudes decreased as n increased. When the frequency of Klystron A passed through the values f a pip signal passed through the filter to the Y_2 plates. The overall effect is depicted in Fig. 25b.

The procedure for measuring the fractional bandwidth of the resonance curve was as follows:

1. The resonant frequency was found with the precision absorption-cavity wavemeter ($Q \approx 5000$).
2. The reflector voltage of Klystron B was varied until the centre pip coincided with the resonance peak (Fig. 25c).
3. The 'half-power points' of the resonance were found with the aid of the calibrated precision attenuator, and the $f_B \pm f_o$ marker pips were shifted until they coincided with the half-power points (Fig. 25d).

4. The half-bandwidth was read off the calibrated R.F. oscillator dial. The Q of the cavity combined with its coupler was then given by

$$Q = \frac{f_B}{2f_o} \tag{5.5}$$

Since the cavity was critically coupled to the input waveguide, the unloaded Q was given by

$$Q_o = \frac{2f_B}{2f_o} \tag{5.6}$$

Values of Q above 1500 were accurate to about $\pm$ 1% when measured by this method, and useful estimates could be made down to about 800.

5.3.3.3 Measurement of r_{sh}/Q_o

No theoretical estimate was made of the test cavity's shunt impedance. Once the cavity had been made to resonate at the selected magnetron frequency without high ohmic losses, and had been critically coupled to the input waveguide the ratio of r_{sh} to Q_o was measured by the bead peturbation method.

From Slater's equation[54] giving the change in resonant frequency due to a peturbation in a cavity boundary we can deduce that when a small metallic bead is located in the cavity at a position of zero magnetic field,

$$\left|\frac{\delta f}{f}\right| = \frac{\alpha E^2}{U} \tag{5.7}$$

where α is a constant depending chiefly upon the size of the bead in relation to the wavelength, U is the energy stored in the cavity, f is the resonant frequency of the cavity, δf is the increase in f due to the peturbation, and E is the electric field originally in the region occupied by the bead.

If the perturbing object is small compared with the wavelength, as is the case with the metallic bead mentioned in Section 5.3.3.1, then δf can give us a measure of the average electric field over a relatively small region. In all the measurements discussed here this conditional relationship was satisfied. In Fig. 26 the apparatus is shown in use on a low-power test cavity to be discussed in Chapter VII. The copper bead can be seen on the twine above the cavity in Fig. 26, and in close-up in Fig. 27.

To measure the maximum axial electric field E_{zm} in the E_{011} cylindrical mode we draw the bead along the cavity axis and measure δf_m the maximum perturbation in the resonant frequency with the wavemeter or the frequency marker pips. Then from equation (5.7) for the critically coupled cavity we have,

$$E_{zm} = \left[\frac{|\delta f_m|}{f} \cdot \frac{U}{\alpha}\right]^{\frac{1}{2}} \tag{5.8}$$

$$= \left[\frac{P\, Q_o |\delta f_m|}{4\pi\alpha f^2}\right]^{\frac{1}{2}} \tag{5.9}$$

since $Q_o = \frac{4\pi f U}{P}$

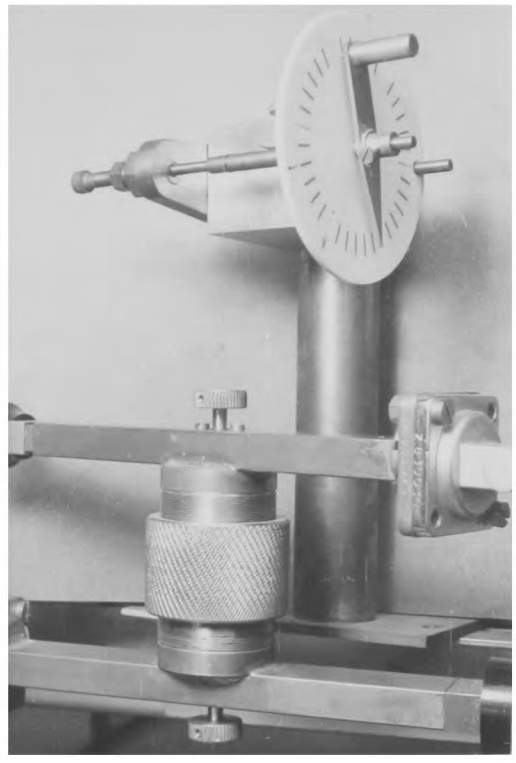
where P is the power flux input to the coupler.

Essentially we are measuring r_{sh}/Q_o, for if Q_o is unknown the equation (5.9) is better written as

$$\frac{E_{zm}^2}{Q_o} = \frac{P|\delta f_m|}{4\pi\alpha f^2} \tag{5.10}$$

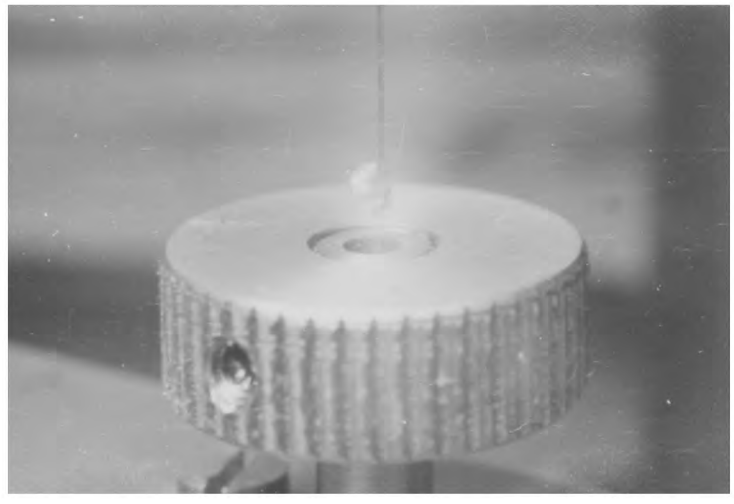
or

$$\frac{r_{sh}}{Q_o} = \frac{l|\delta f_m|}{2\pi\alpha f^2} \tag{5.11}$$



r_{sh}/Q Measurement Apparatus

Fig. 26



1 cm

Copper Bead for Field Perturbations

Fig. 27

$$\text{since} \quad r_{sh} = \frac{2\ell E_{zm}^{\,2}}{P} \tag{5.12}$$

where ℓ is the cavity length.*

The metallic bead was calibrated, i.e. α was determined, by measuring $\delta f_m/f$ and calculating $U/E_{zm}^{\,2}$ in equation (5.8) for an empty cylindrical cavity, 0.750" in diameter, supporting an E_{01n} resonant mode at about $\lambda = 1.8$ cm. The value of n was in practice usually four. The resonant frequency f and the average of the peak frequency peturbations δf_m were measured on an axial bead traverse through the cavity. Since $U \propto E_{zm}^{\,2}$, equation (5.8) may be rewritten as

$$\alpha = \frac{|\delta f_m|}{f} \cdot \alpha' \tag{5.13}$$

$$\text{where} \quad \alpha' = \frac{U}{E_{zm}^{\,2}}$$

The general expression for the energy stored in the cavity may be written

$$U = \frac{2\pi}{\omega} \int_0 \int_{Vol.} \left[\frac{1}{2} \underline{D} \cdot \underline{E} + \frac{1}{2} \underline{B} \cdot \underline{H} \right] dV\, dt \tag{5.14}$$

For an empty cylindrical cavity supporting an E_{01n} resonance, after integrating this becomes

$$U = \mu_o \frac{\pi c^2}{4} \left[\frac{E_{zm}\, \omega \epsilon_o}{\chi} J_1(\chi c) \right]^2 \cdot \ell \tag{5.15}$$

where c = the cavity radius

and $\chi = \frac{2.405}{c}$ *

$$\text{Thus} \quad \alpha' = \mu_o \frac{\pi c^2}{4} \left[\frac{\omega \epsilon_o}{\chi} J_1(\chi c) \right]^2 \cdot \ell \tag{5.16}$$

---

* Here we define r_{sh} for the test cavity as the product of ℓ the cavity length and the ratio of $E_{zm}^{\,2}$ the squared maximum axial field to P/2 the power dissipated in the cavity (critically coupled). This should not be confused with the r_{sh} defined for the linac structure in Section 1.3

* The first root of $J_o(x) = 0$ is $x = 2.405$.

5.3.4 The High Power Tests

Three experiments were performed to investigate the effect of glazing and metallising titania discs under high field conditions set up in the test cavity described in Section 5.3.2.

5.3.4.1 Glazed Titania Disc

A titania disc (Code No.7) with a clean rim (polished and unglazed) was glazed with JD 234 and mounted in the test cavity. The procedure described in Section 5.3.3.1 was carried out to make the cavity resonate in the E_{011} mode with critical coupling at the frequency of the selected magnetron (No. 2071; 16.335 Gc/s). A V.S.W.R. of 1.05 at resonance was achieved. Using very light coupling in a second low-power experiment, Q_o was measured directly and was found to be 1645. The method of Section 5.3.3.3 was used to measure r_{sh}/Q_o for the critically coupled and tuned cavity.

Rewriting equation (5.11) we have

$$\frac{r_{sh}}{Q_o} = \frac{E_{zm}^2 \ell}{\omega U}$$

$$= \frac{|\delta f_m| \ell}{f \omega \alpha} \qquad (5.17)$$

For this cavity $\ell = 0.0178$ m. The bead α was found to be 1.38×10^{-20} $m^2.sec.ohm^{-1}$*, and δf_m was -95 Mc/s, so that

$$\frac{r_{sh}}{Q_o} = 7.33.10^4 \text{ ohm.m}^{-1}.$$

---

* The perturbing bead used in this particular experiment was a steel ball 0.0625" in diameter.

and $E_{zm} = 5.80.10^4.P^{\frac{1}{2}}$

where P = the power input to the coupler

The low power measurements were made on the cavity after it had been degreased and partly assembled for vacuum. After they had been completed the cavity was incoporated in the high power microwave circuit shown in Fig. 28, and was evacuated by a getter ion pump backed by a rotary pump. Small amounts of high vacuum grease were used on neoprene gaskets.

The first high power run was begun when the system pressure was about 10^{-5} torr. The power input to the cavity was increased slowly from about 5 kW, the magnetron frequency being maintained at that of the resonant cavity. At a power level of about 13.5 kW the reflected R.F. pulse from the cavity was seen on the C.R.O. to suddenly jitter over a range of a few dB. An oscillogram of this effect is shown in Fig. 29. The pulse jitter was accompanied by a slight rise in the cavity pressure, and it corresponded closely with the jitter on the ion pump current meter. The power level had to be greatly reduced before the jitter ceased. When the power level was again increased, the effect re-occurred at a slightly lower level than before. The experiment was performed with a pulse length of 0.5 μsec at repetition rates of 500, 400, 325, 250 and 93 per second. On each occasion the threshold peak power for jitter was the same. The jitter was clearly not due to a thermal effect in the cavity.

Before disassembly of the cavity, Q_o was again measured at lower power and was found to have dropped slightly to 1490. Inside

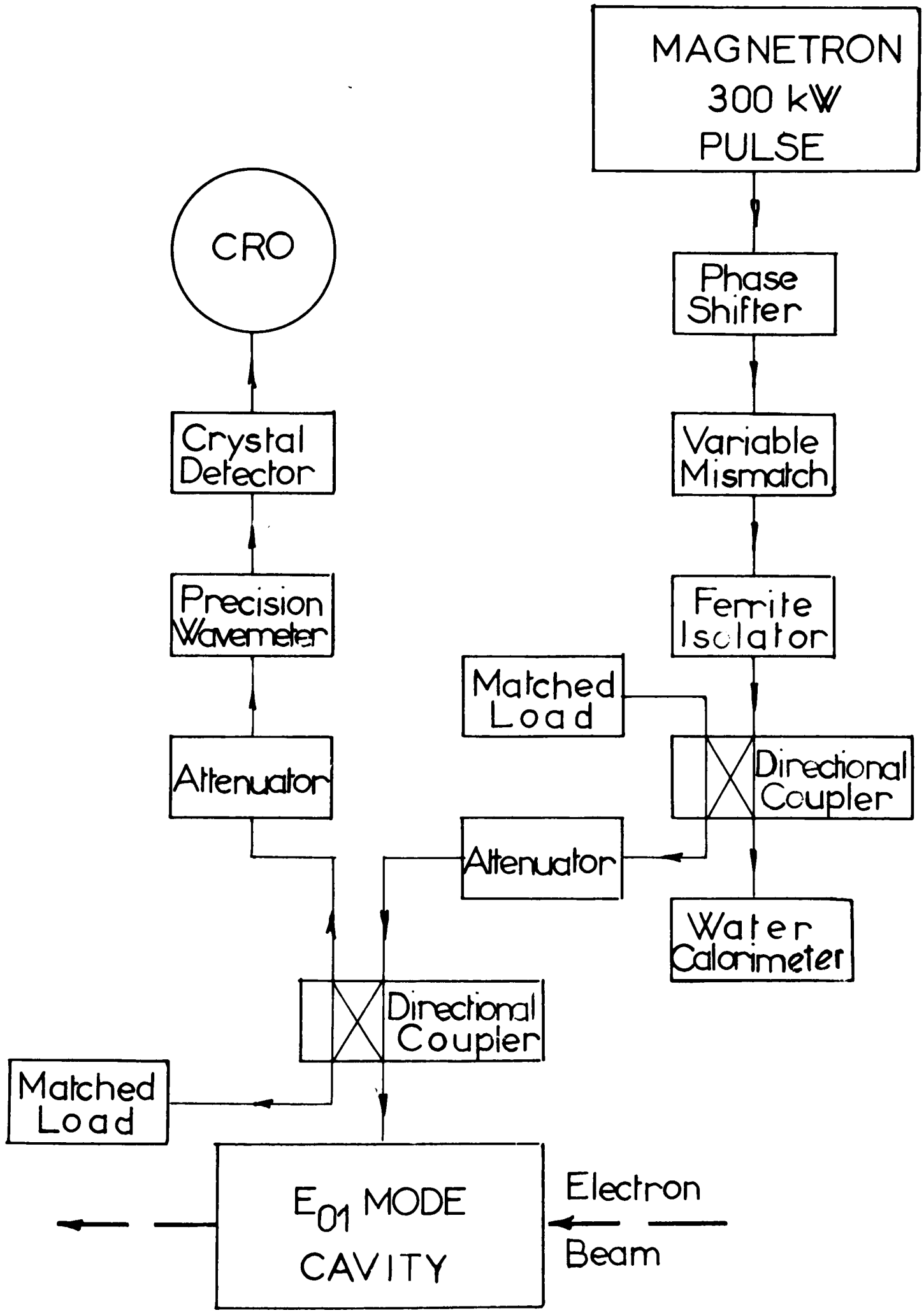
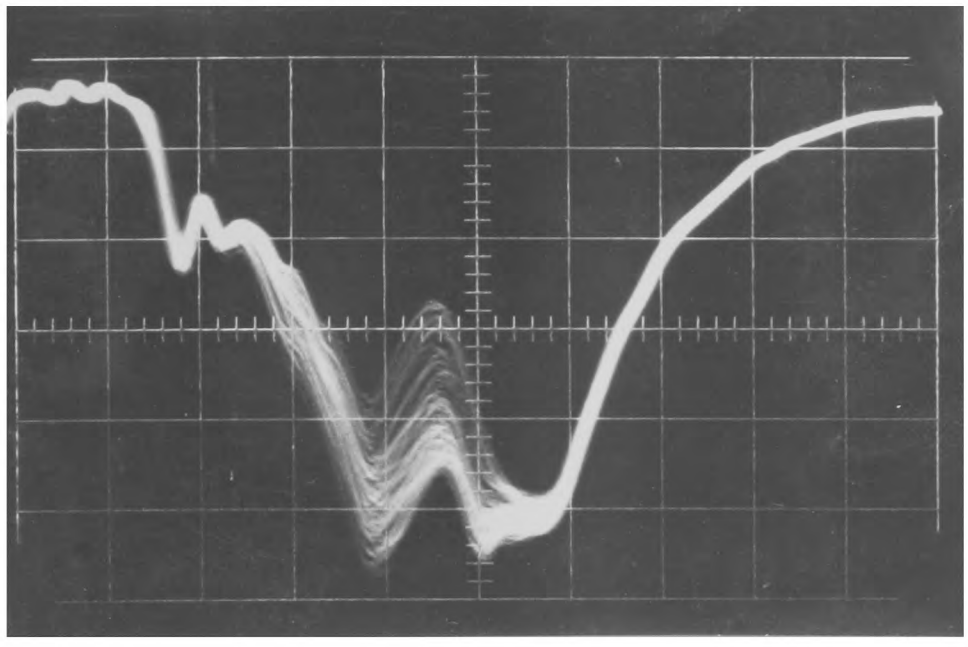
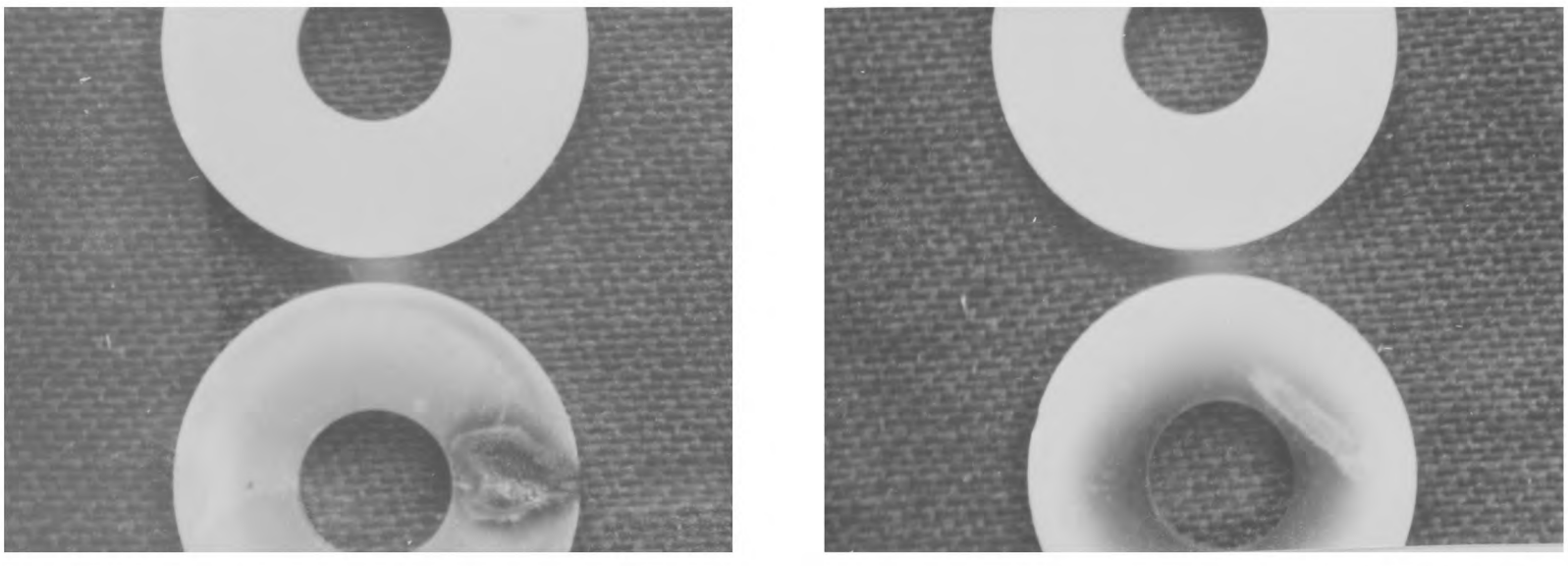

MAGNETRON
300 kW
PULSE
Phase
Shifter
Variable
Mismatch
Ferrite
Isolator
Directional
Coupler
Water
Calorimeter
Matched
Load
Attenuator
Directional
Coupler
Matched
Load
Attenuator
CRO
Crystal
Detector
Precision
Wavemeter
Attenuator
E_{01} MODE
CAVITY
Electron
Beam

FIG. 28.



Effect of Rim Sparking on R.F. Pulse Reflected from Cavity

Fig. 29



(a) (b)

1 cm

Glazed Titania Disc after High Power Test

Fig. 30

the cavity a small quantity of fine dark grey granules were found. They had apparently fallen away from a patch of about 25 mm^2 on one disc face which had broken down drastically with an appearance similar to discs described by Hadden.[46] The matching blackened area on the facing copper end wall suggested that the breakdown was due to a flashover, but this was unlikely at 10^{-5} torr. In contrast to the asymmetric location of the 'black patch' were the annular brown areas on both disc faces which were coaxial with the disc. These were formed by thin films on the glaze which could be easily cleaned off. They corresponded to the brown rings described by Hadden[46] and Hayes[71], and were probably caused by multipacting particles. Fig. 30a shows the disc face with the patch of broken down glaze and titania, and Fig. 30b shows the reverse side with a streak where part of the brown ring had been rubbed off. In both cases the faces are compared with an untouched glazed disc.

Small black patches were evident around the rim of the disc. When the disc was later removed from its copper ring it was seen that these patches were fairly regularly spaced. They were almost certainly patches of reduced titania produced by sparking in the small corrugations which would form when the ring was shrunk on to the disc. In the small air gaps between the titania rim and the copper wall, fields of several hundred MV/m could build up and produce sparking.[67] A high power test was carried out with a second glazed disc on which an attempt was made to coat the rim with the glaze ($K = 16$) as well as the disc faces and the inside of the hole. In this way it was hoped to smooth

out the sharp discontinuity in permittivity between titania and copper, and possibly lessen the chances of sparking. After the test it was apparent that sparking had again occurred but at fewer and more localised points. The rim of this latter disc is depicted in Fig. 31a.

5.3.4.2 Unglazed Titania Disc

For comparison with the glazed disc, an unglazed titania disc (Code No. 12) was subjected to the high-power test procedure just described. The initial unloaded cavity Q was found to be 3750, and the cavity was critically coupled for the E_{011} resonance at 16.5 Gc/s (magnetron number 2114). Pulse jitter was again noted at about the 10 kW input power level. After about one hour's high power running (10 kW) at 500 p.p.s. with a 0.5 μsec pulse width the cavity Q_o was measured at low power and was found to be 2230. The cavity was then dismantled. The dust found inside it was similar to that found after the glazed disc test. Some granules had copper-tinted faces suggesting that they had come from hot-spots which had occurred around the disc rim. The most striking feature about the disc was the regular spacing of thirteen patches of reduced titania around the rim (see Fig. 31b). These were matched by black patches on the copper ring and were probably due to corrugations in the ring, as before. Very slight blackening was noticed in small pits on the disc faces but there was no evidence of serious breakdown. The overall colouring of the disc was slightly grey. This fact, coupled with the 40% drop in Q_o suggested that the titania had been partly reduced to a semiconducting lower oxide. Again there were brown rings on the disc faces which, from their

appearance, suggested slightly carbonised grease (small quantities of high vacuum grease were in use as before).

5.3.4.3 Glazed and Metallised Titania Disc

The test cavity was reassembled to contain a glazed (JD 234) titania disc (Code No.4) the rim of which had been vacuum coated with a layer of copper about 1 micron thick. The cavity was critically coupled at 16.348 Gc/s (magnetron 2071) and its initial Q_o was found to be 1390. The power input to the cavity was run up to about 10 kW as before and although jitter was observed on the reflected R.F. pulse (and on the ion pump meter) it was not nearly so vigorous as it was in the tests on non-metallised discs. An electron beam of about 1 mA peak current at 22 keV was then passed through the cavity (see Fig.21 for arrangement of apparatus). No marked effect on the jitter threshold power or upon the system pressure was noticed, and the collected beam current was not influenced by the R.F. power level in the cavity. Also, the collected current did not vary with time (up to about 15 minutes running) or with the pulse repetition rate so that disc-charging and consequent loss of beam was not immediately apparent. The cavity was finally run for 20 minutes at 12 kW ($E_{zm} \approx 6.5$ MV/m) with an axial beam current of 1 mA at 22 keV.

After the test the cavity Q_o was found to be virtually unchanged, but a small quantity of dark grey granules was again present. The disc was almost undamaged even around the rim although sparking was indicated by blackening of the copper spacer adjacent to the disc ring. It was noted that rim sparking might have been eliminated if the junction

of the disc-ring and its adjacent spacer had not been so close to the high field region at the titania-copper discontinuity. It was proposed to use disc rings of double the disc thickness in any further experiments. The broad brown rings on the disc faces were again in evidence, but in addition there was an annular region, dark violet-grey in colour and about 0.5 mm wide, around the edge of the hole facing the electron gun. The latter effect could have been simply due to poor beam focusing resulting in direct bombardment of the disc. However, rapid surface charging on the disc followed by beam defocusing and bombardment could not be ruled out.

To investigate the extent of the current intercepted by the disc and the end wall the apparatus had been built so that the gun anode, the cavity walls, the collector, and the waveguide feeds were d.c. isolated from one another. It was found that no detectable current (i.e. less than 1 mA peak, using an electrometer valve) was intercepted by the disc or end wall when 1 mA was picked up by the collector. It was realised that the rather simple technique which had been used to produce a narrow electron beam could and should be improved, so that the beam current would be increased and measurements of the type just described would be made less susceptible to electrical interference from the modulators.

When the disc was removed from its ring, the copper metallising was found to be undamaged and adhering reasonably well to the titania. It was concluded that the cleaning techniques which were used to

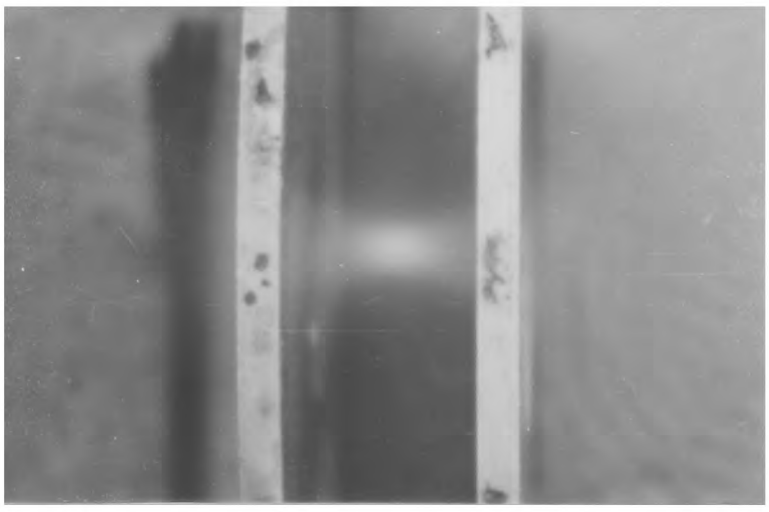
prepare the ceramic before metallising were adequate (see footnote to Section 5.2.2).

5.4 General Assessment

Judged by their chemical and physical properties in low electromagnetic fields, both magnesium titanate and titanium dioxide ceramics are suitable for consideration as loading material for linac structures. Titania can be expected to give a 30% higher shunt impedance than magnesium titanate and is therefore chosen as the better material from the low power point of view. When realistic high-power conditions are considered, the choice is much more difficult to make. The high power tests discussed in Section 5.3, and the work of Hayes[71,75] and Hadden[46] indicate that both materials suffer from oxide reduction (and sometimes surface breakdown) when subjected to R.F. fields greater than a few MV/m, but that glazing can prevent such breakdown by inhibiting the growth of semi-conducting tracks. When the discs are coated with a glaze or some other suitable protective material it is not clear how the substrate affects secondary emission from the coated surface. Hayes[71] found that both glazed and unglazed titania possessed a maximum secondary emission coefficient of about 1.2, although other workers had previously reported a figure of about 3.[28] The magnesium titanate under consideration contained 40% magnesium oxide by weight, and the reported values of maximum secondary emission coefficient for the latter substance varied from 6 to as high as 12.[69] If glazed magnesium titanate possessed a coefficient which approached these

high values, the likelihood of serious damage to the discs due to particle bombardment in a multipactor resonance would be greatly increased. The preliminary experiments described in this chapter have indicated that rim-metallising is the most promising way of eliminating sparking at the rims of titania discs. However, because of its much lower permittivity, magnesium titanate would be less prone to rim-sparking, and might not require metallising.

In view of the above observations, and to avoid excessive duplication of effort, it was decided that titania be chosen as the loading material for the linac waveguide, and that magnesium titanate should serve as the alternative material if great difficulty arose in using titania.



Rim Breakdown on Glazed and Unglazed Discs
FIG. 31

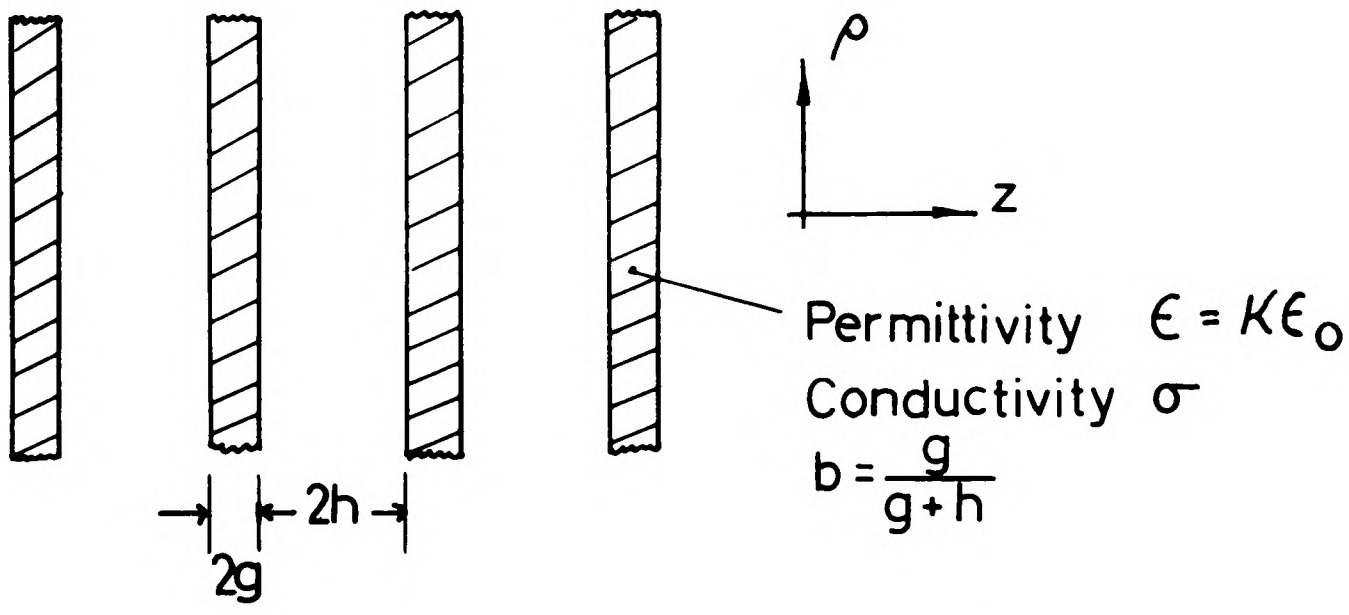


FIG. 32. LAMINATED DIELECTRIC MEDIUM

CHAPTER VI

The Theory of the Accelerator Structure

6.1 The Dielectric-Loaded Slow Wave Structure

In Section 1.2 we outlined the background to Shersby-Harvie's proposal[22] that the loading of a linac slow-wave structure with an anisotropic dielectric medium should yield higher shunt impedances than those obtained in all-metal corrugated structures. A practical simulation of such a medium was suggested where a series of parallel plane laminae was evenly spaced along an axis as depicted in Fig. 32. The capacitance of a parallel-plate condenser with its plates normal to the z axis is found to be the same as if the condenser had been filled with a dielectric of permittivity.

$$\epsilon_z = \frac{\epsilon_o}{1 - b(1 - \frac{1}{\kappa})} \qquad (6.1)$$

where $b = g/g + h$ and κ is the relative permittivity of the laminae.

Similarly the capacitance of a condenser with its plates parallel to the z axis is found to be the same as if the medium between the plates had a permittivity

$$\epsilon_\rho = \epsilon_o\left[1 + b(\kappa - 1)\right] \qquad (6.2)$$

To illustrate the extent of the anisotropy in permittivity that can be achieved in this way let $b = 0.5$ and $\kappa = 100$.

Then

$$\epsilon_\rho = 50.5\,\epsilon_o \text{ and } \epsilon_z = 1.96\,\epsilon_o$$

This degree of anisotropy is much higher than that which can be found in most uniaxial crystals which exhibit the same kind of anisotropy.

A practical form of the anisotropically loaded slow-wave structure consists of a cylindrical metal tube in which parallel dielectric discs are spaced along the axis of the tube. For linac applications there must be a central hole through which the beam passes. A section of such a waveguide structure is depicted in Fig. 2.

We shall see later that a high degree of anisotropy leads to an efficient slow wave structure for electron linacs.

Although we can visualise the outer regions (II and III) of Fig. 2 as constituting a continuous anisotropic dielectric medium, propagation theory developed on this basis can only be reasonably accurate if the phase shift per periodic length $L(= 2(g + h))$ is small compared with 2π radians. In practice we have found that such an 'Anisotropic Theory' is very helpful, but we have followed Harvie[15], Walkinshaw and Bell[65] in seeking an anlysis which takes some account of the discrete nature of the dielectric loading discs. A particular approximation is discussed below as the 'Discrete Disc Theory'.

6.2 The Anisotropic Theory

We wish to determine the frequency at which a dielectric disc loaded waveguide will propagate the lowest order E-mode (E_{01}) for a given phase change per periodic length. Also, we wish to know the corresponding axial electric field, the shunt impedance, and the

series impedance. Given a knowledge of these primary quantities and of how they are influenced by the waveguide dimensions and disc permittivity we can choose the physical properties of the structure which should give us the fields and velocities needed to accelerate and bunch electrons.

We begin by considering the simplest approximation to the problem. Regions II and III of Fig. 2 are assumed to constitute a continuous anisotropic dielectric medium. The fields in region I are assumed to be the normal form of the E_{01} mode in cylindrical waveguide. In the anisotropic region the fields are derived from wave equations deduced from Maxwell's equations using the conditions

$$D_z = \epsilon_z E_z \ , \quad D_\rho = \epsilon_\rho E_\rho \ ,$$

$$\epsilon_\phi = \epsilon_\rho \ , \ D_\phi = \epsilon_\phi E_\phi \ , \ E_z = 0 \text{ at the conducting waveguide wall}$$

and restricting the equations to circularly symmetrical waveguide modes where $H_z = 0$ and $\frac{\partial}{\partial \phi} = 0$. The frequency and axial propagation constant ($\beta = \frac{2\pi}{\lambda_g}$) are made the same for both the axial and the anisotropic regions, and the radial wave impedance $\frac{E_z}{H_\phi}$ is matched across the regional boundary. The details of the procedure can be found in Harvie.[15] We finally obtain the dispersion equation

$$k_1 \frac{I_0(k_1 a)}{I_1(k_1 a)} = \frac{\epsilon_0}{\epsilon_z} \Gamma \left[\frac{J_0(\Gamma a)\, Y_0(\Gamma c) - J_0(\Gamma c)\, Y_0(\Gamma a)}{J_1(\Gamma a)\, Y_0(\Gamma c) - J_0(\Gamma c)\, Y_1(\Gamma a)} \right] \qquad (6.3)$$

where $$\Gamma^2 = \frac{\epsilon_z}{\epsilon_0} k^2 - \frac{\epsilon_z}{\epsilon_\rho} \beta^2 \qquad (6.4)$$

and $k_1^2 = \beta^2 - k^2$ a = radius of axial hole

$k^2 = (2\pi/\lambda)^2$ c = radius of cylindrical conducting wall

J( ), I( ) are Bessel functions of the first kind with real and imaginary arguments respectively.

Y( ) is a Bessel function of the second kind with real argument.

Matching E_z across the boundary at ρ = a reduces the number of arbitrary field constants to one, A, which depends only on the power flux along the waveguide. This arbitrary constant is used to describe the amplitude of the axial electric field of the wave synchronous with the electrons, i.e.

$$E_z = A\, I_o(k_1\rho)\, \cos(\omega t - \beta z) \qquad (6.5)$$

To calculate the shunt impedance we need to know the power dissipated per unit length P_d. This is divided up as

$$P_d = P_{dz} + P_d + P_w$$

where the dielectric losses due to E_z and E_ρ are P_{dz} and $P_{d\rho}$ respectively, and where P_w is the ohmic loss in the waveguide wall.

$$P_{dz} = \frac{1}{2}\int \sigma_z |E_z|^2\, dV$$ over unit length, where V is here a volume.

σ_z is the conductivity of the anisotropic dielectric in the axial direction and we may write

$$\sigma_z = \frac{\omega \epsilon_z}{Q_z} \quad \text{where } Q_z = \frac{1}{\tan \delta_z} = (\text{axial loss tangent})^{-1}$$

Therefore $$P_{dz} = \frac{1}{2}\frac{\omega \epsilon_z}{Q_z}\int E_z^{\,2}\, dV \qquad (6.6)$$

and similarly $$P_{d\rho} = \frac{1}{2}\frac{\omega \epsilon_\rho}{Q_\rho}\int E_\rho^{\,2}\, dV \qquad (6.7)$$

By considering the power losses in the parallel-plate condenser systems described in Section 6.1, we can express Q_z and Q_ρ in terms of the Q of the dielectric discs:-

$$Q_z = Q\epsilon/b\epsilon_z \qquad Q_\rho = Q\epsilon_\rho/b\epsilon \tag{6.8}$$

The waveguide wall loss derived by assuming that the fields are unchanged by the losses is

$$P_w = \frac{1}{2}\left[\frac{\omega\eta\mu_o}{2\sigma}\right]^{\frac{1}{2}} \int (H_\phi H_\phi^*)\, dS \tag{6.9}$$

where η = the relative permeability of the wall, μ_o = the permeability of free space, σ = wall conductivity and where the surface integral is taken over unit length of wall.

The series impedance expresses the peak synchronous field in terms of the power flux P.

$$P = P_{hole} + P_{dielectric}$$

where P_{hole} and $P_{dielectric}$ are the time-averaged Poynting Vector, $\frac{1}{2}\underline{E}\wedge\underline{H}^*$, integrated over the axial hole and annular dielectric cross-sections respectively.

The integrated expressions for P_d and P are rather complicated and are not given here. For the case where the phase velocity equals c they can be found in Reference 24. The expression for P, the power flux, gives the value for the field constant A in terms of Γ and k_1. Therefore when equations (6.3) and (6.4) have been solved for Γ and k_1 we can calculate the series impedance, the shunt impedance and the loss length of the structure.

Lichtenberg programmed a digital computer to solve equations (6.3) and (6.4), and to evaluate the integrals giving P_d and P in terms of the accelerating field. Several variants of the basic programme were written to give the dispersion curve ($\omega - \beta$ diagram) for given structures, the variation of wave velocity with disc pitch and dimensions, and the effects of small changes in the physical properties of the structure. The information gleaned from these programmes is discussed in Chapter VII.

6.3 The Discrete Disc Theory

The 'Anisotropic Theory' describes the laminated dielectric approximation to a continuous anisotropic dielectric medium with reasonable accuracy, as we shall see in the next chapter. However, if we are to produce well bunched electrons we must obtain the most accurate description of the structure compatible with a reasonable amount of computational effort, always remembering that the accuracy to which we can measure the physical properties of the structure will affect the precision of the system.

Bell and Walkinshaw[65] analysed the exact behaviour of the dielectric disc-loaded waveguide, setting down the field and frequency equations and discussing several approximate solutions. They first set up series representations of the possible fields in regions I, II and III basing their equations on the following premises:-

(a) In region I the fields consist of infinite series of harmonic components, each component being of the cylindrical waveguide E_{01} mode form and having a phase change $\beta_n L$ per periodic length.

(b) In region II the fields have the same periodic properties as those in region I. Propagating modes are assumed to exist here.

(c) In region III the same periodic properties exist, and the field modes are assumed to be evanescent.

They then proceed to formulate the equations consequent upon the exact matching of fields at the regional boundaries. Approximations to these equations are then discussed. It is shown that if the disc thickness and spacing are small, i.e. if $g \to 0$ and $h \to 0$, and if the lowest order term only in each of the regional field series is considered, then the general equations reduce to equations (6.3) and (6.4) respectively. In other words, if $g \to 0$ and $h \to 0$ the anisotropic theory is valid. This is the simplest approximation.

A better approximation is given by using the frequency equation derived by precisely matching the fields between regions II and III, but still only matching region I to regions II and III on a first term basis ('anisotropic matching'). We shall refer to this approximation as the Discrete Disc Theory. Equation (6.3) is unchanged but equation (6.4) becomes

$$\cos \beta L = \cosh 2ph \cos 2\gamma g + \tfrac{1}{2}\left[\frac{p\epsilon}{\gamma\epsilon_o} - \frac{\gamma\epsilon_o}{p\epsilon}\right]\sinh 2ph \sin 2\gamma g \qquad (6.10)$$

where $p^2 = \Gamma^2 - k^2$ and $\gamma^2 = \frac{\epsilon}{\epsilon_o} k^2 - \Gamma^2$

Normally we wish to know the value of b (ratio of dielectric disc thickness to pitch) which will give us a certain guide wavelength; we need to simultaneously solve (6.3) and (6.10) for b and Γ. We

cannot directly eliminate Γ from these two transcendental equations as can be done with equations (6.3) and (6.4), but Lichtenberg has devised a numerical method of simultaneous solution (see Appendix IV). This requires three trial solutions for Γ and b respectively. The trial values of Γ and b are obtained from the anisotropic theory, and they are chosen so that their values probably enclose the correct values for the solution, thereby speeding up the rate at which the numerical solution can converge on to the correct result. The method was readily translated into a computer programme. After the dispersion equations, (6.3) and (6.10), have been solved, the power loss and power flux integrals are computed as before, taking only the lowest order terms of the field series into account.

The chief advantage of the Discrete Disc Theory lies in the fact that although the Anisotropic Theory should give us sufficient accuracy in the relatively short bunching section where the discs are closer together (and therefore tending to form a continuous annular anisotropic dielectric), we shall probably need a more accurate knowledge of the phase velocity in the long accelerating section than the Anisotropic Theory can give us. This is because we must maintain the closest beam-wave synchronism during the main acceleration if we are to retain the bunch length produced in the bunching section. Providing the accelerating field decays smoothly in the uniform section it is of secondary importance.

The use of the Anisotropic and Discrete Disc Theories in the design of J-Band linac structures is described in the next Chapter.

CHAPTER VII

The Practical Design of the Accelerator Structure

7.1 The General Design*

To simplify the design procedure, and to avoid constructional complications, it was decided at the outset that c, the radius of the waveguide tube, should be constant along the bunching section and the accelerating (uniform) section. It was also decided that the minimum value of hole radius in a disc should be 0.2 cm as this was thought to be the smallest hole in a 1 m structure through which one could reasonably expect to send a beam of some tens of milliamps without difficulty.

Harvie, et al. showed that the shunt impedance differed only slightly from its optimum value over a broad range of b (the ratio of disc thickness to pitch) around 0.3.[24] It was therefore decided that the accelerating section should have b varying from about 0.35 to 0.25 with the I.D. (twice the hole radius) fixed at 4 mm.

To obtain a first estimate of c, Lichtenberg calculated the left and right hand sides of equation (6.3) for a few trial values of c with $\lambda = 1.8$ cm, $v_s = 0.75$ (expressed as a fraction of the velocity of light), $a = 0.2$ cm, and $b = 0.3$, the latter three quantities relating to the transition region between the bunching and accelerating sections. The value of c satisfying the equation was estimated by graphical interpolation to be 0.622 cm. The series impedance was then calculated by the method described in Section 6.2 and was found to be approximately

---

* A concise description of the general linac design is given in Reference 81.

180 M Ω/m^2. It was estimated that the power flux available at the end of the buncher would be at least 200 kW so that the peak axial field (E_{mso} of Section 4.4.2) would be about 6 MV/m, and this value was therefore adopted in the trajectory calculations discussed in Chapter IV.

In Section 4.2 we chose 0.4c as the phase velocity at the beginning of the buncher. To combine such a large wave slowing factor with a relatively low field it was necessary to make both a and b as large as possible. The phase velocity of 0.4c corresponds to a guide wavelength of 7.2 mm.

In Section 3.3 βL, the average phase change per period, was taken as $\frac{\pi}{3}$ corresponding to six discs per wavelength, and for this reason the average pitch at the beginning of the buncher was chosen to be 1.2 mm. For convenience, 2g, the disc thickness, was chosen to be 1 mm. Keeping $\beta L = \frac{\pi}{3}$ the maximum value of b was thereby set at 0.8, and 2h the minimum spacer thickness (between discs) became 0.2 mm. This latter figure was considered to be the minimum thickness to which a spacer could be readily machined without handling difficulties.

Setting b = 0.8, v_s = 0.4c, 2g = 1 mm, c = 0.622 cm, and λ = 1.8 cm in the anisotropic dispersion relation of equation (6.3) gave a value of a of about 0.45 cm. Evaluation of the series impedance showed that an input power of 250 kW gave a peak axial field of 0.45 MV/m. This field was therefore adopted as the initial field in the trajectory calculations in Chapter IV.

7.2 Bunching Section Design

7.2.1 Use of the Anisotropic Approximation

The first step taken was to take the values of E_{ms} and v_s tabulated in Appendix II and use them in the equations of the anisotropic approximation (Sections 6.1 and 6.2) to find how a and b should be varied along the buncher. The basic form of the equations used is

$$f_1(a,b,c,v_s) = 0 \tag{7.1}$$

$$E_{ms} = P^{\frac{1}{2}} f_2(a,b,c,v_s) \tag{7.2}$$

and

$$-\frac{\partial P}{\partial z} = P\ell_o(a,b,c,v_s) \tag{7.3}$$

Equations (7.1) and (7.2) were solved simultaneously by a computer programme to give a and b in terms of P. The initial values of b, c and v_s were taken as those given in Section 7.1, with $\lambda = 1.823$ cm corresponding to the available source frequency. Equation (7.3) was then solved for P.

Table 6 sets out the results obtained at intervals of 1 cm along the buncher when the titania tan δ and K were taken as 4.3×10^{-4} and 97 respectively, and the effective copper wall resistivity was taken as the handbook value of $1.74.10^{-8}$ ohm-metre. Table 7 shows the results obtained when the copper resistivity was doubled to take some account of surface effects and deficiencies in waveguide joints. It can be seen that the power flux and the dimensions were not greatly affected although the variation in loss length changed considerably.

a	b	P	ℓ_o	z	v_s/c	Other Parameters
cm		MW	m	cm		
0.4633	0.8939	0.2500		0	0.400	$\rho = 1.74 \times 10^{-8} \Omega$ m
0.4459	0.8661	0.2432	0.3963	1	0.414	$K = 97$
0.4274	0.8330	0.2376	0.4767	2	0.432	
0.4067	0.7917	0.2331	0.5763	3	0.453	$\tan \delta = 4.3 \times 10^{-4}$
0.3829	0.7394	0.2295	0.6968	4	0.478	$\lambda = 1.823$ cm
0.3566	0.6771	0.2265	0.8265	5	0.509	
0.3289	0.6078	0.2239	0.9445	6	0.544	$c = 0.622$ cm
0.3006	0.5374	0.2217	1.0236	7	0.583	$2g = 1$ mm
0.2739	0.4745	0.2195	1.0521	8	0.625	
0.2500	0.4244	0.2175	1.0413	9	0.666	
0.2309	0.3886	0.2154	1.0144	10	0.706	
0.2178	0.3657	0.2132	0.9875	11	0.742	

Bunching Section : Anisotropic Approximation

TABLE 6

a	b	P	ℓ_o	z	v_s/c	Other Parameters
cm		MW	m	cm		
0.4633	0.8939	0.2500	0.4432	0	0.400	As for Table 6
0.4463	0.8668	0.2449	0.5311	1	0.414	except that
0.4282	0.8344	0.2407	0.6376	2	0.432	$\rho = 3.48 \times 10^{-8} \Omega$ m
0.4079	0.7940	0.2373	0.7699	3	0.453	
0.3844	0.7427	0.2345	0.9301	4	0.478	
0.3586	0.6813	0.2322	1.1033	5	0.509	
0.3313	0.6128	0.2302	1.2617	6	0.544	
0.3034	0.5431	0.2285	1.3689	7	0.583	
0.2772	0.4806	0.2269	1.4092	8	0.625	
0.2540	0.4307	0.2253	1.3972	9	0.666	
0.2356	0.3951	0.2236	1.3636	10	0.706	
0.2234	0.3726	0.2220	1.3309	11	0.742	

Bunching Section : Anisotropic Approximation

TABLE 7

7.2.2 Comparison of Theory with Experiment

Two test cavities were constructed by Free to check the theory at the beginning and end of the bunching section.[67] They were of uniform pitch and were designed to be about two guide wavelengths long at the accelerator design frequency. A ring and spacer construction technique was used. The important parameters were as follows:-

Cavity I	Cavity II
10 titania discs	10 titania discs
c = 0.622 cm	c = 0.622 cm
a = 0.346 cm	a = 0.208 cm
b = 0.647	b = 0.333
2g = 0.099 cm	2g = 0.100 cm

The test cavities were connected to the microwave circuit shown in Fig. 23 via coaxial lines and axial probes giving loose coupling. Using the techniques described in Section 5.3.3 the frequencies of the E_{01} resonances for βL between 0 and π were identified and plotted in Figs. 33 and 34. These curves should be compared with those derived from the anisotropic and discrete disc theories which are also shown. Neither theory agreed well with the experimental results when the disc holes were large, but the discrete disc theory differed by only 3% in frequency for Cavity II at the end of the buncher and agreed closely with the measured group velocity. The reasonable agreement between the discrete disc theory and the experiments when the holes were small, stems from the fact that as a tends to zero the exact theoretical field matching between the dielectric and the air space (regions II and III of Fig. 2) leads to an exact solution of the

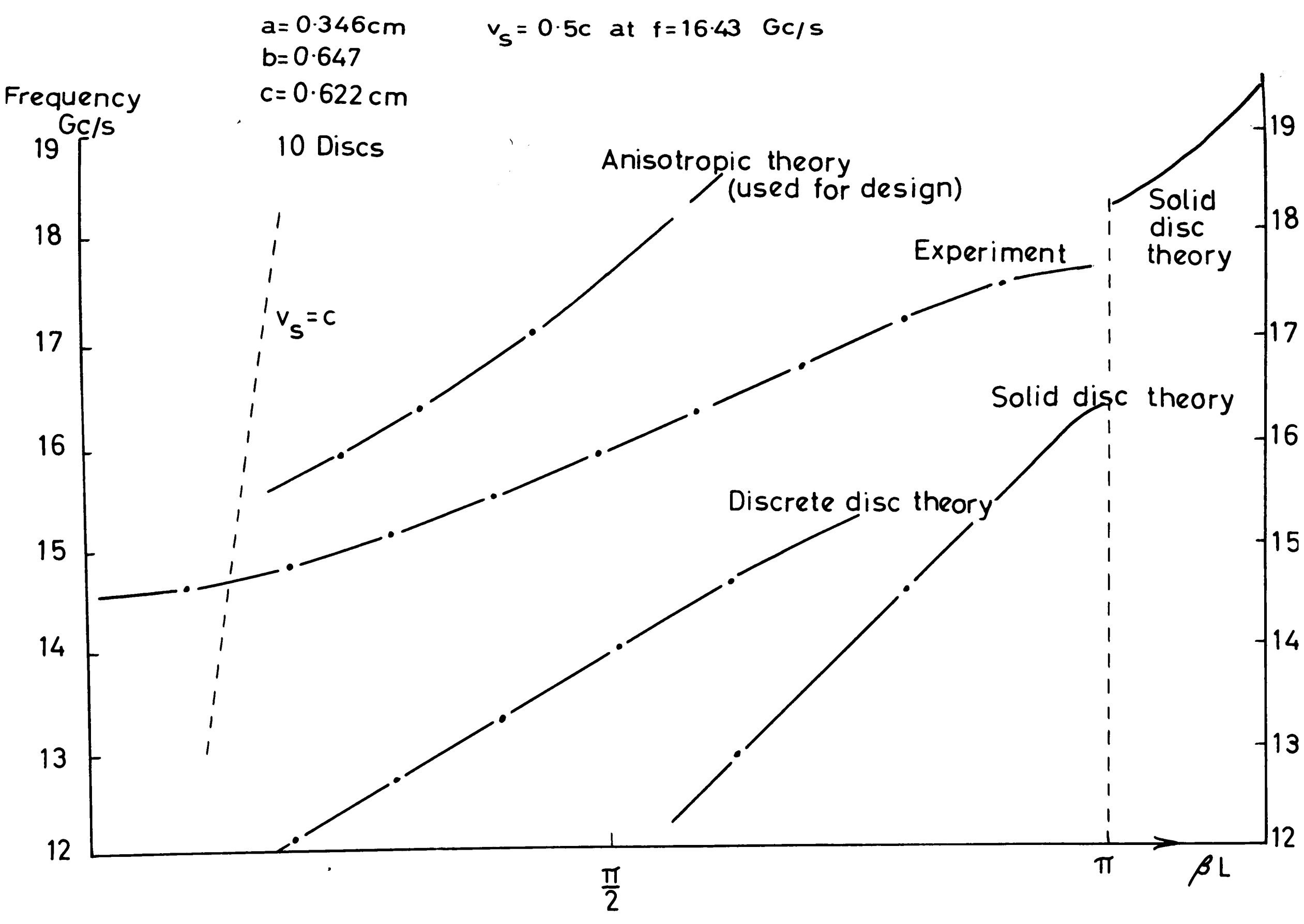


FIG. 33. DISPERSION CURVES: TITANIA LOADING

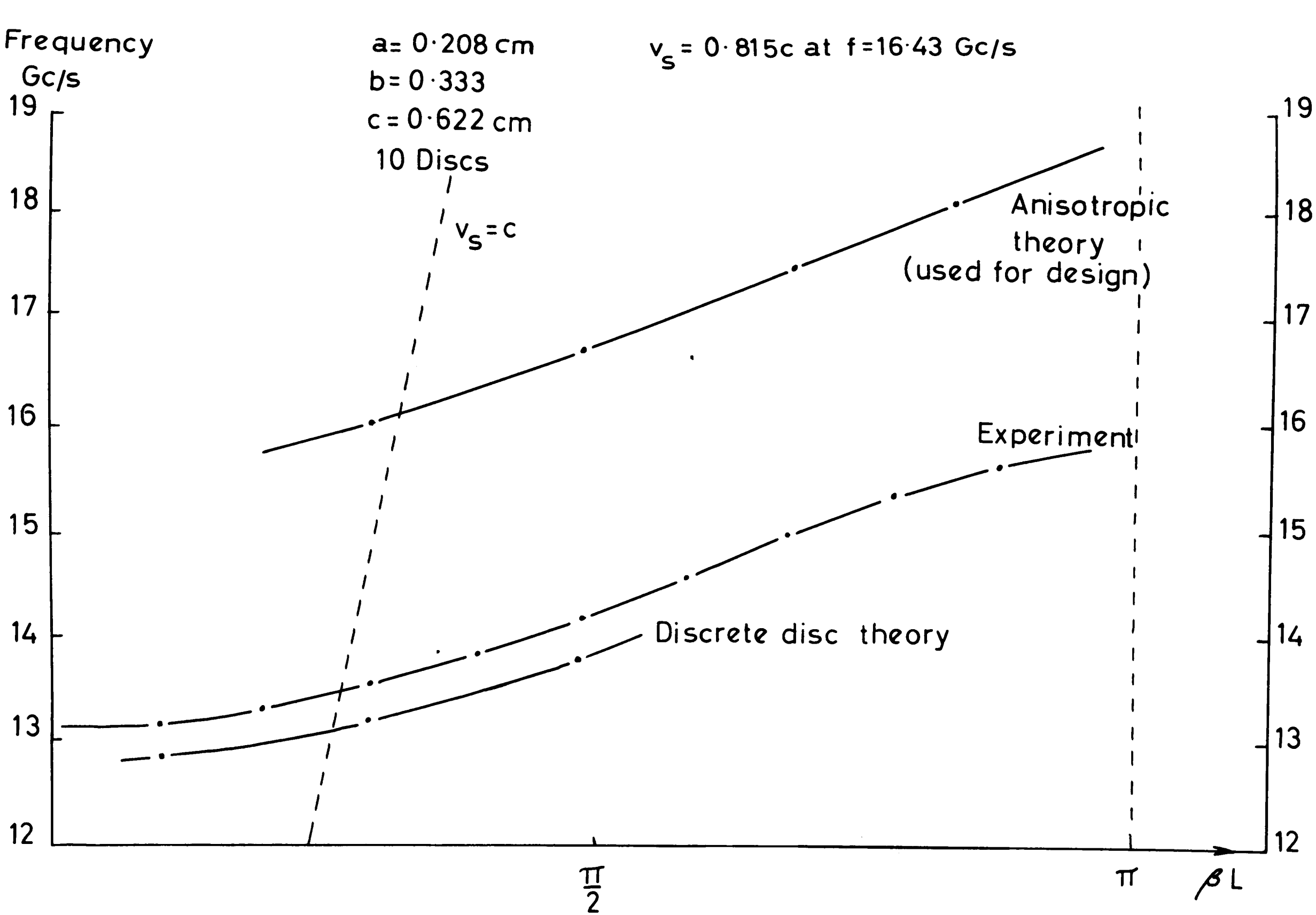


FIG. 34. DISPERSION CURVES: TITANIA LOADING

frequency equation.

The group velocity results were as follows:-

Cavity I		Cavity II	
Experimental	$v_s = 0.4\ c$	Experimental	$v_s = 0.71c$
Experimental	$v_g = 0.04c$	Experimental	$v_g = 0.17c$
D.D. Theory	$v_g = 0.063c$	D.D. Theory	$v_g = 0.17c$
Anis. Theory	$v_g = 0.085c$	Anis. Theory	$v_g = 0.21c$

Since the group velocity equals the energy velocity (Section 3.2.5) we can estimate the filling time of the structure by doubling the length of the buncher (where v_g is small), adding this to the length of the uniform section and dividing by the average group velocity in the uniform action. For a buncher of length 10 cm and a total length of 75 cm, we have

$$t_f = 1.67 \times 10^{-8} \text{ sec.}$$

This is almost negligible when compared with the 0.5 μsec R.F. pulse that is likely to be used.

An attempt was also made to compare the theoretical and experimental field parameters in the bunching section. Free found that the methods of Section 5.3.3 were inadequate for measuring r_{sh}/Q_o near the beginning of the buncher (Cavity I).[67] The fields were so low that the frequency perturbations produced by a small bead were not measurable to any reasonable degree of accuracy.* Experiments on Cavity II and other cavities of similar dimensions and construction

---

* It should be noted here that the apparatus was at an early stage of development when these experiments were done.

were more successful. Before we examine the results we shall express the loss length l_o in terms of the measurable quantities v_g, Q_o, and and ω.[63] At any cross-section of the linac we have

$$\frac{\partial U}{\partial t} + \frac{\partial P}{\partial z} + P_d = 0 \qquad (7.4)$$

where U is the stored energy per unit length and other notation is as before.

Now $$P_d = \frac{\omega U}{Q_1} \qquad (7.5)$$

and $$P = U v_g \qquad (7.6)$$

since the energy velocity equals the group velocity.

Substituting for P_d and U in equation (7.4) and setting $\frac{\partial U}{\partial t} = 0$ for steady state conditions we have

$$\frac{\partial P}{\partial z} + \frac{\omega}{v_g Q_1} P = 0 \qquad (7.7)$$

whence $$P = P_1 e^{-\frac{\omega z}{v_g Q_1}} \qquad (7.8)$$

giving $$l_o = \frac{v_g Q_1}{\omega} \qquad (7.9)$$

If we ignore the effects of end walls upon test cavity Q_o, then $Q_1 = Q_o$ and

$$l_o = \frac{v_g Q_o}{\omega} \qquad (7.10)$$

From equation (3.1) we know that in the linac

$$r_{sh}\ (T.W.) = 2\ r_{sh}(S.W.) \qquad (3.1)$$

and that $$E_{zm} = 2\ E_{ms}$$

where E_{zm} is the maximum axial field in a resonant test cavity.

Therefore $$r_{sh}(T.W.) = 2\ \frac{(E_{zm}/2)^2 \ell}{W} \qquad (7.11)$$

where ℓ is the cavity length and W is the power dissipated in the cavity. Using the notation of Section 5.3.3. we may re-write equation (7.8) as

$$r_{sh}(T.W.) = \frac{\delta f_m\ Q_o \ell}{4\pi f \alpha} \qquad (7.12)$$

and therefore $$r_{se}(T.W.) = \frac{\delta f_m\ Q_o \ell}{4\pi f \alpha\ \ell_o} \qquad (7.13)$$

since $$\ell_o = r_{sh}/r_{se} \qquad (1.7)$$

Equations (7.7), (7.9) and (7.10) express ℓ_o, $r_{sh}(T.W.)$ and $r_{se}(T.W.)$ in terms of quantities which are measurable in resonant cavity experiments.

From the dispersion curve for Cavity II in Fig. 34, and from measurements of Q_o and r_{sh}/Q_o for the E_{013} and E_{014} resonances, the following results were found[67]:-

		E_{013}	E_{014}
f	Gc/s	13.6	13.8
v_s/c		0.93	0.71
v_g/c		0.12	0.17
$Q_o(\simeq Q_l)$		1800	2000
r_{sh}	$M\Omega/m$	43	45
r_{se}	$M\Omega/m^2$	51	35
ℓ_o	m.	0.84	1.30

According to the anisotropic theory the phase velocity should have been 0.815c at 16.43 Gc/s. Interpolating between the E_{013} and the E_{014} results the following figures were found for the actual cavity when $v_s = 0.815c$. The figures given by the two theories for $v_s = 0.815c$ in Cavity II are also shown.

		Anisotropic Theory	Discrete Disc Theory	Experiment
f	Gc/s	16.43	13.35	13.70
v_s/c		0.815	0.815	0.815
v_g/c		0.17	0.17	0.15
Q_o		2200	2600	1900
r_{sh}	$M\Omega/m$	210	450	44
r_{se}	$M\Omega/m^2$	160	280	42
ℓ_o	m.	1.35	1.61	1.05

It is difficult to explain the differences between the theoretical and experimental values of shunt impedance. The experimental Q_o is only about 20% less than the theoretical values (which were calculated using the handbook value of copper resistivity) so that the large difference between the theoretical and experimental values of r_{sh} is not likely to be due to excessive wall losses. In both theories the matching of fields between region I and the outer two regions (see Fig. 2) is inexact so that we cannot expect a very accurate description of the field on the axis, but the difference between theory and experiment is disappointing.

7.2.3 The Relaxation Method

The main consideration in the linac project is the minimising of the output bunch length and energy spread. The behaviour of the bunching section must therefore be under close control. The work described in the previous sub-section indicated that neither the anisotropic theory nor the discrete disc theory could accurately describe the fields and velocities in the bunching section except near the transition to the main accelerating section. It was therefore decided that a different approach to the theoretical determination of buncher dimensions should be investigated, and that the experimental effort should be directed towards the construction of the main accelerating section. Apart from the detailed dimensions, everything gleaned from the latter effort would be directly relevant to the eventual fabrication of the bunching section.

The new theoretical approach to the buncher problem was the application of the well-known relaxation methods originally introduced by Southwell[82] in the analysis of mechanical frames. The availability of a Mercury computer was instrumental in the decision to attempt this type of solution to the problem, for the iterative procedures of relaxation methods lend themselves quite well to computer programming. The complexity of the problem has proved to be quite severe in certain respects. For example, the small radius of curvature of boundaries such as that around the periphery of the hole in a titania disc has made it difficult to meet boundary conditions without halting the computer programme because of the incidence of infinite values of fields

and their derivatives. The high density of mesh points needed to overcome this kind of problem leads to long computing time. Most of this work has been carried out by A.G.A.M. Armstrong and E.V. Gilbert under the guidance of Dr. H. Motz. It will not be discussed further here.

7.3 The Main Accelerating Section

A great deal of the work done on the buncher design was concerned with the transition region between buncher and accelerator proper, and the results obtained served as a starting point for accelerating section design.

7.3.1 The Primary Objectives

The primary objectives of the work on the main accelerating section were:-

(a) To determine the structural dimensions which will give the required fields and wave velocities

(b) To find the tolerable and attainable physical accuracies in the structure, and to devise an appropriate means of fabrication

(c) To investigate more fully the problems of high-power operation in the titania loaded structure, and to find acceptable remedies

(d) To construct a complete main accelerating section, and to test it at high power with a suitable injected electron beam ($\approx$ 250 keV).

Considerable progress has been made towards objectives (a), (b) and (c). Their full and satisfactory attainment would virtually ensure the attainment of objective (d).

7.3.2 Fabrication Methods

Four basic construction techniques were considered:

(a) The ring-and-spacer system[67]
(b) The clamped split tube[24]
(c) The waveguide tube electroformed around metallised discs and washers
(d) The shrunk-on tube

The ring-and-spacer system has proved to be a flexible technique for use in high and low power tests, but it implies a large number of metallic junction planes which are orthogonal to the direction of R.F. current flow. Also, dielectric disc alignment is difficult to control. This latter difficulty is even more pronounced in the clamped split tube scheme[24], and the system of locating pins would be difficult to arrange accurately in a split tube only 1 cm in internal diameter. Problems with the electroformed tube method arise chiefly because of the non-metallic nature of the dielectric discs and the chemical instability of their glaze, as discussed in Section 5.2.5. The shrunk-on tube scheme affords a rigid structure with minimal disc alignment problems, and allows a wider range of spacer materials to be considered. This latter scheme was investigated as a probable successor to the ring-and-spacer system.

The first test structure consisted of three unglazed titania discs. The technique used for locating them inside a heated copper tube was simply an extension of the method used for placing discs in thin copper rings.[67] The copper tube was reamed to an I.D. nominally 0.025 mm less than that of the discs. The copper tube was then placed

on a hotplate and heated to about 300°C at which temperature its I.D. exceeded the O.D. of the discs by about 0.025 mm. The three discs together with their Duralumin spacers were eased into the tube and the assembly was cooled. The spacers were later dissolved in caustic soda solution and the assembly was dried in a vacuum oven. Although this early method was crude, it served to show up several points:

(a) The titania discs fractured easily when flexural stresses occurred, but displayed their high bulk modulus of elasticity by making substantial indentations in the metal when radially compressed by the copper tube.

(b) The titania disc rims chipped easily.

(c) The disc rim chipping was aggravated by a surface roughness on the copper (about 10 microinches peak to valley), and a machining tolerance on the tube I.D. (± 0.010 mm) which was incompatible with that on the disc O.D. (± 0.002 mm).

(d) Stacking of discs and spacers before insertion was vital if adequate precision in disc location was to be achieved.

To attempt to accommodate these and other features, and to supplant the Duralumin spacers by spacers made of a material which could be dissolved out without damaging glazed discs, a more refined technique was adopted. To minimise the danger of unwanted chemical reaction between a spacer solvent and the structure, cellulose acetate was a first choice for a spacer material; the solvent was acetone. It was found that this plastic could be machined quite well (to within ± 0.015 mm) and could be quickly dissolved in warm acetone. To reduce

the roughness on the inner surface of the tube and to improve the accuracy on the I.D. after reaming, arrangements were made for the tube to be honed automatically using a hard stone (by Delapena), and to be measured internally with a Mercer air gauge which could be read to within ± 0.0005 mm.

A special jig, depicted in Fig. 35, was designed to hold the tube during the heating and shrinking process. After the accuracies on the tube I.D. and disc O.D. had been closed to ± 0.002 mm and the surface roughness on the inner tube surface had been reduced to about 2 microinches peak-to-valley, it was found practicable to proceed as follows. The waveguide tube was heated in air to about 200°C at which stage its I.D. was about 0.01 mm greater than the O.D. at room temperature of the titania discs which were stacked with plastic spacers on a retractable mandrel. The disc stack was then inserted in the waveguide tube, the heating tape was quickly removed, and the entire jig and mandrel were immediately immersed in cold water. In this way the waveguide tube was cooled to room temperature and the disc stack was under radial compression within a few seconds. The process has been carried out many times and on no occasion has insertion proved difficult or a disc fractured. The waveguide wall thickness was normally about 4 mm so that short lengths of structure were self-supporting. The longest section made to date contains 25 discs and is 6 cm long. Such sections could be collimated and held under axial compression to form the whole linac structure. Contact between sections was made at highly machined annuli about 0.5 mm wide around the edges

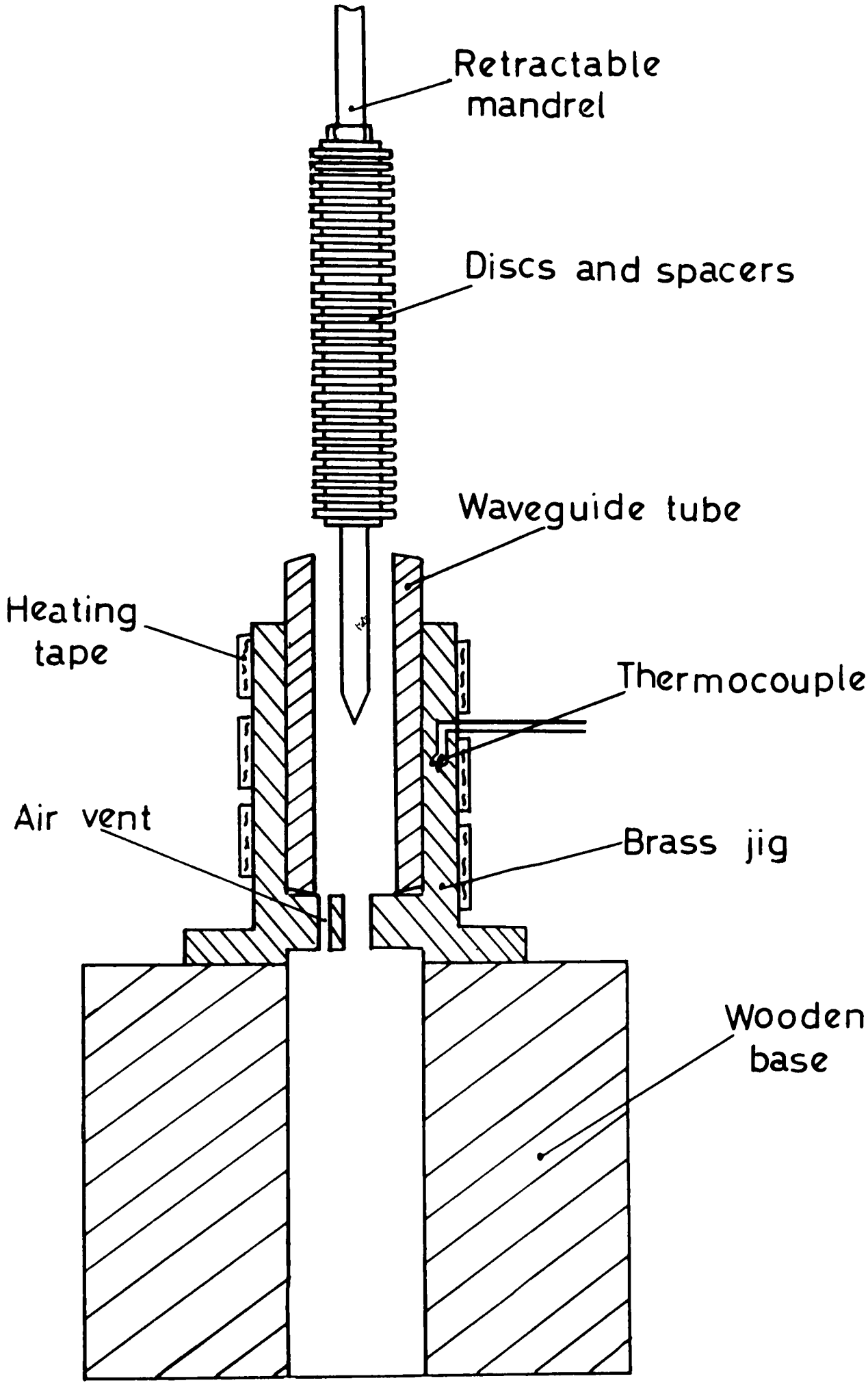


FIG.35 STRUCTURE JIG AND MANDREL

of the waveguide holes. Beyond the annuli the section ends were bevelled to an angle of 10^{o}.

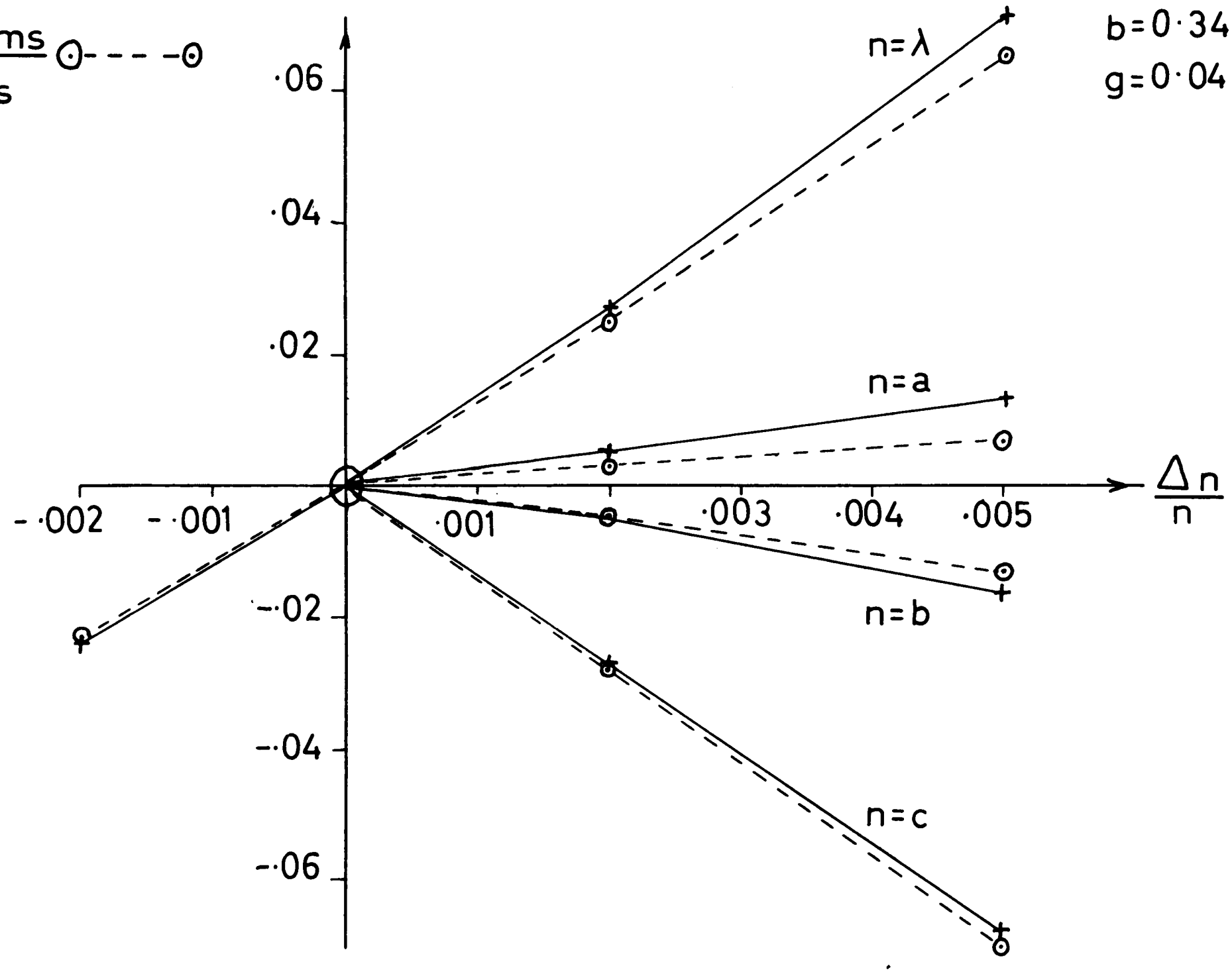
As an alternative to the honing method of producing a precision waveguide tube, Dr. D.J. Walliker of Decca Radar undertook to electroform and machine a copper tube to accommodate a 6 disc structure (about 1.5 cm long). The machining and polishing of the mandrel were expensive, but the finished tube was accurate and uniform in I.D. along its length to within $\pm$ 0.001 mm. Further tubes of the same I.D. could be produced relatively cheaply, but the method was unsuitable for producing single experimental cavities of different dimensions. However, electroformed tubes might well prove to be valuable for the final linac structure, especially if lengths of about 10 cm can be produced to the same high degree of accuracy. The entire linac could then be made up of only half a dozen sections.

7.3.3. Theoretical Perturbation Results: Physical Tolerances

To discover the required physical tolerances on the structure and to assist in making the experimental structure conform with the design characteristics, it is important to know how the performance is affected by small perturbations in the physical parameters. A series of perturbation computations was therefore carried out for points at the beginning of the main accelerating section using the anisotropic and the discrete disc theories. The results are shown in Fig. 36 and Fig. 37 as graphs of the fractional changes in the phase velocity v_s and the peak axial electric field E_{ms} versus the fractional perturbations in wavelength λ, hole radius a, the ratio of dielectric thickness 2g to

$\frac{\Delta v_s}{v_s}$ +——+

$\frac{\Delta E_{ms}}{E_{ms}}$ ⊙- - - -⊙



c = 0·622 cm
v_s = 0·753 c
a = 0·2 cm
b = 0·3474
g = 0·04 cm

FIG. 36. PERTURBATION RESULTS: ANISOTROPIC THEORY

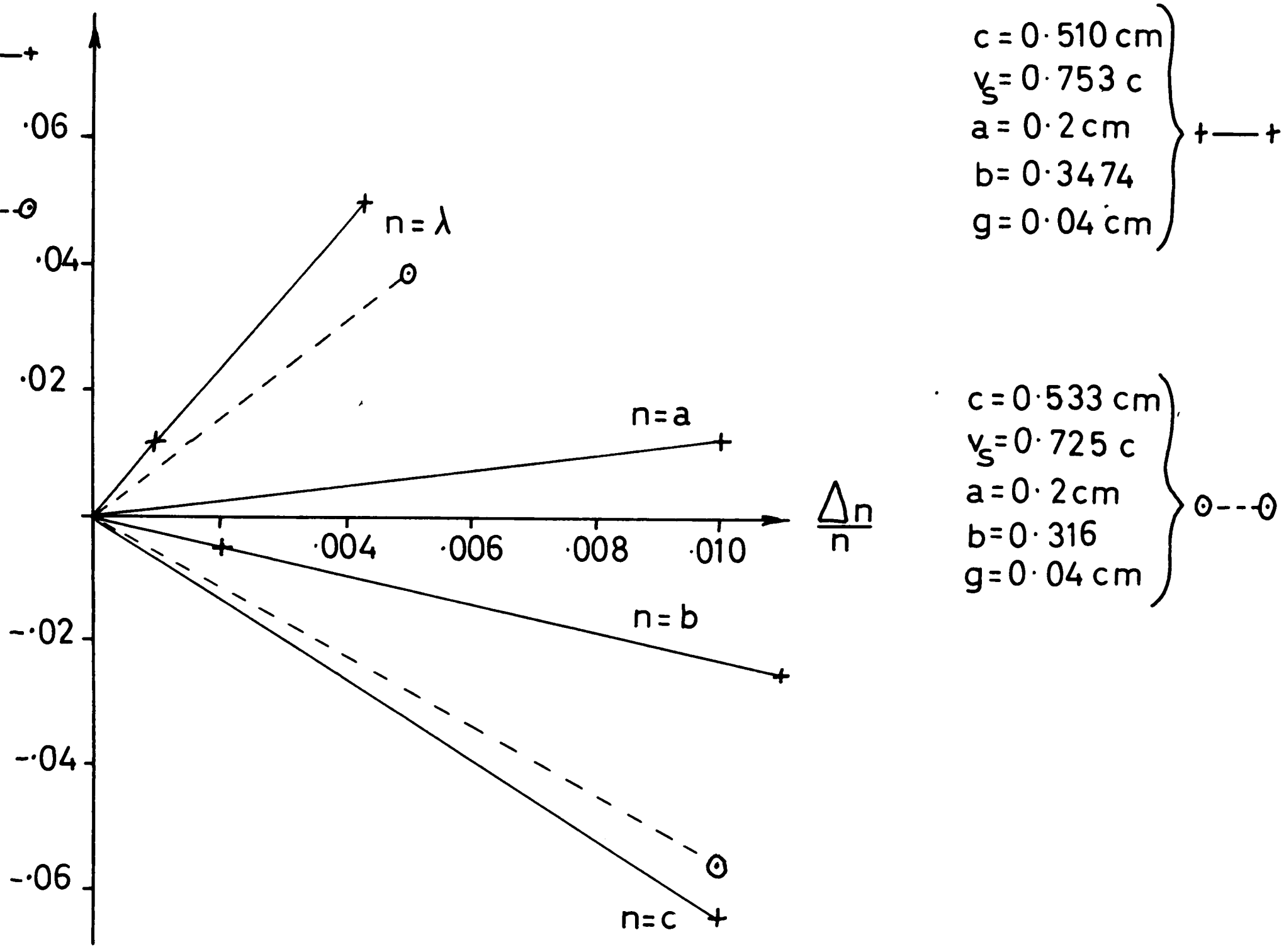


FIG. 37. PERTURBATION RESULTS: DISCRETE DISC THEORY

the pitch 2(g + h), and disc radius c. Both v_s and E_{ms} are clearly more sensitive to changes in λ and c than in a and b. Therefore a check computation was carried out on the effects of perturbations in λ and c at the end of the linac (discrete disc theory only). The results are shown in Fig. 38, and it is clear that the sensitivities of v_s and E_{ms} to λ and c increased only slightly as v_s increases.

The influence on v_s and E_{ms} of the relative permittivity was also investigated. When $v_s = 0.725c$ the discrete disc theory showed that percentage changes in v_s were of opposite sign to and greater than the percentage perturbation in K by a factor of (-)3.44. The corresponding factor for E_{ms} was (-)2.48. At $v_s = 0.975c$ the respective factors were (-)4.11 and (-)2.70.

We can make use of these perturbation results in two ways. Firstly, they can show how dimensions should be altered when the structure behaviour is close to the design characteristic; this procedure is exemplified in Section 7.3.4. Secondly, we can deduce the dimensional tolerances demanded by the bunching theory in Chapter IV.

From Sections 4.6.1 and 4.6.2 we note that the tolerable standard deviations in phase velocity and peak axial field are approximately 0.02 v_s and 0.2 E_{ms} respectively when the errors occur at 1 cm intervals along the linac. The corresponding approximate standard deviations in dimensions along the structre, taken from

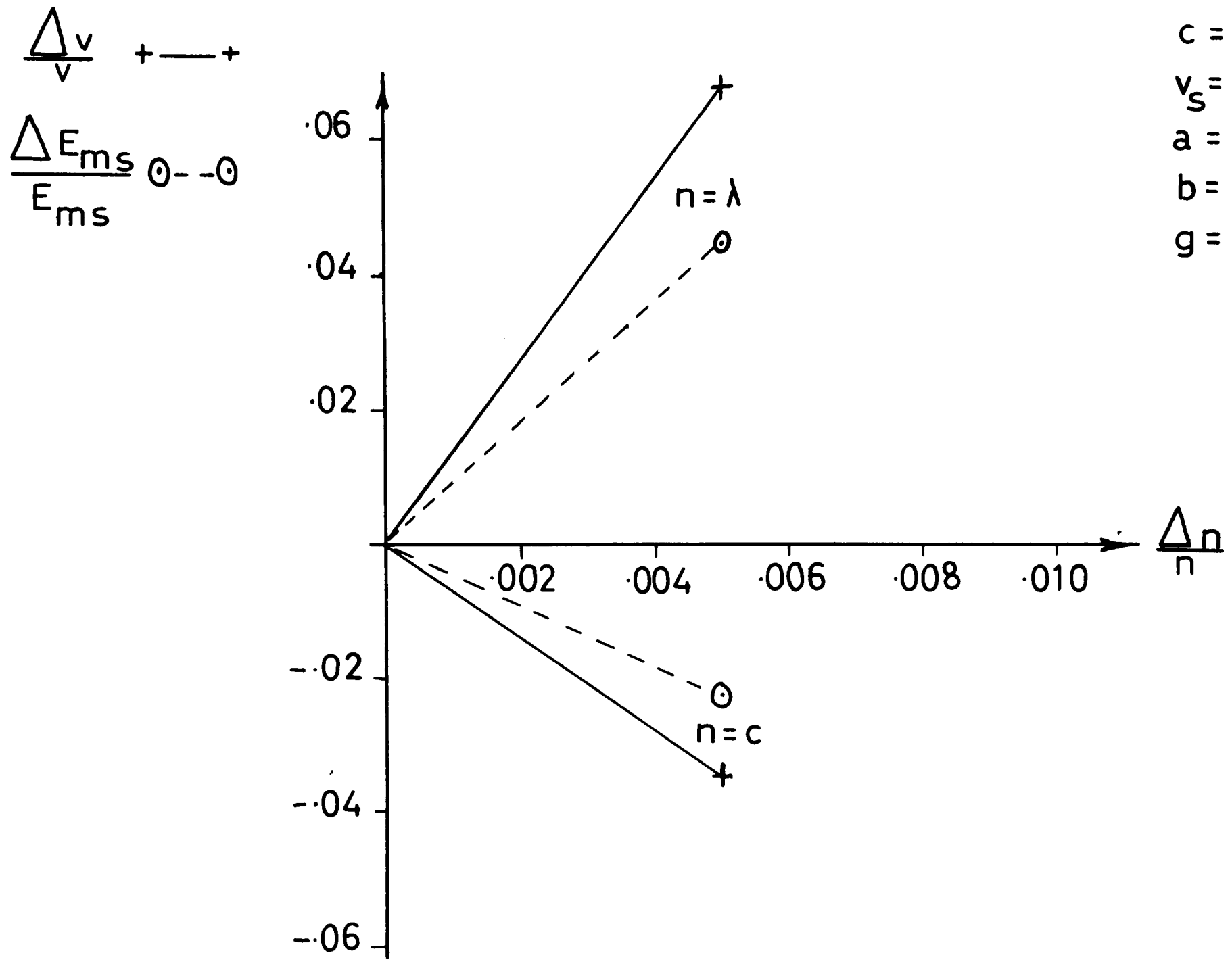


FIG. 38. PERTURBATION RESULTS: DISCRETE DISC THEORY

Figs. 36, 37 and 38, are set out below:

For	$\sigma_{v_s} = 0.02\ v_s$	For	$\sigma_{E_{ms}} = 0.2\ E_{ms}$
	$\sigma_a \approx 0.012a$		$\sigma_a \approx 0.13a$
	$\sigma_b \approx 0.0074b$		$\sigma_b \approx 0.08b$
	$\sigma_c \approx 0.0025c$		$\sigma_c \approx 0.031c$

It is clear that excessive perturbations in phase velocity are the more difficult to avoid, and that the waveguide tube diameter (disc O.D.) is the dimension requiring the highest accuracy. The errors were introduced in Section 4.6 at 1 cm intervals corresponding to 1 disc per cm, whereas in the main section of the linac there will be 3 or 4 discs per cm. It is not completely clear how this will effect the integrated particle motion, but in a strictly statistical sense σ decreases as the square root of the number of samples, and it should therefore be a reasonable approximation to allow an increase in dimensional accuracy by a factor equal to the square root of that by which the number of samples has increased. Taking this factor to be $\sqrt{3}$ we find that

$$\sigma_a \approx 0.021a$$

$$\sigma_b \approx 0.013b$$

$$\sigma_c \approx 0.0043c$$

In practical terms these standard deviations imply the following approximate dimensional tolerances:

$\pm$ 0.04 mm in a, $\pm$ 0.01 mm in 2g and 2h,

and $\pm$ 0.0025 mm in c

In view of the work described in Section 5.2.7, with care in machining, it should be just possible to achieve these dimensional accuracies.

By a similar method we find that the tolerable standard deviation in K for the discs is about 0.009, so that the manufacturer's quoted maximum variation of $\pm$ 0.5% in K throughout a batch of discs (even if not fired together) should be acceptable.

Once the R.F. power has built up along the linac there should be no difficulty in maintaining the source magnetron frequency within tolerable limits. The perturbation theory shows that a 25 Mc/s change in frequency produces a change of only 2% in synchronous wave velocity.

7.3.4 Design Procedure for Main Section

In this section we shall proceed from the results obtained for Cavity II in Section 7.2.2 to a dimensional design curve for the main section of the linac by employing theoretical and experimental perturbation procedures. The most important object of the work is attainment of the desired phase velocities in the structure at the design wavelength.

The first step was to linearly scale the dimensions of Cavity II with wavelength so that βL, which equalled $\pi/3$ at 13.70 Gc/s in Cavity II, would be the same value at 16.45 Gc/s (1.823 cm) in a new cavity. This gave $2g = 0.83$ mm, $2c = 10.4$ mm and $2a = 3.3$ mm. The hole diameter had already been set at a minimum of 4 mm for the main section, and it was decided that the disc thickness should be set at 0.8 mm.

The latter choice was made to lessen the chance of an unwanted half-wavelength resonance occurring within a disc. Such a resonance could occur in a disc of thickness 0.9 mm, of diameter about 10 mm, and in which K was about 100, when the free space wavelength was 18 mm. For, inside the disc propagation would be by almost plane waves, and the wavelength would be about 1.8 mm.

In Section 7.2.2 it became apparent that the discrete disc theory gave the more accurate solution to the dispersion equation when the hole size was small, i.e. at points in the main accelerating section. Therefore, the discrete disc theory was normally used for further computation in the main section, but parallel computation using the anisotropic theory was usually carried out as a check. Accordingly, perturbation theory was used* to determine that by increasing c from 0.520 cm to 0.547 cm we could annul the deviation from linear frequency scaling caused by setting 2a to 4 mm and 2g to 0.8 mm. At the $\beta L = \pi/3$ point in Cavity II, v_s equalled 0.815c. If we do not change b in scaling to 16.45 Gc/s the value of v_s should become 0.791c at $\beta L = \pi/3$. Because we wish our experimental cavity to represent a point in the transition region between buncher and accelerator proper where $v_s \approx 0.75c$, we increase b from 0.333 to 0.347 in accordance with the equation for $\beta L = \pi/3$,

$$b = \frac{12g}{\lambda v_s}$$

to give $v_s = 0.753$ at $\lambda = 1.823$ cm.

---

* In perturbation calculations, linear relations were assumed to hold and the following straightforward equation was used:-

$$\Delta x_1 = \frac{2x_1 \alpha \Delta y_1}{y_1 + y_2 - \alpha \Delta y_1} \quad \text{where } \alpha = \frac{\Delta x/x}{\Delta y/y}$$

The new cavity dimensions were then as follows:

$c = 0.547$ cm $\qquad$ $a = 0.2$ cm

$b = 0.347$ $\qquad$ $g = 0.04$ cm

A six titania disc cavity was built to these dimensions by the shrunk-on tube method. This particular cavity was the first to be made by this method and, for experimental reasons, was made up of four sections. Three sections were single integral ring-and-spacers, and the fourth comprised three discs in a copper tube. The dispersion curve (shown in Fig. 42) was determined by incorporating the cavity in the circuit of Fig. 23 and using the test methods described in Section 5.3.3 to locate the E_{01n} resonances from n = 0 to n = 3. Small coaxially-fed probes were used as couplers, and the perturbations in resonant frequency due to coupling were found to be negligible.

The $\beta L = \pi/3$ resonance occurred at 16.08 Gc/s ($\lambda = 1.867$ cm) giving $v_s = 0.742$ instead of 0.753. In view of the large changes in dimension which had been made and which could have led to errors in the perturbation theory, this disparity was not thought to be serious. It was inferred from perturbation theory that v_s was 0.753 at $\lambda = 1.869$ cm and slightly more than six discs per wavelength. Although it was not necessary for βL to be exactly $\pi/3$ when the velocity and frequency were as desired, the proximity of the $\pi/3$ resonance in an experimental cavity to the designed value of wavelength improved the accuracy of theoretical perturbation computations. In the case of the present cavity βL was only about 1% less than $\pi/3$ when v_s equalled 0.753.

The next step was to reduce c slightly so that the phase velocity would equal 0.753c at a wavelength of 1.823 cm instead of 1.869 cm. Perturbation theory was again used and a three disc cavity was constructed with c equal to 0.530 cm and other dimensions the same as those of the previous cavity. The $\pi/3$ resonance was found to occur at 16.55 Gc/s (1.812 cm) giving $v_s = 0.763$. Perturbation theory showed that for this cavity $v_s = 0.753$ at $\lambda = 1.810$ cm.

We had now reached the point where the results were within one or two per cent of their design figures. As we converged on the design figures the experimental difficulty of making precise measurements became greater. It was realised that greater care was now called for both in cavity fabrication and in frequency measurement. To these ends several steps were taken. Mechanical tolerances were reduced to the following values:

2a	:	$\pm$ 0.004 mm
2g	:	$\pm$ 0.005 mm
Disc Diameter	:	$\pm$ 0.0025 mm
Tube Diameter	:	$\pm$ 0.002 mm
Tube Length ($\approx$ 1.5 cm)	:	$\pm$ 0.005 mm
b	:	$\pm$ 1%

The precision wavemeters used in all experiments were recalibrated by the National Physical Laboratory so that they were effectively accurate to the nearest megacycle. New test cavities were made by the improved method described in Section 7.3.2 with up to 25 discs in a single tube. A new low power cavity test rig was constructed with facilities for end-wall hole coupling via tunable

'door knob' transformers, and with provision for perturbing bead experiments, including calibration in the 0.750" diameter cylindrical shell of the rig (see Figs. 26 and 39).

A check was carried out on the agreement between experiment and the two perturbation theories for the variation of λ with c for constant v_s. For the last two cavities we have,

$c = 0.547$ cm $\qquad\qquad$ $c = 0.530$ cm

and, for $v_s = 0.753$,

$\lambda = 1.869$ cm $\qquad\qquad$ $\lambda = 1.810$ cm

These two values of λ were themselves deduced from perturbation theory, but they should be quite reliable because of the reasonably close agreement between experiment and both theories over the determination of group velocity (see Section 7.2.2). These figures give the following result.

	Experiment	Discrete Disc Theory	Anisotropic Theory
$\frac{\Delta_{\lambda/\lambda}}{\Delta c/c}$	0.986	0.548	1.03

Clearly, the anisotropic theory gives the more accurate value for the rate of change of wavelength with disc diameter for constant v_s.

The final adjustment to c in the sequence under discussion was intended to make $\lambda = 1.823$ cm with six discs per wavelength. Taking $\Delta\lambda/\lambda$ divided by $\Delta c/c$ as the mean of the values given by experiment and anisotropic theory, it was found that c should be increased to 0.533 cm.

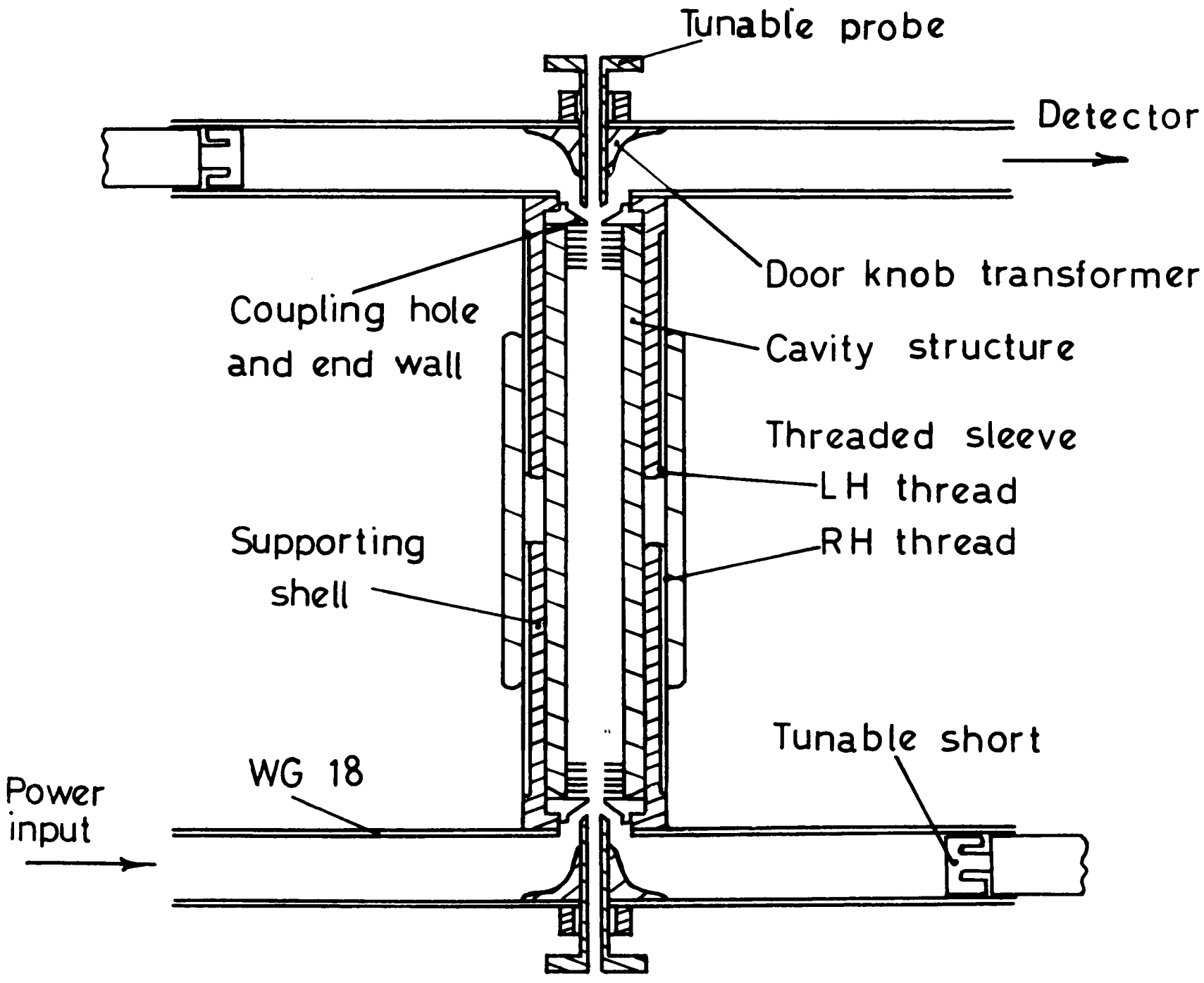


FIG. 39. LOW POWER CAVITY TEST RIG

The effect of this increase in c was not immediately investigated experimentally because it was felt that the reasonable degree of success with c = 0.530 cm afforded the opportunity to construct a cavity to give information about the control we can exert over v_s by varying b. A second sequence of experiments was therefore begun.

The first step in the second series of experiments was to decrease b and aim for a phase velocity of 0.85c at 1.823 cm and $\beta L = \pi/3$. By increasing c to 0.533 cm and keeping b at 0.347 we have changed the value of v_s at $\beta L = \pi/3$ from 0.763 to 0.757. From discrete disc theory it was found that the theoretical value for b was then 0.311. Hence,

$$\frac{b_{experimental}}{b_{theoretical}} = \frac{0.347}{0.311} = 1.116 \qquad (7.14)$$

The theoretical value for b when $v_s = 0.85c$ at $\lambda = 1.823$ cm was 0.294 and so it was thought reasonable to set the practical value of b for the new cavity at 1.116 x 0.294 = 0.328. The variation of v_s with b as given by discrete disc theory for c = 0.533 cm and $\lambda = 1.823$ cm is plotted in Fig. 40.

The fabrication technique had been so improved at the time this cavity was designed that a 25 titania disc section was thought to be a practical proposition. Because the discs were to be unglazed and the feasibility of cellulose acetate spacers had not been fully investigated, Duralumin spacers were specified. The important

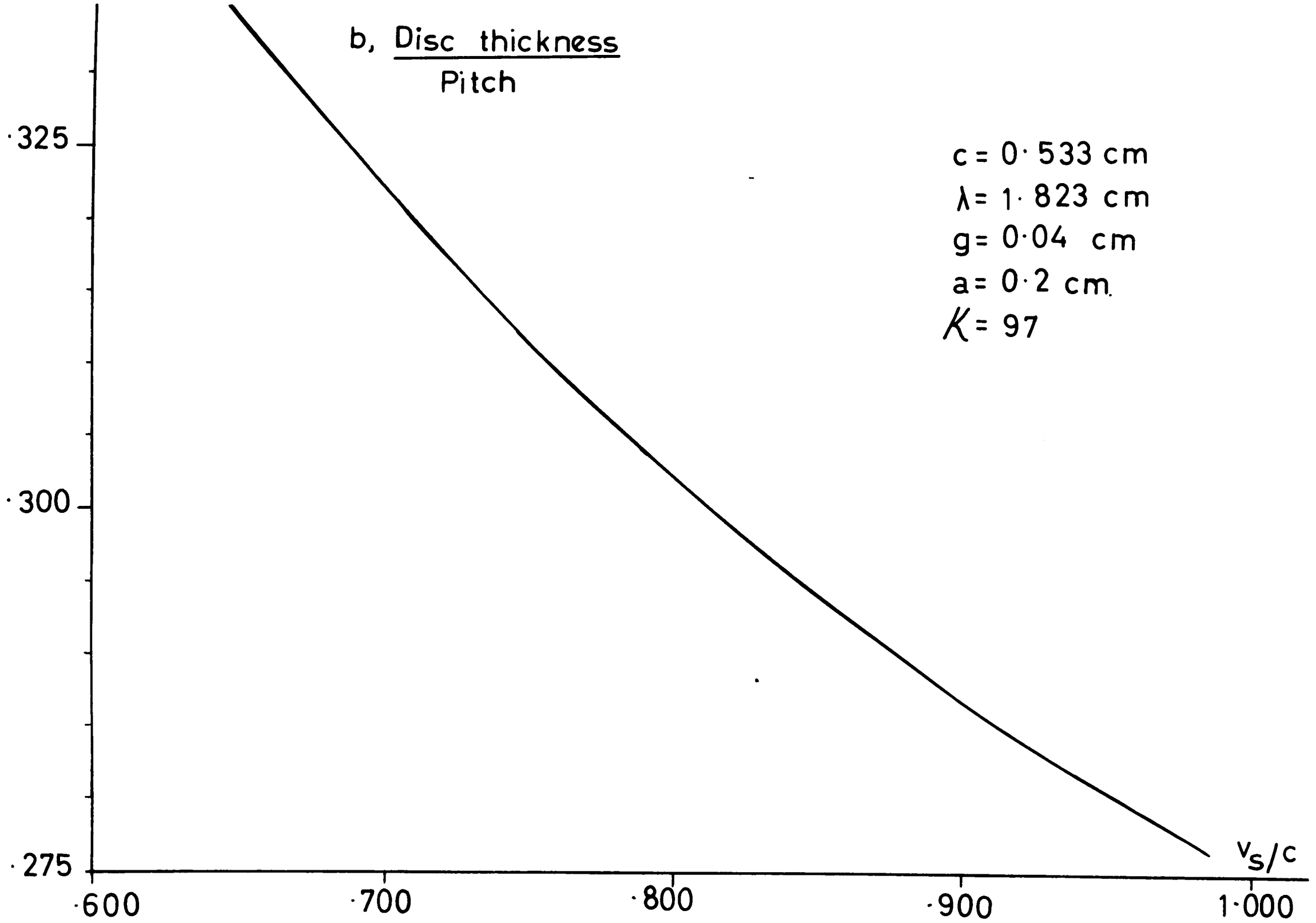


FIG. 40. VARIATION OF v_s WITH b : DISCRETE DISC THEORY

cavity dimensions were as follows:

c = 0.533	± 0.0001	cm
b = 0.328	± 0.002	
a = 0.2	± 0.0002	cm
h = 0.082	± 0.0003	cm
g = 0.04	± 0.0002	cm
Cavity Length = 6.1000	± 0.0005	cm
Tube O.D. = 0.750	+ 0.000 − 0.0015	inches
Tube I.D. = 1.0645 (after silver plating)	± 0.0002	cm

The waveguide tube was of brass, and after it had been fully machined the inside surface was uniformly electroplated with a layer of silver 0.00025 cm thick prior to the heat-shrinking process. The finished cavity is depicted in Fig. 41.

The experimentally determined dispersion curve for the 25 disc section is shown in Fig. 44. It was found that the nearest resonance to $\beta L = \pi/3$ was, as expected, the E_{018} at 16.415 Gc/s (1.825 cm) where $v_s = 0.835c$. Using the mean of the discrete disc and anisotropic theoretical values for $\Delta v/v$ divided by $\Delta\lambda/\lambda$, viz. 12.5, the value of v_s at $\lambda = 1.823$ cm was computed to be 0.825c, to be compared with the designed value of 0.850c. The disparity was unexpectedly large and so the value of the 'b ratio' (equation 7.14) was examined. The 'b ratio' of 1.116 was derived from the c = 0.530 cm cavity where b was thought to be 0.347. The cavity dimensions were checked and it was found that b was in fact 0.350. The $\pi/3$ resonant frequency was also carefully checked using improved R.F. couplers and the newly calibrated



Approximately Full Size

25 Titania Disc

Test Section

Fig. 41

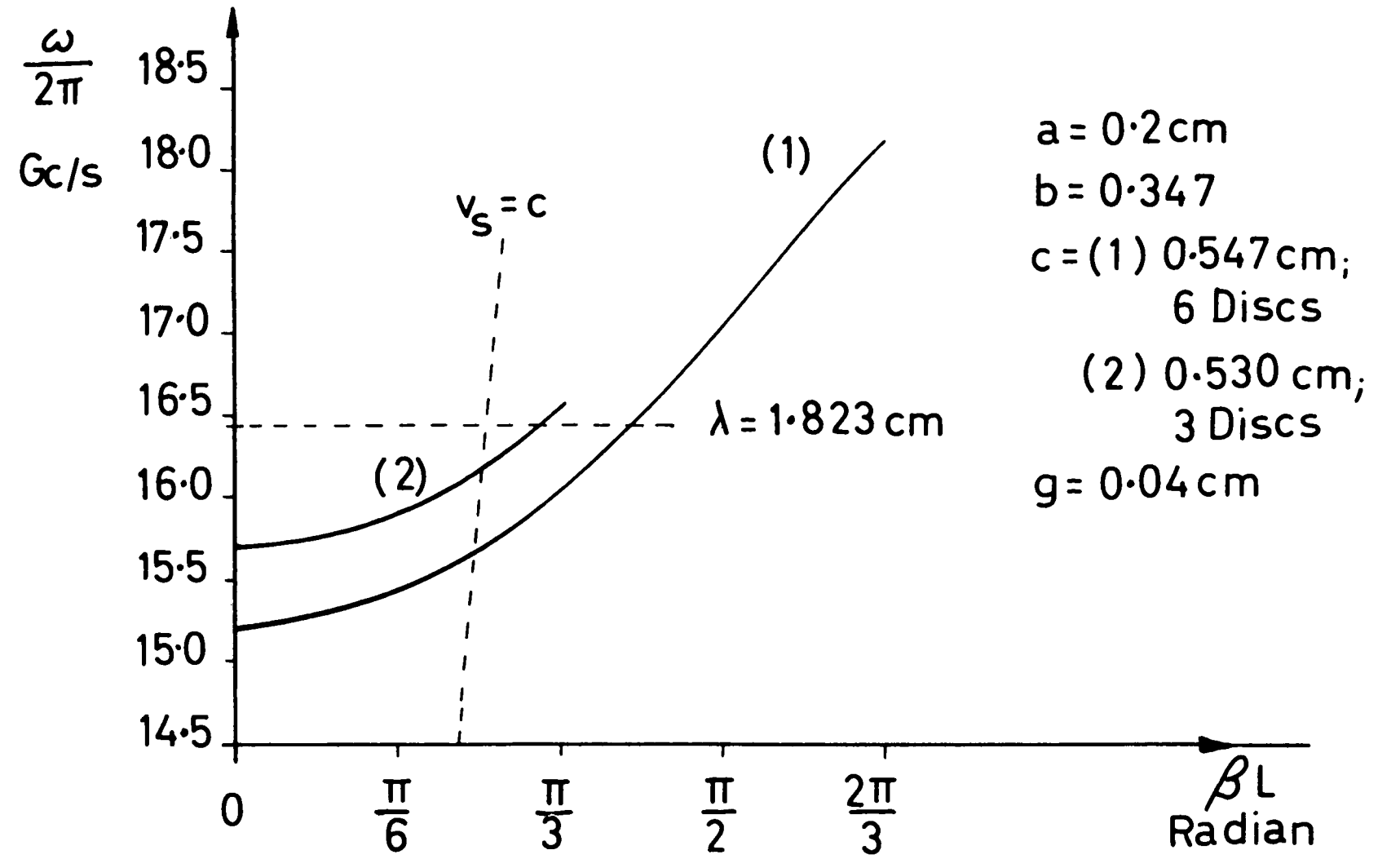

ω/2π
Gc/s
18·5
18·0
17·5
17·0
16·5
16·0
15·5
15·0
14·5
$v_s = c$
(1)
(2)
λ = 1·823 cm
a = 0·2 cm
b = 0·347
c = (1) 0·547 cm; 6 Discs
(2) 0·530 cm; 3 Discs
g = 0·04 cm
0
π/6
π/3
π/2
2π/3
βL
Radian

FIG. 42.

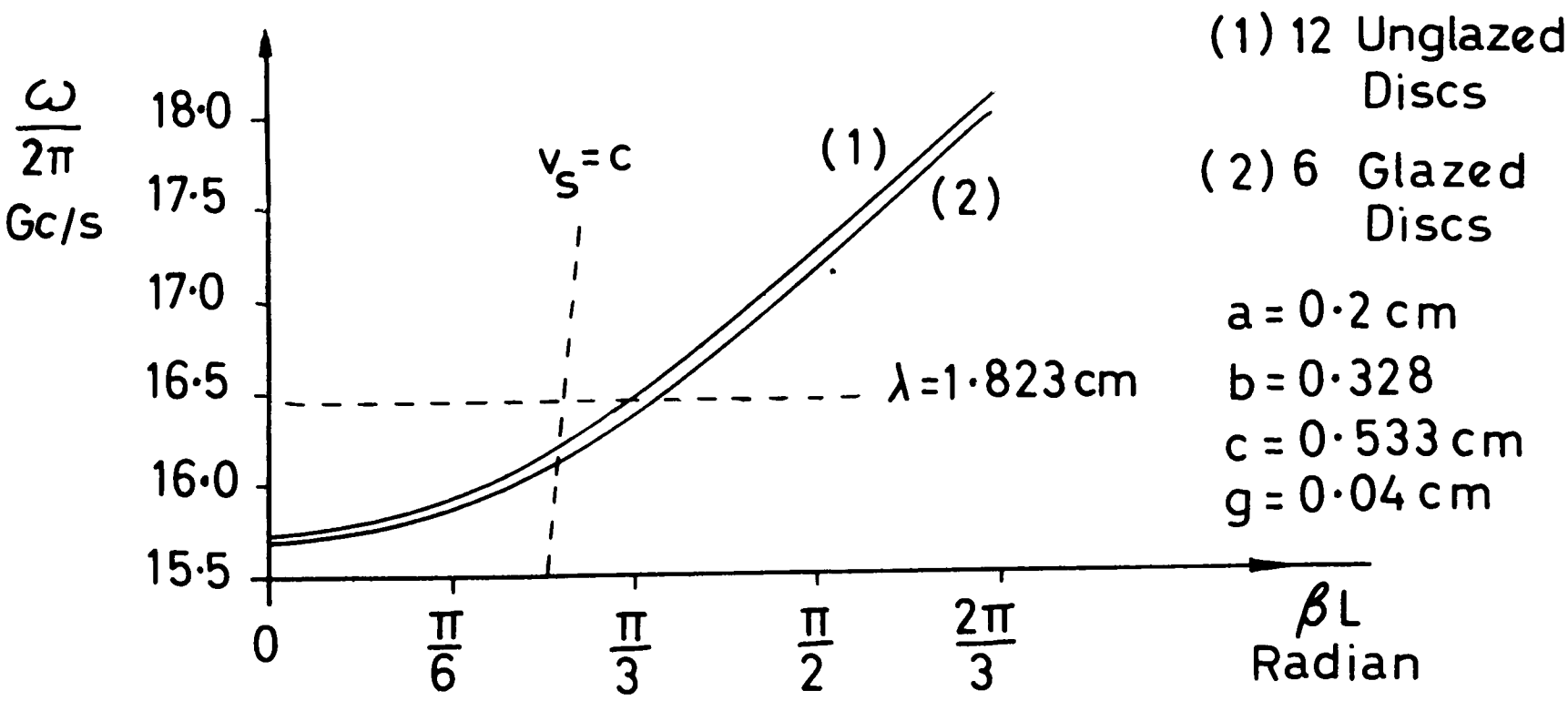

ω/2π
Gc/s
18·0
17·5
17·0
16·5
16·0
15·5
$v_s = c$
(1)
(2)
λ = 1·823 cm
(1) 12 Unglazed Discs
(2) 6 Glazed Discs
a = 0·2 cm
b = 0·328
c = 0·533 cm
g = 0·04 cm
0
π/6
π/3
π/2
2π/3
βL
Radian

FIG. 43.

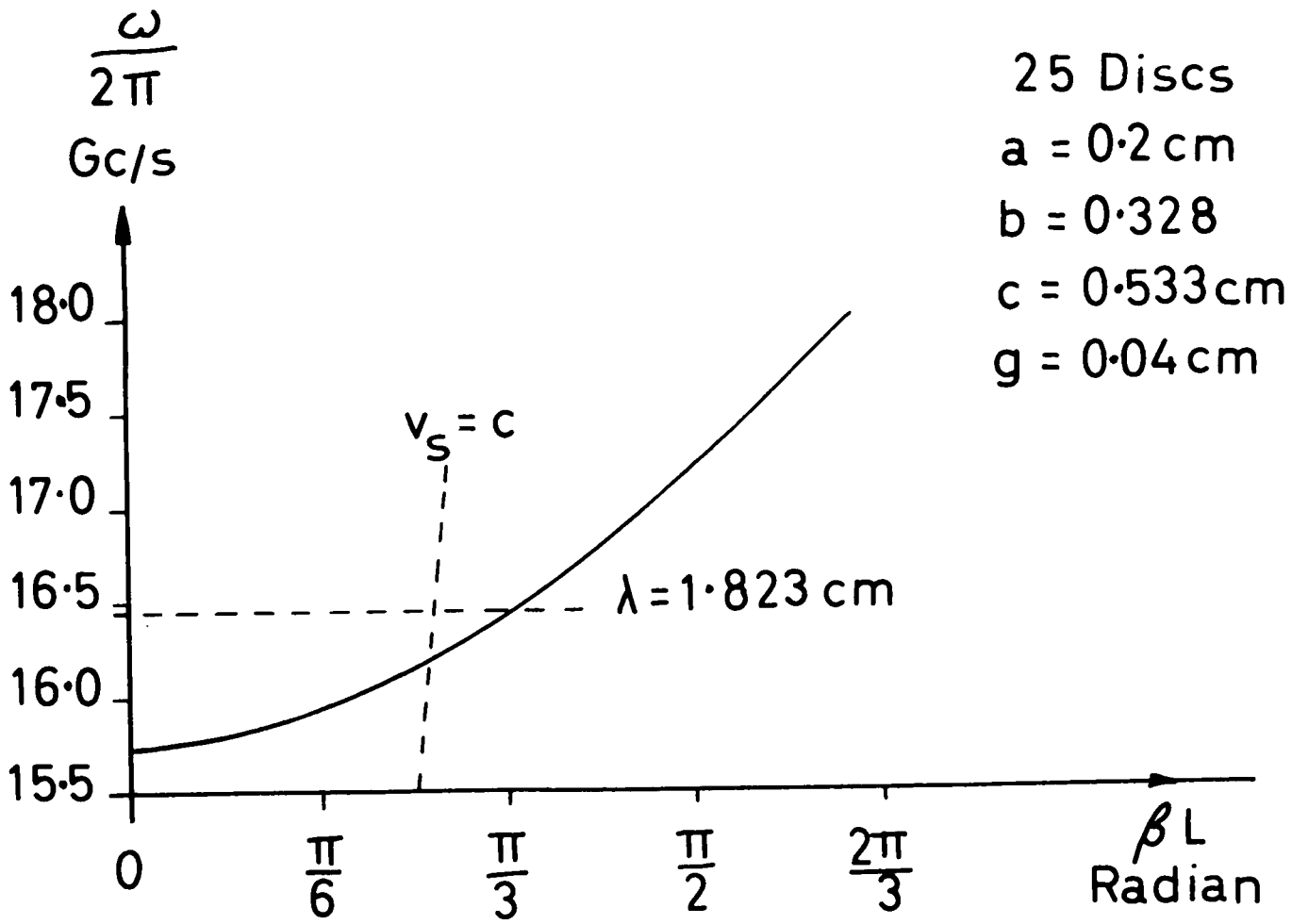

ω/2π
Gc/s
18·0
17·5
17·0
16·5
16·0
15·5
$v_s = c$
λ = 1·823 cm
0
π/6
π/3
π/2
2π/3
βL
Radian
25 Discs
a = 0·2 cm
b = 0·328
c = 0·533 cm
g = 0·04 cm

FIG. 44.

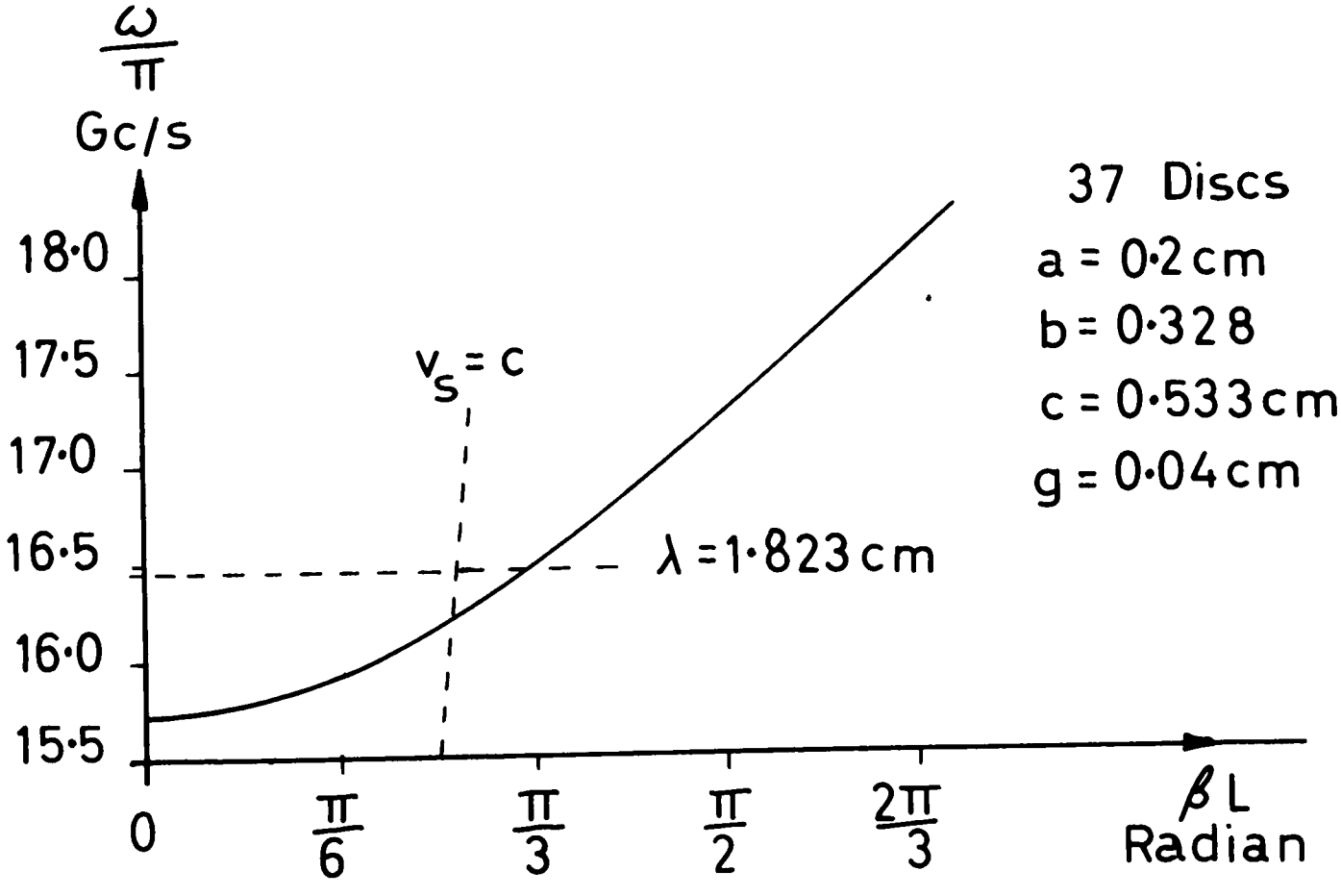

ω/π
Gc/s
18·0
17·5
17·0
16·5
16·0
15·5
$v_s = c$
λ = 1·823 cm
0
π/6
π/3
π/2
2π/3
βL
Radian
37 Discs
a = 0·2 cm
b = 0·328
c = 0·533 cm
g = 0·04 cm

FIG. 45.

wavemeter. The resonance was located at 16.52 Gc/s (1.817 cm) as measured previously. Perturbation theory then gave $v_s = 0.728c$ at $\lambda = 1.823$ cm corresponding to a theoretical value of b of 0.3157 (see Fig. 40). Hence the 'b ratio' was 1.108 rather than 1.116 as used in the design of the 25 disc cavity in which, therefore, v_s should equal $0.837c$ at $\lambda = 1.823$ cm. Thus the experimental figure of $0.825c$ was well within 2% of the design value. The experimental value of the 'b ratio' was 1.101.

The next step was to confirm the results obtained with the 25 disc cavity using other sections of various lengths but with the same value of b. Two six disc sections with nominally identical dimensions were constructed using cellulose acetate spacers. As with the 25 disc cavity, several experimental measurements were made on both cavities over a period of weeks before the results were averaged. It was found that the mean $\pi/3$ resonant frequencies were 16.478 Gc/s and 16.475 Gc/s giving $v_s = 0.821c$ at $\lambda = 1.823$ cm and a 'b ratio' of 1.098 for both cavities. The good agreement between the results was encouraging.

Further experiments with the two six disc cavities together to form a 12 disc section, and with the 25 disc section added to form a 37 disc section, gave the dispersion curves shown in Figs. 43 and 45. The mean value of the 'b ratio' for the 6, 12, 25 and 37 disc section experiments was 1.096.

For successful high-power operation it will probably be necessary to glaze the titania discs in the structure. A further series of low

power experiments were therefore planned to investigate the influence on the 'b ratio' of glazing the discs. The first cavity was of six titania discs coated with the 'new glaze' of Section 5.2.3. The glaze thickness was not included in g, the disc thickness, and the cellulose acetate spacers were made thinner to keep b at 0.328. The mean value of a, the unglazed hole radius, was slightly increased to 0.2009 cm to maintain a (glazed) hole radius of 0.2 cm after a coating of 0.0009 cm had been applied.* The dispersion curve was measured (see Fig. 43) and after allowing for the increased value of a the value of v_s at $\lambda = 1.823$ cm was found to be 0.749c corresponding to a $\pi/3$ resonance at $\lambda = 1.833$ cm and a 'b ratio' of 1.053.

Because of practical delays in obtaining a further batch of several dozen dimensionally acceptable glazed discs, it was decided to draw up a main section design on the basis of results to date, and to carry out a second series of high power tests on coated discs (see Section 7.4).

Included in the above experiments were measurements of Q_o and r_{sh}/Q_o at the resonances close to $\lambda = 1.823$ cm using the methods of Section 5.3.3. The group velocity was deduced from the slope of the dispersion curve, and the loss length was computed from equation (7.10). The series impedance was then known since $r_{sh} = \ell_o r_{se}$. Table 8 summarises the results obtained for the cavities mentioned above and four others to be discussed in the next section. Several trends are apparent in the Table. The values of r_{sh} were markedly lower, probably

* In fact the coating was ground to a thickness of about 0.0006 cm.

Cavity		1	2	3	4	5	6	7	8	9
Coating		None	None	None	Glaze	P.T.F.E	None	None	None	None
No. of Discs		37	25	12	6	6	6	55	6	6
No. of Sections		3	1	2	1	1	1	6	1	1
Tube Material		SPB	SPB	SPB	OFHC	OFHC	OFHC	Mixed	SPB	SPB
v_s/c	Exp.	0.797	0.825	0.815	0.749	-	0.821	0.818	0.821	0.821
'b ratio'		1.084	1.101	1.096	1.053	-	1.098	1.097	1.098	1.098
v_g/c	Theo.	0.0590	0.0611	0.0602	-	-	0.0599	0.0606	0.0608	0.0608
	Exp.	0.0679	0.0646	0.0715	0.0737	-	0.0748	0.0627	0.0748	0.0750
Q_o	Theo.	8420	8100	8250	-	-	-	8175	8150	8150
	Exp.	1650	1860	1650	1300	1650	1750	1750	1650	1650
r_{sh}(T.W.)	Theo.	437	455	448	-	-	-	450	452	452
$M\Omega/m$	Exp.	-	590	45.9	23.1	28.4	32.6	58.8	29.4	28.4
r_{se}(T.W.)	Theo.	303	316	310	-	-	-	312	314	314
$M\Omega/m^2$	Exp.	-	169	132	81.8	-	85.7	184	79.9	76.9
l_o	Theo.	1.444	1.437	1.440	-	-	-	1.439	1.438	1.438
m.	Exp.	0.340	0.349	0.348	0.279	-	0.380	0.319	0.368	0.370
c	cm	0.5330	0.5330	0.5330	0.5330	0.5330	0.5326	0.5330	0.5330	0.5330
a	cm	0.2000	0.2000	0.2000	0.2009	0.2000	0.2076	0.2000	0.2000	0.2000

Notes:
1) SPB = Brass, silver plated to a thickness of 0.00025 cm (5 skin depths).
2) OFHC = Oxygen-free high conductivity copper.
3) 'b ratio' = $b_{experimental}/b_{theoretical}$ for same value of v_s.
4) v_g/c Theo. = Theoretical value of v_g corresponding to experimental value of v_s.
5) Theoretical values are given by the discrete-disc theory using the accepted bulk value of the resistivity of copper (1.7421×10^{8} ohm.metre)
6) Titania discs are used, b = 0.328 and g = 0.08 cm in all cavities
7) λ = 1.823 cm for all practical purposes

TABLE 8

because of relatively high end-wall losses when the cavities were shorter than about four guide-wavelengths, and they were no higher than those of the ring-and-spacer cavities discussed in Section 7.2. The values of r_{se} were four or five times higher than those in Section 7.2, due mainly to the reduction in c from 0.622 cm to 0.533 cm. It is reasonable to scale up r_{sh} for the glazed 6 disc cavity by a factor equal to the ratio of r_{sh} for the unglazed 25 and 55 disc cavities to r_{sh} for the unglazed 6 disc cavities. This gives r_{sh} = 47.1 MΩ/m for a long glazed disc structure. Similarly r_{se} = 187 MΩ/m^2 and ℓ_o = 0.251 m. We then see that a power flux of about 200 kW at the output from the bunching section, which should easily be attainable, would give a peak axial electric field E_{mso} of 6 MV/m as planned.

We shall now solve equation (4.41) to give us the variation of phase velocity throughout the main accelerating section which will ensure that the wave and the electron bunch keep in step. Two solutions will be given. One will take into account beam loading and the other will not. The first solution is perhaps unnecessary because the trajectory computations of Section 4.5 showed that when the wave velocity variation derived from equation (4.41) for synchronism without beam loading is used with 75 mA beam loading, then the bunch does not spread in phase or energy but merely slips back into a phase of higher electric field, and the mean energy drops by only 12%. However, the computation for synchronism with beam loading gives a lower limit to the output energy which can be expected if the design for no beam loading is used in the practical structure. To clarify this point we refer to Figs. 16 and 17. With

no beam loading U_{sf}, the output energy of the phase stable particle is 2.598 MeV when the bunch and wave are in exact synchronism. Using the same velocity variation U_{sf} is 2.364 MeV for I = 75 mA. Using the velocity variation for exact synchronism with I = 75 mA results in U_{sf} = 2.008 MeV. We shall therefore use the velocity variation for I = 0 in the practical structure.

In solving equations (4.39) and (4.40) using the prescribed fields and velocities for the buncher (see Appendix II for detail) ϕ_{so} the phase of the stable particle emerging from the buncher was found to be 0.834 radian. In solving equation (4.41) for the phase stable particle ϕ_s was set to this value. The other parameters were E_{mso} = 6 MV/m, λ_o= 0.251 m and r_{sh} = 47.1 MΩ/m for the glazed disc structure, and E_{mso} = 6 MV/m, λ_o= 0.336 m and r_{sh} = 58.9 MΩ/m for the unglazed disc structure, in accordance with the results shown in Table 8. The variation of beam energy for I = 0 and I = 25 mA along the entire structure, and the variation of v_s for I = 0 along the main section are shown in Fig. 46.* Numerical details are given in Appendix II.

Referring to Table 8 we note that the 'b ratio' does not vary systematically with structure length, and that deviations from the mean value for the unglazed cavities 1, 2, 3, 8 and 9 do not exceed 1%. We should therefore not introduce much error by using the value for

---

* Taking I = 75 mA as previously gave an unacceptable output energy of only 1 MeV (maximum) for the glazed disc structure.

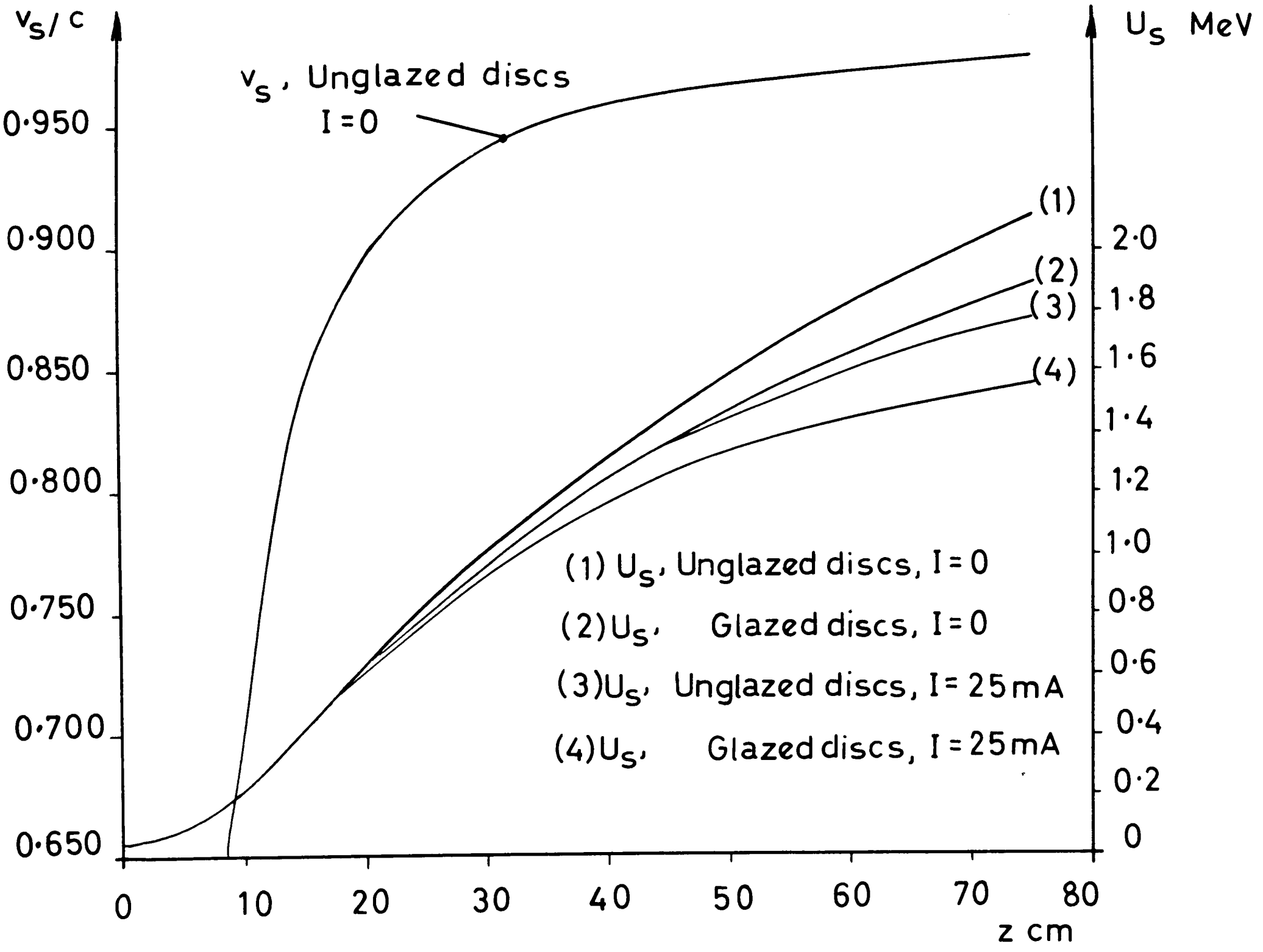


FIG. 46. VARIATION OF v_s AND U_s: SYNCHRONOUS CONDITIONS

the only glazed disc cavity so far tested in determining the practical variation of b (b_{exp}) along a glazed disc structure. Fig. 47 shows the resulting variation of b_{exp} along both glazed and unglazed structures for synchronism with $\lambda = 0$ and $I = 25$ mA. The numerical details are again given in Appendix II.

To summarise this section, we may say that the variation of the ratio of disc thickness to pitch which should result in the acceleration of the electron beam without debunching up to about 1.7 MeV has been calculated for the main accelerating section of the structure. The corresponding disc radius is 0.533 cm, the hole radius is 0.2 cm, and the disc thickness is 0.08 cm. The phase change per periodic length is maintained at about $\pi/3$ radian. To ensure that there will be a smooth variation in phase velocity it is suggested that the stepped decrements in b should occur at intervals of one periodic length. Further comment on the low power cavity results is given below.

7.3.5 Summary of Low Power Test Cavity Results

The results shown in Table 8 were obtained using the experimental methods described earlier in the thesis. We shall now discuss one or two special features about the results themselves.

Shunt impedance measurements were made by measuring δf_m the maximum resonant frequency perturbation caused by the axial traverse through the cavity of a metallic bead with an α of 7.76×10^{-21} $m^2.sec.ohm^{-1}$ (see Section 5.3.3 and Fig. 27). The expectation that the amplitudes of second and higher space harmonics in the cavities would be negligibly small because of the relatively high number of

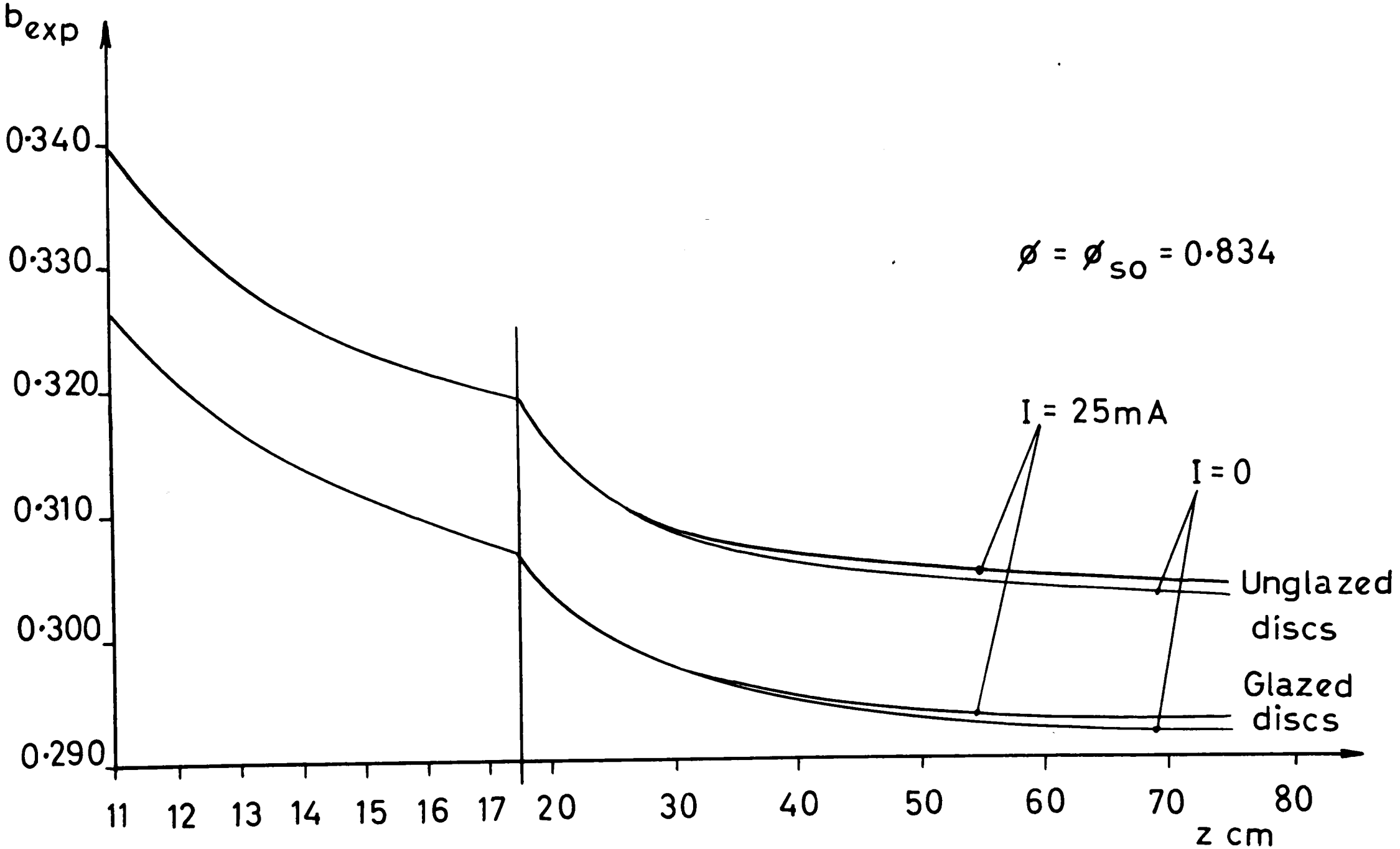


FIG. 47. VARIATION OF DISC THICKNESS / PITCH, SYNCHRONOUS CONDITIONS

periodic obstacles per wavelength (six) was confirmed by examining the form of the axial electric field. A plot of a typical axial field distribution is shown in Fig. 48. The expected increase in in and near the holes in the discs is apparent, and clearly the higher space harmonics ($\beta L = \pi/3 + 2\pi n$) are dominated by the large amplitude of the fundamental ($\beta L = \pi/3$). We are therefore justified in using δf_m directly when deducing the value of r_{sh}. The theoretical determination of space harmonic amplitudes has been discussed by Bell and Walkinshaw[65].

Cavity No. 6 was constructed because a large batch of titania discs delivered from the manufacture was found to have unacceptable hole ovality. Grinding the holes until they were truly circular naturally resulted in oversize hole diameters, and the extent to which this could be offset by slightly reducing the disc diameter needed investigating. The holes were opened up to 0.2076 ± 0.0002 cm radius and the disc radii were reduced to 0.5326 ± 0.0001 cm in accordance with perturbation theory. This procedure was quite successful in view of the close agreement between the values of v_s at $\lambda = 1.823$ cm for this cavity and cavities 8 and 9.

The P.T.F.E. coated disc cavity is discussed in Section 7.4.2 but it is worth noting here that its shunt impedance was not significantly different from those of the unglazed disc cavities. For this reason it was included in the multi-section cavity No. 7.

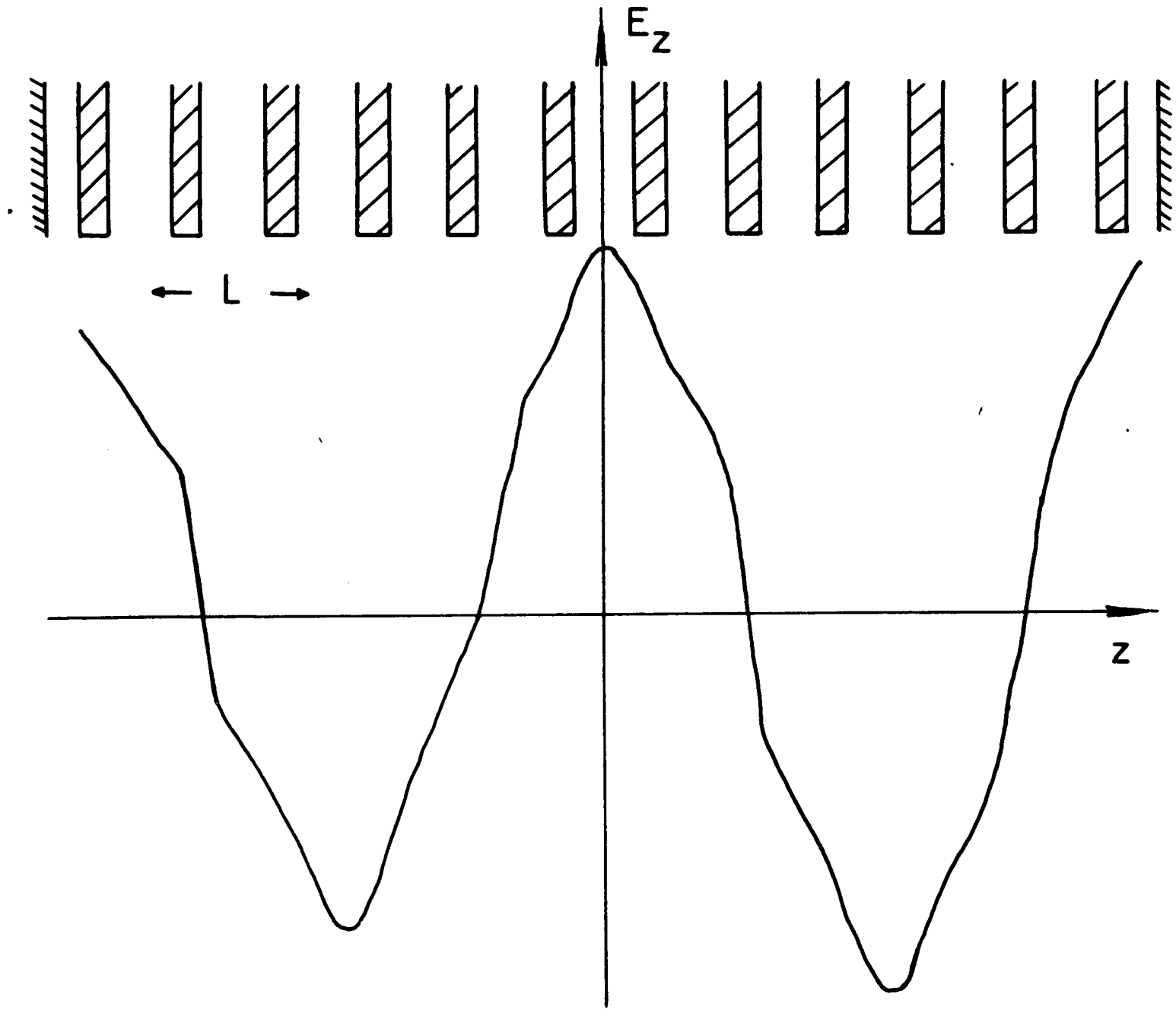


FIG. 48. AXIAL FIELD MEASURED IN 12 DISC CAVITY

$$\beta L = \frac{\pi}{3}$$

Even in the long cavities where the effects of end-wall losses should be negligible, the measured values of Q_o were disappointingly low. No satisfactory explanation has been found for the large disparity between the theoretical and experimental values of Q_o and r_{sh}. However, two points should be noted here. Firstly, the theories show that about 30% of the ohmic loss occurs in the waveguide walls. Secondly, the value of resistivity used for the wall material (assumed to be copper) in the theoretical calculations was the published bulk value. It is common experience for the apparent resistivity of waveguide at the higher microwave frequencies to be considerably greater than the accepted bulk value.

The measured series impedances were in much closer agreement with the theoretical values than they had been in the early test cavities. The improvement was almost certainly due to the drop in disc radius from 0.622 cm to 0.533 cm. This is a clear demonstration of the fact that r_{se} depends chiefly upon the structural geometry and is not directly dependent upon ohmic losses in the structure.

7.4 High Power Tests : Second Series

The purpose of the second series of high power tests was to examine the behaviour of multi-disc sections of the same dimensions (except length) as those likely to be used in the linac itself. Comment on the results of the tests is left until Section 7.4.3.

7.4.1 Glazed Disc Structure

The structure used for this test was fabricated using the method described in Section 7.3.2. The results of low power tests

with it have been given in the previous section. It contained six titania discs coated with the new glaze discussed in Section 5.2.3, and mounted in an O.F.H.C. copper tube 14.640 mm long. The glaze thickness after grinding and polishing was approximately 0.00075 cm on the disc faces, and 0.0006 cm on the surface inside the hole. After the glazing process the discs were ground to an outside radius of 0.5330 cm with no glaze remaining on the rim.

After being cleaned and dried the cavity was mounted in the high power test rig (see Fig. 21), and the E_{012} mode was identified at low power in the usual way (see Section 5.3.3.1) The maximum frequency perturbation on the bead traverse was 21 Mc/s so that, for $Q_o = 1300$ (from Table 8) and the bead α of 7.76×10^{-21} $m^2.sec.ohm^{-1}$, substitution in equation (5.9) gives

$$E_{zm} = 3.22\ P^{\frac{1}{2}} \times 10^4 \quad V/m \tag{7.14}$$

where P is the power delivered to the cavity and its coupler at critical coupling. As a check we take the value of r_{sh}(T.W.) from Table 8, double it, and substitute in equation (5.12) giving

$$E_{zm} = 3.97\ P^{\frac{1}{2}} \times 10^4 \quad V/m \tag{7.15}$$

since $\ell = 1.464$ cm, and the ordinary resonant cavity shunt impedance is twice r_{sh}(T.W.) and four times r_{sh}(S.W.) (See Footnote on p.105). As the cavity was critically coupled to the input waveguide and the coupling hole was therefore large, we shall use equation (7.14) to evaluate E_{zm}. In high power tests it is better to err on the low side when evaluating the electric field to which the test cavity is being subjected.

The cavity was finally tuned to the mid-band frequency (16.492 Gc/s) of magnetron number 2114 before being fully assembled, evacuated, and incorporated in the high power test circuit shown in Fig. 28.

On the first run P was increased to about 18 kW before the R.F. pulse reflected from the cavity showed any amplitude jitter on the monitoring oscilloscope (see Fig. 29). The power level was then reduced and maintained at 10 kW for approximately 10 minutes. As with the tests described in Section 5.3.4, the R.F. pulse jitter was accompanied by sporadic variations in the ion vacuum gauge and ion pump currents, together with a gradual rise in the average cavity pressure from 10^{-5} torr to 10^{-4} torr over the 10 minute period. The resonant frequency did not alter during this time, and by occasionally pulling the magnetron frequency through the resonance it was observed that the cavity bandwidth was not changing perceptibly. In the light of the first series of tests, it was thought that no serious breakdown in the cavity was indicated.

The test circuit was then rearranged so that the cavity fields might be increased. The main power was monitored by the water calorimeter via a 10 dB directional coupler, and the reflection coefficient of the cavity was monitored by comparing the responses of a pair of balanced crystal detectors arranged as in Fig. 49. The power fed to the cavity was slowly increased to approximately 250 kW but no catastrophic cavity breakdown was observed externally on the oscilloscope traces or vacuum gauges. This high power run lasted

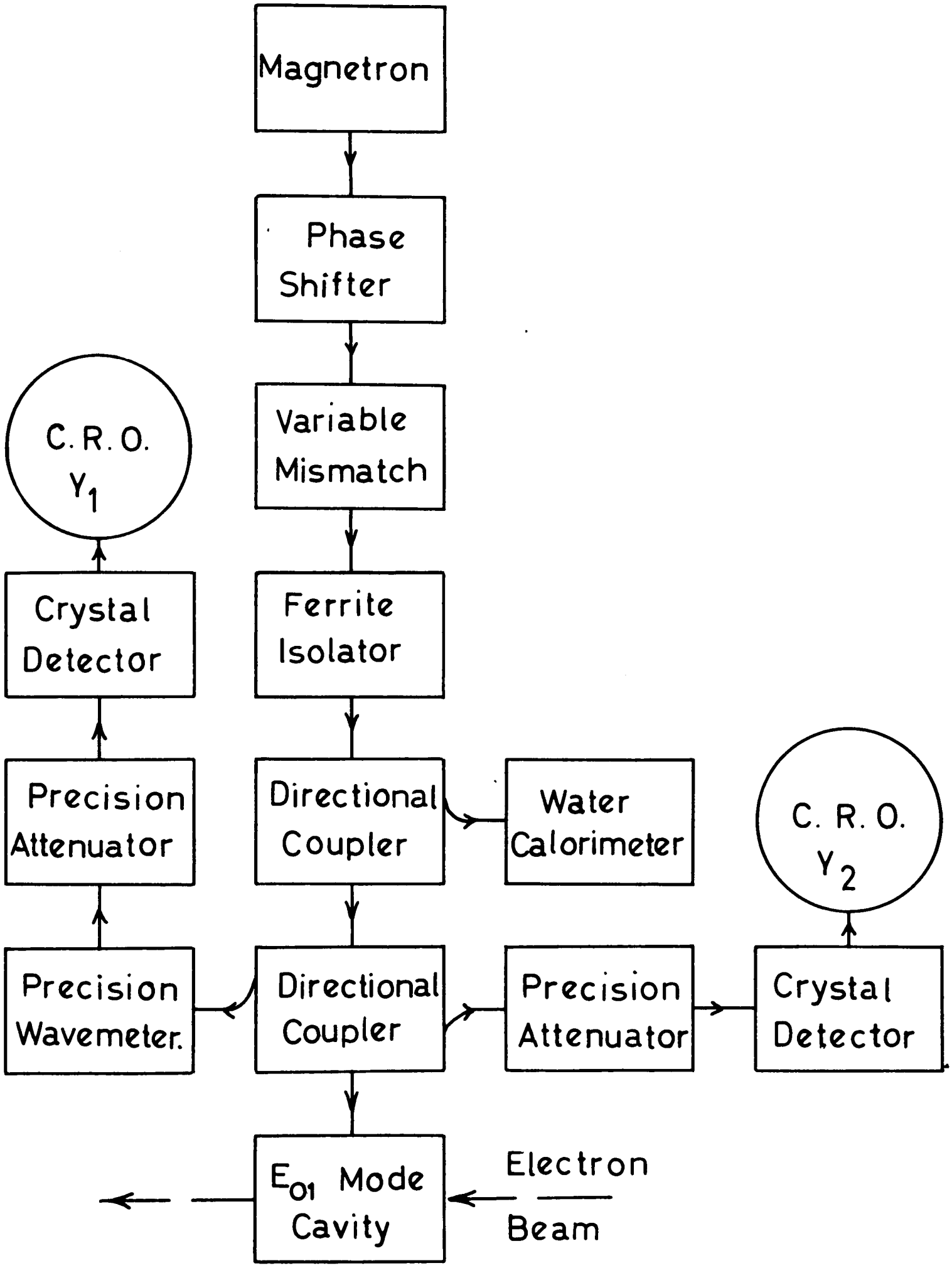

Magnetron
Phase Shifter
Variable Mismatch
Ferrite Isolator
Directional Coupler
Water Calorimeter
Precision Attenuator
Crystal Detector
C. R. O. Y1
Precision Attenuator
Directional Coupler
Precision Wavemeter.
C. R. O. Y2
Crystal Detector
E01 Mode Cavity
Electron Beam

FIG. 49.

for about two hours with a pulse length of 1 μsec and a repetition rate of 500 per second. The cavity pressure rose from about 10^{-5} torr to 10^{-4} torr during the first 30 minutes but then remained fairly steady.

A further test run was carried out with a beam of 25 keV electrons passing axially through the cavity. The electrons were collimated to give an effective beam diameter of about 2 mm, and the current flowing through the cavity was estimated to be 100 mA peak (sychronised with the R.F. pulse). After the beam had been established, the R.F. power was increased slowly from zero. At a level of 150 kW there was a sudden increase in the reflected power from the cavity accompanied by a rapid increase in the cavity pressure. The power was reduced, the electron beam was cut off, and the high vacuum was allowed time to recover. The pumping speed of the getter ion pump used in these experiments falls to almost zero at about 10^{-2} torr. Since the high vacuum did in fact recover within a few minutes, it was concluded that the cavity pressure did not reach 10^{-2} torr during the rapid evolution of gas. The power was then increased and the phenomenon recurred at a slightly higher power level than before. The procedure was repeated and again the threshold power level was found to have increased. The limit was eventually reached at about 200 kW, and on subsequent applications of the R.F. power the threshold progressively decreased to a relatively low level.

The structure was then removed to the low power test rig (Fig. 39) where Q_o and r_{sh}(T.W.) were found to have dropped from 1300 to 990, and from 23.1 MΩ/m to 15.5 MΩ/m respectively. When the

discs were removed from the waveguide tube, the surfaces of two discs which faced one another were found to be badly marked, and on one of them was a relatively large patch of reduced glaze and titania (see Fig. 50a). The dark grey discolouration on the other (Fig. 50b) could be removed by scraping off a thin surface layer. Except for the two facing the copper end walls, the other dielectric surfaces in the cavity were slightly yellower than they were before the high power tests, and there was slight browning around the holes in one or two of the discs. The disc surface facing the input coupling hole was markedly stained brown as in Fig. 30b. A short tuning screw had been inserted through the small probe coupling hole at the opposite end of the cavity, and the end disc surface facing this was also stained brown but over an elliptic rather than circular area centred on the cavity axis. There was very little evidence of rim breakdown on the discs except on the one where the serious surface reduction had occurred (Fig. 50a).

7.4.2 P.T.F.E. Coated Disc Structure

This structure was fabricated in the usual way (see Section 7.3.2), but the cellulose acetate spacers were made slightly thinner to maintain b at 0.328 with a P.T.F.E. surface coating 0.00125 cm thick on the disc faces. Measurements at low power indicated that $Q_o = 1650$ and $r_{sh}(T.W.) = 28.4\ M\Omega/m$ at $\lambda = 1.823$ cm. The structure was thenincorporated in the second version of the high power test circuit (Fig. 49), and coupling to the waveguide feed from the magnetron (No. 2114) was arranged to be critical at 16.474 Gc/s.

(a)



(b)

Glazed Titania Discs after High Power Tests
(Second Series)

Fig. 50

(a)



(b)

P.T.F.E. Coated Titania Discs after High Power Tests
(Second Series)

Fig. 51

Ignoring coupling hole effects, the maximum axial electric field was given by

$$E_{zm} = 4.4\ P^{\frac{1}{2}} \times 10^{4}\ \ V/m \qquad (7.16)$$

The R.F. power (P) was increased from about 60 kW to 150 kW without any evidence of breakdown other than the sporadic amplitude jitter on the pulse reflected from the cavity. At P = 160 kW the cavity pressure rose suddenly to about 5×10^{-3} torr, but, although the shape of the R.F. pulse reflected from the cavity changed considerably, the reflection coefficient remained unaltered. The power was reduced after a few seconds. The R.F. pulse returned to its original form and the vacuum slowly improved. When the pressure had fallen to about 10^{-5} torr the power was increased and the pressure 'avalanche' effect occurred again but at a reduced power level. This procedure was repeated several times and eventually the 'avalanche' occurred at P = 60 kW.

The cavity was then tested at low power. The values of Q_o and r_{sh}(T.W.) had dropped from 1650 to 925, and from 28.4 to 14.1 MΩ/m respectively.

On dismantling the cavity it was found that severe surface breakdown had occurred on one disc face (Fig. 51a) located at the same position relative to the shell of the cavity as that where the same effect occurred in the glazed disc cavity. Similarly the facing disc was less drastically affected (Fig. 51b). Again, rim breakdown had occurred on the severely damaged disc. As with the glazed disc cavity, there was slight browning around the holes in the discs, but

markedly brown stains on the outward-facing surfaces of the end discs were absent. The surface of the copper waveguide near to the broken down disc surface was covered with a sooty deposit. This effect was also present in the glazed disc cavity.

7.4.3 Interpretation of the Results

There is little doubt that the brown annular stains on the disc surfaces in both cavities were due to multipactoring electrons. (See Section 5.3). It is difficult to give a quantitative explanation of the situation because of uncertainty about fields in the cavity when breakdown phenomena occur, but expressions given by Mullett, Clay and Hadden[28] for the fields and gap widths required to promote multipactoring taken in conjunction with the secondary emission data given for titania by Hayes[71] suggested that multipactor resonances between discs were possible throughout our second series of high power tests. However, the discs were not apparently damaged by the multipactoring electrons, and the brown discolourations ranged from 'slight' to 'barely perceptible' on ill-defined areas, in sharp contrast to those found in the A.E.R.E. machine (see Fig. 5 of Ref.46). Here the affected annular areas were sharply defined and markedly discoloured, and the multipactor resonance increased the loss over 80 cm of travelling wave linac by nearly ten times. In the experiments described above, any appreciable R.F. absorption due to a multipactor resonance would have had a pronounced effect on the reflection coefficient from the cavity, for such a resonance would

have affected the resonant frequency of the cavity and the coupling system in use was highly frequency dependent. Apart from the amplitude jitter described earlier, which was independent of the R.F. power level and which was almost certainly associated with rim breakdown, no change in the reflection coefficient from the cavity was observed. It was concluded that in both glazed and P.T.F.E. coated titania disc cavities, careful degreasing during assembly and the use of oil-free vacuum pumps result in surfaces with secondary emission coefficients sufficiently low to prevent the build-up of serious multipactor resonances absorbing large amounts of R.F. energy.

The description of the outer faces of the two end discs in the glazed disc cavity could be reasonably explained by recalling that when the R.F. power is introduced into copper-loaded linacs for the first time after evacuation, the system pressure rises greatly and then falls away very slowly. The exact reason for this out-gassing of copper is not known, although explanations in terms of secondary emission phenomena have been given.[28] Gas evolved in this way from the copper end walls of the glazed disc cavity would be partly ionised by the R.F. fields and would thereby contribute electrons which could be accelerated and bombard the end discs of the cavity. To support this explanation we can record that although no marked browning was observed on the end discs in the P.T.F.E. coated disc cavity, the inner surfaces of the holes in these two discs, which were found to be devoid of P.T.F.E. after cavity fabrication, were dark grey suggesting that the exposed titania had been

reduced by electron bombardment.

In both test cavities the catastrophic breakdown occurred on the second disc away from the input coupling hole, across the surface facing the first disc. Referring to Fig. 48 we note that in the standing wave pattern of the E_{012} resonant mode for our test cavities the axial electric field is zero in the region of the second disc. Correspondingly, the radial electric field at the periphery of the disc has a maximum value. In view of this fact we can explain the sequence of events leading to breakdown in both cavities as follows:

(a) Rim breakdown first occurred where the radial electric field was highest, namely, around the rims of discs 2 and 5. Rim breakdown was seen to be severe near the reduced patches on disc 2 in both cavities. There were one or two minute black spots on the rims of disc 5 in the glazed disc cavity and disc 1 in both cavities. Otherwise the rims were perfectly clean. The disc 1 rim breakdown was almost certainly induced when the surface breakdown occurred on disc 2.

(b) The protective coatings prevented the rim sparks from initiating surface breakdown across the disc faces until a certain field strength had been reached. In the case of the glazed disc cavity the 25 keV electron beam lowered the breakdown threshold field, possibly by inducing a higher surface conductivity by electron bombardment.[71] Breakdown first occurred with E_{zm} = 7.0 MV/m, but previously, when no electron beam was present, E_{zm} had been up to 9.0 MV/m without breakdown. The increase in the

threshold field once breakdown had occurred was probably due to 'spark conditioning', first reported for glazed titania by Hayes[71]. The breakdown sparks initially vaporize contaminants on the glaze. Consequently the surface breakdown strength increases slightly and the sparking stops. The improvement continues until the cleaned-up glaze breaks down and allows reduction of the titania substrate. After the first semi-conducting track of reduced titania has formed a cumulative process sets in. Intense local heating due to currents in the track causes progressive reduction of the surrounding material. Breakdown first occurred in the P.T.F.E. coated disc cavity when E_{zm} reached 8.4 MV/m with no electron beam present. No 'spark conditioning' was observed.

(c) Intense local heating in the breakdown tracks caused material to be sputtered and condensed on the facing disc and nearby waveguide wall. Electrons were also released and these bombarded the facing disc causing partial reduction of the surface. The cavity field pattern was somewhat altered by the disturbance so that the radial electric field increased near disc 1 and decreased near disc 5 (which was further from the input). This resulted in slight rim sparking on disc 1 but no breakdown on disc 5.

7.4.4 Conclusions

We shall now summarise the conclusions drawn from both series of high power tests:

(a) Surface breakdown across disc faces is probably initiated by sparks at the rim.

(b) Rim breakdown can be greatly reduced by machining the disc rims to a smooth and accurate finish and then metallising them with copper.

(c) Adequate protection from surface breakdown for titania discs for use in the 2 MeV linac should be given by glazing or by coating with P.T.F.E. The evidence suggests that glazing is the better choice, but further experiments with travelling wave structures and properly focussed electron beams are necessary to confirm this point.

(d) Thorough degreasing of the structure and the exclusion of oil from the vacuum system should prevent the build-up of any serious multipactor resonance.

CHAPTER VIII

The Proposed Physical Realisation of the Buncher-Accelerator System

In this Chapter we shall consider in fairly general terms the problem of building up a working linac system centred on the type of slow wave structure which has been under discussion. It is beyond the scope of this treatise to go into great detail about the ancillary equipment. Other workers at this laboratory will treat these aspects in due course.

8.1 The Microwave Circuit

8.1.1 General Features

At this stage we can only generalize about the microwave circuit and suggest an appropriate scheme. The most important point to be considered is whether or not to use R.F. feedback in view of the disappointing and unexpected high losses found in the test cavities. In the previous Chapter we deduced that the loss length of a long glazed disc structure, such as that which will probably constitute the main linac structure, was about 0.25 m. Theory suggests that this figure can be doubled to give an average value for the bunching section. If the buncher is 11.2 cm long and the total structure length is 75 cm then we obtain an overall loss length of 0.31 m. From equation (3.5) we see that the optimum length of the structure is then 0.78 m so that $\ell/\ell_{opt} = 75/78 = 0.96$. The curves of Fig. 8 imply that for this value of ℓ/ℓ_{opt} only a 10% improvement in the figure of merit is achieved by using R.F. feedback.

However, a feedback system requires a phase shifter in the feedback arm (see Fig. 7), and this allows close control to be kept over the R.F. fields without the need to vary the source power, as pointed out in Section 3.3. We have therefore included feedback in the general circuit arrangement shown in Fig. 52. The specialised R.F. components shown are discussed below.

8.1.2 Special Waveguide Components

8.1.2.1 R.F. Source Protection

The frequency of the magnetron can be pulled by controlling the phase and magnitude of an impedance mismatch at its output window. The maximum pulling figure for the Ferranti J-Band magnetrons is 20 Mc/s for a V.S.W.R. of 1.5. Under the supervision of A.G. Armstrong, a calibrated variable mismatch with micrometer control giving a maximum V.S.W.R. of 1.5, and a variable phase shifter were designed and constructed. Both were high power waveguide components which could be pressurised at approximately 40 p.s.i.g. with negligible leakage.

Additional reflection from the load would disturb this frequency tuning system and might damage the magnetron window and frequency puller elements through heating. Therefore, to protect the magnetron, a high power ferrite isolator following the phase shifter was incorporated in the circuit. The two-port device acquired for this purpose was limited to the isolation of a load V.S.W.R. of 2.0 which restricted its usefulness in test experiments involving breakdown phenomena. It was realised that a high-power waveguide four-port ferrite circulator was a more suitable, albeit more expensive, device.

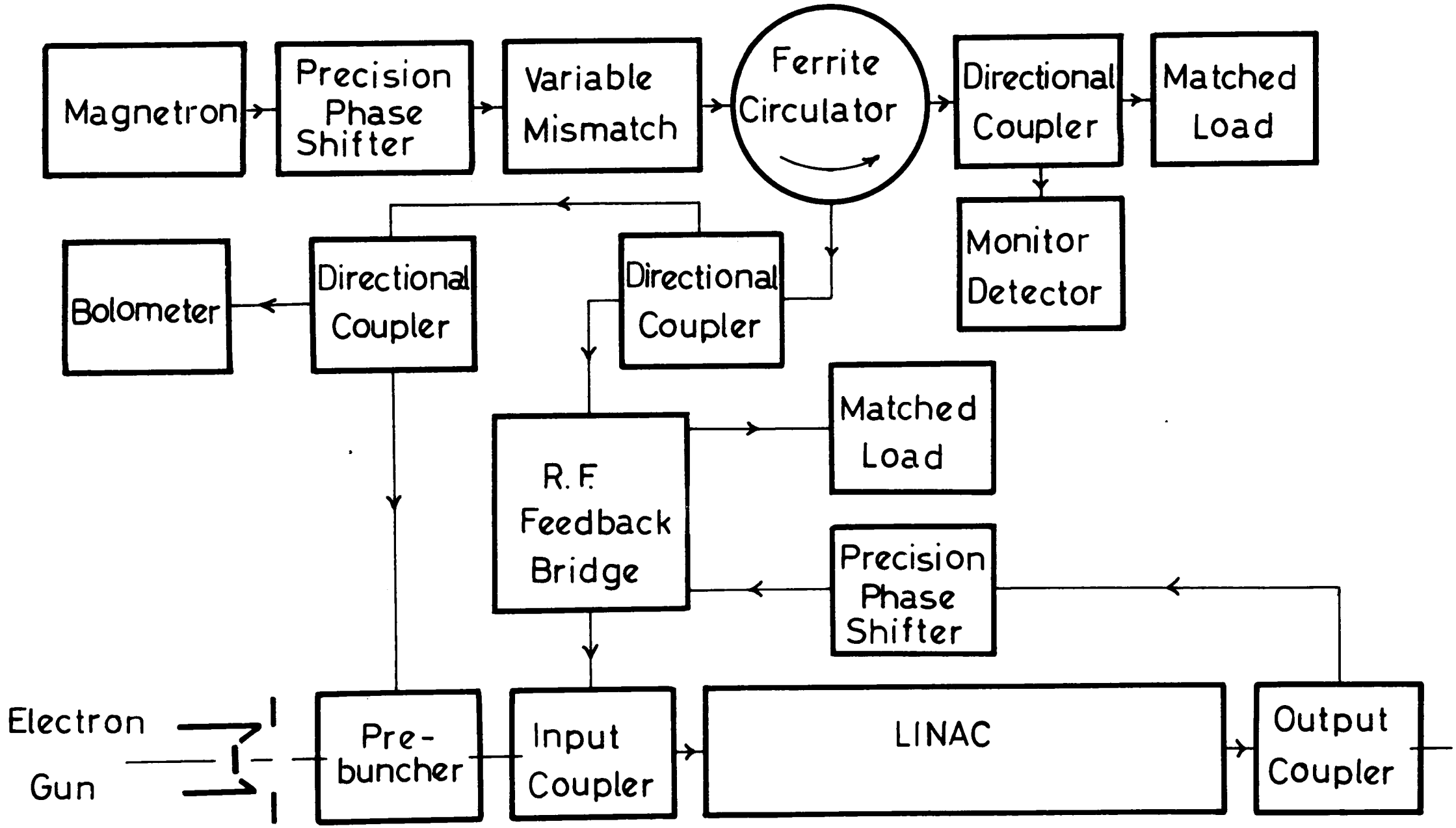


FIG. 52. LINAC MICROWAVE CIRCUIT

It would facilitate the monitoring of reflected power from the load and would avoid ferrite heating problems by transferring the requisite absorption of reflected energy to an appropriate matched load. Its operation would not be sensitive to the load V.S.W.R. A suitable circulator has recently been purchased which matches the magnetron performance admirably.*

8.1.2.2 R.F. Feedback Bridge

To achieve the maximum field build-up, the feedback bridge should be matched to the linac structure in the following way. The nature of the feedback bridge must be that of a four-port directional coupler. If we connect an R.F. source to one port then the field will divide in a certain proportion between two other ports, to either of which we may connect the linac, as in Figs. 53a and 53b. The action of the coupler may be defined by the relations between the electric fields E_1, E_2, E_3 and E_4 at the four ports:

$$E_2 = r\,E_4 + (1 - r^2)^{\frac{1}{2}} E_1 \qquad (8.1)$$

$$E_3 = r\,E_1 + (1 - r^2)^{\frac{1}{2}} E_4 \qquad (8.2)$$

where r is termed the bridge ratio.

If $E_1 = S$ the source field amplitude, $E_2 = A$ the initial accelerator field amplitude, and $20 \log_{10} q$ decibels is the linac attenuation, then with the linac connected to port 2, a matched load

---

*Microwave Associates 122G; bandwidth 16.2 to 16.6 Gc/s; maximum operating power 400 kW peak, 400 W mean; minimum isolation 20 dB; maximum insertion loss 0.4 dB; maximum input V.S.W.R. 1.15.

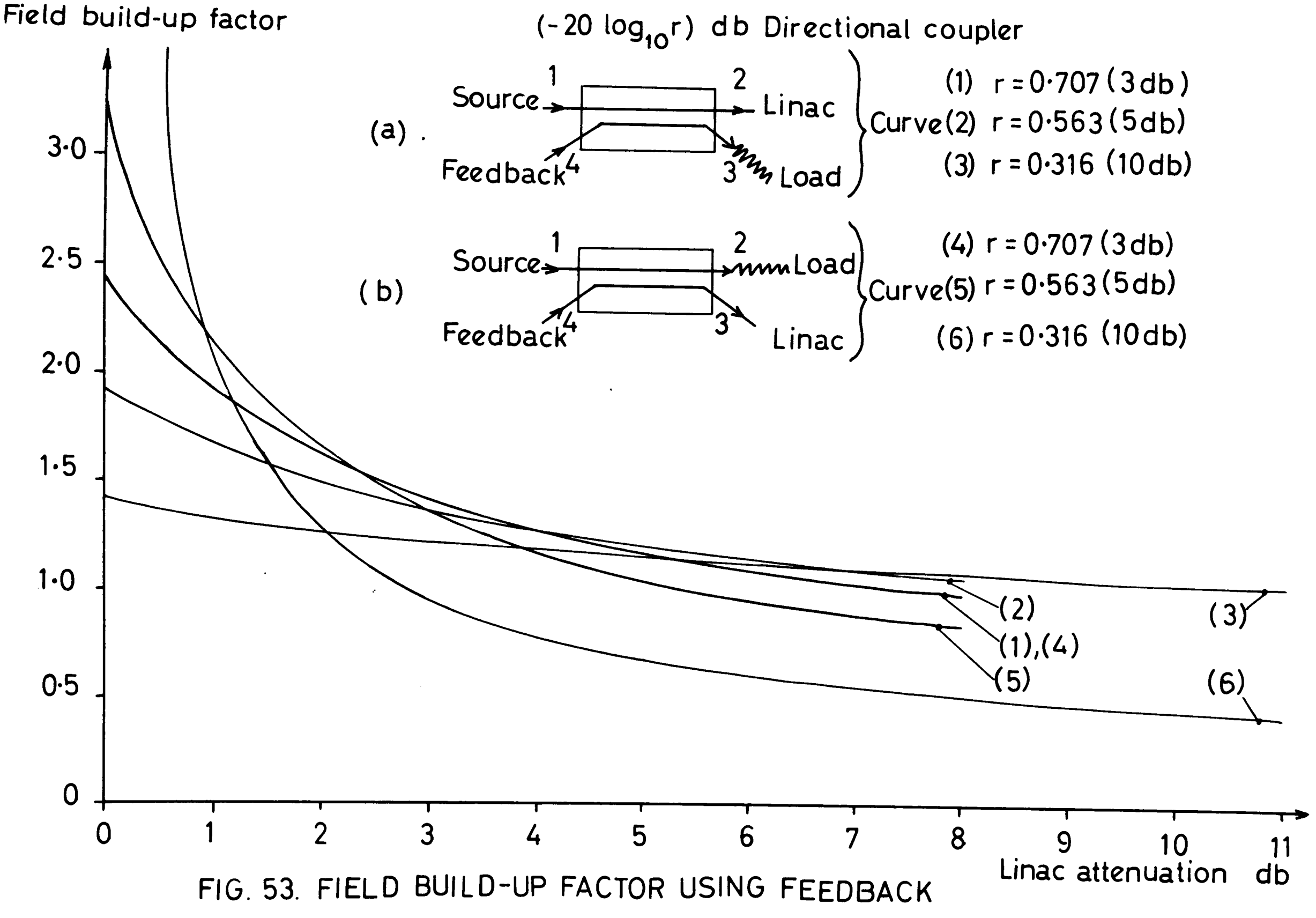


FIG. 53. FIELD BUILD-UP FACTOR USING FEEDBACK

connected to port 3 (Fig. 53a), and the feedback phase suitably adjusted we have from (8.1)

$$A = rqA + (1 - r^2)^{\frac{1}{2}} S \tag{8.3}$$

giving a field build up factor

$$\frac{A}{S} = \frac{(1 - r^2)^{\frac{1}{2}}}{1 - rq} \tag{8.4}$$

Similarly, for the configuration of Fig. 53b we have from (8.2)

$$\frac{A}{S} = \frac{r}{1 - q(1 - r^2)^{\frac{1}{2}}} \tag{8.5}$$

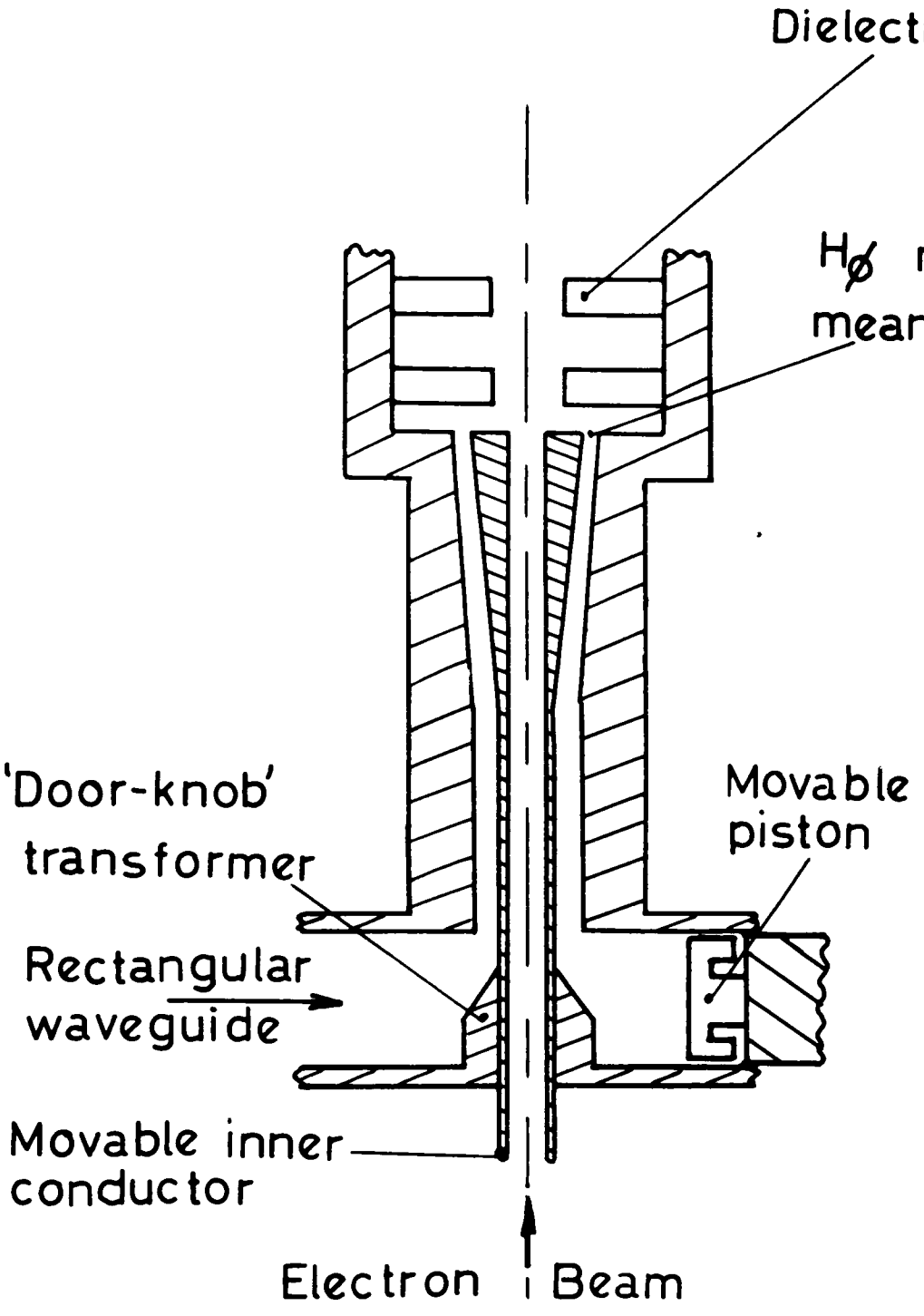
Using equations (8.4) and (8.5) we have plotted in Fig. 53 the variation of A/S with linac attenuation for r = 0.707, 0.563 and 0.316, corresponding to 3 dB, 5 dB and 10 dB directional couplers in microwave engineering parlance. It can be seen that if the linac attenuation exceeds about 3 dB configuration (a) with r = q gives the optimum field build up factor, and if the attenuation is greater than about 6 dB, it is generally necessary to match r and q to avoid A/S falling below unity. If the linac attenuation is 3 dB or less, adequate field build-up can be achieved with r = 0.707 corresponding to the 'rat-race' ring circuit which is readily available. Higher values of A/S can, however, be attained for $1 > q > 0.707$ if configuration (b) is used and r is chosen so that rq = 0.5.

The experiments described in the previous Chapter suggest that the linac attenuation might be as high as 10 dB. Neglecting coupler and waveguide feed losses we conclude that configuration (a)

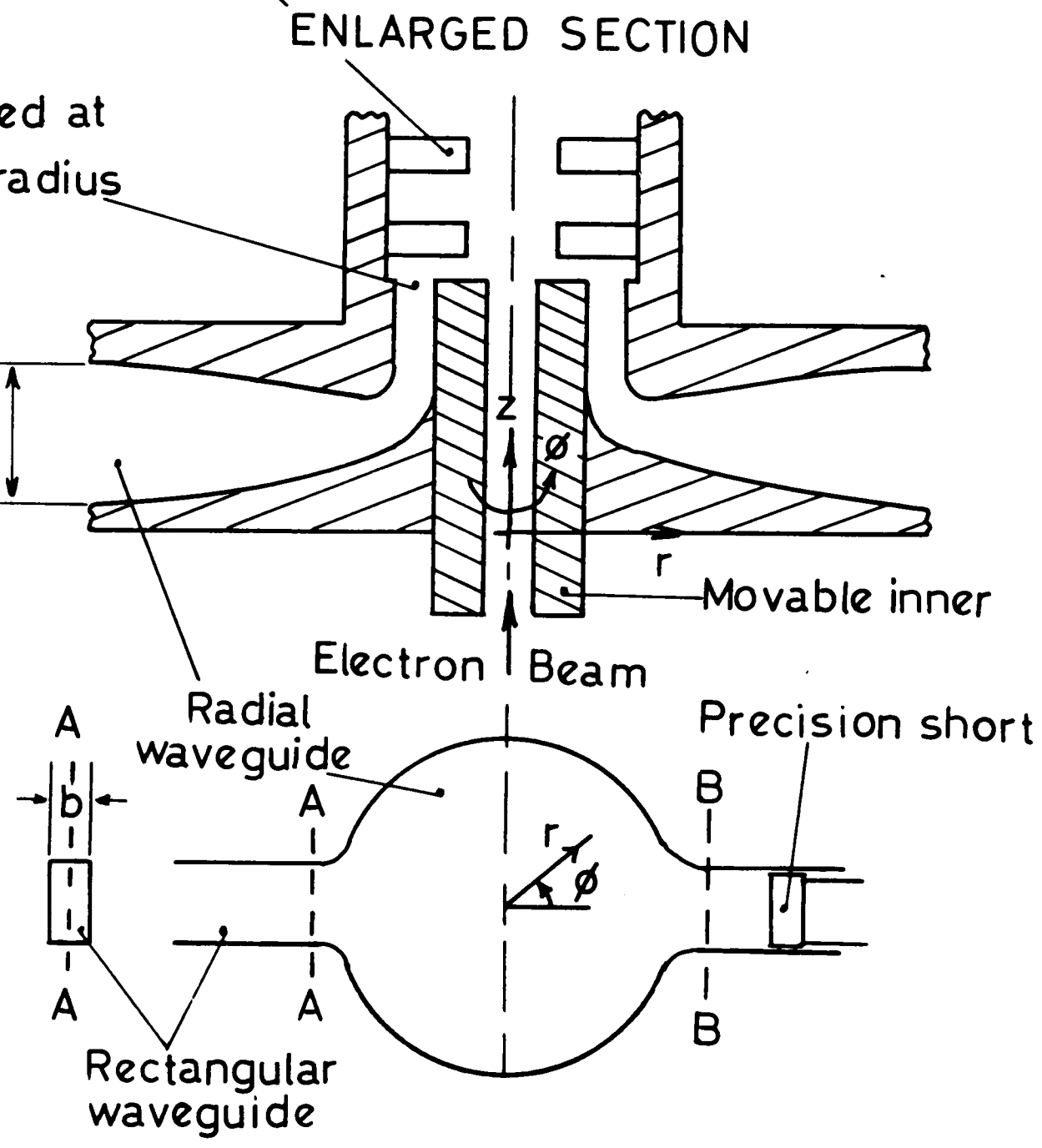
of Fig. 53 using a 10 dB directional coupler would constitute the optimum arrangement if feedback is to be used. However, the maximum field build-up factor would be only 1.05 for such a high linac attenuation.

8.1.2.3 R.F. Couplers

Previous workers found that the design of R.F. couplers used earlier for metal loaded linacs served as a useful starting point for the problem of feeding R.F. power to dielectric loaded structures.[24,44] The power was coupled from rectangular waveguide to a coaxial line via a 'door-knob' transformer as shown in Fig. 54a. The dimensions of this line at the input were carefully chosen to ensure that only the principal mode was propagated. Dielectric-loaded linacs can propagate modes that have angular (Ø) field variations and therefore care must be taken to avoid their excitation. This implies that coaxial line feeds must either not support asymmetric modes or must be themselves fed so that such modes are not excited in them. Reverting to the feed shown in Fig. 54a, the coaxial line was flared out near the linac so that the magnetic fields at the mean radius of the coaxial line output and the same radius in the linac (at the middle of an air space) were matched for equal power flux in both line and linac. Fine adjustments to the coupling were made by moving the inner line conductor axially. The scheme worked well, but it was no doubt difficult to fabricate the necessarily long inner conductor even when the transition from the uniform section of the line to the requisite coaxial gap at the junction with the linac was



(a) S - BAND COUPLER, REF. 24.



(b) J - BAND COUPLER

FIG. 54.

eventually shortened by using quarter wavelength transformers. To avoid this problem on the J-Band linac it was proposed that the alternative approach should be considered, namely, that a short coaxial feed of higher characteristic impedance should be used, care being taken to excite only the principal mode. Only preliminary experiments at low power have so far been carried out, but we can give here a general description of the design. The figures given relate to the R.F. output coupler for the linac. A similar approach can be made to the design of the input coupler when more is known about the bunching section.

The radius of the inner conductor was chosen to be 3 mm for two reasons. Firstly, it was planned that the match in H_ϕ should be made at a radius where its value was relatively high, as is the case in regions II and III of Fig. 2. Secondly, fabrication of the electron beam hole and the axial movement mechanism is made simpler as the outer diameter of the inner conductor is increased. Using anisotropic theory to express the magnetic field, and using the experimentally determined values of linac series impedance and axial phase constant, the equation giving the match in H_ϕ at the mean radius of the coaxial line was solved for the radius of the outer conductor. The matching equation may be written in the notation of Chapters VI and VII,

$$\frac{(r_{se})^{\frac{1}{2}}\, ka}{2} \cdot \frac{F_1(\Gamma\rho)}{F_1(\Gamma a)} = \left[\rho \log_e\left(\frac{r_2}{r_1}\right)\right]^{-\frac{1}{2}} \qquad (8.6)$$

where $F_1(\Gamma\rho) = Y_o(\Gamma c)\, J_1(\Gamma\rho) - J_o(\Gamma c)\, Y_1(\Gamma\rho)$

$$\rho = \frac{r_1 + r_2}{2}$$

r_1 = 3 mm, the radius of the inner conductor

and r_2 = the radius of the outer conductor

The other parameters were taken as follows:

$r_{se} = 185\ M\Omega/m^2$

$K = 97$

$a = 2$ mm

$c = 5.33$ mm

$\lambda = 1.823$ cm

$\beta = 382$ radian/metre

Equation (8.6) was solved graphically and gave $r_2 = 5.08$ mm. This result implied that all higher modes would be cut-off except for the H_{11} mode for which $\lambda_c = 2.5$ cm (> 1.8 cm). Taking the limiting electric field for R.F. breakdown as 10 MV/m, the maximum power flux that can be transferred through the coaxial line for $r_1 = 3$ mm and $r_2 = 5.08$ mm is about 8 MW (peak) so that we have a considerable safety margin in hand.

The chief remaining problem was to ensure that the H_{11} mode was not excited in the coaxial line. It was suggested that the coaxial line should be coupled to rectangular waveguide by a radial waveguide of cylindrical section, as shown in Fig. 54b in simplified form. The dominant mode in the rectangular waveguide would excite radial

waveguide modes with zero transverse magnetic field, i.e. $H_z = 0$ in cylindrical coordinates (see Fig. 54b). It has been shown that the form of E_z in such radially propagating modes may be expressed as[85]

$$E_z = c_1 \cos \frac{n\pi}{b} \cos m \phi \tag{8.7}$$

where b is the breadth of the radial waveguide and narrow dimension of the rectangular waveguide

and c_1 depends upon n and b; m and n are integers $\geqslant 0$.

The associated cut-off wavelength varies with the radius and is given by

$$\lambda_c = \frac{1}{\left[\left(\frac{n}{2b}\right)^2 + \left(\frac{m}{2\pi r}\right)^2\right]^{\frac{1}{2}}} \tag{8.8}$$

We can ignore modes where $n > 0$ since the value of b for J-Band rectangular waveguide is 0.79 cm giving $\lambda_c = 1.6$ cm (< 1.8 cm) for $n = 1$, $m = 0$. Hence, for practical purposes,

$$\lambda_c = \frac{2\pi r}{m} \tag{8.9}$$

The dominant mode is the $m = n = 0$ mode which is a TEM mode with angular symmetry about the z axis. If the rectangular-radial waveguide junction occurs at $r = 4$ cm we see from equation (8.9) that $m = 1, 2, 3, \ldots\ldots, 13$ yields asymmetric propagating modes at $\lambda = 1.823$ cm and $r = 4$ cm. All but one of these modes are cut-off at $r = r_2 = 5.08$ mm. The excitation of the remaining $m = 1$ mode can be inhibited by adjusting the short circuit in Fig. 54b to cause the fields at junctions A and B to be in phase. We have chosen the outer radius of the radial waveguide as 4 cm so that a slow reduction

in b as r decreases and a smooth transition to the coaxial feed can be achieved.

Design problems involving the movable inner conductor, vacuum seals, waveguide windows and electron beam focussing all remain to be tackled. However, a specially designed pressurised precision short circuit has been successfully operated at high power, and preliminary travelling wave experiments with two prototype copper couplers at low power have indicated a loss per coupler of about 0.1 dB and an overall loss of 1.2 dB when operated with a 30 disc test structure.

8.1.3 The Modulators

Two modulators have been developed under the supervision of A.G. Armstrong. A detailed report about them will be published in due course, but we should note the general specifications here.

The magnetron modulator design is based upon a hydrogen thyratron which discharges a delay line through the primary winding of a high voltage pulse transformer. Pulses of up to 25 kW at 40 A with a rise time of 500 kV/μsec can be delivered to the magnetron at several repetition rates between 50 and 2000 pulses per second. Lumped circuit delay lines were used to give various pulse lengths during testing, but best results were obtained with an extended coaxial line (a 'natural' delay line) giving a pulse length of 0.5 μsec and a $\pm$ 2% variation in amplitude during each R.F. pulse. The consequent $\pm$ 1% variation in R.F. field during the pulse would cause a $\pm$ 1% variation in energy between the electron bunches output from the linac. The accompanying phase variation would be small and so if the bunches

were injected into an undulator, the effect on the phase coherence between radiation from successive bunches would also be small. The bandwidth of the major lobe on the observed magnetron frequency spectrum was of the order of 5 Mc/s. This degree of frequency spread would have negligible effect upon linac and undulator operation.

The electron gun modulator was designed in a similar way to the magnetron modulator, but lumped circuit delay lines were used as the ripples on the voltage pulse were of lesser consequence. A ripple of $\pm$ 1% in gun voltage would lead to a $\pm$ $\frac{1}{2}$% variation in beam velocity. This would have little effect upon linac and undulator operation. Pulses of up to about 80 kV at 2A could be supplied by this modulator.

8.2 The Linac Structure

8.2.1 General Scheme

As experiments with test cavities have proceeded, several constructional developments have taken place which will form the basis of the mechanical design for the whole linac structure. It will probably be feasible to fabricate the buncher in a single waveguide section, and the main accelerator will probably comprise six sections each about 10 cm long and containing between 35 and 40 discs. Thus there would be only eight waveguide joints along the whole slow-wave structure. The waveguide wall thickness of just over 4 mm would ensure that each 10 cm section would be sufficiently rigid. The technique used in the low power test rig (Fig. 39) could be developed so that the waveguide sections would

be collimated by sections of outer tube linked with threaded coupling sleeves as in Fig. 55. The outer tube sections would be supported by X-section trestles resting on a flat bed which, in turn, could run on guide rails within the surrounding focusing-solenoid structure. Faulty waveguide sections could be easily replaced without the need to dismantle the whole structure.

Such a scheme is reasonably flexible and is in keeping with the experimental nature of a prototype machine. It cannot, of course, be more than a tentative proposal until a detailed design study is made.

8.2.2 Evacuation

To avoid contaminating the discs with oil, getter ion pumps backed by molecular sieve sorption pumps will be used to evacuate the system. A convenient size of getter ion pump which matches the air conductance at low pressures ($\approx 10^{-5}$ torr) of the 0.5" diameter pipework likely to be used in the system has a constant pumping speed of 5 litre/sec from 10^{-3} torr to 10^{-10} torr. However, if the simplest mechanical arrangement were adopted for pumping out the seven section linac structure, namely, sealing at the R.F. joints and pumping through the disc holes from one end of the structure, the pump down time would be excessive. With a pressure drop of 10^{-5} torr from one end of the structure to the other the air conductance would be only 0.016 litre/sec approximately. This mismatch in conductance can be greatly reduced by the arrangement depicted in Fig. 55. At each R.F. joint four radial holes 1 mm in diameter and effectively 1 mm long are drilled in the

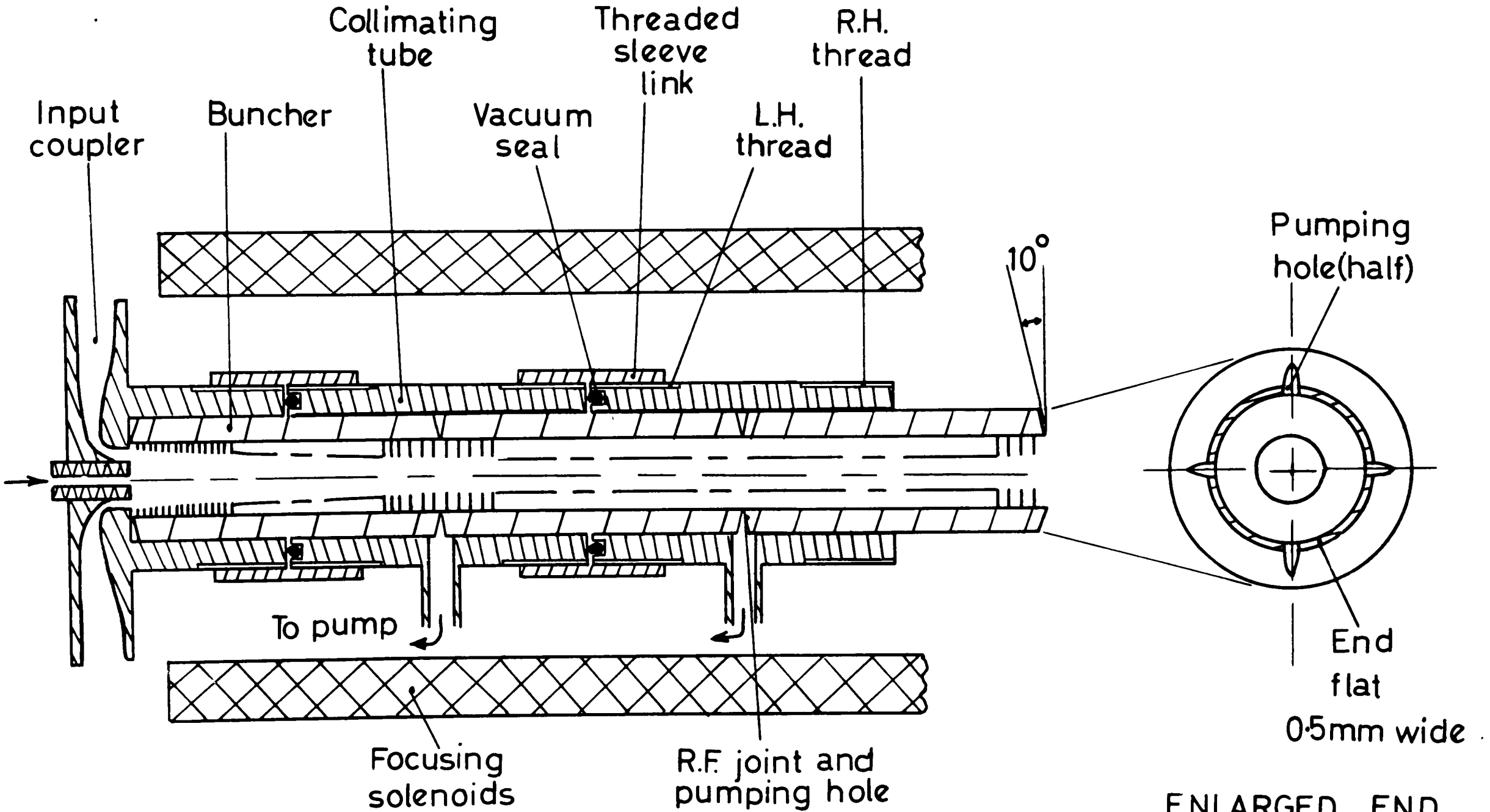


FIG. 55. LINAC STRUCTURE

waveguide wall, and the main pumping line is connected to the outer collimating tube close to the R.F. joints. The radial holes will have negligible effect on R.F. losses, and the arrangement has been estimated to increase the effective air conductance of the structure to about 3 litre/sec.

Ideally, the outer collimating tube should be made of non-magnetic stainless steel. Grease-free copper gaskets could then be used at the vacuum joints, and volatile surface contaminants could be almost eliminated. However, it will probably be necessary to fabricate the tube in brass and slightly greased gaskets may have to be used, but the high flow resistance between the vacuum joints and the linac structure will probably be adequate to protect the latter from any serious influx of oil vapour.

8.2.3 Heat Dissipation

In Chapter VII it was shown that the loss length of the linac structure is likely to be about 25 cm. For a maximum power flux of 400 kW and a duty factor of 2.5×10^{-4}, the mean power dissipated per centimetre in the hottest part of the waveguide is therefore 4 watts. Discrete disc theory indicates that the power lost in the copper waveguide walls (within a few skin depths of the inside surface) is five times that which is lost in the dielectric, hence, neglecting axial thermal conduction, the maximum temperature difference between the inside and outside of the copper tube is about $0.08^{\circ}C$.* The

*Tube O.D. = 19.06 mm; tube I.D. = 10.66 mm; thermal conductivity of copper = 0.92 c.g.s. units.

outer surface of the waveguide tube should make reasonably good thermal contact with the outer collimating tube, and there would be little difficulty in maintaining the inner surface of the collimating tube at room temperature, so that the inner walls of the waveguide should also be at about room temperature. If necessary, the thermal contact between waveguide and collimating tube could be improved by clamping suitable thermal shunts at the vacuum joints.

As there are about four discs per centimetre in the region of maximum power dissipation at the beginning of the main accelerating section, each disc dissipates about 0.17 watts if the overall loss is 4 W/cm. To estimate the rise in the temperature of the hottest disc we shall assume that all the heat energy gained has to be conducted from the periphery of the disc hole to the disc rim. This gives a maximum limiting value for the temperature rise at the periphery of the disc hole. Taking $c = 5.33$ mm, $a = 2$ mm, $2g = 0.8$ mm, and the thermal conductivity of titania ceramic[72] as 0.01 cal.sec^{-1} cm^{-1} ^{o}C^{-1}, and substituting in the ordinary equation for radial thermal conduction through the walls of a cylindrical tube, we obtain a temperature difference of 7^{o}C between the hole and rim of the disc. We can safely assume that the disc rim is in good thermal contact with the waveguide so that the temperature at the hole is unlikely to rise to more than 7^{o}C above room temperature. Even if the whole disc rose by 7^{o}C, the consequent drop in permittivity of 0.7% would only lead to an increase in wave velocity of 2.4%. Such an increase would be almost tolerable (see Sections 7.3.3 and 4.6).

We conclude that there should be no difficulty in ensuring that the linac is virtually unaffected by heat dissipation in the slow wave structure.

8.3 Beam Focusing

Several workers have examined the need for beam focusing, and useful formulae have been published giving the strength of the required steady axial magnetic field[50,54,86]. The main reason for focusing is that the phase region of axial bunching in the linac is also a region of radial 'debunching' or 'defocusing'. We can see this by examining the form of the fields near the axis. In the notation of Chapter VI we have

$$E_z = A\, I_0(k_1\rho)\, \cos(\omega t - \beta z) \tag{6.5}$$

$$E_\rho = -A\frac{\beta}{k_1} I_1(k_1\rho)\, \sin(\omega t - \beta z) \tag{8.10}$$

$$H_\phi = -A\frac{k}{k_1 Z_0} I_1(k_1\rho)\, \sin(\omega t - \beta z) \tag{8.11}$$

so that a particle of charge e travelling with velocity v_s parallel to the axis is subjected to an outward radial force given by

$$F_\rho = e E_\rho - B_\phi e v_s \tag{8.12}$$

From (8.10) and (8.11) we find that $B_\phi = \frac{v_s}{c^2} E_\rho$ since $v_s = kc/\beta$, and so

$$F_\rho = e E_\rho \left[1 - (v_s/c)^2\right] \tag{8.13}$$

Equations (6.5) and (8.10) show that in the phase region of acceleration and axial bunching, where E_z is positive and $\frac{\partial E_z}{\partial z}$ is negative, E_ρ is positive and therefore F_ρ is positive. Thus axial

bunching and acceleration are accompanied by radial defocusing, but the latter effect is small as v_s approaches c.

Following the work of Shersby-Harvie[50] we find that the steady axial magnetic field required to confine the particle trajectory within a cylinder of radius ρ (i.e. $\frac{\partial \rho}{\partial t} = 0$) is given by

$$B_z^2 = \frac{4mE_\rho}{e\rho}\left[1 - \left(\frac{v_s}{c}\right)^2\right] \tag{8.14}$$

where m is the longitudinal mass of the particle. We transform this expression into a more practical form by noting that

$$\left|E_{\rho max}\right| = E_{ms}\frac{\beta}{k_1} I_1(k_1\rho) \approx \frac{E_{ms}\beta\rho}{2} \quad \text{for small values of } \rho ,$$

$$\beta = \frac{1}{v_s\lambda} , \qquad E_\rho = E_{\rho max}\cos\phi_s$$

$$\text{and } m = \frac{m_o}{\left[1 - \left(\frac{v_s}{c}\right)^2\right]^{\frac{1}{2}}}$$

Hence, the paraxial approximation to equation (8.14) is given by

$$B_z = \left[\frac{4\pi m_o E_{ms}\cos\phi_s}{\lambda e v_s}\ (1 - v_s^2)^{\frac{1}{2}}\right]^{\frac{1}{2}} \tag{8.15}$$

where we have changed v_s/c to v_s as in previous Chapters.

Using the values of E_{ms} and v_s given in Appendix II for the glazed disc structure, we have plotted the variation of B_z with z in Fig. 56 for the phase stable particle with no beam loading. It can be seen that the focusing field plays an important role in the bunching section where F_ρ reaches a maximum value. There should be no difficulty in providing the required magnetic field using conventional

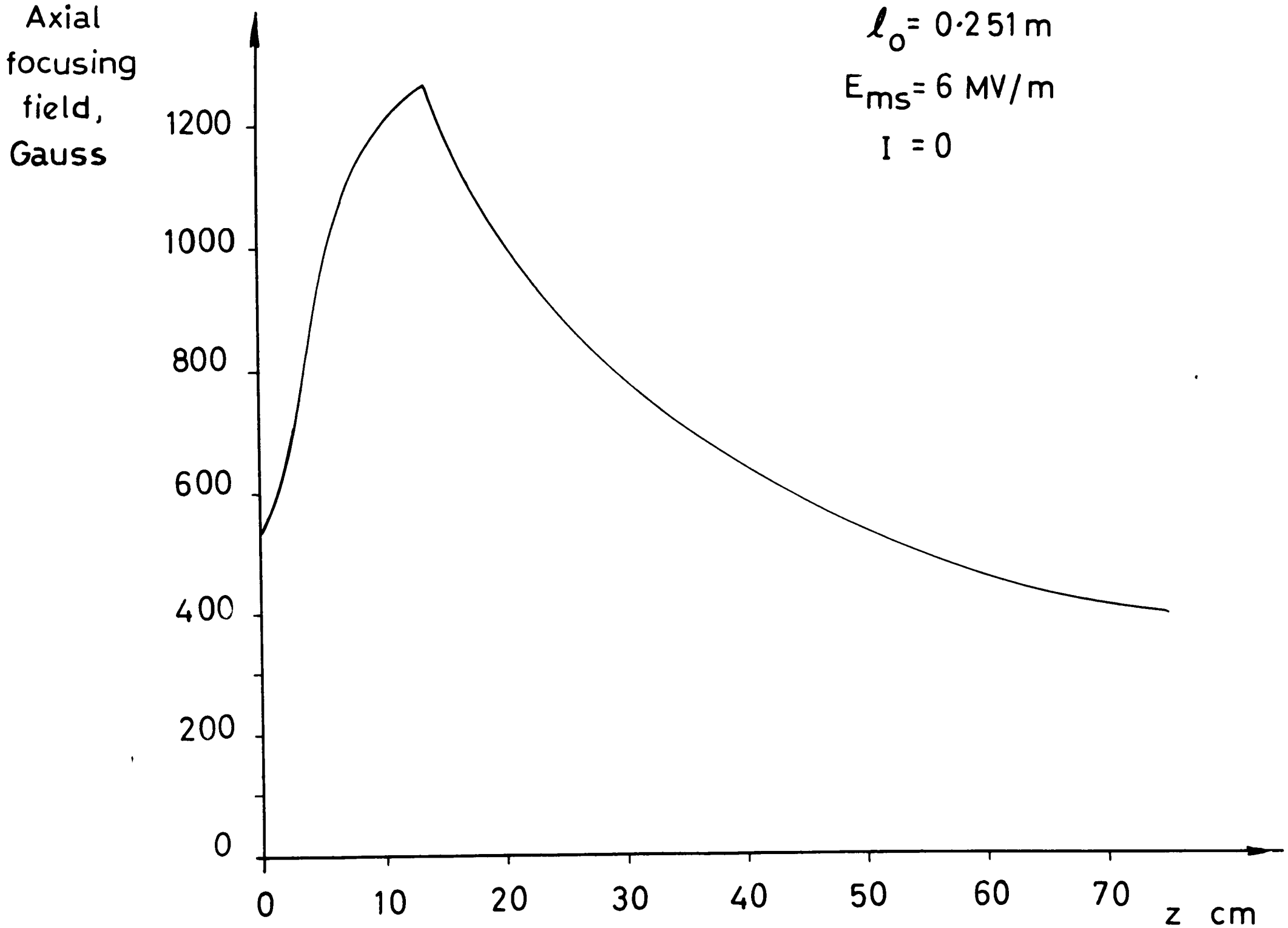


FIG. 56. VARIATION OF FOCUSING FIELD

power supplies and solenoids with water cooling (if necessary).

Finally, we note that space-charge defocusing effects are negligible compared with those described above when the beam current is of the order of 100 mA. This is chiefly because the particles traverse the structure and acquire high velocities in a relatively short time.

Conclusions

We have discussed the use of short bunches of 2 MeV electrons in the generation of interwaves, and we have seen that the J-Band titania-loaded linac is a convenient source of such electrons. Travelling-wave operation at six discs per guide wavelength combines a high figure of merit with a reasonable approximation to the ideal anisotropic dielectric.

Phase-space concepts applied to the design of the buncher fields and velocities yielded an effective bunch length of 0.3 mm that would afford coherent undulator radiation at 0.6 mm free space wavelength. Unfortunately, the design of the practical buncher to give these fields and velocities has proved difficult. Further experiments should be carried out when the work on relaxation methods has given a more accurate description of the electromagnetic fields and wave dispersion in the buncher structure.

Experiments have shown that carefully ground titania discs with metallised rims and glazed faces should withstand the R.F. fields and the proximity of an axial electron beam in the 2 MeV linac structure. The dielectric surface conductivity is very low, and further high power experiments with axial beams should be carried out on longer test sections than hitherto to confirm that surface charging will not be troublesome. Provided that carbonaceous thin films on the dielectric surfaces are avoided by excluding oil and grease from the vacuum system, it appears that no serious electron multipactor resonance and consequent R.F. absorption will occur in the linac structure. This can only be

confirmed in an operational linac structure.

The discrete disc theory of the slow-wave structure gives the better agreement with experiment when the disc holes are small, and the anisotropic theory is better when they are large. The first case can be understood because the discrete disc theory is exact when there is no hole, but when the holes are large most of the energy flows through the hole and it is then not apparent which theory should give the better agreement.

The experimental results for several test cavities fabricated by the shrunk-on tube method were in good agreement with one another. It was concluded that the required high degree of physical accuracy was being achieved. Although a fourfold improvement in series impedance was obtained during the course of cavity development the shunt impedance remained at a disappointingly low value relative to the theory. This was thought to be due partly to inexact theoretical boundary-matching of the fields, and partly to surface effects giving rise to a relatively high resistivity in the waveguide wall.

Finally, a practical design for the main accelerator section was evolved. Further work should include the fabrication of this section, which could eventually be coupled to a bunching section. Intermediate acceleration tests could be conducted using appropriate -ray sources to give the requisite 0.278 MeV beam energy at injection into the main section.

APPENDIX I

The Equations of Motion for Exponential Change in Axial Ratio

The equation giving the rate of change of axial ratio is

$$\frac{d}{dz}(m_\ell \omega_o) = \epsilon \frac{m_\ell \omega_o^2}{v_s} \tag{4.36}$$

In terms of momentum p_s we have the relationships

$$m_\ell = \frac{m_o(p_s^2 + m_o^2 c^2)^{\frac{3}{2}}}{m_o c^3}$$

$$\omega_o^2 = \frac{e\,\omega \cos \phi_s \; m_o^2 c^2 E_{ms}}{p_s(p_s^2 + m_o^2 c^2)} \tag{I.1}$$

$$v_s = \frac{p_s c}{(p_s^2 + m_o^2 c^2)^{\frac{1}{2}}}$$

Substituting (I.1) in (4.36) we get

$$\frac{d}{dz}\left[\frac{(e\,\omega \cos \phi_s)^{\frac{1}{2}}}{m_o^2 c^2} \cdot \frac{m_o(p_s^2 + m_o^2 c^2)\, E_{ms}^{\frac{1}{2}}}{p_s^{\frac{1}{2}}}\right]$$

$$= \epsilon \frac{e\,\omega \cos \phi_s}{m_o c^2} \cdot \frac{m_o(p_s^2 + m_o^2 c^2)}{p_s^2} E_{ms}$$

Differentiating we get

$$\tfrac{1}{2}(p_s^2 + m_o^2 c^2) p_s^{-\frac{1}{2}} E_{ms}^{-\frac{1}{2}} \cdot \frac{d E_{ms}}{dz}$$

$$+ \left[2(p_s E_{ms})^{\frac{1}{2}} - \frac{1}{2}(p_s^2 + m_o^2 c^2)\, p_s^{-\frac{3}{2}} E_{ms}^{\frac{1}{2}}\right] \frac{dp_s}{dz}$$

$$= \epsilon (e\,\omega \cos \phi_s)^{\frac{1}{2}} m_o (p_s^2 + m_o^2 c^2) p_s^{-2} E_{ms}$$

and dividing throughout by the coefficient of $\frac{d\,E_{ms}}{dz}$

$$\frac{d\,E_{ms}}{dz} + \left[4p_s\,E_{ms}(p_s^{\,2} + m_o^{\,2}\,c^2)^{-1} - p_s^{\,-1}\,E_{ms}\right]\frac{dp_s}{dz}$$

$$= 2\epsilon\,(e\,\omega\,\cos\phi_s)^{\frac{1}{2}}\,m_o\left(\frac{E_{ms}}{p_s}\right)^{\frac{3}{2}} \qquad (I.2)$$

We can rewrite the force equation as

$$v_s\frac{dp_s}{dz} = e\,E_{ms}\sin\phi_s$$

and if we divide by v_s and substitute for v_s from (I.1) we obtain

$$\frac{dp_s}{dz} = \frac{e\,\sin\phi_s}{c}\,.\,\frac{(p_s^{\,2} + m_o^{\,2}\,c^2)^{\frac{1}{2}}}{p_s}\,E_{ms} \qquad (I.3)$$

and substituting for $\frac{dp_s}{dz}$ from (I.3) in (I.2) we have

$$\frac{d\,E_{ms}}{dz} = \frac{e\,\sin\phi_s}{c}\left[(p_s^{\,2} + m_o^{\,2}\,c^2)^{\frac{1}{2}}\,p_s^{-2}\,E_{ms}^{\,2} - 4(p_s^{\,2} + m_o^{\,2}\,c^2)^{-\frac{1}{2}}\,E_{ms}^{\,2}\right]$$

$$+ 2\epsilon(e\,\omega\,\cos\phi_s)^{\frac{1}{2}}\,m_o\left(\frac{E_{ms}}{p_s}\right)^{\frac{3}{2}} \qquad (I.4)$$

where equations (I.3) and (I.4) are equations (4.37) and (4.38)

in the text.

APPENDIX II

The Accelerating Field and the Phase Velocity

As described in Section 4.4.1, when the parameter a equals 2.4, a field and phase velocity variation is determined in the bunching section such that $\frac{\partial E_s}{\partial z} \approx 0$ at the transition from bunching section to accelerating section. The following table shows the computed values of the peak field and the phase velocity at intervals of 0.5 cm along the bunching section for a = 2.4. Trajectory calculations have shown that these values form the basis of good bunching in the accelerator (see Chapter IV).

E_{ms} MV/m	v_s/c	z m
0.450	0.400	0
0.511	0.407	0.005
0.582	0.414	0.010
0.665	0.423	0.015
0.764	0.432	0.020
0.880	0.442	0.025
1.016	0.454	0.030
1.177	0.466	0.035
1.365	0.480	0.040
1.583	0.495	0.045
1.834	0.511	0.050
2.121	0.529	0.055
2.441	0.548	0.060
2.793	0.568	0.065
3.170	0.589	0.070
3.566	0.611	0.075
3.968	0.633	0.080
4.364	0.655	0.085
4.744	0.676	0.090
5.094	0.697	0.095
5.409	0.716	0.100
5.681	0.735	0.105
5.910	0.753	0.110

TABLE II.1

The peak axial field of 6 MV/m is reached at z = 11.2 cm. The following tables set out the variation of v_s throughout the main accelerating section ($z \geqslant 11.2$ cm) to keep the phase stable particle at ϕ_{so} the phase at which it emerges from the buncher, namely 0.834 radian (for a = 2.4). The calculations are based on equations (4.40) and (4.41) as described in Chapter IV and Section 7.3.4.

Unglazed Discs: (See also Figs. 46 and 47)

r_{sh} = 58.9 MΩ/m ϕ_{so} = 0.834 ℓ_o = 0.336 m

E_{mso} = 6 MV/m v_{so} = 0.762c U_{so} = 0.278 MeV

'b ratio' = 1.096

	I = 0			I = 25 mA		
z	U_s	v_s/c	b_{exp}	U_s	v_s/c	b_{exp}
m	MeV			MeV		
0.112	0.278	0.762	0.338	0.278	0.762	0.338
0.132	0.370	0.813	0.328	0.364	0.811	0.328
0.162	0.505	0.864	0.321	0.489	0.859	0.321
0.212	0.700	0.907	0.314	0.681	0.904	0.314
0.262	0.885	0.930	0.310	0.857	0.927	0.310
0.362	1.213	0.955	0.306	1.150	0.951	0.307
0.462	1.496	0.965	0.305	1.383	0.963	0.306
0.562	1.740	0.974	0.304	1.559	0.970	0.305
0.662	1.952	0.977	0.303	1.694	0.973	0.304
0.750	2.112	0.978	0.303	1.778	0.975	0.304

Glazed Discs: (See also Figs. 46 and 47)

r_{sh} = 47.1 MΩ/m ϕ_{so} = 0.834 ℓ_o = 0.251 m

E_{mso} = 6 MV/m v_{so} = 0.762c U_{so} = 0.278 MeV

'b ratio' = 1.053

	I = 0			I = 25 mA		
z m	U_s MeV	v_s/c	b_{exp}	U_s MeV	v_s/c	b_{exp}
0.112	0.278	0.762	0.325	0.278	0.762	0.325
0.132	0.369	0.813	0.316	0.369	0.813	0.316
0.162	0.490	0.860	0.309	0.484	0.858	0.309
0.212	0.679	0.903	0.302	0.666	0.900	0.302
0.262	0.851	0.926	0.299	0.827	0.923	0.299
0.362	1.151	0.952	0.295	1.088	0.948	0.296
0.462	1.398	0.963	0.294	1.283	0.958	0.295
0.562	1.598	0.971	0.293	1.416	0.964	0.294
0.662	1.762	0.975	0.292	1.505	0.968	0.293
0.750	1.882	0.977	0.292	1.555	0.969	0.293

APPENDIX III

The Effect of the Beam on the Accelerating Field

Beam loading in travelling wave linear electron accelerators has been treated by Neal,[64] Lichtenberg[61], and Johnsen[63]. Following the analysis of Johnsen we shall derive equation (4.41) which applies to the uniform accelerating section of the structure.

We know that the ohmic power loss per unit length can be written

$$P_d = \frac{E_{ms}^2}{r_{sh}} \qquad \text{(III.1)}$$

and that the R.F. power converted to beam kinetic energy is

$$P_b = (E_{ms} \sin \phi_s) I \text{ per unit length} \qquad \text{(III.2)}$$

Therefore, in the presence of the beam the total R.F. power loss per unit length is

$$P_t = P_b + P_d$$

$$= (1 + k \frac{E_{mso}}{E_{ms}}) \frac{E_{ms}^2}{r_{sh}} \qquad \text{(III.3)}$$

where k is the beam loading factor $\frac{r_{sh} I \sin \phi_s}{E_{mso}}$

and E_{mso} is the peak synchronous field at the end of the buncher.

Now $$E_{ms}^2 = P\, r_{se}$$

where P is the power flux at an axial distance z from the beginning of the uniform section. Therefore

$$P_t = -\frac{dP}{dz}$$

$$\text{or} \quad dP = -\frac{r_{se}}{r_{sh}} (P + k(P_o P)^{\frac{1}{2}}) dz$$

$$= -(P + k(P_o P)^{\frac{1}{2}}) \frac{dz}{l_o} \qquad \text{(III.4)}$$

where $P = P_o$ at the beginning of the uniform section. We shall assume as before that r_{sh}, r_{se}, and ϕ_s are independent of z. Then we can integrate equation III.4 to get

$$\frac{z}{2\ell_o} = -\log e\left[\frac{E_{ms}/E_{mso} + k}{1 + k}\right]$$

$$\text{or} \quad E_{ms} = E_{mso}\, e^{-\frac{z}{2\ell_o}} - r_{sh}\, I \sin\phi_s\left(1 - e^{-\frac{z}{2\ell_o}}\right) \qquad \text{(III.5)}$$

The second term in this equation gives the effect upon the peak synchronous field of the induced electric field due to the beam charge. At the (phase stable) bunch centre this induced field is

$$-r_{sh}\, I\left(1 - e^{-\frac{z}{2\ell_o}}\right)$$

hence the accelerating field at the phase stable particle is given by

$$\frac{dV}{dz} = E_{mso} \sin\phi_s\, e^{-\frac{z}{2\ell_o}} - r_{sh}\, I\left(1 - e^{-\frac{z}{2\ell_o}}\right) \qquad \text{(III.6)}$$

which is equation (4.41).

APPENDIX IV

A Method of Solution of Transcendental Equations

Consider a transcendental equation such as the dispersion relation (6.3) which may be written

$$D(b) = 0$$

and which we wish to solve for b. Let us guess two values of b, namely b_1 and b_2, which we think may be near to the correct solution. In general $D(b_1)$ and $D(b_2)$ will differ from zero. We can plot these two values as in Fig. IV.1. The correct value of b which makes $D(b) = 0$ is shown as b', and we can make a better approximation to b' with b_3 which is the abscissa at which the line joining (D_1, b_1) and (D_2, b_2) cuts the b axis. Again, using b_3 and b_2 we can obtain a better solution with b_4. The process can be repeated until the desired degree of convergence is attained.

To find the value of b_3 we note that

$$D_1 = m(b_1 - b_3)$$

$$D_2 = m(b_2 - b_3)$$

where m is the slope of the line joining (D_1, b_1) to (D_2, b_2). Rearranging terms we get the two simultaneous equations

$$b_3 + D_1\alpha = b_1$$

$$b_3 + D_2\alpha = b_2 \qquad \text{where } \alpha = \frac{1}{m}$$

with solution for b_3

$$b_3 = \frac{\begin{vmatrix} b_1 & D_1 \\ b_2 & D_2 \end{vmatrix}}{\begin{vmatrix} 1 & D_1 \\ 1 & D_2 \end{vmatrix}}$$

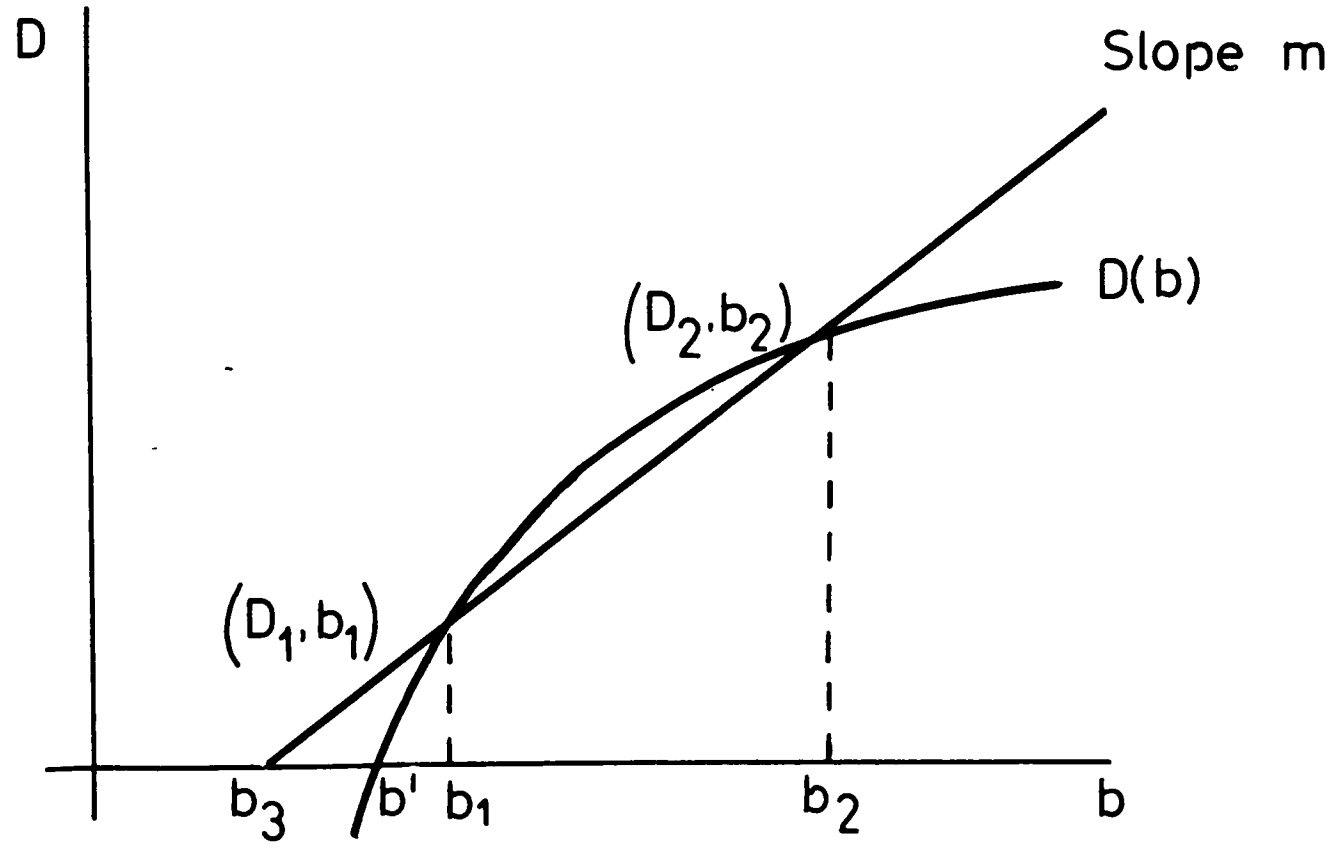


FIG. IV.1.

This method can be extended to any number of simultaneous equations. Consider the two equations

$$D(a,b) = 0$$

$$E(a,b) = 0$$

which we wish to solve for a and b. We here need three trial values for a and b, and we have the six relationships

$$b_1 = b_4 + \alpha D_1 + \beta E_1 \qquad a_1 = a_4 + \gamma D_1 + \delta E_1$$

$$b_2 = b_4 + \alpha D_2 + \beta E_2 \qquad a_2 = a_4 + \gamma D_2 + \delta E_2$$

$$b_3 = b_4 + \alpha D_3 + \beta E_3 \qquad a_3 = a_4 + \gamma D_3 + \delta E_3$$

where a_1, a_2, a_3, b_1, b_2, b_3 are the trial values, b_4 is the next approximation to the value of b which satisfied the equations, and α, β, γ, δ are dependent upon the six trial values.

Solving for b_4 we get

$$b_4 = \frac{\begin{vmatrix} b_1 & D_1 & E_1 \\ b_2 & D_2 & E_2 \\ b_3 & D_3 & E_3 \end{vmatrix}}{\begin{vmatrix} 1 & D_1 & E_1 \\ 1 & D_2 & E_2 \\ 1 & D_3 & E_3 \end{vmatrix}}$$

This method was used by Lichtenberg in his computer programme to solve equations (6.3) and 6.10).

Reprinted from the *British Journal of Applied Physics*, VOL. 14, pp. 289–291, MAY 1963

Dielectric properties of titania ceramics at microwave frequencies

J. M. FREE,*‡ M. E. B. MOFFAT*§ and G. B. WALKER†

*Oxford University Engineering Laboratory
†Department of Electrical Engineering, University of British Columbia, Vancouver
MS. received 7th December 1962

The determination of the relative permittivity κ and the loss tangent $\tan\delta$ of the ceramics titania ($\kappa \simeq 95$, $\tan\delta \simeq 0{\cdot}0004$) and magnesium titanate ($\kappa \simeq 14{\cdot}3$, $\tan\delta \simeq 0{\cdot}0001$) by H_{01} mode and 'ghost' mode cavity techniques is outlined.

Results are presented for the frequency range 3 to 35 Gc/s at room temperature. It is noted that κ varies by 5% in both materials, and that $\tan\delta$ rises significantly but remains at a relatively low value as the frequency is raised from 3 to 35 Gc/s.

Experiments are described in which 1·8 cm wavelength cavities loaded with single glazed titania disks have been successfully operated at electric field strengths up to 10 MV m^{-1} with 20 kev axial electron beams.

The use of these materials in slow-wave structures is briefly discussed.

1. Introduction

Ceramic materials are often used in microwave circuit elements, vacuum windows and tube structures. For any of these applications the relative permittivity κ and the loss tangent $\tan\delta$ must be known. Further, for uses in high power devices the stability of possible ceramics has to be carefully assessed. This paper summarizes results obtained by the authors and the manufacturer (Dr. Erich Schaefer, Cambridge) in developing techniques to handle the low-loss ceramics titanium dioxide and magnesium titanate at wavelengths of 10, 3, 1·8 and 0·8 cm, i.e. at S-, X-, J- and Q-band frequencies (Atkinson, Cooper and Machin unpublished,‖ Free and Walker 1960, Walker and Luthra 1962). The authors are particularly interested in applications to slow-wave structures for travelling-wave tubes and linear accelerators (Free 1962).

2. Choice of experimental method

The two chief factors which set a limit to the usefulness of any technique are (i) the ratio of the total loss in the system to the loss in the specimen, and (ii) the geometrical accuracy to which specimens have to be manufactured and set up in the test apparatus. Whilst in practice neither of these factors need prevent an accurate determination of permittivity, both can be crucial in the determination of loss tangent.

3. H_{01} mode cavity

At the higher end of our frequency range we used well-known techniques employing an H_{01} mode to reduce cavity wall loss (Free and Walker 1960). The relative permittivity of the disk specimen is deduced from the displacements of the plunger required to restore cavity resonances on insertion of the specimen. The loss tangent is calculated from knowledge of Q value of the cavity, allowance being made for cavity wall losses by taking measurements with and without the specimen. The circuit arrangement is such that the cavity resonance curve is displayed on an oscilloscope with adjustable frequency marker pips appearing on a second trace, thus enabling the Q of the cavity to be measured. For a Q of 10000 the measurement was accurate to about ±3%.

In determining κ and $\tan\delta$ in such an H_{01} mode cavity the most important errors are brought about by tilted or uneven surfaces. It is found that the effect of a small gap between the periphery of the disk and the cavity wall is negligible, for here virtually no electric field exists and the wall currents are almost unaffected. This gap enables the specimen to be supported only by the end wall, and since the metal walls of the cavity can be machined to a sufficiently high accuracy, non-parallel and uneven disk surfaces are now the geometrical factors which cause the most trouble. Their effect is to excite unwanted modes and to reduce the Q of the cavity by the resulting energy transfer. A titanium dioxide specimen tested at Q-band appeared to have very large losses when its face was tilted by 0·2 degree. The same specimen gave the same permittivity (within 0·2%) but one-tenth of the former loss tangent after it had been ground true (tilt less than 0·01 degree). The accuracies of cavity and specimen were checked by investigating the existence of spurious modes, comparing actual and theoretical resonant frequencies. With care in the machining of the cavity and by silver plating the walls, cavity Q's within 10% of the theoretical value based on the bulk conductivity of silver were observed at J- and Q-bands. Moreover the surface conductivity proved to be uniform to within a few per cent. This is a vital point, for in apportioning the losses between the specimen and the cavity walls to calculate $\tan\delta$ for the specimen we assume such a uniform conductivity. This uniformity was indicated by the relatively small differences between results obtained when the circular sections of wall effectively within the resonant cavity were changed by moving the end walls.

‡ Now at the Zenith Radio Corporation, Research Laboratory, Chicago.

§ Now at the British Broadcasting Corporation, Research Department, Kingswood Warren, Surrey.

‖ Technical Report, Dr. Erich Schaefer's Laboratory, Cambridge, June 1962.

4. 'Ghost' mode cavity

At the lower frequencies in our range it becomes practicable to employ a 'ghost' mode method wherein the ratio of specimen loss to total loss is optimized by causing the excited modes to be evanescent in the air spaces but resonant in the specimen. This technique has been described by Walker and Luthra (1962).

Briefly, the method comprises the measurement of the resonant frequencies and Q of a cylindrical cavity containing a disk or rod specimen for several mode patterns. Identity of the modes together with an estimate of the permittivity complete the information necessary to calculate κ and tan δ. The geometry of the specimen must be controlled to a rather higher degree of precision than is the case with an H_{01} cavity to obtain a similar accuracy in determining κ. However, the accuracy in measuring tan δ is not so impaired and is better than in the H_{01} cavity method at X- and S-band. At higher frequencies the increase in metal wall losses and experimental difficulties in mode launching and identification make the 'ghost' mode rather less attractive.

5. Experimental results

Figure 1 illustrates the general trends in results obtained for several specimens with H_{01} mode and 'ghost' mode cavity techniques. The titania samples were of 96% titanium

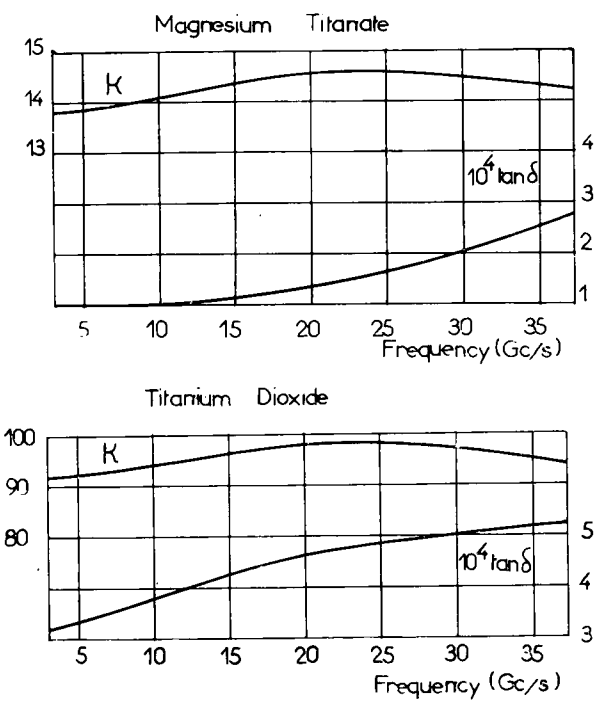


Figure 1. Variations of κ and tan δ with frequency.

dioxide and 4% stabilizing material by weight, and the magnesium titanate samples were of approximately 60% magnesium oxide and 40% titanium dioxide by weight. The measurements of κ are accurate to about $\pm\frac{1}{2}\%$ and they show a variation of about 5% over the frequency range. Because of uncertainties in the geometry and positioning of specimens the measurements of tan δ are only accurate to about $\pm 50\%$ at the higher frequencies but the upward trend is definite. However, even at Q-band the value of tan δ is low enough to make projected practical applications of the materials seem very reasonable. Consequently these low loss materials should prove useful in realizing the efficient high frequency performance that is theoretically attainable in many microwave dielectric structures (Free 1962).

6. High power breakdown tests

For applications in linear accelerators the ceramics must be able to retain their dielectric properties under high field conditions. At S-band, titania-loaded accelerator structures have withstood axial fields of up to about 5 MV m^{-1} before a surface breakdown occurred. By glazing the disks with a lead borate enamel and metallizing their rims to ensure intimate contact with the wall, operation at much higher fields has proved possible. To investigate the effect at J-band on a typical glazed and metallized accelerator disk with a low voltage beam passing through its central hole, the high power E mode resonant cavity circuit shown in figure 2 was set up. The coupling to the cavity was arranged

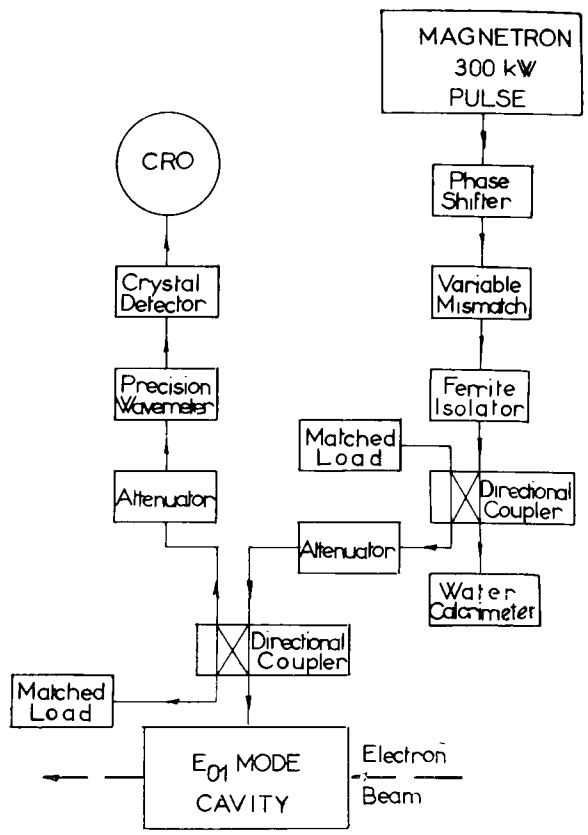


Figure 2. A microwave circuit used in J-band tests at high power.

to be critical during low power tests to measure resonant frequency and Q. The system was then fed with high power J-band radiation and the signal reflected from the cavity was observed. In this way any breakdown across the surface of the disk or sparking between the rim of the disk and the cavity wall could be detected immediately. It was found that the disk could withstand an axial field of about 10 MV m^{-1} with a reasonably focused 22 kev electron beam of 1 mA flowing through the central hole, the pressure being about 10^{-5} torr. Instability in the magnitude of the reflected signal at the highest power levels was apparently due to breakdown in small air gaps between disk and wall. However, this breakdown must have caused only slight damage as the Q of the cavity was unaltered, and the effect recurred at the same high power levels in subsequent experiments. Hayes (Report ML4, 1961, Department of Electrical Engineering, University of British Columbia) gives a detailed discussion of dielectric surface breakdown; again, titania and magnesium titanate are the main ceramics under investigation.

7. Further work

Experiments are being continued with multiple disk cavities in which more suitable glazes are used and disk rims are vacuum-coated with copper in an effort to reduce rim breakdown. The effects of using oil-free high vacuum systems and higher beam currents are being investigated at

Oxford. Particular attention is being given to time-varying properties at high power and the troublesome multipactor effect experienced in accelerator structures (Mullett, Clay and Hadden 1957, A.E.R.E. Report GP/R 1076).

Acknowledgments

The authors gratefully acknowledge the support of the following bodies in this work: the Admiralty, the Department of Scientific and Industrial Research, the Paul Fund of the Royal Society, and the Defence Research Board of Canada. Support was also received from the United States Air Force under Grant AF EOAR 62–62 and monitored by the European Office, Office of Aerospace Research.

References

FREE, J. M., 1962, *Special Ceramics*, Ed. P. Popper (London: Academic Press), p. 411.

FREE, J. M., and WALKER, G. B., 1960, *Proc. Instn Elect. Engrs* B, **107**, 354.

WALKER, G. B., and LUTHRA, S. P., 1962, *Proc. Instn Elect. Engrs* B, **109**, 853.

UNWIN BROTHERS LIMITED, WOKING AND LONDON

References

1. CONVERT, G., et al., 'Production et Amplification d'Ondes Millimétriques et Submillimétriques', in 'Microwaves', Proc. 4th International Congress on Microwave Tubes, Scheveningen, Holland, Centrex Publishing Company, Eindhoven (1963).

2. COLEMAN, P.D., 'Spanning the Microwave-Infra-red Gap', Proc. I.R.E., 50, 1219 - 1224, (1962).

3. MOTZ, H., 'Applications of Radiation from Fast Electron Beams', J.App.Phys., 22, 527, (1951).

4. WIDEROE, R., Ark. f. Elektrotech., 21, 287, (1929).

5. SLOAN, D.H. and LAWRENCE, E.O., 'The Production of Heavy High Speed Ions without the Use of High Voltages', Phys. Rev., 38, 2021, (1931).

6. SLOAN, D.H., 'A Radio-Frequency High Voltage Generator', Phys. Rev., 47, 62, (1935).

7. ALVAREZ, L.W., 'Design of a Proton Linear Accelerator', Phys. Rev., 70, 799A, (1946).

8. HALPERN, J., et al., 'Microwave Linear Accelerators', Phys. Rev., 69, 688A (1946).

9. SLATER, J.C., 'The Design of Linear Accelerators', Rev. Mod. Phys., 20, 473-518, (1948).

10. GINZTON, E.L., HANSEN, W.W., and KENNEDY, W.R., 'Linear Electron Accelerator', Rev. Sci. Instr., 19, 89, (1948)

11. FRY, D.W., et al., 'Travelling Wave Linear Accelerator for Electrons', Nature, 160, 351, (1947).

12. WOODYARD, J.R., 'A Comparison of the High Frequency Accelerator and Betatron as a Source of High Energy Electrons', Phys. Rev., 69, 50, (1946).

13. WILLSHAW, W.E., and LAMONT, H.R., 'Notes on a Linear Electron Accelerator operated at 3000 Mc/s', Report No. 8766 (B), General Electric Company, (1945).

14. WALKINSHAW, W., 'Comparison of Partially Filled Dielectric and Corrugated Circular E_o Waveguide', T.R.E. Memo., H/44, (1946).

15. R.-SHERSBY-HARVIE, R.B., 'Theory of Dielectric Loaded Waveguides applied to Linear Electron Accelerators', A.E.R.E. Report EL/R402, (1949).

16. FRANKEL, S., 'TM_{01} Mode in Circular Waveguides with Two Coaxial Dielectrics', J. App. Phys., 18, 650, (1947).

17. PINCHERLE, L., 'Electromagnetic Waves in Metal Tubes filled longitudinally with Two Dielectrics', Phys. Rev., 66, 118 (1944).

18. OLINER, A.A., 'Remarks on Slow Waves in Cylindrical Guides', J. App. Phys., 18, 766, (1947).

19. FLESHER, G.T., and COHN, G.I., 'Dielectric Loading for Waveguide Linear Accelerators', Trans. Amer. I.E.E., 70, Part 1, 887, (1951).

20. COHN, G.I., and FLESHER, G.T., 'Design, Construction, and Initial Operation of a Continuous Dielectric Loaded Linear Accelerator', Electronics Research Labs., Illinois Inst. of Tech., Report No. 2,(1952).

21. BRUCK, G.C., and WICKER, E.R., 'Slow TM Waves in Cylindrical Guides', J. App. Phys., 18, 766, (1947).

22. R.-SHERSBY-HARVIE, R.B., 'A Proposed New Form of Dielectric-Loaded Waveguide for Linear Electron Accelerators', Nature, 162, 890, (1948).

23. R.-SHERSBY-HARVIE, R.B., British Patent Application, No. 9532/48.

24. R.-SHERSBY-HARVIE, R.B., et al., 'A Theoretical and Experimental Investigation of Anisotropic-Dielectric-Loaded Linear Electron Accelerators', Proc. I.E.E., Part B, 104, 273, (1957).

25. WALKER, G.B., and LEWIS, E.L., Nature, 101, 38, (1958).

26. WEST, N.D., Ph.D. Thesis, London University, (1958).

27. HYMAN, J.T., Ph.D. Thesis, London University, (1957).

28. MULLETT, L.B., CLAY, R.E., and HADDEN, R.J.B., 'Multipactor Effect in Linear Accelerators and other Evacuated R.F. Systems, and a New Cold Cathode Valve', A.E.R.E. Report GP/R1076, (1953).

29. WALKER, G.B., and WEST, N.D., 'Mode Separation at the π-Mode in a Dielectric Loaded Waveguide Cavity', Proc. I.E.E., Part C, 104, 381, (1957).

30. MOTZ, H., and WALSH, D., 'Undulator Experiment', Proc. Third International Conference on Microwave Tubes (U.R.S.I.), Munich, 242, (1960).

31. LICHTENBERG, A.J., ARMSTRONG, A.G., FREE, J.M., MOFFAT, M.F.B., Engineering Laboratory Report, Oxford University, November, 1960.

32. MOTZ, H., THON, W., and WHITEHURST, R.N., 'Experiments on Radiation by Fast Electron Beams', J. App. Phys., 24, 826, (1953).

33. THON, W., 'Design and Operation of Magnetic Undulators', Report M.L.262, Stanford University, (1955).

34. MOTZ, H., and MALLORY, K.B., 'Generation of Sub-Millimetre Waves', J. App. Phys., 26, 1384, (1955).

35. COMBE, R., 'Réalisation d'un Accélérateur Linéare d'Électrons. Application à la Production d'Ondes Millimétriques', Theses de l'Université de Paris, (1956).

36. MOTZ, H., 'Cerenkov and Undulator Radiation', Trans. I.R.E., AP4, 374, (1956).

37. SIRKIS, M.D., and COLEMAN, P.D., 'The Harmodotron - a Megavolt Electronics Millimetre Wave Generator', J.App.Phys., 28, 944-950, (1957).

38. WHITEHURST, R.N., 'A Study of the Generation of Sub-Millimetre Radiation by High Energy Electrons,' Report M.L.443, Stanford University, (1958).

39. SZENTE, P.A., 'Generation of Sub-Millimetre Radiation by a Bunched Beam of Relativistic Electrons', Report M.L.935, Stanford University, (1962).

40. WALSH, D., 'Generation of Coherent Millimetre Waves', D.Phil.Thesis, Oxford University, (1961).

41. See Ref. 30.

42. ISING, G., Ark. f. Matematik och Fysik, 18, No.30, (1924).

43. FRY, D.W., et al., 'A Travelling-Wave Linear Accelerator for 4 MeV Electrons', Nature, 162, 859, (1948).

44. MULLETT, L.B., and LOACH, B.G., 'Experimental Work on Corrugated Waveguides and Associate Components for Linear Electron Accelerators', Proc. Phys. Soc., 61, 271, (1948).

45. MALLORY, K.B., 'A Comparison of the Predicted and Observed Performance of a Billion-Volt Electron Accelerator', Report H.E.P.L.46, Stanford University, (1955).

46. HADDEN, R.J.B., 'Linear Electron Accelerator with a Dielectric Loaded Waveguide', A.E.R.E. Report No. GP/R1161, (1953).

47. (See also Ref. 74) MILLER, C.W., Nature, 171, 297, (1953).

48. CHU, E.L., and HANSEN, W.W., 'The Theory of Disk-Loaded Waveguides', J. App. Phys., 18, 996-1008, (1947).

49. WALKINSHAW, W., 'Theoretical Design of Linear Accelerator for Electrons', Proc. Phys. Soc., 61, 246, (1948).

50. R.-SHERSBY-HARVIE, R.B., 'Travelling Wave Linear Accelerators', Proc. Phys. Soc., 61, 255, (1948).

51. WALKINSHAW, W., T.R.E. Report M/118/WW (AE1005), (1947).

52. ADLAM, J.H., and ROSS, M., 'An Electromagnetic Resonator for Measuring the Dielectric Constant and Dielectric Power Factor of Low-Loss Ceramic Dielectrics', A.E.R.E. Report G/R 949, (1952).

53. FREE, J.M., and WALKER, G.B., 'Determination of the Dielectric Properties of Low-Loss Ceramics at Q-Band Frequencies', Proc. I.E.E., 107, Part B, 354, (1960).

54. SLATER, J.C., 'Microwave Electronics', Van Nostrand, Princeton, (1950).

55. FRY, D.W., and WALKINSHAW, W., 'Linear Accelerators', Reports on Progress in Physics, 12, 102, (1949).

56. NEWBERY, G.R., and WILLSHAW, W.E., Nature, 161, 519, (1948).

57. MULLETT, L.B., 'Dielectric Loaded Waveguides for Linear Electron Accelerators at 10 cm Wavelength', A.E.R.E. Report G/R 448, (1950).

58. R.-SHERSBY-HARVIE, R.B., A.E.R.E./T.R.E. Memo. S1/M20/RBRSH, (1948).

59. WALKER, G.B., and ENGELFIELD, C.G., 'An Apparent Anomaly in the Group and Energy Velocity in a Dielectrically Loaded Slow-Wave Structure', Trans. I.R.E., MTT-10, 30, (1962).

60. WALKER, G.B., 'Dielectric for Tube Windows and Slow Wave Structures', Report M.L. 2, University of British Columbia, (1960).

61. LICHTENBERG, A.J., 'The Application of Phase Space Concepts to the Design of an Electron Linac Buncher', Technical Report No. 9, Engineering Lab., Oxford University, (1962).

62. LICHTENBERG, A.J., D.Phil.Thesis, Oxford, (1961).

63. JOHNSEN, K., 'On the Theory of the Linear Accelerator', Chr. Michelsens Institutt, Bergen, (1954).

64. NEAL, R.B., 'Design of Linear Electron Accelerators with Beam Loading', Report M.L.379, Stanford University, (1957).

65. BELL, J.S., and WALKINSHAW, W., 'Review of Theory of Dielectric Loaded Linear Accelerator', A.E.R.E. Report G/R 544, (1950).

66. BRUCE, J.M., and WALKINSHAW, W., 'Guide Dimensions for 1 metre Dielectric Loaded Accelerator', A.E.R.E. Memo. G/M 42, (1950).

67. FREE, J.M., D.Phil.Thesis, Oxford, (1962).

68.* FREE, J.M., MOFFAT, M.E.B., and WALKER, G.B., 'Dielectric Properties of Titania Ceramics at Microwave Frequencies', Brit. J. App. Phys., 14, 289-291, (1963).

69. WRIGHT, D.A., in Encyclopaedic Dictionary of Physics, Ed. THEWLIS, J., Pergamon, Oxford, (1962).

70. DUSHMAN, S., Scientific Foundations of Vacuum Technique', Wiley, New York, (1949).

71. (See also Ref. 84) HAYES, R., 'Phenomena Associated with Electrical Breakdown at Certain Dielectric Surfaces in Vacua', Report M.L. 4, University of British Columbia, (1961).

72. VON HIPPEL, A., (Editor) 'Dielectric Materials and Applications', M.I.T. and Wiley, (1954).

73. R.-SHERSBY-HARVIE, R.B., and MULLETT, L.B., 'A Travelling-Wave Linear Accelerator with R.F. Power Feedback, and an Observation of R.F. Absorption by Gas in Presence of a Magnetic Field', Proc. Phys. Soc., B, 62, 270, (1949).

74. MILLER, C.W., and SAXON, G., 'Effect of Anomalous Attenuation in a Linear Accelerator', 172, 463, (1953).

75. HAYES, R., 'Vacuum Breakdown at Dielectric Surfaces', Report M.L. 3, University of British Columbia, (1960).

76. COLEMAN, P.D., 'State of the Art : Background and Recent Developments - Millimeter and Submillimeter Waves', Trans. I.E.E.E., MTT-11, 271, (1963).

77. ADLAM, J.H., JAMES, F.H., and MULLETT, L.B., 'A Method of Measuring the Q-factor of an Electromagnetic Mode in a Resonator, employing a Frequency-Modulated Klystron', A.E.R.E. Report G/R 767, (1951).

* Appendix V

78. BLANC-LAPIERRE, A., et al., L'Onde Electrique, Issue on the 1 GeV Orsay Linear Accelerator, No. 435, June,(1963).

79. MARGENAU, H., and MURPHY, G.M., 'The Mathematics of Physics and Chemistry', Van Nostrand, New York (1943).

80. FREE, J.M., 'Special Ceramics', p. 411, Ed. POPPER, P., Academic Press, London, (1962).

81. LICHTENBERG, A.J., MOFFAT, H.E.B., and MOTZ, H., 'Production of a Highly Bunched Beam for a Submillimetre Wave Undulator', in 'Microwaves', Proc. 4th International Congress on Microwave Tubes, Scheveningen, Holland; Centrex Publishing Company, Eindhoven,(1963).

82. SOUTHWELL, R.V., 'Relaxation Methods in Engineering Science', Oxford University Press, (1940).

83. DUNSHEATH, P., 'High Voltage Cables', Pitman, London, (1929).

84. HAYES, R., and WALKER, G.B., Proc. I.E.E., 111, 600, (1964).

85. MARCUVITZ, N., 'Waveguide Handbook', McGraw-Hill, New York, (1951).

86. NEAL, R.B., 'A High-Energy Linear Electron Accelerator', Report M.L. 185, Stanford University, (1953).

87. COLEMAN, P.D., and ENDERBY, C., 'Megavolt Electronics Cerenkov Coupler for the Production of Millimetre and Sub-Millimetre Waves', J. App. Phys., 31, 1695-1696, (1960).

88. COLEMAN, P.D., 'Theory of the Rebatron - a Relativistic Electron Bunching Accelerator for Use in Megavolt Electronics', J. App. Phys., 28, 927-935, (1957).

89. FROELICH, H., 'Theory and Design of a Racetrack Microtron with Application to the Generation of Millimeter Waves', Ph.D. Thesis, University of Western Ontario, London, Ont., Canada, (1962).

Principal Symbols Used

Rationalised m.k.s. units are used unless otherwise stated.

a	Disc hole radius; Broad dimension of rectangular waveguide; Special parameter (Ch. IV).
b	Ratio of dielectric thickness to periodic length (pitch); Narrow dimension of rectangular waveguide.
'b ratio'	Ratio of experimental value of b to theoretical value of b for a given wave velocity.
c	Velocity of light; Radius of loading disc
e	Base of natural logarithms; Electronic charge
f	Frequency
g	Half disc thickness
h	Half space between discs
j	$\sqrt{-1}$
k	$2\pi/\lambda$
k_1	Radial propagation constant
ℓ	Structure length; Drift distance (Section 4.3.2)
ℓ_a	Attenuation limited length
ℓ_o	Loss length
ℓ_{opt}	Optimum length
m	Integer; Mass of particle
m_o	Rest mass of particle
n	Integer; Feedback ratio
p	Momentum; Propagation constant
r_{sh}	Shunt impedance
r_{se}	Series impedance
s	Subscript denoting synchronous value
t	Time
t_f	Filling time
v, v_{ph}	Phase velocity
v_b	Beam velocity; Particle velocity (Ch. IV)
v_g	Group velocity
v_s	Synchronous phase velocity

x	Rectangular co-ordinate; Feedback loss
y	Rectangular co-ordinate
z.	Axial displacement co-ordinate
A	Field amplitude
B_ρ, B_ϕ, B_z	Cylindrical components of magnetic flux density
D_ρ, D_ϕ, D_z	Cylindrical components of electric flux density
E_ρ, E_ϕ, E_z	Cylindrical components of electric field
E_s	Accelerating field
E_{ms}	Field amplitude of synchronous wave
E_{mso}	E_{ms} at output from buncher
H_ρ, H_ϕ, H_z	Cylindrical components of magnetic field
$\mathcal{H}$	Hamiltonian function
I	Beam pulse current
$I_m(\ )$	Bessel function, first kind, order m, imaginary argument
$J_m(\ )$	Bessel function, first kind, order m, real argument
L	Periodic length
P	Power flux
P_1	P at input to structure
P_d	Power dissipated per unit length
P_s	Power delivered by source
Q	Q-factor of resonant cavity
Q_o	Unloaded Q-factor
Q_L	Loaded Q-factor
Q_1	'Q per unit length'
R	Axial ratio of phase plane ellipse
S	Field amplitude
S.W.	Standing Wave
T.W.	Travelling Wave
U	Stored energy in cavity or per unit length of T.W. structure; Total energy of particle
U_o	Rest energy of particle
U_s	Kinetic energy of phase stable particle

V	Voltage; Volume
V.S.W.R.	Voltage Standing Wave Ratio
W	Power dissipated in resonant cavity
$Y_m( )$	Bessel function, second kind, order m, real argument
Z_o	Impedance of free space $(\mu_o/\epsilon_o)^{\frac{1}{2}}$
α	Reciprocal of loss length; Constant
β	Phase constant
γ	v_b/c; Propagation constant
δ	Dielectric loss angle
ϵ	Absolute permittivity; Arbitrary constant
ϵ_o	Permittivity of free space $(36\pi \times 10^9)^{-1}$
$\epsilon_\rho, \epsilon_\phi, \epsilon_z$	Components of anisotropic permittivity
η	Efficiency; Relative permeability
η'	Figure of merit
κ	Relative permittivity
λ	Free space wavelength
λ_c	Cut-off wavelength
λ_g	Guide wavelength
μ	Absolute permeability
μ_o	Permeability of free space $(4\pi \times 10^{-7})$
ρ	Radial cylindrical co-ordinate; Electrical resistivity
σ	Electrical conductivity; Standard deviation
ϕ	Phase angle; Angular cylindrical co-ordinate
X	Bunching parameter; Radial propagation constant
ω	Angular frequency
ω_o	Angular frequency of phase oscillations
Γ	Radial propagation constant
Δx	Small increment in x.